Winter 2015

Measurement of the Drell--Yan differential cross section with the CMS detector at the LHC

Alexey Svyatkovskiy
Purdue University

Recommended Citation

Svyatkovskiy, Alexey, "Measurement of the Drell--Yan differential cross section with the CMS detector at the LHC" (2015). *Open Access Dissertations*. 564.
https://docs.lib.purdue.edu/open_access_dissertations/564

Graduate School Form 30
Updated 1/15/2015

PURDUE UNIVERSITY
GRADUATE SCHOOL
Thesis/Dissertation Acceptance

This is to certify that the thesis/dissertation prepared

By Alexey Svyatkovskiy

Entitled
MEASUREMENT OF THE DRELL-YAN DIFFERENTIAL CROSS SECTION
WITH THE CMS DETECTOR AT THE LHC

For the degree of Doctor of Philosophy

Is approved by the final examining committee:

Norbert Neumeister Chair	Matthew Jones
Sergei Khlebnikov	
Denes Molnar	
Robert Skeel	

To the best of my knowledge and as understood by the student in the Thesis/Dissertation Agreement, Publication Delay, and Certification Disclaimer (Graduate School Form 32), this thesis/dissertation adheres to the provisions of Purdue University's "Policy of Integrity in Research" and the use of copyright material.

Approved by Major Professor(s): Norbert Neumeister

Approved by: Andrew Hirsch 2/27/2015
Head of the Departmental Graduate Program Date

MEASUREMENT OF THE DRELL–YAN DIFFERENTIAL CROSS SECTION WITH THE CMS DETECTOR AT THE LHC

A Dissertation

Submitted to the Faculty

of

Purdue University

by

Alexey Svyatkovskiy

In Partial Fulfillment of the

Requirements for the Degree

of

Doctor of Philosophy

May 2015

Purdue University

West Lafayette, Indiana

To my parents, Ekaterina Svyatkovskaya and Vladimir Svyatkovskiy.

ACKNOWLEDGMENTS

First of all, I would like to thank Norbert Neumeister for his support and guidance over all these years. He has always provided insightful discussions about the research and taught me a lot of things about scientific approach and methods. Working with him was truly a character building experience. Special thanks to my Purdue colleagues and friends Adam Everett and Hwidong Yoo for their patience, help and advice on a day to day basis, which was especially helpful in the beginning of my graduate studies. I cannot imagine completing my graduate studies without their help. I would also like to thank David Miller for mentoring and teaching me a number of things about scientific writing.

Next, I would like to thank all my friends and collaborators in CMS. I have had a pleasure to meet and work with a number of smart and intelligent people throughout my graduate studies who have shared their profound knowledge with me and taught me a lot of things I know today. The list includes but is not limited to the following: Stoyan Stoynev, Ilya Kravchenko, Slava Krutelyev, Giovanni Abbiendi, Dimitri Bourilkov, Juan Rojo and Georgios Daskalakis.

Finally, I would like to give special thanks to my parents who continue to support me and do anything to make my life better. I would also like to thank all my friends at Purdue who gave me strength and happiness through these years.

TABLE OF CONTENTS

LIST OF TABLES

LIST OF FIGURES

ABSTRACT

Svyatkovskiy, Alexey Ph.D., Purdue University, May 2015. Measurement of the Drell–Yan Differential Cross Section with the CMS Detector at the LHC. Major Professor: Norbert Neumeister.

This thesis describes precision measurements of electroweak interactions in a new energy regime and the application of these measurements to improve our understanding of the structure of the proton. The results are based on proton-proton collision data at $\sqrt{s} = 7$ and 8 TeV recorded with the Compact Muon Solenoid detector at the CERN Large Hadron Collider during the first years of operation. Measurements of the differential Drell–Yan cross section in the dimuon and dielectron channels covering the dilepton mass range of 15 to 2000 GeV and absolute dilepton rapidity from 0 to 2.4 are presented. The Drell–Yan cross section in proton-proton collisions depends on empirical quantities known as parton distribution functions (PDFs) which parameterize the structure of the proton. In addition to the differential cross sections, the measurements of ratios of the normalized differential cross sections (double ratios) at $\sqrt{s} = 7$ and 8 TeV are performed in order to provide further constraints for PDFs, substantially reducing theoretical systematic uncertainties due to correlations. These measurements are compared to predictions of perturbative QCD at the next-to-next-to-leading order computed with various sets of PDFs. The measured differential cross section and double ratio in bins of absolute rapidity are sufficiently precise to constrain the proton parton distribution functions. The inclusion of Drell–Yan data in PDF fits provides substantial constraints for the strange quark and the light sea quark distribution functions in a region of phase space which has not been accessible at hadron colliders in the past.

1. INTRODUCTION

The Standard Model (SM) of particle physics has been successfully tested in a wide variety of experiments. Despite this striking success, it is conceptually incomplete as it does not provide consistent answers to several questions. Among the questions that are still not answered within the SM are the large hierarchy in energy scales [1–3], the presence of dark matter in the universe [4], and the origin of the many fundamental parameters [5]. For deeper understanding of the properties of existing elementary particles and for the discovery of physics beyond the SM high-energy particle accelerators are utilized. In particular, the Large Hadron Collider (LHC) provides collisions at TeV energies and currently has the highest energy and the highest intensity beams in the world.

The Compact Muon Solenoid (CMS) experiment is one of two major experiments at the LHC at CERN. The new energy frontier probed by the LHC and the large data samples collected made it possible to re-measure the parameters of SM of particle physics with high precision and to discover new physics. Currently many precision measurements at the LHC are limited by our knowledge of the structure of the proton, which is described by so-called parton distribution functions (PDFs). To overcome this limitation new PDFs based on LHC measurements are needed.

Electroweak boson production is an important benchmark process at hadron colliders and events containing W and Z bosons appear as dominant components in Higgs searches and in most of the searches for physics beyond the SM, either as signal or as background. The Drell–Yan (DY) lepton pair production is a fundamental process well established in the SM up to the next-to-next-to-leading order (NNLO) in perturbative quantum chromodynamics (QCD) [6–9]. At hadron colliders, the DY dilepton production at tree level is described by s-channel γ^*/Z exchange. The PDFs provide the essential link between the theoretically calculated partonic cross sections, and the experimentally measured physical cross sections involving hadrons. This link is crucial for incisive tests of the SM, and searches for subtle deviations which might signal new physics beyond the SM. It is not possible to calculate PDFs within perturbative QCD. The DY process provides valuable information on PDFs in the proton and may be used to constrain the parton distribution functions in general, and the strange quark PDF, in particular.

The rapidity and the invariant mass of the dilepton system produced in proton-proton collisions are related at leading order to the longitudinal momentum fractions (Bjorken scaling variables) x_+ and x_- carried by the two interacting partons according to the formula $x_\pm = (m/\sqrt{s})e^{\pm y}$. The high center-of-mass energy at the CERN LHC permits the study of DY production in regions of the Bjorken scaling variables $x_\pm$ and the evolution scale $Q^2 = x_+ x_- s$ that were not accessible in previous experiments [10–15]. The present analysis covers the ranges $0.0003 < x_\pm < 1.0$ and $600 < Q^2 < 750000\,\mathrm{GeV}^2$ in the double-differential cross section measurement. The differential cross section $d\sigma/dm$ is measured in an even wider range $300 < Q^2 < 3000000\,\mathrm{GeV}^2$.

It provides between 5–30% smaller statistical uncertainty as compared to the previous measurements due to large sample sizes collected by CMS, 1–25% reduced systematic uncertainty achieved by using data-driven analysis techniques, and it is the most precise measurement of the cross section in the Z peak region at $\sqrt{s} = 7$ and 8 TeV in CMS.

Measuring the DY cross-section provides a way to test and verify the SM predictions at a high level of precision. Besides the PDF constraints, a number of predictions can be extracted from DY dilepton analysis including the precise transverse momentum, invariant mass measurements and the measurements of angular distributions of DY dileptons. Measuring the DY differential cross section in bins of invariant mass is important for various LHC physics analyses. Indeed, DY events pose a major source of background for processes such as top quark pair production and diboson production, as well as for searches for new physics beyond the SM, such as the production of high-mass dilepton resonances.

Imperfect knowledge of PDFs is the dominant source of theoretical systematic uncertainties on the DY cross section predictions at low mass. The corresponding uncertainty is larger than the achievable experimental precision, making the double-differential cross section and the double ratio measurements in bins of rapidity an effective tool for PDF constraints. The current knowledge of the PDFs and the importance of the LHC measurements are reviewed in [16,17]. The inclusion of DY cross section and double ratio data in PDF fits is expected to provide substantial constraints for the strange quark and the light sea quark PDFs in the small Bjorken x region ($0.001 < x < 0.1$).

The increase in the center-of-mass energy at the LHC from 7 to 8 TeV provides the opportunity to measure the ratios of cross sections and double-differential cross sections of various hard processes, including the DY process. Measurements of the DY process in proton-proton collisions depend on various theoretical parameters such as the QCD running coupling constant, renormalization and factorization scales and a choice of PDFs. The theoretical systematic uncertainties in the cross section calculations for a given process at different center-of-mass energies are substantial but correlated, so the ratios of differential cross sections normalized to the Z boson production cross section (double ratios) can be predicted very precisely [18].

This thesis presents the measurements of the differential and double-differential Drell–Yan cross sections, based on proton-proton collision data recorded with the CMS detector at the LHC. The differential cross section measurements are performed in the dielectron and dimuon channels over the mass range 15 to 1500 GeV at 7 TeV [19], and the mass range 15 to 2000 GeV at 8 TeV [20] center-of-mass energy. The double-differential cross section $d^2\sigma/dm\,d|y|$ is measured in the mass range 20 to 1500 GeV and absolute dilepton rapidity from 0 to 2.4. The measurement in the dimuon channel only is performed at 7 TeV while both channels are considered at 8 TeV center-of-mass energy. Integrated luminosities of $4.8\,\mathrm{fb}^{-1}$ (dielectron) and $4.5\,\mathrm{fb}^{-1}$ (dimuon) at $\sqrt{s} = 7\,\mathrm{TeV}$, and $19.7\,\mathrm{fb}^{-1}$ at $\sqrt{s} = 8\,\mathrm{TeV}$ are used for the measurements. In addition, the ratios of the normalized differential cross sections measured at $\sqrt{s} = 7$ and $8\,\mathrm{TeV}$ are presented.

An efficient and robust muon reconstruction is an important prerequisite for performing these measurements. Careful understanding and proper treatment of the detector misalignment effects and alignment position uncertainties is important for accurate reconstruction of high-p_{T} muons. A study of the alignment position errors (APEs) and proper implementation of the full APE covariance matrix in the muon reconstruction software has been performed.

This thesis is arranged in the following order: after this brief introduction, a general theoretical background and motivation for high-energy physics research are presented in Chapters 2-4. The design and performance of the LHC and the CMS detector are described in Chapter 5. In Chapter 6, the Drell–Yan analysis procedure and methods are described in detail and the results of the measurements are presented and discussed. Finally, in Chapter 7 the PDF constraints with DY experimental data are summarized. A set of appendices is included in the thesis to better document various aspects of the DY analysis.

2. STANDARD MODEL OF PARTICLE PHYSICS

2.1 Fundamental Constituents of Matter and Interactions

The fundamental constituents of matter are quarks and leptons. They have a half-integer spin and are fermions. All known hadrons are constructed from 6 types of quarks. All the known quarks and leptons form 3 families each containing 4 elementary particles. The first family contains the building blocks of all ordinary matter while the second and third families are heavier copies of the first. Each lepton family together with the corresponding family of quarks forms a multiplet known as generation. The classification of fermions can be seen in Table 2.1. The SM is based on the principle of local gauge symmetry under the gauge group $SU(3)_c \times SU(2)_L \times U(1)_Y$. Leptons all have negative electric unit charge whereas neutrinos carry no electric charge. Quarks carry fractional electric charge: up, charm and top quarks have an electric charge equal to 2/3 and down, strange and bottom quarks have an electric charge equal to -1/3. There is a quantum number called “flavor” associated with each quark type. Fermion charges related to the strong interactions of the particles are called colors. Each quark exists in a certain color state, however, the observed hadrons are always colorless.

Table 2.1
The three generations of spin $\frac{1}{2}$ particles.

charge	-1	-2/3	-1/3	0	+1/3	+2/3	+1
1^{st} family	e^-	$\bar{\mathrm{u}}$	d	$\nu_\mathrm{e}, \bar{\nu}_\mathrm{e}$	$\bar{\mathrm{d}}$	u	e^+
2^{nd} family	μ^-	$\bar{\mathrm{c}}$	s	$\nu_\mu, \bar{\nu}_\mu$	$\bar{\mathrm{s}}$	c	μ^+
3^{rd} family	τ^-	$\bar{\mathrm{t}}$	b	$\nu_\tau, \bar{\nu}_\tau$	$\bar{\mathrm{b}}$	t	μ^+

Particles having an integer spin are referred to as bosons. In the Standard Model of particle physics, the gauge bosons are responsible for mediation of interactions between fermions, while the scalar Higgs boson H [21] is responsible for providing the non-zero masses to fermions and $W^{\pm}$ and Z bosons. The gauge bosons are summarized in Table 2.2 and the Higgs boson is discussed in Section 2.2.1 in detail.

Table 2.2
The four forces and their associated gauge bosons. Charge is in units of the proton charge.

Force	Boson	Charge	Mass
Gravitational	graviton(G)	0	?
Electromagnetic	photon(γ)	0	0
Weak	W boson($W^{\pm}$)	±1	81 GeV
	Z boson(Z)	0	92 GeV
Strong	gluon(g)	0	0

Within the SM, elementary particles can participate in strong, electromagnetic and weak interactions. Gravity is essential only for very massive objects and at very high energies which cannot be obtained in current laboratory experiments. Each fundamental interaction is characterized by its range and is described by a corresponding gauge theory which determines the particles participating in a given interaction and the gauge mediators.

2.2 Electroweak Interactions

Quantum Electrodynamics (QED) is a quantum field theory that describes the electromagnetic interaction. It is based on the abelian gauge group $U(1)_{\mathrm{EM}}$. The quantum number in this theory that is conserved is the electric charge Q. Local invariance under the $U(1)_{\mathrm{EM}}$ group leads to a massless vector boson which is the photon.

The theory of electroweak (EW) interactions is the unified theory of two of the four known fundamental interactions: electromagnetism and the weak interaction. It was constructed in the 1960s by S. Glashow, S. Weinberg, A. Salam, M. Veltman and G. t'Hooft [5, 22–24]. The EW theory is based on the Yang–Mills model with the non-abelian gauge group $SU(2)_I \times U(1)_Y$. The $SU(2)_I$ group of weak isospin has three generators $t^a = \frac{1}{2}\tau^a$ (where τ^a with $a = 1,\ 2,\ 3$ are the Pauli matrices) which satisfy the following commutation and normalization relations:

$$[t^a, t^b] = i\epsilon^{abc}t^c, \quad \mathrm{Tr}(t^a t^b) = \frac{1}{2}\delta^{ab}. \tag{2.1}$$

The weak hypercharge Y is the generator of the $U(1)_Y$ group. The electric charge Q, the third component of the weak isospin I_3, and the hypercharge satisfy the following equation:

$$Q = I_3 + \frac{Y}{2}. \tag{2.2}$$

The Lagrangian density of the EW theory can be written as a sum of four terms:

$$\mathcal{L} = \mathcal{L}_{\text{gauge}} + \mathcal{L}_{\text{matter}} + \mathcal{L}_{\text{Higgs}} + \mathcal{L}_{\text{Yukawa}}. \tag{2.3}$$

The part of the Lagrangian describing the gauge fields is given by:

$$\mathcal{L}_{\text{gauge}} = -\frac{1}{4}\mathrm{Tr}(W_{\mu\nu}W^{\mu\nu}) - \frac{1}{4}B_{\mu\nu}B^{\mu\nu}, \tag{2.4}$$

here, the field tensors $B_{\mu\nu}$ and $W_{\mu\nu}$ are defined as:

$$B_{\mu\nu} = \partial_\mu B_\nu - \partial_\nu B_\mu, \quad W_{\mu\nu} = \partial_\mu W_\nu - \partial_\nu W_\mu - ig[W_\mu, W_\nu] = W^a_{\mu\nu}t^a, \tag{2.5}$$

where g is the $SU(2)_I$ gauge coupling constant.

The real observable particles in the EW theory – the photon, Z and W$^\pm$ bosons – responsible for mediation of EW interactions, are expressed as linear combinations of the abelian gauge field B_μ and the non-abelian gauge fields W^a_μ ($a = 1,\ 2,\ 3$) as:

$$\text{photon:} \quad A_\mu = \sin\theta_{\text{W}} W_{3\mu} + \cos\theta_{\text{W}} B_\mu, \tag{2.6}$$

$$\text{Z:} \quad Z_\mu = -\cos\theta_{\text{W}} W_{3\mu} + \sin\theta_{\text{W}} B_\mu, \tag{2.7}$$

and

$$\mathrm{W}^{\pm}: \quad W^{\pm}_{\mu} = \frac{W_{1\mu} - W_{2\mu}}{\sqrt{2}}. \tag{2.8}$$

The Weinberg angle θ_{W} is defined in terms of the EW coupling constants as:

$$\sin\theta_{\mathrm{W}} = \frac{g'}{\sqrt{g'^2 + g^2}}, \quad \cos\theta_{\mathrm{W}} = \frac{g}{\sqrt{g'^2 + g^2}}, \tag{2.9}$$

where g' is the weak hypercharge coupling constant.

The term in the Lagrangian describing the interactions of the quarks and leptons reads as (assuming zero neutrino mass):

$$\mathcal{L}_{\mathrm{matter}} = \sum_{\mathrm{generations}} [i\bar{L}\not{D}L + i\bar{Q}\not{D}Q + i\bar{u}_R\not{D}u_R + i\bar{d}_R\not{D}d_R + i\bar{e}_R\not{D}e_R], \tag{2.10}$$

where the fields Q and L – for quarks and leptons – belong to fundamental representations of the gauge group $SU(2)_I$. The fermion fields having negative helicity are referred to as left-handed (L), while fermions having positive helicity are referred to as right-handed (R). The fields Q and L are $SU(2)_I$ doublets:

$$Q = \psi_L = \begin{pmatrix} \psi_L^{(u)} \\ \psi_L'^{(d)} \end{pmatrix} \quad L = \psi_L = \begin{pmatrix} \psi_L'^{(\nu)} \\ \psi_L^{(e)} \end{pmatrix},$$

where $\psi_L^{(u)}$ is the field describing the physical u quark, and $\psi_L'^{(d)}$ is the linear combination of the fields describing the physical d, s and b quarks obtained via a unitary transformation (performed by the Cabibbo-Kabayashi-Maskawa matrix [25,26]). Analogously, $\psi_L'^{(\nu)}$ is a linear combination of neutrino states with definite mass, and the $\psi_L^{(e)}$ is the field describing the electron. The spinors $\bar{u}_R$, u_R, $\bar{d}_R$, d_R, $\bar{e}_R$, and e_R for the right-handed fermions transform as singlets under the action of group the $SU(2)_I$.

The notation $\not{D} = \gamma^{\mu}D_{\mu}$ is used as a shorthand throughout the text, where D_{μ} denotes the covariant derivative defined as:

$$D_{\mu} = \partial_{\mu} - ig\frac{\vec{\tau}}{2}\vec{W}_{\mu} - ig'\frac{Y}{2}B_{\mu}, \tag{2.11}$$

here, g and g' are the gauge coupling constants for the non-abelian and abelian interactions correspondingly and γ^{μ} are the Dirac matrices.

2.2.1 The Higgs Mechanism

According to the EW theory, $W^{\pm}$ and Z boson masses appear as a result of the spontaneous symmetry breaking $SU(2)_I \times U(1)_Y \to U(1)_{\mathrm{EM}}$, and fermions acquire mass as a result of the Yukawa interactions of the corresponding massless fields with the Higgs boson H [21]. Introducing a mass term in the EW Lagrangian for the gauge bosons would violate gauge invariance. However, to agree with experimental observations, some of the gauge bosons must have mass. Introducing the complex scalar doublet ϕ, which can be written as:

$$\phi = \begin{pmatrix} \varphi^+ \\ \varphi^0 \end{pmatrix},$$

is providing the non-zero masses to fermions and vector bosons with the use of the Higgs mechanism related to the appearance of its vacuum condensate as a result of the spontaneous breaking of the $SU(2)_I \times U(1)_Y$ gauge symmetry to the $U(1)_{\mathrm{EM}}$ symmetry [27]. The corresponding scalar fields φ^+ and φ^0 have the quantum numbers as shown in Tab. 2.3.

Table 2.3
Electric charge (Q), isospin (I_3), and hypercharge (Y) of the ϕ field.

	Q	I_3	Y
φ^+	1	$^1/_2$	1
φ^0	0	$-^1/_2$	1

The Higgs field is introduced in the Eq. (2.3) using the following term:

$$\mathcal{L}_{\mathrm{Higgs}} = |D_\mu \phi|^2 + V(\phi^+\phi), \tag{2.12}$$

Where the potential has the form:

$$V(\phi^+\phi) = \mu^2 \phi^+\phi - \lambda(\phi^+\phi)^2 \tag{2.13}$$

and is shown in Fig. 2.1. The parameter λ is the corresponding self-coupling for the

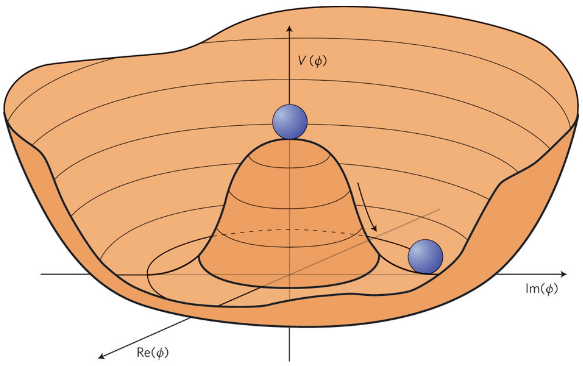

Figure 2.1. An effective potential, $V(\phi)$, leading to the spontaneous symmetry breaking.

Higgs field.

The last term in the Eq. (2.3) describes the interaction of the (scalar) Higgs field with the fermions:

$$\mathcal{L}_{\text{Yukawa}} = \sum_{\text{generations}} [-\lambda_e \bar{L}\phi e_R - \lambda_d \bar{Q}\phi d_R - \lambda_u \epsilon^{ab}\bar{Q}_a \phi_b^{+} u_R + h.c.] \tag{2.14}$$

where ϵ^{ab} is the completely asymmetric tensor with $\epsilon^{12} = 1$ ($a, b = 1, 2$ are the spinor indices). The parameters $\lambda_{e,d,u}$ are the Yukawa coupling constants of the scalar Higgs field to products of a right and a left-handed fermion field.

Only left-handed fermion fields interact with the Yang–Mills fields W_μ^a, and quarks and leptons with both helicities interact with the abelian field B^μ.

Three independent linear combinations of these four gauge-boson fields W_μ^a and B_μ acquire mass as a result of the Higgs mechanism of spontaneous symmetry breaking, while one remains massless. The three massive gauge bosons are the W$^\pm$ bosons mediating the charged weak current, and the Z boson mediating the neutral weak current. The massless boson is identified as the photon of the electromagnetic interaction.

The experimental evidence of the EW interactions was obtained with the discovery of neutral currents in neutrino scattering by the Gargamelle collaboration in 1973 [28, 29], and the discovery of the $W^{\pm}$ and Z gauge bosons in proton-antiproton collisions at the Super Proton Synchrotron in 1983 by the UA1 and the UA2 collaborations [30–32].

The existence of the SM Higgs boson was still not verified at the start up of the LHC. Direct searches for the Higgs have mostly come from the Large Electron-Positron Collider (LEP) at CERN and the Tevatron at Fermilab. This search has been a driving force in high-energy experiments for the last several decades. LEP preformed direct searches and excluded a Higgs boson with a mass below 114.4 GeV at a 95% C.L. [33].

The searches of the SM Higgs boson have been continued by the ATLAS and the CMS collaborations at the LHC considering five decay modes: $\gamma\gamma$, ZZ, W^+W^-, $\tau^+\tau^-$, and $b\overline{b}$. In 2012 an excess of events was observed above the expected background, with a local significance of 5.0 standard deviations, at a mass near 125 GeV, signaling the production of the Higgs boson [34, 35], as shown in Fig. 2.2. The most significant excess was observed in the two decay modes with the best mass resolution, $\gamma\gamma$ and ZZ.

2.3 Quantum Chromodynamics

Quantum chromodynamics is a theory of strong interactions – the color forces. It is described by a gauge theory based on the Yang–Mills model with the non-abelian gauge group $SU(3)_c$ of color.

The QCD Lagrangian has the form:

$$\mathcal{L} = -\frac{1}{4}F^a_{\mu\nu}F^{\mu\nu a} + \sum_n \bar{\psi}_n(i\not{D} - m_n)\psi_n, \tag{2.15}$$

here, n=1,...,6 is a flavor index. The summation runs over the 8 generators of the corresponding gauge group $SU(3)_c$, and the quark field fermion multiplets $\psi_{i,j}$ $(i, j = 1, 2, 3)$ belong to its irreducible representation.

The field strength tensor for the spin-1 gluon fields A^a_ν is given by:

$$F^a_{\mu\nu} = \partial_\mu A^a_\nu - \partial_\nu A^a_\mu - g_s f^{abc} A^b_\mu A^c_\nu \tag{2.16}$$

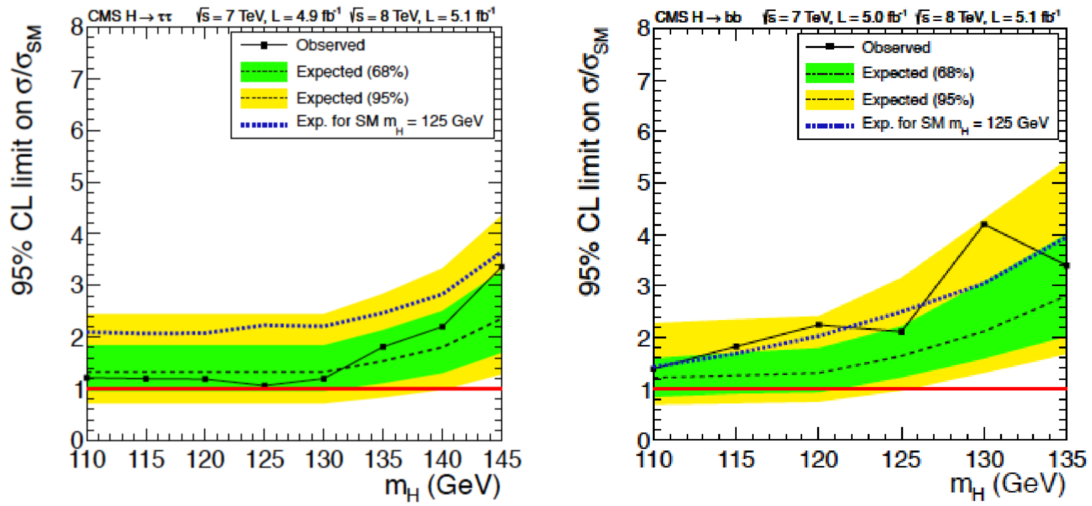

Figure 2.2. The 95% CL limit on the signal strength $\sigma/_{SM}$ for a Higgs boson decaying to τ pairs (left) and two b quarks (right), for the combined 7 and 8 TeV data sets. The symbol $\sigma/_{SM}$ denotes the production cross section times the relevant branching fractions, relative to the SM expectation. The background only expectations are represented by their median (dashed line) and by the 68% and 95% CL bands. The dotted curve shows the median expected limit for a SM Higgs boson with $m_{\mathrm{H}} = 125\,\mathrm{GeV}$.

where f^{abc} denote the corresponding structure functions. Indices a, b, c run over the 8 color degrees of freedom of the gluon field. The third term gives rise to triple and quartic gluon self-interactions and ultimately to asymptotic freedom [36].

The covariant derivative is:

$$D_\mu = \partial_\mu + i g_s A^a_\mu t^a, \tag{2.17}$$

defined by means of the t^a matrices in the fundamental representation of $SU(3)$, which satisfy the commutation relations

$$[t^a, t^b] = i f^{abc} t^c. \tag{2.18}$$

There is one more gauge invariant term that can be written down in the QCD Lagrangian Eq. (2.15):

$$\mathcal{L}_\theta = \theta_{\mathrm{QCD}} \frac{\alpha_s^2}{64\pi^2} \epsilon^{\mu\nu\rho\sigma} F^a_{\mu\nu} F^a_{\rho\sigma}. \tag{2.19}$$

here, $\epsilon^{\mu\nu\rho\sigma}$ is the totally antisymmetric tensor (in four dimensions) and $\alpha_s \equiv \frac{g_s^2}{4\pi}$. Adding this term to the Lagrangian leads to the so-called strong CP-problem [37]. The θ_{QCD} is the vacuum angle parameter, which is a free parameter of QCD.

2.4 Parameters of the Standard Model

The SM has 19 free parameters: three gauge couplings (electromagnetic coupling g', strong coupling g_s and EW coupling g), 9 fermion masses (3 lepton masses and 6 quark masses, assuming massless neutrinos), 3 Cabibbo-Kobayashi-Maskawa (CKM) matrix mixing angles and one CP-violating CKM phase, two parameters to characterize the Higgs sector that can be taken as the expectation value v corresponding to the minimum of the Higgs effective potential shown in Fig. 2.1, the Higgs mass m_{H}, and the non-perturbative QCD vacuum angle parameter θ_{QCD}. Tab. 2.4 summarizes these parameters and gives the current experimentally determined values.

2.5 Open Questions of the Standard Model

The SM of elementary particle interactions is in excellent agreement with all the experimental data, however, it is conceptually incomplete as it does not provide consistent answers to several questions. In the following a non exhaustive list of the main open questions of the SM are presented.

- Can the theory constrain the free parameters in the Lagrangian of the SM (there are 19 free parameters)?
- Why are there three families of quarks and leptons?
- Why do quarks have fractional charge?
- In the SM, only left-handed particles couple to the charged weak bosons while right-handed particles do not. Such an asymmetry is described in the SM but no reason is provided as to the origin of the asymmetry.
- No description of gravitation is present in the SM. The latter needs to be extended to include the theory of gravitation. There is no quantum theory of gravitation which has been tested experimentally.

Table 2.4
Parameters of the SM [38].

Parameter	Description	Value
m_e	Electron mass	510.99893 ± 0.00001 keV
m_μ	Muon mass	105.658372 ± 0.000004 MeV
m_τ	Tau mass	1776.82 ± 0.16 MeV
m_u	Up quark mass	2.3 ± 0.7 MeV
m_d	Down quark mass	4.8 ± 0.5 MeV
m_s	Strange quark mass	95 ± 5 MeV
m_c	Charm quark mass	1.28 ± 0.03 GeV
m_b	Bottom quark mass	4.18 ± 0.03 GeV
m_t	Top quark mass	173.21 ± 0.87 GeV
θ_{12}	CKM 12 mixing angle	$13.04 \pm 0.05°$
θ_{23}	CKM 23 mixing angle	$2.38 \pm 0.06°$
θ_{13}	CKM 13 mixing angle	$0.201 \pm 0.011°$
δ	CKM CP-violating phase	1.20 ± 0.08 rad
g'	$U(1)_Y$ gauge coupling	0.357 ± 0.001
g	$SU(2)_I$ gauge coupling	0.652 ± 0.001
g_s	$SU(3)$ gauge coupling	1.221 ± 0.001
θ_{QCD}	QCD vacuum angle	$< 10^{-10}$
v	Higgs vacuum expectation value	246 GeV
m_{H}	Higgs mass	125.7 ± 0.4 GeV

- The hierarchy mass problem raises the question of the difference of orders of magnitude between the EW scale and the Planck scale. While the former is found to be around 10^3 GeV, the latter represents the scale at which quantum gravitational effects become important and is expressed by:

$$M_{Pl} = \sqrt{\frac{hc}{G}} = 1.12 \times 10^{19} \text{ GeV}$$

- Naturalness problem: in the SM, the Higgs mass is naturally very large, unless there is a fine tuning calculation between the quadratic radiative corrections and the bare mass.

The questions listed above indicate that the SM should be viewed only as an effective low-energy theory and a wider theory embedding the results of the SM may be discovered at TeV energies accessible at the LHC.

3. PHYSICS OF PROTON-PROTON COLLISIONS

To measure the properties of elementary particles and to discover physics beyond the Standard Model large particle accelerators are utilized. New particles are likely to be produced in collisions with high center-of-mass energy.

The physics of proton-proton collisions is complex and involves various fundamental processes. At hadron colliders, the parton level cross sections are folded with the parton distribution functions (PDFs). Any calculation of cross sections with hadrons in the initial state involves PDFs as an input.

In this chapter, the collision kinematics, the PDF definitions, and currently available PDF parameterizations are discussed.

3.1 Collision Kinematics

Let $P_1^\mu = (p_x^1, p_y^1, p_z^1, E^1)$ and $P_2^\nu = (p_x^2, p_y^2, p_z^2, E^2)$ denote the four momenta of colliding protons, which propagate along the z axis in the reference frames considered. The variables used in the analysis of proton-proton collision experiments are described below.

Transverse momentum (p_T). The transverse momentum is defined as

$$p_\mathrm{T} = \sqrt{p_x^2 + p_y^2}$$

and represents the component of the particle momentum transverse to the beamline.

Rapidity (y). Rapidity is defined as

$$y = \frac{1}{2}\ln\frac{E + p_z}{E - p_z},$$

where E is the energy of the particle and p_z is its momentum along the proton beamline. Rapidity is generally used to present the angular distribution of particles. The shape of the rapidity distribution is invariant under a relativistic boost along the z axis, so y is a better choice of a variable than the polar angle θ.

Pseudorapidity η. Pseudorapidity is approximately equal to the rapidity in the limit where a particle's momentum is much greater than its mass. Pseudorapidity is defined as:

$$\eta = -\ln(\tan(\frac{\theta}{2})) = \frac{1}{2}\ln\frac{|p| + p_z}{|p| - p_z}$$

where θ is the polar angle with respect to the positive z axis. The advantage of using pseudorapidity in place of rapidity is that the knowledge about the energy and momentum of the particle is not needed.

Invariant mass (m). The invariant mass of two particles is defined as

$$m^2 = (P_1 + P_2)_\mu (P_1 + P_2)^\mu.$$

It is invariant under Lorentz transformations.

In the high-energy limit, when the particles can be considered massless, one can write:

$$\begin{aligned} m^2 = [(p_1, 0, 0, p_1) + (p_2, 0, p_2 \cdot \sin\theta, p_2 \cdot \cos\theta)]^2 = \\ (p_1 + p_2)^2 - p_2^2 \cdot \sin^2\theta - (p_1 + p_2\cos\theta)^2 = \\ 2p_1 p_2 (1 - \cos\theta), \end{aligned} \tag{3.1}$$

analogously, in terms of azimuthal angle and pseudorapidity we get:

$$m^2 = 2p_{\mathrm{T}}^1 p_{\mathrm{T}}^2 (\cosh(\eta_1 - \eta_2) - \cos(\phi_1 - \phi_2)).$$

Bjorken scaling variables. The rapidity y and the invariant mass m of the two particles produced in proton-proton collisions are related at leading order (LO) to the Bjorken scaling variables defined as the momentum fractions x_+ (x_-) carried by the parton in the forward-going (backward-going) proton as described by the formula:

$$x_\pm = (m/\sqrt{s})e^{\pm y}, \tag{3.2}$$

where the forward direction is defined as the positive z direction of the detector coordinate system.

Evolution scale Q^2. The momentum transfer to the particles in the hard collision can be written as:

$$Q^2 = x_+ x_- s = m^2, \tag{3.3}$$

where $x_\pm$ are the Bjorken scaling variables corresponding to the colliding partons and s is the center-of-mass energy squared. The momentum transfer Q^2 sets the QCD renormalization and factorization scales.

3.2 Parton Distribution Functions

The parton distribution functions, $f_{i/\mathrm{p}}(x_i, Q^2)$, give the probability density to find the parton of type i with the longitudinal momentum fraction x (Bjorken scaling variable) at an evolution scale Q^2 inside the proton [39]. PDFs are process independent, non-perturbative quantities which are extracted by means of global analysis at some initial momentum scale Q^2. The Q^2_{initial} scale is set by factorization of the QCD process into a hard scattering part that can be calculated via perturbative QCD and a soft part described by the PDFs.

In the naive parton model, the proton is considered as consisting of only three valence quarks. A more complete QCD framework considers valence quarks embedded in a sea of virtual quark-antiquark pairs generated by the gluons. Within this framework, a set of 11 different PDFs has to be considered to describe the structure of the proton:

$$\mathrm{u},\ \overline{\mathrm{u}},\ \mathrm{d},\ \overline{\mathrm{d}},\ \mathrm{s},\ \overline{\mathrm{s}},\ \mathrm{c},\ \overline{\mathrm{c}},\ \mathrm{b},\ \overline{\mathrm{b}},\ g. \tag{3.4}$$

Parton distribution functions corresponding to physical quarks consist of valence and sea contributions:

$$\mathrm{q} = \mathrm{q}_{\mathrm{V}} + \mathrm{q}_{\mathrm{sea}} \tag{3.5}$$

Only a set of 7 parton distribution functions is independent:

$$\begin{aligned} \mathrm{u_V} &= \mathrm{u} - \overline{\mathrm{u}}, \\ \mathrm{d_V} &= \mathrm{d} - \overline{\mathrm{d}}, \\ f_{\mathrm{sea}} &= 2 \cdot (\overline{\mathrm{u}} + \overline{\mathrm{d}} + \overline{\mathrm{s}}), \\ \mathrm{s}^+ &= \mathrm{s} + \overline{\mathrm{s}}, \\ \mathrm{s}^- &= \mathrm{s} - \overline{\mathrm{s}}, \\ &\overline{\mathrm{d}} - \overline{\mathrm{u}}, \\ &g \end{aligned} \tag{3.6}$$

The net number of partons of each type inside the proton at a fixed scale Q^2 are given by the sum-rules [40]:

$$\begin{aligned} \int_0^1 dx \mathrm{u}_V(x, Q^2) &= \int_0^1 dx[\mathrm{u}(x, Q^2) - \overline{\mathrm{u}}(x, Q^2)] = 2, \\ \int_0^1 dx \mathrm{d}_V(x, Q^2) &= \int_0^1 dx[\mathrm{d}(x, Q^2) - \overline{\mathrm{d}}(x, Q^2)] = 1, \\ \int_0^1 dx \mathrm{s}_V(x, Q^2) &= \int_0^1 dx[\mathrm{s}(x, Q^2) - \overline{\mathrm{s}}(x, Q^2)] = 0, \end{aligned} \tag{3.7}$$

At low Q^2 or large x the three valence quarks contributions are dominant in the proton. At high Q^2, more sea quark-antiquark pairs carrying a low momentum fraction x are produced. Quarks and antiquarks account for only about a half of the proton momentum, with the remainder being carried by the gluons. The fraction carried by gluons increases with increasing Q^2.

Figure 3.1 shows an example of parton distributions at different scales.

As expected, at small Q^2 and x values above 0.1, the u quarks are dominant, contributing more than twice as much as the d quarks at high x and is much larger than the heavier quarks (s, c, b, and t). At low x, there are significantly less strange quarks than up and down quarks due to flavor asymmetry. The charm density is null below Q=1.5 GeV and increases slowly with energy. As seen from the right plot in Fig. 3.1, the shape of the quark and gluon distributions changes rapidly at very low x and high Q^2. The sea becomes more flavor symmetric, since at low x the evolution is

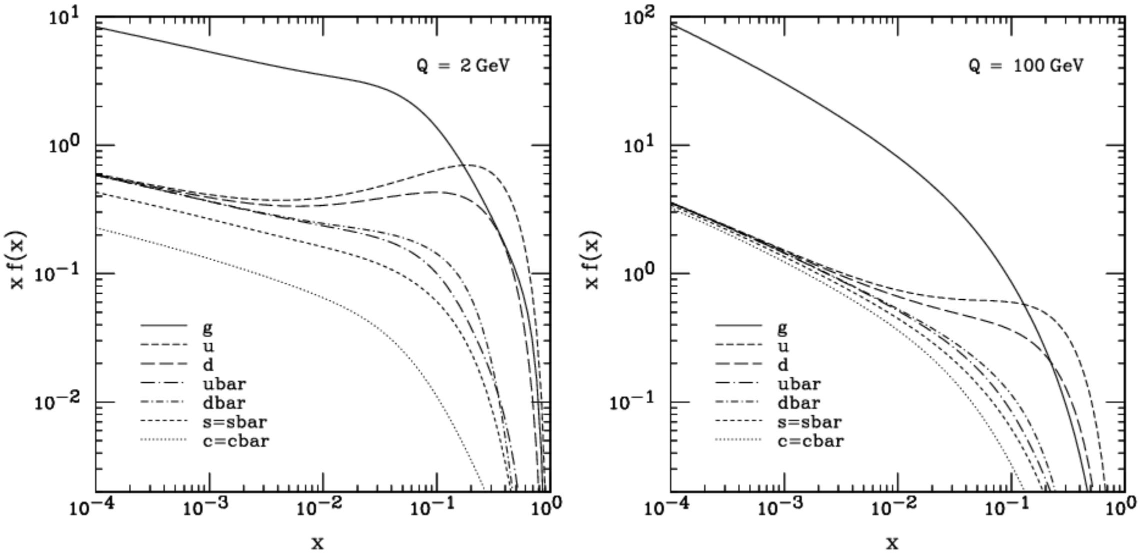

Figure 3.1. Example of the PDFs at Q = 2 GeV (left) and at Q = 100 GeV (right) [39].

flavor-independent, and there are more sea quarks and gluons. The rise of the parton densities at low x and high Q^2 values is an important prediction of QCD [41].

3.2.1 Global Analysis of Parton Distributions

Global analysis of parton distributions makes use of experimental data from various physical processes and the Dokshitzer-Gribov-Lipatov-Altarelli-Parisi (DGLAP) evolution equations [42–44] for partons to extract a set of PDFs which best fit the existing data. These distributions can then be used to predict other physical observables at energy scales far beyond those used in the derivation.

A typical procedure for global analysis involves the following necessary steps:

- Choose experimental datasets, such that the data can give the best constraints on PDFs
- Select the factorization scheme
- Choose the parametric form for the input parton distributions at some scale Q^2_{initial},

- Evolve the distributions to any other scales Q^2_{final}
- Use the evolved distributions to calculate global χ^2 between theory and data
- Parameterize the final parton distributions at discrete values of Bjorken x and Q^2_{final} by some analytic functions

Each of these analysis steps is described below in more detail.

Theoretical and Experimental Inputs

Theoretical inputs to the global analyses of parton distributions are the perturbatively calculated hard cross sections and the QCD evolution equations which control the scale dependence of the PDFs. Determined from experimental data at some scale Q^2_{initial}, the PDFs can be obtained at any scale Q^2_{final} by using the DGLAP evolution equations, provided that both scales are in the perturbative domain.

Given a variety of experimental data and corresponding theoretical calculations, it is possible to suggest which new types of data are necessary in order to further improve the PDF precision. Besides that, with an over-constrained set of PDFs it becomes possible to explore whether or not the parton-level calculations in perturbative QCD (pQCD) constitute a consistent theoretical framework to account for all the available experimental data relevant for pQCD studies. This may point to areas where improved theoretical treatments are required.

Deep-inelastic scattering (DIS), inclusive jet, ν-nucleon, DY, and W charge asymmetry data are most commonly used in modern global analyses of parton distributions. The DIS experimental data provides important constraints to the quarks and antiquark distributions, as well as to the gluon distributions at medium and small x. DY data from fixed-target experiments helped improving the understanding of the antiquark contributions. The collider vector boson production data helped in constraining the u/d ratio at high x and the valence quark distributions. The collider inclusive jet data was particularly important to constrain the high x gluon distribution.

Fitting Methodology

An important step in the PDF extraction is the choice of the parameterization. The standard parameterization has the following form:

$$f_i(x,Q^2) = a_0 x^{a_1}(1-x)^{a_2} P(x,a_3,a_4,...) \tag{3.8}$$

where the normalization parameter a_0 is typically determined from the sum rules Eq. (3.6). The factor a_1 is motivated by physics in the low x kinematic region. The factor a_2 is constrained by the physics in the limit $x \to 1$. Since the probability to observe a parton carrying the total momentum of the proton goes to zero, then the PDFs are supposed to be zero in that region. Finally the function $P(x)$ is a smooth polynomial function of x which interpolates between the low x and the large-x regions. The number of free parameters should be large enough to accommodate all the data used in the fit.

3.2.2 PDF Uncertainties

The uncertainties on PDFs have various theoretical or experimental origins. The experimental uncertainties are related to the measurement errors as they are extracted from an experiment. The theoretical uncertainties are related to the PDF parameterization used and the model assumptions made.

Several model assumptions are imposed to extract a PDF set. These assumptions are often intended to reduce the parameter space, which is achieved by assuming symmetries and neglecting some phenomena. The uncertainties related to the QCD theoretical framework can be subdivided into the following categories:

- the truncation of the higher-order Feynman diagrams in the theoretical calculations of hard cross sections,
- the dependency on the choice of the factorization (μ_F) and renormalization (μ_R) scales,

- the assumption on the validity of the DGLAP evolution equations in the entire phase space where PDFs are considered, which is a questionable assumption in the region of small x ($<< 10^{-3}$) and small Q^2 (~ 1 GeV^2).

3.2.3 PDF Parameterizations

The most widely used PDF sets are: MSTW [45], CTEQ [46], HERAPDF [47], and NNPDF [48], which make use of the data from H1-ZEUS [10], SLAC [11], FNAL E665, E772, E866 [12,13,49], CDF and D0 [14,15] experiments. The main differences between these PDFs are in the data categories used for the fit, the parameterization, the theoretical assumptions made on the physics behind the parameterization and the uncertainty estimation methods.

The CT10 PDF set is a general-purpose NLO PDF set with 52 eigenvectors of the Hessian error matrix [46] that uses a variable strong coupling $\alpha_s(M_Z)$ in the range 0.116 – 0.120 and 0.112 – 0.127. The CT10 (NNLO) is also a general purpose PDF set. It includes a part of the data sample for the D0 W-charge asymmetry measurement [15] that is not included in the CT10 NLO fit. The W-charge asymmetry data primarily modifies the slope of the ratio $\mathrm{d}(x, Q^2)/\mathrm{u}(x, Q^2)$ at large x. The CT10 (NNLO) PDF set uses a variable strong coupling $\alpha_s(M_Z)$ in the range of 0.116 – 0.120 and 0.110 – 0.130. The NNPDF2.1 PDF set is another general-purpose NNLO PDF set, composed of 100 simulated replications and available for a range of values of the strong coupling $\alpha_s(m_\mathrm{Z})$. It is based on a global data set including data from DY fixed-target experiments and W, Z production at the Tevatron that constrain the quark-antiquark separation (see Section 3.2.3 for more details).

Current parameterizations cover a kinematic range down to $x \sim 10^{-6}$ (at small values of $Q^2 \sim 0.1$ GeV^2, and up to $Q^2 \sim 10^5$ GeV^2 at large Bjorken x. Current PDF uncertainties on the cross section are 3–5% and increasing with smaller x. In the (x, Q^2)-region accessible by LHC experiments (as shown in Fig. 3.2), these PDF sets are not well constrained, and the uncertainties go up to 10%.

Fig. 3.3 summarizes PDF distributions and associated uncertainties obtained with various modern parameterizations. As seen, all PDF parameterization considered

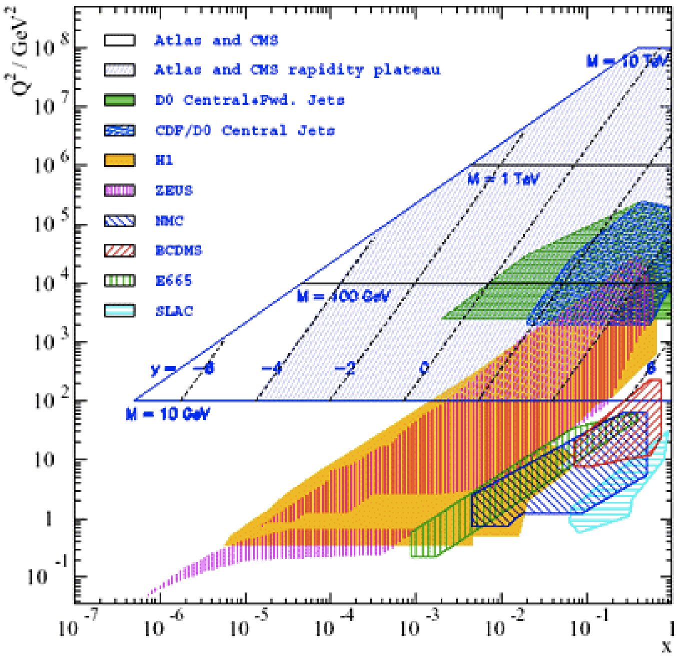

Figure 3.2. Kinematic coverage (x-Q^2 plane) of the DIS and collider experiments in the past and the expected phase space to be covered by the Large Hadron Collider (LHC) experiments [50].

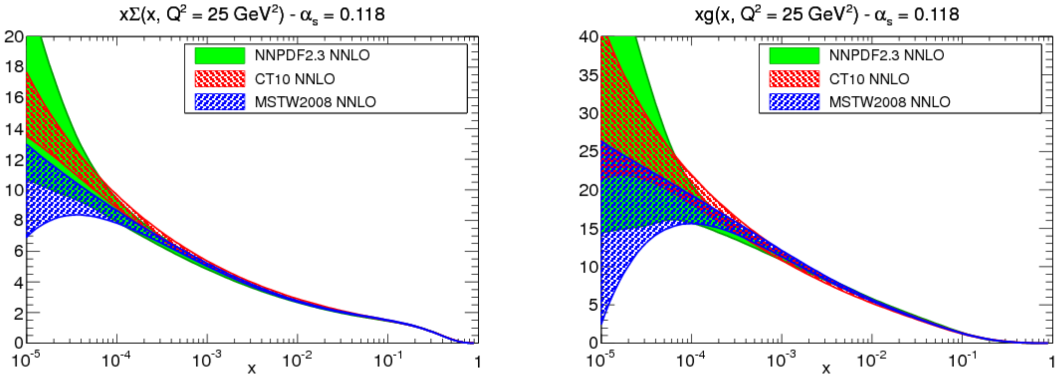

Figure 3.3. The quark (left) and gluon (right) PDFs at $Q^2 = 25$ GeV^2 plotted versus x on a logarithmic scale. The plots show the comparison between NNPDF2.3, CT10 and MSTW08 parameterizations. All PDFs are shown for a common value of $\alpha_s = 0.118$.

show similar distributions in the region of the intermediate longitudinal momenta, while the difference at low x is rather significant.

NNPDF Approach

One of the modern approaches to PDF extraction is the neural network parton distribution function (NNPDF) approach [51]. The NNPDF approach is based on a combination of a Monte-Carlo method for experimental data sampling with the use of neural networks as basic interpolating functions [48].

The NNPDF approach can be divided into four main steps:

- Generation of a large sample of MC replications of the original experimental data, by varying the measured cross section within $\pm 1 \cdot \sigma$ and recomputing the result in each rapidity bin. The value of σ of the random Gaussian is taken to be the total (statistical and systematic) error per bin.

- Training of a set of PDFs parameterized by neural networks on each of the MC replications of the data. The neural network training is stopped dynamically before entering into the over-learning regime.

- As the training of the MC replications has been completed, a set of statistical estimators is applied to the set of PDFs, in order to assess the statistical consistency of results.

- The set of replica PDF sets – trained neural networks – is then extracted, providing a representation of the underlying PDF probability density.

Fig. 3.4 summarizes the NNPDF approach as a block diagram.

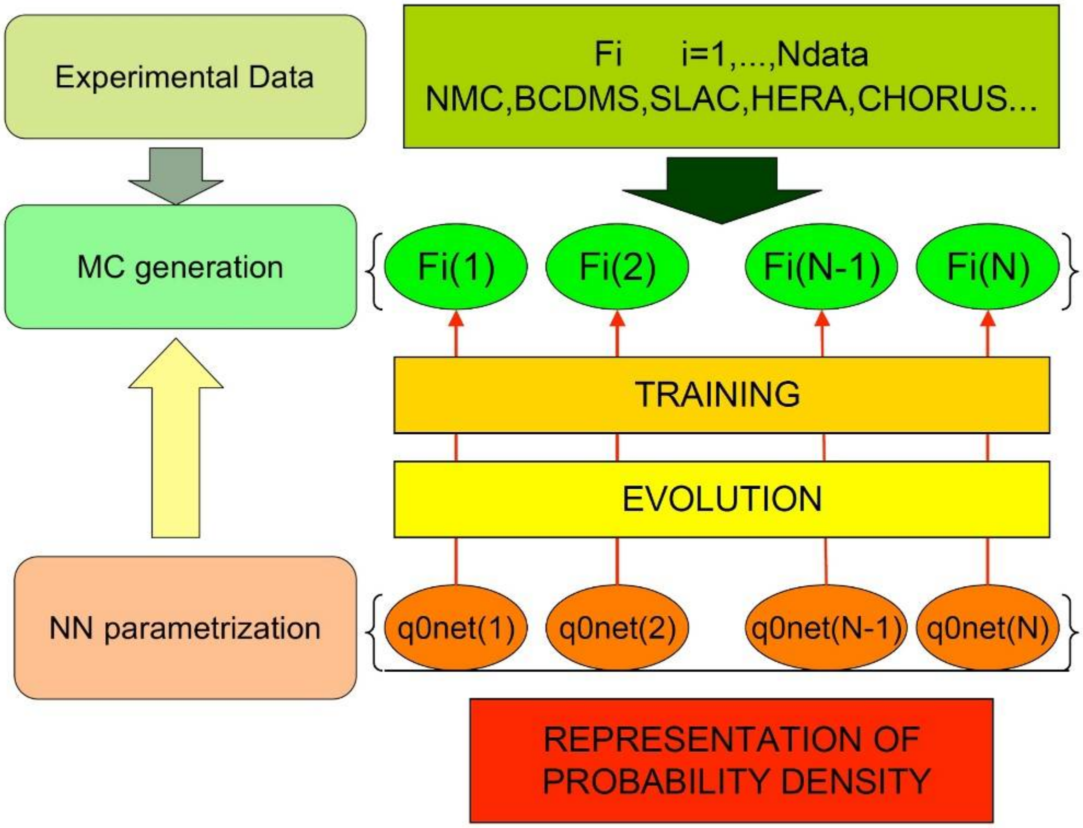

Figure 3.4. General strategy for PDF extraction with NNPDF technique [52].

4. THE DRELL–YAN PROCESS

The Drell–Yan process is described at leading order by a quark and antiquark annihilation producing a virtual photon or a Z boson, with a subsequent decay into two oppositely charged leptons. Quark-quark and quark-gluon sub-processes give contributions to DY production in higher perturbation orders [53, 54].

This process was first described by S. Drell and T.M. Yan in 1970 [55]. It had been experimentally observed in 1968 by a group led by L. Lederman at Brookhaven, by colliding protons on a fixed uranium target and observing the resulting lepton pairs [56].

Studies of the DY process have historically been a good probe of the parton distribution functions of the proton and have played an important role in our understanding of QCD.

4.1 Drell–Yan Production

In hadron collisions, the DY cross section is calculated as a cross section of the hard process convoluted with PDFs. The schematic diagram for this process is shown in Fig. 4.1.

4.1.1 Cross Section of Hard Process

The differential cross section is directly proportional to the square of the corresponding scattering amplitude:

$$|M|^2 = |M_\gamma + M_{\mathrm{Z}}|^2 = |M_\gamma|^2 + |M_{\mathrm{Z}}|^2 + 2ReM_{\mathrm{Z}}^\dagger M_\gamma, \tag{4.1}$$

including the photon, the Z-exchange contributions, and the corresponding interference term $2ReM_{\mathrm{Z}}^\dagger M_\gamma$. Here, $M_{\mathrm{Z}}^\dagger$ is the complex-conjugated scattering amplitude.

The couplings describing the $Zf\bar{f}$ and $\gamma^* f\bar{f}$ interactions within the $SU(2)_L$ and $U(1)_Y$ groups are shown in Fig. 4.2. The corresponding analytic expressions are given

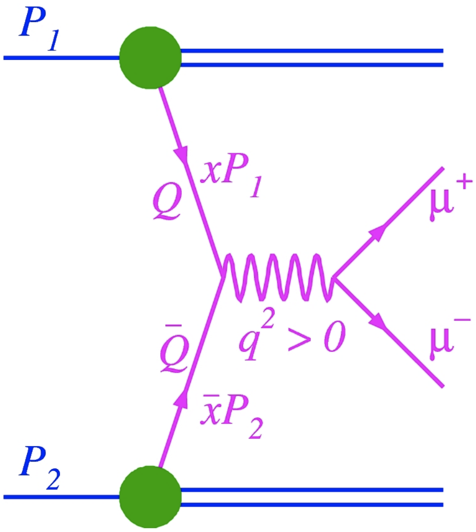

Figure 4.1. The DY production at hadron colliders.

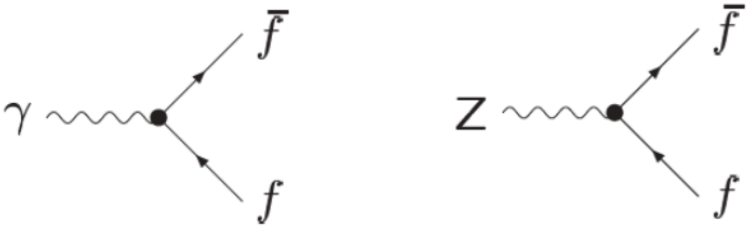

Figure 4.2. Feynman diagrams illustrating the $Zf\bar{f}$ and $\gamma^* f\bar{f}$ vertices defined by the $SU(2)$ and $U(1)$ groups.

in a compact form by Eq. (4.2):

$$\begin{aligned} \alpha(Zf\bar{f}) &= -i\gamma^\mu(lP_L + rP_R), \\ \alpha(\gamma^* f\bar{f}) &= -ieQ\gamma^\mu, \end{aligned} \tag{4.2}$$

where e is the positron charge and Q is the electric charge of a fermion in units of the positron charge e. Whereas for the $\alpha(Zf\bar{f})$ coupling $l = \frac{e}{s_W c_W}(\pm\frac{1}{2} - 2Qs_W^2)$, and $r = \frac{-2Qes_W}{c_W}$. Here, s_W and c_W denote the sine and cosine of the Weinberg angle.

The projection operators are defined as follows:

$$P_L = \frac{1-\gamma^5}{2}, \quad P_R = \frac{1+\gamma^5}{2}. \tag{4.3}$$

In the limit of massless fermions (which is a very good approximation at the LHC for all particles except for the top quark), the scattering amplitude can be written as

$$M = -i\bar{v}(k_2)\gamma^\mu(lP_L + rP_R)u(k_1)\epsilon_\mu, \tag{4.4}$$

where k_1 and k_2 are the momenta of the massless incoming fermion and anti-fermion, and ϵ_μ is the photon polarization vector.

Squaring the above amplitude, for the partonic process $\mathrm{q\bar{q}} \to \gamma^*/\mathrm{Z}$ in the unitary gauge, we obtain:

$$\begin{aligned}
|M|^2 = \sum_{\text{spin,polar,color}} & \bar{u}(k_1)\gamma^\nu(lP_L + rP_R)v(k_2)\bar{v}(k_2)\gamma^\mu(lP_L + rP_R)u(k_1)\epsilon_\mu\epsilon^*_\nu = \\
&= N_c\mathrm{Tr}[\not{k}_1\gamma^\nu(lP_L + rP_r)\not{k}_2\gamma^\mu(lP_L + rP_r)](-g_{\mu\nu} + \frac{q_\mu q_\nu}{m_\mathrm{Z}^2}) = \\
&= \frac{N_c}{2}(l^2 + r^2)\mathrm{Tr}[\not{k}_1\gamma^\nu\not{k}_2\gamma^\mu](-g_{\mu\nu} + \frac{q_\mu q_\nu}{m_\mathrm{Z}^2}) = \\
&= 2N_c(l^2 + r^2)[k_1^\mu k_2^\nu + k_1^\nu k_2^\mu - (k_1k_2)g^{\mu\nu}](-g_{\mu\nu} + \frac{q_\mu q_\nu}{m_\mathrm{Z}^2}) = \\
&= 2N_c(l^2 + r^2)[-2(k_1k_2) + 4(k_1k_2) + 2\frac{(-k_1k_2)^2}{m_\mathrm{Z}^2} - \frac{(k_1k_2)q^2)}{m_\mathrm{Z}^2}] = \\
&= 2N_c(l^2 + r^2)q^2 = 2N_c(l^2 + r^2)M_\mathrm{Z}^2,
\end{aligned} \tag{4.5}$$

where the color factor N_c accounts for the number of $SU(3)_c$ states which can be combined to form a color singlet like the Z, and the $q = -k_1 - k_2$ is the momentum of outgoing gauge boson.

The following notations are used for the Mandelstam variables of the partons:

$$s = (k_1 + k_2)^2, \quad t = (k_1 - k_3)^2, \quad u = (k_1 - k_4)^2. \tag{4.6}$$

The matrix element for the corresponding $2 \to 2$ process, the process of dilepton production through s channel γ^*/Z exchange Eq. (4.2), can be written as:

$$M = (-i)^2\bar{u}(p_1)\gamma^\nu(l^{'}P_L + r^{'}P_R)u(k_1)\frac{i}{q^2 - m_\mathrm{Z}^2}(-g_{\mu\nu} + \frac{q_\mu q_\nu}{m_\mathrm{Z}^2}), \tag{4.7}$$

where k_1, k_2, p_1 and p_2 refer to the four-momenta of the incoming fermion, incoming anti-fermion, outgoing fermion and outgoing anti-fermion correspondingly. The gauge boson couplings are l and r for incoming fermions and $l^{'}$ and $r^{'}$ for outgoing fermions. Momentum conservation implies $k_1 + k_2 + p_1 + p_2 = 0$.

With intermediate massless photons only, one has: $l^2 + r^2 = 2Q^2e^2$ and $l^{'2} + r^{'2} = 2Q^{'2}e^2$ for the outgoing leptons. Since only the lepton final states are discussed one can put: $Q = Q^{'} = 1$. Eq. (4.5) can then be written as:

$$\begin{aligned}
|M_\gamma|^2 &= 12(2e^2)(2e^2)\frac{1}{q^4}[k_1^\mu k_2^\nu + k_1^\nu k_2^\mu - (k_1k_2)g^{\mu\nu}](-g_{\mu\rho})[p_1^\rho p_2^\sigma + p_1^\sigma p_2^\rho - \\
&- (p_1p_2)g^{\rho\sigma}](-g_{\nu\sigma}) = 48e^4\frac{1}{q^4}[k_{1\rho}k_2^\nu + +k_1^\nu k_{2\rho} - (k_1k_2)g_\rho^\nu][p_1^\rho p_{2\nu} + p_{1\nu}p_2^\rho - \\
&- (p_1p_2)g_\nu^\rho] = 96e^4\frac{1}{q^4}[(k_1p_1)(k_2p_2) + (k_1p_2)(k_2p_1)] = \\
&= 96e^4\frac{1}{s^2}[\frac{t^2}{4} + \frac{u^2}{4}] = 24e^4[1 + 2\frac{t}{s} + 2\frac{t^2}{s^2}],
\end{aligned} \tag{4.8}$$

The two-particle phase space integration of the square of the matrix element derived in Eq. (4.8) assuming massless particles gives:

$$s^2\frac{d\hat{\sigma}(\mathrm{q\bar{q}} \to \gamma^* \to ll)}{dt} = \frac{1}{144\pi}|M_\gamma|^2, \tag{4.9}$$

where $t = \frac{s}{2}(\cos\theta - 1)$. The $N_c = 3$, considering the q$\bar{\text{q}}$ initial state. Then using $\alpha_{\mathrm{EM}} = e^2/(4\pi)$, we get the following expression for the differential cross section of the DY process:

$$\begin{aligned}
\frac{d\hat{\sigma}(\mathrm{q\bar{q}} \to \gamma^* \to ll)}{dt} &= \frac{1}{s^2}\frac{\pi}{(4\pi)^2}\frac{2}{3}(4\pi\alpha_{\mathrm{EM}})^2(1 + 2\frac{t}{s} + 2\frac{t^2}{s^2}) = \\
&= \frac{1}{s^2}\frac{2\pi\alpha_{\mathrm{EM}}^2}{3}(1 + 2\frac{t}{s} + 2\frac{t^2}{s^2}).
\end{aligned} \tag{4.10}$$

Integrating Eq.(4.11) over the Mandelstam variable t gives the total cross section:

$$\begin{aligned}
\hat{\sigma}(\mathrm{q\bar{q}} \to \gamma^* \to ll) = \frac{1}{s^2}\frac{2\pi\alpha_{\mathrm{EM}}^2}{3}\int_{-s}^{0} dt(1 + 2\frac{t}{s} + 2\frac{t^2}{s^2}) &= \\
\frac{1}{s^2}\frac{2\pi\alpha^2}{3}(t + \frac{t^2}{s} + \frac{2t^3}{3s^2})_{-s}^{0} &= \\
\frac{1}{s}\frac{4\pi\alpha_{\mathrm{EM}}^2}{9}&.
\end{aligned} \tag{4.11}$$

With intermediate on-shell or off-shell Z boson exchange introduced, we get additional terms in the amplitude, including the interference term given by Eq. (4.1). In the regions where the invariant masses of lepton pairs for both intermediate states are the same, an interference may occur (which happens in the 60–120 GeV invariant mass range, mostly pronounced in the tails of the Z peak).

The propagator of the Z boson in the s channel (corresponding to the DY process, $\mathrm{q\bar{q}} \rightarrow \mathrm{Z} \rightarrow l^+l^-$) has the form: $\frac{1}{s-m_\mathrm{Z}^2+im\Gamma}$, and the corresponding contribution to the DY cross section is:

$$\begin{aligned}\hat{\sigma}(\mathrm{q\bar{q}} \rightarrow \mathrm{Z} \rightarrow l^+l^-) &= \frac{4\pi\alpha_\mathrm{EM}^2}{3} r_\mathrm{tot}^f \frac{s}{(s-m_\mathrm{Z}^2)^2-(m_\mathrm{Z}^2\Gamma_\mathrm{Z}^2)} = \\ &= \frac{12\pi}{m_\mathrm{Z}^2}\frac{\Gamma_{ee}\Gamma_{ff}}{\Gamma_\mathrm{Z}^2}\frac{s\Gamma_\mathrm{Z}^2}{(s-m_\mathrm{Z}^2)^2-(m_\mathrm{Z}^2\Gamma_\mathrm{Z}^2)},\end{aligned} \tag{4.12}$$

where the $r_\mathrm{tot}^f = \frac{12}{m_\mathrm{Z}^2\alpha_\mathrm{EM}^2}\Gamma_{ee}\Gamma_{ff}$ and the partial decay width Γ_{ff} of the $\mathrm{Z} \rightarrow ff$ decay is given by:

$$\Gamma_{ff} = \frac{\alpha_\mathrm{EM} m_\mathrm{Z}}{4s_\mathrm{w}^2c_\mathrm{w}^2}[g_{Vf}^2 + g_{Af}^2], \tag{4.13}$$

here $g_{Vf} = l = I_3 - 2Qs_\mathrm{w}^2$ and $g_{Af} = I_3$ – Z boson coupling strengths to fermionic vector and axial-vector currents, respectively.

Finally, the $\gamma^* - \mathrm{Z}$ interference term can be written as:

$$\hat{\sigma}(\mathrm{q\bar{q}} \rightarrow \gamma^*/\mathrm{Z} \rightarrow l^+l^-) = \frac{4\pi\alpha_\mathrm{EM}^2}{3} j_\mathrm{tot}^f \frac{(s-m_\mathrm{Z}^2)}{(s-m_\mathrm{Z}^2)^2-(m_\mathrm{Z}^2\Gamma_\mathrm{Z}^2)}, \tag{4.14}$$

where $j_f^\mathrm{tot} = \frac{3Qeg_{Ve}g_{Vf}}{2s_\mathrm{w}^2c_\mathrm{w}^2}$. As seen, the interference contribution vanishes in the limit $\sqrt{s} \rightarrow m_\mathrm{Z}$.

Fig. 4.3 shows the contribution of the various terms of the scattering amplitude corresponding to the DY process discussed above (γ^*-exchange, Z boson exchange and the interference term). As seen, the Z exchange is the dominant contribution to the cross section in the Z peak region, while the γ^* exchange is dominant outside the Z peak. In the tails of the Breit-Wigner distribution the effect of $\gamma^* - \mathrm{Z}$ interference is significant. In the limit of $\sqrt{s} \rightarrow \infty$ all the terms behave like $1/s$. The $\gamma^* - \mathrm{Z}$ interference leads to the effect of the so-called forward-backward asymmetry [57].

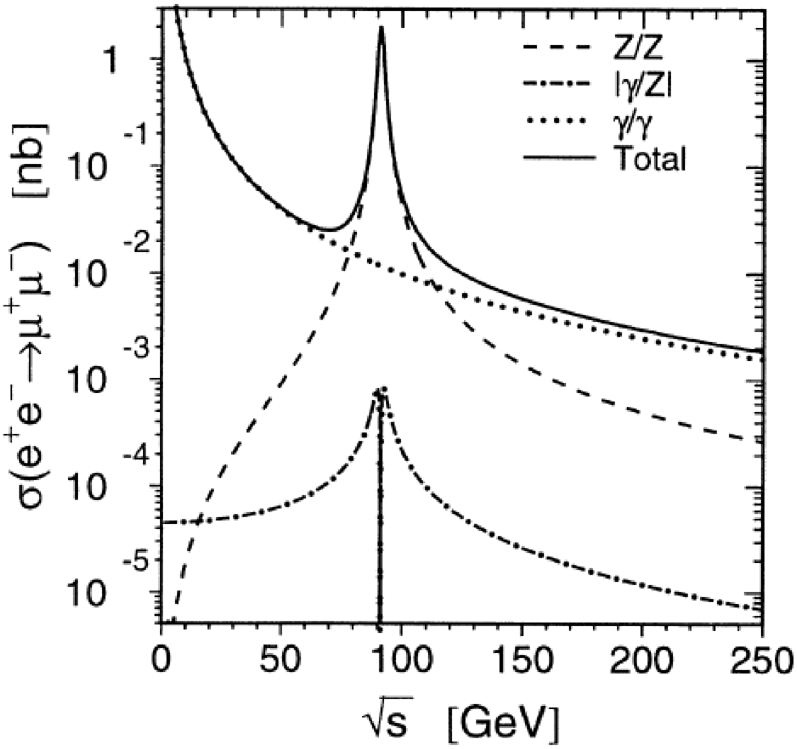

Figure 4.3. The total cross section and the contributions arising from γ^* exchange, Z exchange, and the γ^*-Z interference shown separately.

Higher Order QCD and EW Effects

The NLO QCD predictions of cross sections have uncertainties of about 10%, and therefore are insufficient for a precise comparison with data. The NNLO QCD theoretical predictions must be used. The inclusive $O(\alpha_s^2)$ corrections to the Z boson production are known with 1% theoretical precision [6].

However, in the TeV energy regime, $\alpha \sim \alpha_s^2$ which makes it necessary to take the NLO electroweak corrections into account along with the NNLO pQCD corrections. The second order virtual weak radiative corrections are large at high energies, due to the presence of logarithms of the form $(\alpha/\pi)\log^2(\hat{s}/Q^2)$, where $\hat{s}$ is the squared parton center-of-mass energy, and $Q = m/2$ is the renormalization scale, equal to the mass of the intermediate gauge boson [58]. These logarithms, originating from collinear and infrared divergences, are, however, canceled in QED by the corresponding divergences originating from real photon radiation diagrams [59]. Below, all these corrections are discussed in more detail.

At the next-to-leading order pQCD, which takes the $O(\alpha_s)$ corrections into account [53, 54], the gluon bremsstrahlung and processes with gluons in the initial state

$$\begin{aligned} \mathrm{q}\bar{\mathrm{q}} &\to \gamma^*/\mathrm{Z} + g, \\ g + \mathrm{q}(\bar{\mathrm{q}}) &\to \gamma^*/\mathrm{Z} + \mathrm{q}(\bar{\mathrm{q}}), \end{aligned} \tag{4.15}$$

contribute to the DY production cross section. The size of perturbative corrections depends on the lepton-pair mass and on the overall center-of-mass energy. At low energies, the correction to the DY cross section is generally large and positive - reaching the value of 10% as shown in Fig. 4.4. The corresponding corrections can reach as high as 50% if a lepton p_{T} cut is applied to the phase space. In this regime, the (negative) contribution from the quark-gluon scattering terms is quite small.

The effect of the higher-order corrections can be illustrated with the k-factor. It is defined as the ratio of the theoretical cross sections calculated at different orders. Fig. 4.4 shows the various k-factors as a function of dilepton invariant mass.

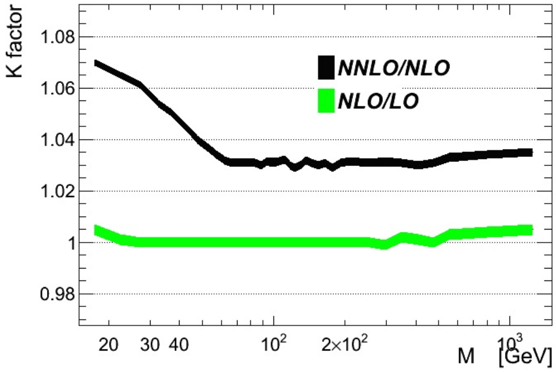

Figure 4.4. The effect of higher-order QCD corrections. The error band shows the uncertainty on the k-factor due to the integration.

The electroweak corrections to the neutral current DY process consist of QED and pure weak contributions and thus will be discussed separately. For a complete analysis see [60].

QED radiative corrections consist of the emission of real and virtual photons by quarks and charged leptons. The $O(\alpha_{\mathrm{EM}})$ QED corrections to the $\mathrm{q\bar{q}} \rightarrow \gamma^*/\mathrm{Z} \rightarrow l^+l^-$ can be further split into initial and final state radiation (ISR and FSR) effects. The initial state radiation effects lead to collinear singularities and can be absorbed by renormalization of the PDFs in a complete analogy to the calculation of QCD radiative corrections. This introduces a dependency of parton distribution functions on the QED factorization scale μ^2_{QED} [61]. The QED induced terms in the DGLAP evolution equations lead to small negative corrections at the per-mille level in the wide range of x and μ^2_{QED}. Only at large $x{>}0.5$ and large $\mu^2_{\mathrm{QED}}{>}10^3$ GeV^2 do these corrections reach the level of 1%.

The FSR effect causes the lowering of the invariant mass of observed dileptons compared to the propagator mass, and subsequently, their migration to the lower mass. Since the DY cross section around the Z peak is few orders of magnitude larger as compared to the adjacent mass bins, the mass region just below the Z peak (40–80 GeV) will experience a large excess of dilepton events migrating in from the 80–100 GeV mass region. The QED final state radiation correction to the cross section, reaches up to 80% in that mass region.

Fig. 4.5 shows the ratio of the dilepton yields after the FSR photon emission and before.

The non-QED corrections consist of self-energy contributions to the photon and Z propagators, vertex corrections to the $\gamma^*/\mathrm{Z} - l^+l^-$ and $\gamma^*/\mathrm{Z} - \mathrm{q\bar{q}}$ couplings and the box diagrams with the massive gauge bosons, see Fig. 4.6-4.7.

It is crucial to take these corrections into account for an accurate description of the DY production. The NLO differential cross section at the parton level, including weak $O(\alpha)$ and $O(\alpha^2)$ corrections has the form:

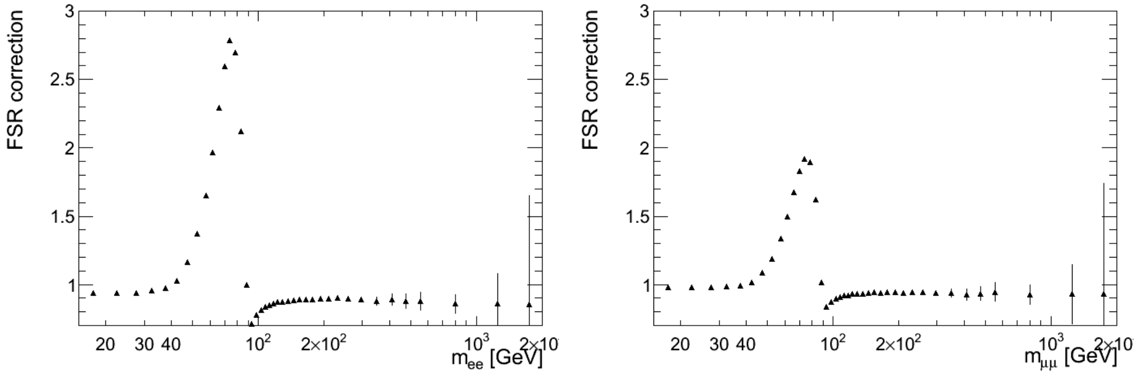

Figure 4.5. The effect of QED final state radiation on the cross section.
Left: dielectron, right: dimuon channel.

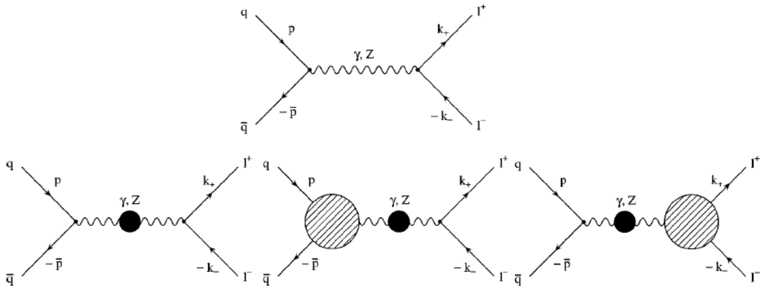

Figure 4.6. Diagrams illustrating the weak contributions to $q\bar{q} \rightarrow \gamma^*/Z \rightarrow l^+l^-$.

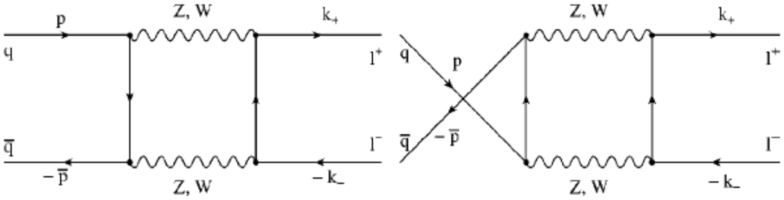

Figure 4.7. Box diagrams contributing to $q\bar{q} \rightarrow \gamma^*/Z \rightarrow l^+l^-$.

$$d\hat{\sigma}^{0+1} = dP_{2f}\frac{1}{12}\sum |A_{\gamma}^{(0+1)} + A_{\mathrm{Z}}^{(0+1)}|^2(\hat{s},\hat{t},\hat{u}) + d\hat{\sigma}_{box}(\hat{s},\hat{t},\hat{u}). \tag{4.16}$$

where $d\hat{\sigma}_{box}$ describes the contribution of the box diagrams, with hatted variables referring to the partons. This term cannot be absorbed into effective couplings.

However, in the Z resonance region, the box diagram can be neglected, and the dominant contributions to the non-photonic electroweak corrections can be taken into account by redefining the fine structure function, vertex and self-energy.

Overall, the combined QED and non-QED electroweak corrections are negligibly small in the wide mass range, but becoming important at high masses and large x region reaching the value of 10% on average. The QED final state radiation correction can reach the level of 80% in the Z peak region.

4.1.2 Differential Cross Sections

The parton cross section $\hat{\sigma}(ij \rightarrow kl)$, describing the hard scattering of two partons carrying the longitudinal momentum fractions x_i and x_j, was derived above. The cross section of the DY process in proton-proton collisions is expressed by the partonic cross section folded with the parton distribution functions (see Section 3.2 for more details):

$$\begin{aligned} \frac{d^2\sigma}{dydm^2} = \sum_{i,j} \hat{\sigma}(ij \rightarrow \gamma^*/\mathrm{Z})\hat{\sigma}(ij \rightarrow \gamma^*/\mathrm{Z}) \int dx_i \int dx_j \times \\ \times f_{j/p}(x_j, Q^2) f_{i/p}(x_i, Q^2) \Delta_{ij}(x_i, x_j, x_1, x_2, Q^2) \end{aligned} \tag{4.17}$$

where i, j refer to partons participating in the hard collision and the Δ_{ij} is the perturbative QCD coefficient function for the DY process, and $f_{i/p,j/p}(x_{i,j}, Q^2)$ denote the parton distribution functions for a parton of type i, j carrying the longitudinal momentum fraction x_i and x_j, respectively.

The coefficient function Δ_{ij} is the convolution kernel for the full perturbative QCD description of the hard parton-parton collision.

The term Δ_{ij} can be expanded as a power series in the running coupling constant $\alpha_s(\mu^2)$ as follows:

$$\Delta_{ij} = \sum_{n=0}^{\infty} (\frac{\alpha_s(\mu^2)}{4\pi})^n \Delta(\mu^2, Q^2) \tag{4.18}$$

In the case of the lowest order perturbative QCD, the coefficient function is given by

$$\Delta^{(0)}_{\mathrm{q\bar{q}}} = \delta(x_i - x_1)\delta(x_j - x_2) \tag{4.19}$$

The corresponding differential cross section can be obtained by integrating Eq. (4.17) over the dilepton rapidities:

$$\begin{aligned}\frac{d\sigma}{dm^2} = \int dy \sum_{i,j} \hat{\sigma}(ij \to \gamma^*/\mathrm{Z})\hat{\sigma}(ij \to \gamma^*/\mathrm{Z}) \int dx_i \int dx_j \times \\ \times f_{j/p}(x_j, Q^2) f_{i/p}(x_i, Q^2) \Delta_{ij}(x_i, x_j, x_1, x_2, Q^2)\end{aligned} \tag{4.20}$$

Double Ratio Measurements

The ratios of cross sections for final states X and Y between different center-of-mass energies $E_{1,2} = \sqrt{s_{1,2}}$, are defined as:

$$R_{E_2/E_1}(X, Y) = \frac{\sigma(X, E_2)/\sigma(Y, E_2)}{\sigma(X, E_1)/\sigma(Y, E_1)}. \tag{4.21}$$

Measurements of the DY process in proton-proton collisions depend on various theoretical parameters such as the QCD running coupling constant, PDFs and renormalization and factorization scales. Substantial correlations of the theoretical systematic uncertainties in the cross section calculations at different center of mass energies leads to very precise predictions for the cross section ratios and the normalized cross section ratios (double ratios) as described in [18].

Angular differential cross section

The general expression for angular distributions of DY dileptons [62] can be factorized as:

$$\begin{aligned}\frac{d^4\sigma}{dP_{\mathrm{T}}dyd\cos\theta d\phi} \propto \frac{d^2\sigma}{dP_{\mathrm{T}}dy}[&(1+\cos^2\theta)+ \\ &+\frac{1}{2}A_0(1-3\cos^2\theta) + A_1\sin2\theta\cos\theta + \\ &+\frac{1}{2}A_2\sin^2\theta\cos2\phi + A_3\sin\theta\cos\phi + \\ &+ A_4\cos\theta + A_5\sin^2\theta\sin2\phi + \\ &+ A_6\sin2\theta\sin\phi + A_7\sin\theta\sin\phi],\end{aligned} \tag{4.22}$$

where the polar θ and azimuthal ϕ are the emission angles of the lepton relative to the quark momentum in the Collins-Soper frame (see Appendix A for more details on the reference frames). The angular coefficients A_i are in general functions of dilepton rapidity y and the transverse momentum P_{T} of the dilepton in the laboratory frame [63].

Integrating over the dilepton rapidity and transverse momentum yields:

$$\begin{aligned}\frac{d^2\sigma}{d\cos\theta d\phi} \propto (1+\cos^2\theta) + \frac{1}{2}A_0(1-3\cos^2\theta) + \frac{1}{2}A_2\sin^2\theta\cos2\phi +\\ + A_4\cos\theta + A_5\sin^2\theta\sin2\phi + A_6\sin2\theta\sin\phi + A_7\sin\theta\sin\phi,\end{aligned} \tag{4.23}$$

as the angular coefficients A_1 and A_3 become vanishingly small after integrating over y [64]. The expression for the angular DY cross section can be further simplified taking into account that A_5, A_6 and A_7 are all very close to zero:

$$\begin{aligned}\frac{d^2\sigma}{d\cos\theta d\phi} \propto (1+\cos^2\theta) + \frac{1}{2}A_0(1-3\cos^2\theta) +\\ + \frac{1}{2}A_2\sin^2\theta\cos2\phi + A_4\cos\theta,\end{aligned} \tag{4.24}$$

Integrating over the azimuthal angle, one gets:

$$\frac{d\sigma}{d\cos\theta} \propto (1+\cos^2\theta) + \frac{1}{2}A_0(1-3\cos^2\theta) + A_4\cos\theta. \tag{4.25}$$

Considering the quark-antiquark initial state, the A_0 term can be ignored, and the corresponding angular distribution of DY dileptons can be written as:

$$\frac{d\sigma}{d\cos\theta} \propto (1+\cos^2\theta) + A_4\cos\theta. \tag{4.26}$$

The second term in Eq. (4.26) introduces the so-called forward-backward asymmetry. The forward-backward asymmetry depends on the vector and axial-vector couplings of the quarks and leptons to the Z boson. The largest asymmetry occurs in the Z peak region, where it is dominated by the couplings of the Z boson and arises from the interference of the vector and axial components of its coupling. At high invariant masses, the asymmetry is dominated by $\gamma^* - \mathrm{Z}$ interference and is almost constant independently of invariant mass.

4.2 Measurements in the Past

The DY process has been extensively studied in the past. Various cross sections have been measured in fixed target and collider experiments for a wide variety of physical process and beam energies at FNAL E605, E772, E866, E906, D0, CDF experiments, and CERN E605, E772, E866, E906, NA3, NA10, UA2 experiments. In general, the data were in excellent agreement with the predictions of the SM.

The most relevant comparison to the LHC measurements can be made with the neutral current DY results.

Various experiments to test the predictions of the DY model were performed. The fixed target experiments, making use of $\pi^{\pm}$, $\mathrm{K}^{\pm}$, p, $\bar{\mathrm{p}}$, were the earliest [65–67]. The center-of-mass energy for these experiments was limited to 28 GeV for a beam momentum of 400 GeV.

Since the cross sections of DY production are rapidly falling with invariant mass (10^{-38} cm^2 GeV^{-1} nucleon^{-1} at a mass 10 GeV with 400 GeV protons incident), most of the fixed target experiments used heavy nuclear targets. In colliding beam experiments the data rate is normally lower due to the lower luminosity and smaller cross section at the higher center-of-mass energies.

A large number of predictions for the DY physics were extracted from the past experiments:

- transverse and invariant mass distributions of DY dileptons,
- PDF constraints,
- the beam and mass number (A) dependence of the cross sections.

The most important predictions of pre-LHC era are discussed in the following.

Invariant Mass Distributions of Drell–Yan Dileptons

The basic information on the shape of the DY continuum can be extracted from studying the $d\sigma/dm$ cross section. There are a number of $d\sigma/dm$ cross section measurements performed in the past in the dielectron and dilepton channels. The most recent and the most precise measurements were performed by the CDF and D0 collaborations. The corresponding CDF measurement [68] was performed in the mass range from 40 GeV to 1 TeV. The measurement is dominated by systematic uncertainties at low masses and in the Z peak region, where the total uncertainty is 3–20%

at low masses, and 2–8% in the Z peak region. At high masses ($m >$120 GeV), the measurement is dominated by statistical uncertainties, where the total uncertainty is 15–100%. The additional overall luminosity error is 3.9%. The corresponding D0 measurement [69] was performed in the mass range from to 120 GeV to 1 TeV. It is dominated by systematic uncertainties. The total uncertainty is 22–74% in the 120–400 GeV mass range. No events were observed with the mass $m >$400 GeV. In that region (the 3 highest mass bins), the 95% confidence level (CL) upper limits on the cross section were quoted.

PDF Constraints

Another relevant use of the DY data is to constrain the PDFs. Depending on the energy, double-differential cross sections $d^2\sigma/dmdx$, $d^2\sigma/dmp_{\mathrm{T}}$ and $d^2\sigma/dmdy$ can be used to constrain various kinematic regions and to be later combined in the global fit (see section (3.2)).

Most of the parton distribution functions were significantly influenced by the fixed target DY experimental data. It is mainly the FNAL experiments using the 800 GeV proton beams and different targets, such as hydrogen (E-866), copper (E-605) and deuterium (E-772, E-866). The center-of-mass energy of the DY process for these three experiments was 38.8 GeV. These experiments therefore cover a broad range of dilepton invariant mass and Bjorken x: $m \leq 20$ GeV and $x > 0.01$.

Later, high statistics W-charge asymmetry measurements at the Tevatron experiments D0 and CDF provided the latest constraint for the u and d quark distributions, specifically the slope of the d(x)/u(x) ratio in the x range down to as low as 0.007 [70, 71]. The agreement between data and theory calculated using the corresponding PDFs was improved by up to 5% in the low-x region.

4.3 Standard Model Cross Sections

The DY process has one of the largest SM cross sections for leptonic final states. Fig. 4.8 shows the cross sections of various physics processes and the total inclusive cross section as a function of the center-of-mass energy $\sqrt{s}$.

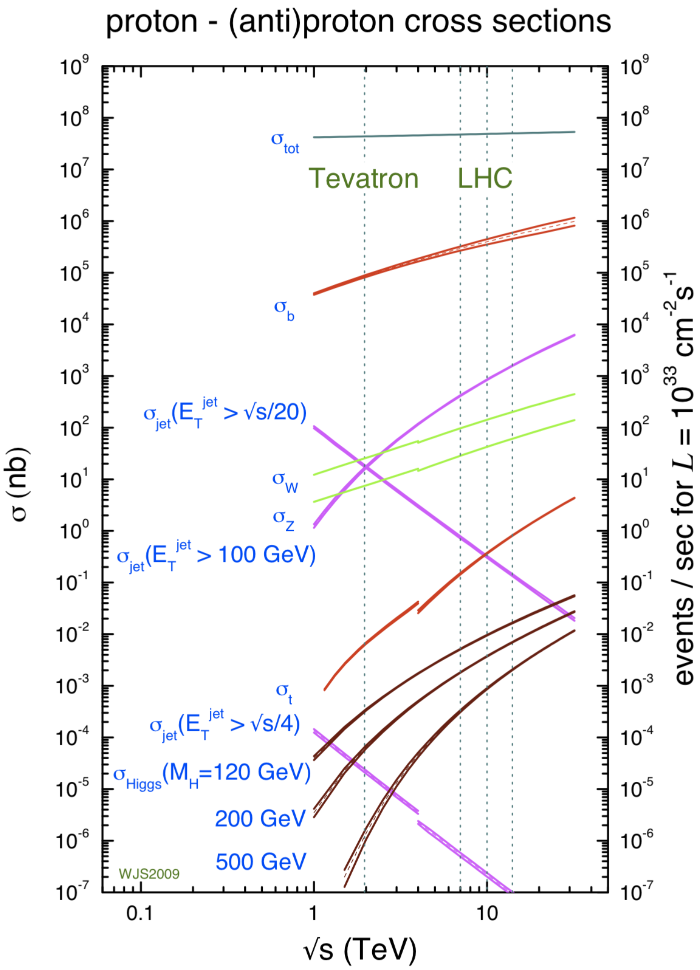

Figure 4.8. Standard Model cross sections at the LHC [72].

As seen, with an instantaneous luminosity of $L = 10^{34}$ cm^{-2}s^{-1} at the LHC energies (7–8 TeV), the total cross section reaches 100 mb. The DY cross section through the Z boson exchange, σ_{Z}, is reaching 3000 pb (and is about 5000 pb if the virtual photon contribution is included, considering the invariant masses $m > 20$ GeV), making up to 0.2% of the total cross section (which is a significant increase compared to 0.05% at the Tevatron energy). At $\sqrt{s} = 8$ TeV, the DY cross section is about 15% larger than at $\sqrt{s} = 7$ TeV, mainly due to the enhanced contribution from heavy quarks.

The most significant backgrounds to the DY process $-$ QCD multijets, top quark decays into leptons and the Z decays into τ lepton-pairs $-$ all have smaller yet significant contributions to the total cross section. Note, that both inclusive cross section of the top quark production and the jet cross section are rapidly increasing with center of mass energy (by 2 and 3 orders of magnitude respectively). The cross sections of the new physics processes are suppressed by few orders of magnitude, although are rapidly increasing with the collision energy.

At the LHC, multiple proton bunches (order of 1000 bunches) are colliding at ultra-relativistic energies ($7 - 8$ TeV). In this regime, a multiple parton scattering effect on the DY production is not negligible, and must be taken into account. A process with multiple hard parton scattering occurs when an outgoing state from one scattering becomes the incoming state of another. At LHC energies, the probability of a minimum-bias single re-scattering event is about 20%; the probability of double re-scattering is still relatively low: $\sim 0.5\%$ [73]. The effect of multiple hard parton scattering is implemented in the Monte-Carlo simulation software used for this thesis.

5. EXPERIMENTAL APPARATUS

5.1 The Large Hadron Collider

The Large Hadron Collider (LHC) is designed to probe physics at the high energy frontier. The LHC is a proton-proton accelerator at CERN located on the French-Swiss border near Geneva. It is the largest and most powerful particle accelerator in the world [74].

The LHC has generated first proton-proton collisions on November 23, 2009. After a set of runs at 450 GeV and 1.18 TeV beam energies, the first 7 TeV center-of-mass energies have been achieved on March 30, 2010. In 2010, approximately 47 fb^{-1} of integrated luminosity was delivered at $\sqrt{s} = 7$ TeV (see Fig. 5.1), with an instantaneous luminosity of $2 \times 10^{32}\text{cm}^{-2}\text{s}^{-1}$.

The LHC machine was collecting data for almost the entire year 2011. The total integrated luminosity delivered in 2011 was 5.7 fb^{-1} (see Fig. 5.1). In 2012 the beam energy was increased to 4 TeV and the LHC continued to perform smoothly, delivering over 23 fb^{-1} of integrated luminosity (see Figure 5.1).

In the coming years the LHC will continue to increase its energy and instantaneous luminosity, eventually reaching the collision energy of around 13 TeV and an instantaneous luminosity of $10^{34}\text{cm}^{-2}\text{s}^{-1}$.

5.2 The Compact Muon Solenoid Detector

The central feature of the CMS detector is a superconducting solenoid of 6 m internal diameter, providing a magnetic field of 3.8 T. Within the superconducting solenoid volume are a silicon pixel and strip tracker, a lead tungstate crystal electromagnetic calorimeter (ECAL), and a brass and scintillator hadron calorimeter (HCAL), each composed of a barrel and two endcap sections. Muons are measured in gas-ionization detectors embedded in the steel flux-return yoke outside the solenoid. Extensive

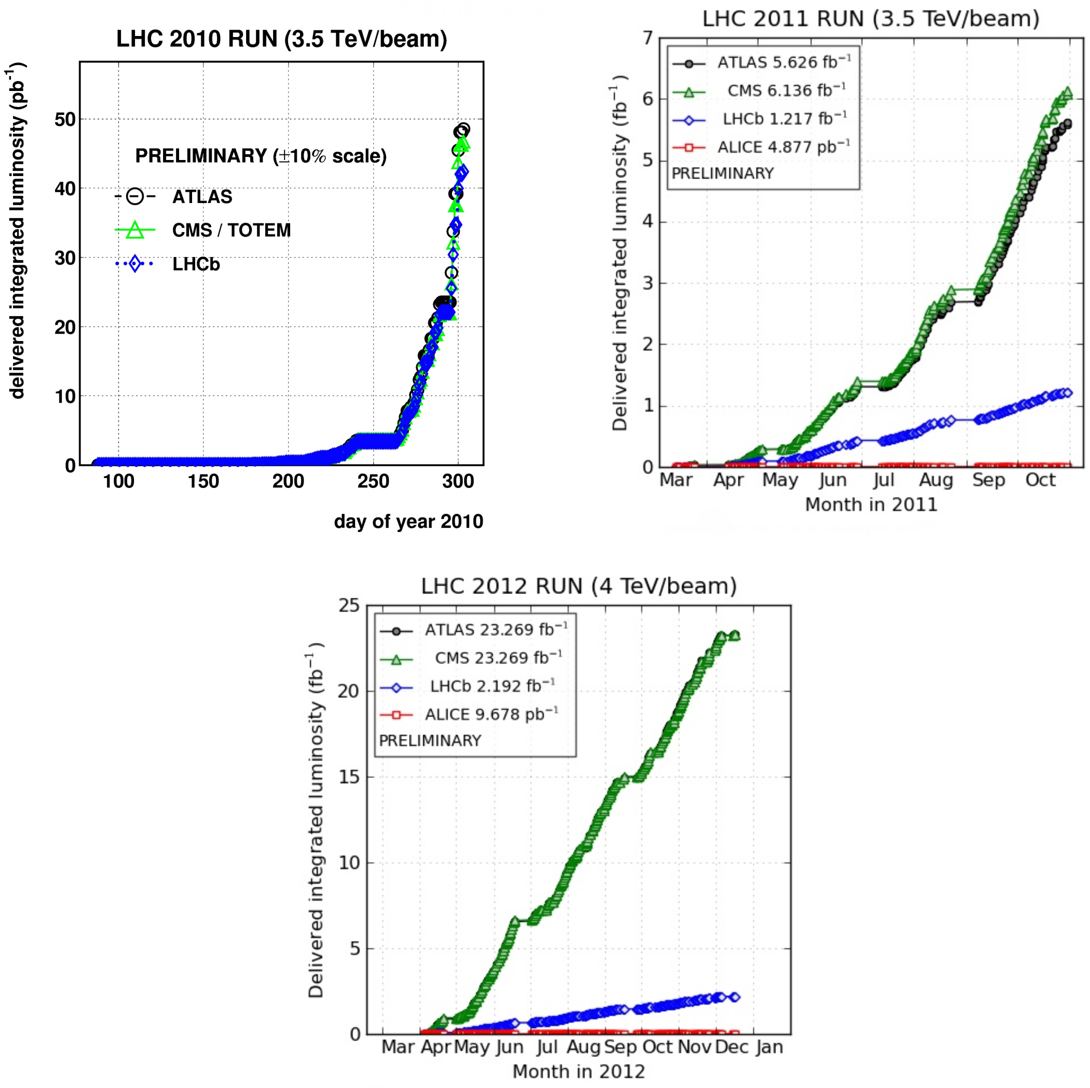

Figure 5.1. Integrated luminosity delivered by the LHC experiments in 2010-2012 [75].

forward calorimetry complements the coverage provided by the barrel and endcap detectors. Fig. 5.2 shows the $r\phi$-view of the CMS detector slice.

5.2.1 The Tracker

The inner tracking detectors are designed to reconstruct charged particles with good momentum resolution and high efficiencies in the range of $|\eta| < 2.5$.

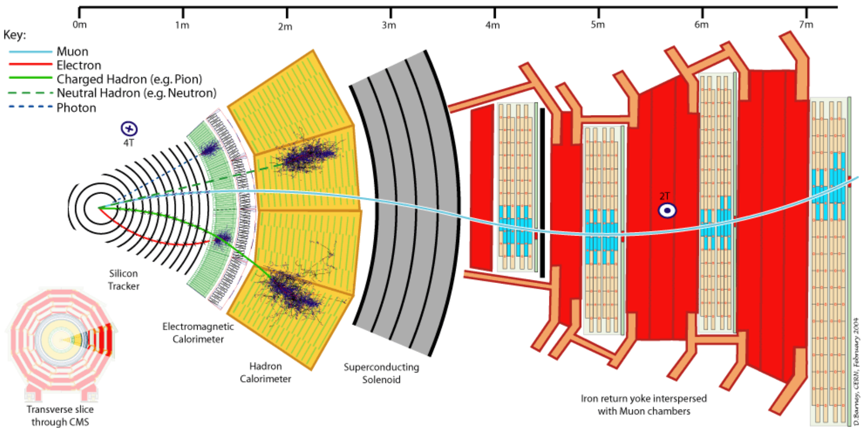

Figure 5.2. The $r\phi$-view of a slice of the CMS detector.

The most important aim of the pixel detector is to precisely reconstruct the primary interaction vertex and secondary vertices from the decay of short flight-path particles. The primary and secondary vertices can be distinguished by measuring the impact parameter of particles. The pixel detector is the innermost subdetector of the CMS and is composed of three barrel layers and two endcap disks at each endcap. The barrel layers have a length of 53 cm and are located at cylinders with mean radii of 4.4 cm, 7.3 cm, and 10.2 cm respectively. The endcap layers are arranged in a turbine-like shape with a 20° tilt, covering the radius from 6 to 15 cm and are placed at $|z| = 34.5$ cm and 46.5 cm. The design of the pixel detector allows the measurement of tracks originating within 2 m from the interaction point in the $|\eta| < 2.2$ region.

The silicon strip tracker (see Fig. 5.3) is located just outside the pixel tracker. There are four inner barrel layers called the tracker inner barrel (TIB) and six outer barrel layers called the tracker outer barrel (TOB). At each endcap side, there are three inner layers called tracker inner disks (TID) and nine outer layers called tracker endcap (TEC). The first two TIB layers and the first two TOB layers are made of double-sided (*stereo*) modules, composed of two modules mounted back-to-back with their strips tilted by 100 mrad. The rest of the TIB and TOB are made of single-sided (*mono*) modules. The silicon tracker has 10 million channels with an active area close to 198 m^2.

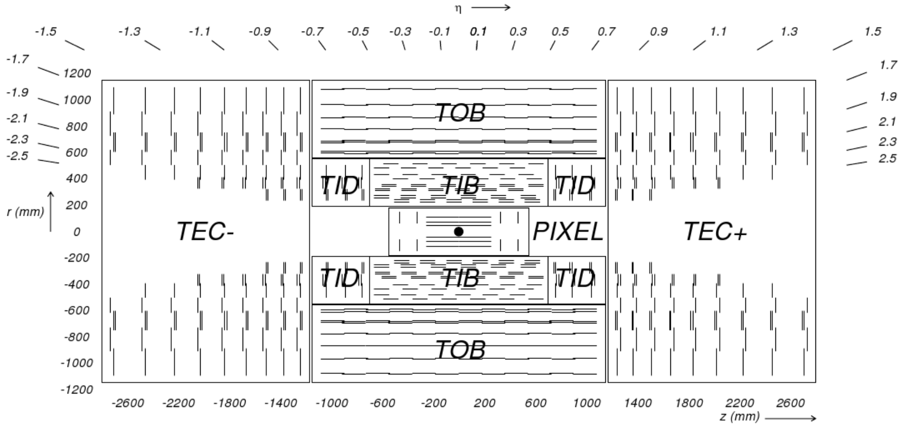

Figure 5.3. View of the CMS tracker in the rz-plane. Each line in the strip tracker represents a silicon strip detector, whereas lines in the pixel detector represent ladders and petals on which the detectors are mounted in the barrel and endcaps, respectively.

5.2.2 The Calorimeters

The purpose of the electromagnetic calorimeter (ECAL) is to measure the energy of electrons and photons.

The ECAL is a hermetic homogeneous calorimeter made of lead-tungstate ($PbWO_4$) crystals and is placed inside the magnetic coil. Lead tungstate has the property of excellent radiation hardness. Lead tungstate crystals have a short radiation length ($X_0 = 0.89$ cm) and a small Moliere radius ($R_{\mathrm{M}} = 2.2$ cm). The ECAL is composed of 61200 crystals in the central barrel part, and 7324 crystals in each endcap.

In the barrel region, silicon avalanche photodiodes (APDs) are employed, while vacuum phototriodes (VPTs) are used in the endcaps. The temperature of the system is kept stable at 0.15°C by a water cooling system since both the crystals and the APDs response are sensitive to temperature changes. The barrel region of the ECAL covers the pseudorapidity region up to $\eta < 1.479$. The barrel part has an inner radius of 129 cm and is composed of 36 supermodules, each containing 1700 crystals. The barrel crystals have a front face cross section of 2222 mm^2 and a length of 230 mm corresponding to $25.8X_0$. The endcaps cover the η region from 1.48 to 3.0. The endcap crystals have dimensions of $28.6 \times 28.6 \times 220$ mm^2. A preshower device is located in front of the endcaps. Two planes of silicon strip detectors are placed behind disks of lead absorber at depths of $2X_0$ and $3X_0$. The energy resolution for electrons from Z boson decays is better than 2% in the central region of the ECAL barrel and is 2-5% elsewhere. The derived energy resolution for photons varies from 1.1% to 2.6% in the barrel and from 2.2% to 5% in the endcaps [76].

The hadron calorimeter (HCAL) is placed outside the electromagnetic calorimeter and inside the superconducting coil. The HCAL is designed to reconstruct jets and missing energy (missing E_{T}) with high precision. The HCAL barrel region covers an η range up to 1.74, and the endcaps cover an η region up to 3. The HCAL is composed of brass layers as absorbers, interleaved by thick plastic scintillator layers. The brass layers have thicknesses of 60 mm in the barrel and 80 mm in the endcaps. The scintillator layers are 4 mm thick. The light is collected by wavelength shifters. The scintillator in each layer is divided into tiles with a granularity matching the granularity of the ECAL trigger towers.

5.2.3 The Solenoid

The remarkable feature of the CMS detector is its strong magnetic field provided by its 13 m long superconducting cylindrical Niobium-Titanium coil. This coil has a diameter of 5.9 m with a uniform magnetic field of 3.8 T at its center. The magnetic flux is returned by a double duty iron yoke support structure [77].

5.2.4 The Muon System

The muon system is designed to identify muons and to accurately measure their momenta. It is one of the most important subdetectors used for the Drell–Yan analysis. The detector design allows to reconstruct muons with high efficiency and measure their momenta with high accuracy. The muon system is the outermost part of the CMS detector. The muon chambers are instrumented in the magnetic iron return yoke. The magnetic field inside the plates of the yoke is used to bend the particles which allows the measurement of the momenta from the measurement of their curvature. The muon system is composed of three independent subsystems. In the barrel region ($|\eta| < 1.0$) Drift Tube (DT) detectors are installed, and Cathode Strip Chambers (CSC) are used in the endcap regions ($0.8 < |\eta| < 2.4$). Resistive Plate Chambers (RPC) are installed in the $|\eta| < 1.6$ region, covering both the barrel and the endcaps. RPCs have limited spatial resolution, but good time resolution thus can provide excellent bunch crossing identification. The muon p_{T} resolution is between 0.8% and 3% depending on η and in good agreement with the simulation [78].

The Drift Tube Chambers

The barrel muon system consists of five wheels placed along the z axis, each one divided into 12 sectors and four stations called MB1, MB2, MB3, MB4 from the inside out. Each sector covers a 30° region in ϕ. Each station consists of 12 chambers, except for MB4, which has 14 chambers. Each DT chamber consists of two or three superlayers, one or two superlayers measure the $r\phi$ coordinate, and the remaining orthogonal superlayer measures the rz coordinate. Each superlayer is composed of four layers of parallel cells. The most basic element is a drift tube cell, with dimensions of 42×13 mm^2. A layer of cells is placed in between two parallel aluminum planes with I-shaped aluminum beams defining their boundaries and also serving as cathodes. The anode is a 50 meter stainless steel wire placed in the center of the cell. The distance of the track from the wire is measured by the drift time of electrons. To improve the distance-time linearity, additional field shaping is obtained with two positively-biased insulated strips, glued on the planes in correspondence to the wire. Typical voltages are +3600 V, +1800 V and −1200 V for the wires, the strips and the cathodes, respectively. The gas used is an 85%/15% mixture of Ar/CO$_2$, which provides good quenching properties and a drift velocity of about 5.6 cm/s.

The Cathode Strip Chambers

The endcap muon system is located at both ends of the barrel cylinder having four stations at each side. They are numbered from ME1 to ME4 ordered based on their distances from the center of the detector. The innermost CSC stations are composed of three concentric rings (ME1/1, ME1/2, ME1/3), while the other stations are composed of two disks only (MEn/1 and MEn/2).

Each ring consists of 18 or 36 trapezoidal chambers overlapping in ϕ. Each CSC chamber is composed of six layers. Each of which consists of an array of anode wires bound between two cathode planes. Strips are intended to measure the ϕ coordinate, and are arranged in the radial direction. Wires are arranged in the orthogonal direction and measure the r coordinate.

5.2.5 The Trigger System

At the LHC design luminosity, the total event rate is expected to be about 1 GHz. However it is impossible to record all events. Therefore the trigger system must reduce the input rate down to a few hundred Hz as well as maintain high efficiencies on the potentially interesting events by selecting events based on their physics signatures. The online filtering process consists of two main steps: the Level-1 (L1) trigger and the High-Level trigger (HLT).

The L1 trigger is implemented in dedicated programmable hardware. It uses information from the calorimeters and muon system to reduce the overall event rate to less than 100 kHz. The L1 trigger has to make an accept-reject decision of an event within 3.2 μs to allow more time for more sophisticated algorithms in the HLT. The L1 trigger is organized into a calorimeter trigger and a muon trigger and the information is transferred to the Global Trigger (GT) which makes the final accept-reject decision.

Upon receipt of a L1 trigger accept, the data are transferred to the front-end readout buffers. The HLT processes all events triggered by the L1 trigger and reduces the rate down to a few hundred Hz. The HLT rate is controlled by the trigger menu, which is designed with a target luminosity in mind to keep the overall rate under control. The CPU usage of the HLT is optimized by the concept of regional reconstruction and by rejecting events as early as possible. The basic strategy is to reconstruct each physics object in different subsystems which can be used to make decisions first and then involve information from more subsystems and make decisions at a higher level. HLT paths are usually divided into several virtual levels, each level involves more information than its previous level, and reduces the event rate from its previous level. A more detailed description of the CMS detector, together with a definition of the coordinate system used and the relevant kinematic variables, can be found in [74].

6. DRELL–YAN CROSS SECTION MEASUREMENT

Measuring the DY cross section is one way to test and verify the predictions of the Standard Model of particle physics at high level of precision. The DY differential cross section in bins of invariant mass allows to assess both the absolute value and the shape of the DY spectrum. The rapidity distributions are particularly important as they are sensitive to the PDFs of the interacting partons. The measurements of the DY differential cross section $d\sigma/dm$, and the double-differential cross section $d^2\sigma/dm\,d|y|$ in the dimuon and dielectron channels are presented. It is crucial to perform the DY analysis in two individual channels in order to avoid possible biases in the measurement results and to verify the correctness of the analysis techniques in each decay channel. The DY analysis in the dimuon and dielectron channels relies on different parts of the CMS detector, and uses independent online and offline selection criteria. Performing the measurement using dimuons allows the extraction of a cleaner signal at low and high invariant masses providing higher signal significance after event selection. The muon momentum resolution degrades as the momentum increases, which requires special care to be taken of the migration effects in the high-mass region. A major reason for carrying out the DY cross section measurement with dielectrons is to take advantage of the electron energy resolution at high mass, which allows a precise measurement up to TeV scale invariant masses. In addition, a fundamental SM principle – lepton universality – can be tested. After carrying out the measurements in the individual lepton channels and checking consistency a combination is performed to achieve a higher precision. Since the initial-state parton configuration is symmetric in the proton-proton collisions, as shown in Fig. 6.1, the resulting rapidity distribution of DY dileptons is also symmetric. As a result, the $d\sigma/dy$ differential cross section is symmetric around zero in a given dilepton invariant

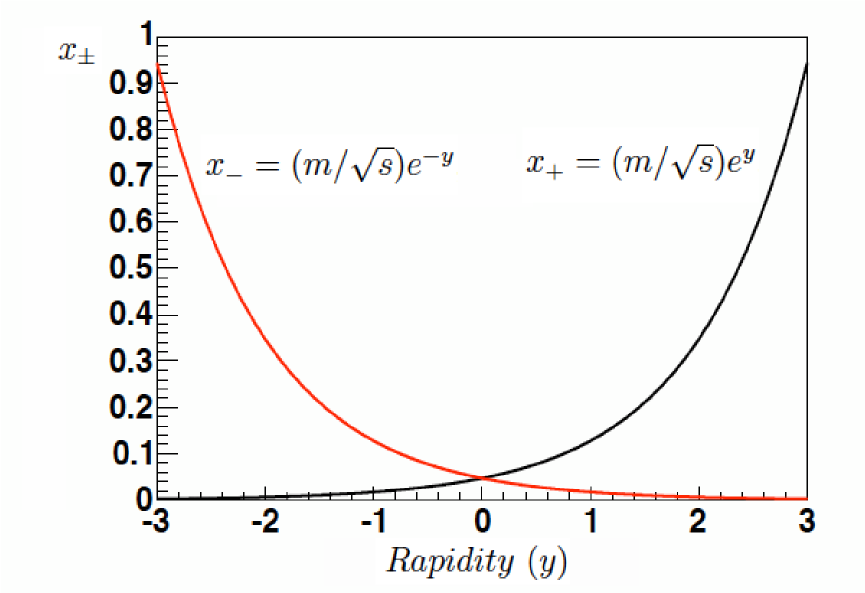

Figure 6.1. The relationship of the Bjorken scaling variables of the initial-state partons ($x_\pm$) and the dilepton rapidity y.

mass region [79]. Thus, we consider only the differential cross section in $|y|$ in order to reduce the statistical errors.

The measurement $d\sigma/dm$ was first performed with 7 TeV data in the mass range $15 < m < 1500\,\text{GeV}$ [19]. Dominated by statistical uncertainties above 160 GeV, it has provided very precise measurement at the Z peak and low mass. A more precise and complete measurement was then performed at 8 TeV, extending the mass range to 2000 GeV [20]. The double-differential cross section $d^2\sigma/dm\,d|y|$ are performed in the mass range $20 < m < 1500\,\text{GeV}$ and absolute dilepton rapidity from 0 to 2.4 at 7 and 8 TeV center-of-mass energies. Almost 5 times as large an amount of data available in the 8 TeV dataset had lead to a significant reduction of statistical uncertainties and made it possible to apply data-driven methods for a larger set of analysis steps. The 8 TeV measurement is dominated by systematic uncertainties up to around 320 GeV and statistically dominated at higher masses. The $d\sigma/dm$ measurements at 7 and 8 TeV are performed in dimuon and dielectron channels. The $d^2\sigma/dm\,d|y|$ measurements at 7 TeV are performed in the dimuon channel only, because adding the dielectron cross section did not increase the overall precision of the combined measurement. However, both dimuon and dielectron channels are considered at 8 TeV.

The increase in the center-of-mass energy at the LHC from 7 to 8 TeV provides the opportunity to measure the ratios of normalized DY cross sections – the double ratios. The double ratios predicted at 7 and 8 TeV are presented, providing substantial cancellations of theoretical systematic uncertainties.

The measurements are based on a data sample of proton-proton collisions collected with the CMS detector and corresponding to integrated luminosities of 4.8 fb^{-1} (dielectron) and 4.5 fb^{-1} (dimuon) at $\sqrt{s} = 7\,\text{TeV}$ and 19.7 fb^{-1} at $\sqrt{s} = 8\,\text{TeV}$.

6.1 Analysis Procedure

The first step of the analysis is the event selection. A set of features is identified and combined into a classifier in order to increase the signal significance and suppress backgrounds. After event selection, the remaining backgrounds are estimated. Next, the observed background-subtracted yield is corrected for the effects of the migration of events among bins of mass and rapidity due to the detector resolution. The acceptance and the efficiency corrections are then applied. Finally, the migration of events due to FSR is corrected. Systematic uncertainties associated with each of the analysis steps are evaluated.

Monte Carlo (MC) samples are used in the analysis for determining efficiencies, acceptances, and for the determination of systematic errors. Data-driven methods are applied to determine efficiency correction factors and backgrounds. MC event samples have been generated using a variety of generators discussed in Appendix D.

The POWHEG simulated sample is based on NLO calculations, and a correction is applied to take into account higher-order QCD and electroweak (EW) effects. The correction factors binned in dilepton rapidity y and transverse momentum p_{T} are determined in each invariant-mass bin to be the ratio of the double-differential cross sections calculated at NNLO QCD and NLO EW with FEWZ and at NLO with POWHEG, as described in Appendix C. The corresponding higher-order effects depend on the dilepton kinematic variables. Higher-order EW corrections are small in comparison to FSR corrections. They increase for invariant masses in the TeV region [80], but are insignificant compared to the experimental precision for the whole mass range under study. It is important to apply this correction because NNLO QCD effects are rather important in the low-mass region (below 40 GeV). Namely, the effect of the NNLO kinematic correction factors on the acceptance reaches up to 50% in the low-mass region, although it is almost negligible in the high-mass region (above 200 GeV).

Fig. 6.2 summarizes the analysis procedure for the $d\sigma/dm$ and $d^2\sigma/dm\,d|y|$ differential cross section measurements.

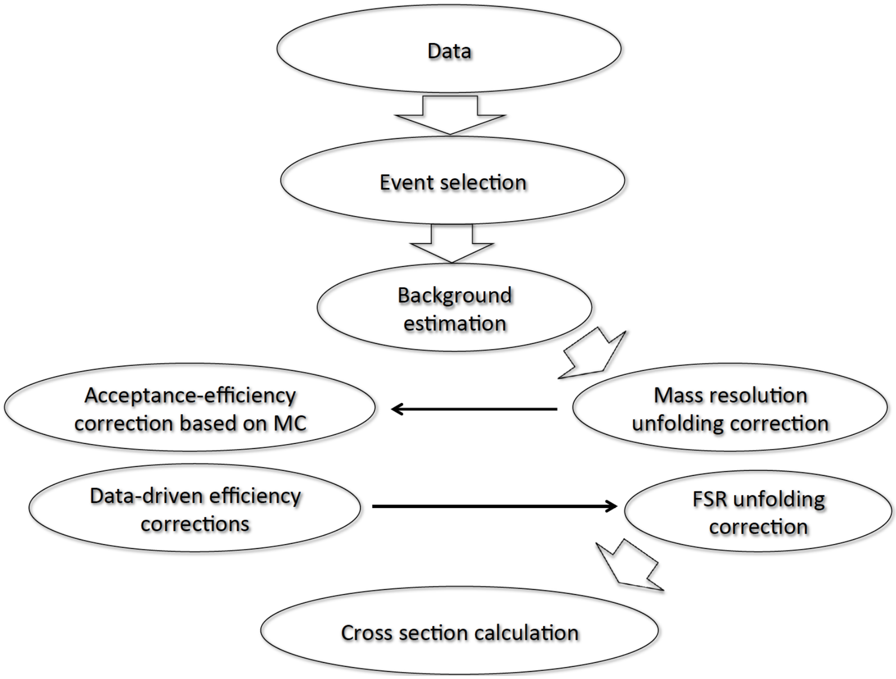

Figure 6.2. The analysis procedure for the $d\sigma/dm$ and $d^2\sigma/dm\,d|y|$ differential cross section measurements.

The measured cross sections are calculated using the following formula:

$$\frac{d\sigma}{dv} = \frac{N_{\text{u}}}{A \cdot \epsilon \cdot \rho \cdot L_{\text{int}}}, \tag{6.1}$$

where v is a variable in which bins the measurement is performed (for instance, invariant mass or absolute rapidity), N_{u} denotes the background-subtracted yield obtained using a matrix inversion unfolding technique to correct for the effects of the migration of events in mass due to the detector resolution. The acceptance A and the efficiency ϵ are both estimated from simulation, while ρ, the correction (scale) factor accounting for the differences in the efficiency between data and simulation, is extracted using a technique described in Appendix F.

The double-differential cross section measurement is performed within the detector acceptance in order to reduce model dependence and increase the sensitivity to PDFs.

The correction for FSR is performed to facilitate the comparison to the theoretical predictions and to properly combine the measurements in the dielectron and dimuon channels. The FSR correction is estimated separately from the detector resolution correction by means of the same unfolding technique.

The differential cross sections are normalized to the Z peak region ($60 < m < 120$ GeV) and thus the integrated luminosity L_{int} is only used for the Z boson production cross section discussed in Section 6.8.

The differential $d\sigma/dm$ cross section measurement is carried out in a number of bins sufficient to measure the shape of the distribution. However, there is a number of competing factors setting a lower bound on the size of the analysis bin. Namely: the mass resolution scale, the number of events, and the size of the systematic uncertainties. As a result, 41 mass bins with the following boundaries are considered for the measurement:

$$\begin{gathered}15,\ 20,\ 25,\ 30,\ 35,\ 40,\ 45,\ 50,\ 55,\ 60,\ 64,\ 68,\ 72,\ 76,\ 81,\ 86,\ 91,\\ 96,\ 101,\ 106,\ 110,\ 115,\ 120,\ 126,\ 133,\ 141,\ 150,\ 160,\ 171,\ 185,\\ 200,\ 220,\ 243,\ 273,\ 320,\ 380,\ 440,\ 510,\ 600,\ 1000,\ 1500,\ 2000\ \text{GeV}\end{gathered} \tag{6.2}$$

The measurement at 7 TeV center-of-mass energy was performed up to 1500 GeV. The mass range have been extended to 2000 GeV as more statistics become available at high mass at 8 TeV.

The binning for the double-differential $d^2\sigma/dm\,d|y|$ cross section is chosen in order to maximize the sensitivity of the measurements for the PDF constraints. It is essential to measure the rapidity dependence of the cross section with high accuracy in order to increase the PDF constraining power. Thus, the double-differential $d^2\sigma/dm\,d|y|$ measurement is performed in only 6 invariant mass bins using bin edges: 20, 30, 45, 60, 120, 200, 1500 GeV. This choice of mass bins splits the low-mass region, FSR region, Z peak region and the high-mass region providing sufficient statistics in each mass region to allow for a very precise measurement of rapidity distribution. For each mass bin, 24 bins of absolute dilepton rapidity are defined, except for the highest mass bin, where only 12 absolute dilepton rapidity bins are used (see Table 6.1). The differential cross sections are first measured separately for both lepton flavors and found to be in agreement. The combined cross section measurement is then compared to the NNLO QCD predictions as computed with Fewz [81] using the CT10 NNLO PDF. The $d^2\sigma/dm\,d|y|$ measurement is compared to the NNLO theoretical predictions as computed with Fewz using CT10, NNPDF2.1, MSTW2008, HERAPDF15, JR09, ABKM09, and CT10W PDFs [47,52,82–85].

Table 6.1

Dilepton rapidity–invariant mass binning for the $d^2\sigma/dmd|y|$ cross section measurement.

Mass bin (GeV)	Number of equidistant rapidity bins	Rapidity range
20-30	24	$\|y\| < 2.4$
30-45	24	$\|y\| < 2.4$
45-60	24	$\|y\| < 2.4$
60-120	24	$\|y\| < 2.4$
120-200	24	$\|y\| < 2.4$
200-1500	12	$\|y\| < 2.4$

6.2 Event Selection

The experimental signature of the DY production is two isolated and oppositely charged leptons originating from the same primary vertex. The analysis presented in this thesis is based on the dilepton data samples selected by inclusive double-lepton triggers.

6.2.1 Muon Selection

The first step in the muon selection is the trigger. The choice of the L1 and HLT trigger path is intended to maximize the number of events collected for further offline analysis. Two alternative strategies are considered: (1) select events containing at least one muon having p_{T} above a certain threshold (single muon triggers), and (2) select events containing at least two muons, each having p_{T} above a certain threshold (dimuon triggers). The corresponding p_{T} thresholds are set in the trigger-menu for each data-taking period to keep trigger input rates suitable for storage. The dimuon trigger strategy is selected for the DY analysis because it allows to achieve larger statistics gains in low-mass region. A combination of the lowest p_{T} threshold unprescaled dimuon triggers without isolation requirement is used to select events for further offline analysis. The triggers selecting events for the data samples are summarized in Table 6.2. Thus, at 7 TeV a combination of lowest p_{T}-threshold dimuon triggers is used while at 8 TeV the single dimuon trigger path is used for the entire data-taking period.

Table 6.2
Summary of the triggers used in the 7 and 8 TeV analyses.

Trigger path	7 TeV	8 TeV
HLT_DoubleMu6	Runs 160403-164236	
HLT_Mu13_Mu8	Runs 165088-180252	
HLT_Mu13_TkMu8		Runs 190645-208686

Each muon is required to be within the acceptance of the muon subsystem ($|\eta| < 2.4$). The leading muon in the event is required to have a transverse momentum $p_{\mathrm{T}} > 14$ GeV ($p_{\mathrm{T}} > 20$ GeV) and the trailing muon $p_{\mathrm{T}} > 9$ GeV ($p_{\mathrm{T}} > 10$ GeV) in the 7 TeV (8 TeV) analyses respectively, allowing to operate on the plateau region of the trigger efficiency.

The muons are required to pass the standard CMS muon identification and quality control criteria that are based on the number of hits found in the tracker, the response of the muon chambers, and a set of matching criteria between the muon track parameters as measured by the CMS tracker and those measured in the muon chambers [78]. Both muons are required to match the HLT trigger objects. Cosmic ray muons that traverse the CMS detector close to the interaction point can appear as back-to-back dimuons; these are removed by requiring both muons to have an impact parameter in the transverse plane of less than 2 mm with respect to the center of the interaction region and the opening angle between the two muons to differ from π by more than 5 mrad. In order to reject muons from pion and kaon decays, a common vertex for the two muons is required. An event is rejected if the dimuon vertex probability is smaller than 2%. More details on muon reconstruction and identification can be found in [78].

To suppress the background contributions due to muons originating from heavy-quark decays and non-prompt muons from hadron decays, both muons are required to be isolated from other tracks within a cone of size $\Delta R = 0.3$, with $\Delta R = \sqrt{(\Delta\eta)^2 + (\Delta\phi)^2}$. The relative combined isolation of the muon, based on the CMS particle-flow algorithm [86, 87] is used. The isolation variable is defined as $I_{\mathrm{rel}}^{\mathrm{comb}} = \sum_{\Delta R<0.3}(E_{\mathrm{T}}+p_{\mathrm{T}})/p_{\mathrm{T}}(\mu)$, where the sum is over the transverse energy E_{T} as measured in the electromagnetic and hadron calorimeters and the transverse momentum p_{T} of charged tracks excluding the muon candidate as measured in the tracker subsystem. The isolation is defined relative to the muon candidate transverse momentum $p_{\mathrm{T}}(\mu)$. The $\mathrm{e}-\gamma$ energy deposits have been excluded from the isolation definition in the 7 TeV analysis to avoid large pileup effect. In the 8 TeV analysis, the contribution due to pileup was explicitly subtracted from the isolation variable. The muons are required to satisfy $I_{\mathrm{rel}}^{\mathrm{comb}} < 0.2$ (0.15) in the 7 TeV (8 TeV) analyses correspondingly. The isolation threshold was changed compared to the 7 TeV measurement [19] to achieve optimum performance in terms of signal efficiency and background misidentification rate.

Events are selected for further analysis if they contain opposite-charge muon pairs meeting the above requirements. If more than one dimuon candidate passes these selections, the pair with the highest χ^2 probability for a kinematic fit to the dimuon vertex is selected.

Table 6.3 summarizes the selection cuts used in the differential and double-differential cross section measurements in the dimuon channel.

Table 6.3
Summary of the event selection cuts in the dimuon analysis.

Selection cut	7 TeV	8 TeV
Kinematic acceptance	$p_{\mathrm{T}} > 9, 14\,\mathrm{GeV}$	$p_{\mathrm{T}} > 10, 20\,\mathrm{GeV}$
Geometric acceptance	$\lvert\eta\rvert < 2.4$	
Muon identification	Each muon reconstructed as Global and Tracker Muon Global $\chi^2/N_{\mathrm{dof}} < 10$ $N_{\mathrm{pixel}} > 0$ $N_{\mathrm{muon}} > 0$ $N_{\mathrm{segments\ matched}} > 1$ $N_{\mathrm{trk.\ layers}} > 5$ $\lvert d_{\mathrm{xy}}(PV)\rvert < 2$ mm	
Isolation	$\sum_i (I_{\mathrm{had}}^{\mathrm{ch}} + I_{\mathrm{had}}^{\mathrm{neut}})/p_{\mathrm{T}}^{\mu} < 0.2$	$\sum_i (I_{e-\gamma} + I_{\mathrm{had}}^{\mathrm{ch}} + I_{\mathrm{had}}^{\mathrm{neut}})/p_{\mathrm{T}}^{\mu} < 0.15$
Angle between muon tracks	$\alpha_{3\mathrm{D}} = \arccos\left((\vec{p_1}^{\mathrm{track}}, \vec{p_2}^{\mathrm{track}})/p_1^{\mathrm{track}}/p_2^{\mathrm{track}}\right) < 5$ mrad	
Vertex Probability	Vertex Probability (dimuon) > 0.02	

Fig. 6.8-6.11 show the distributions for each of the variables listed in Tab. 6.3.

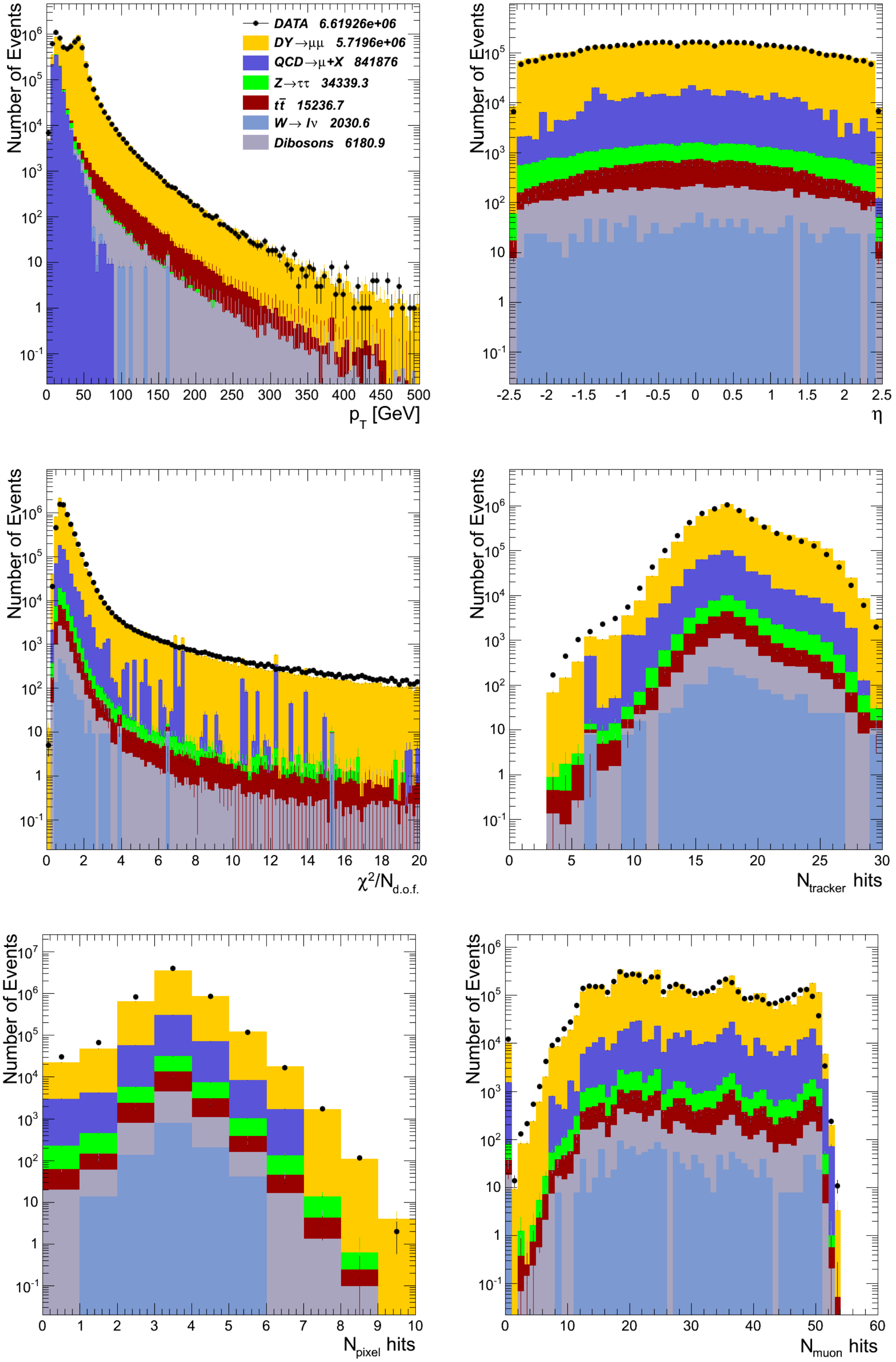

Figure 6.3. Distributions for the variables used to discriminate between signal and various backgrounds in the 7 TeV analysis (as listed in Tab. 6.3), not including the cut on the variable plotted.

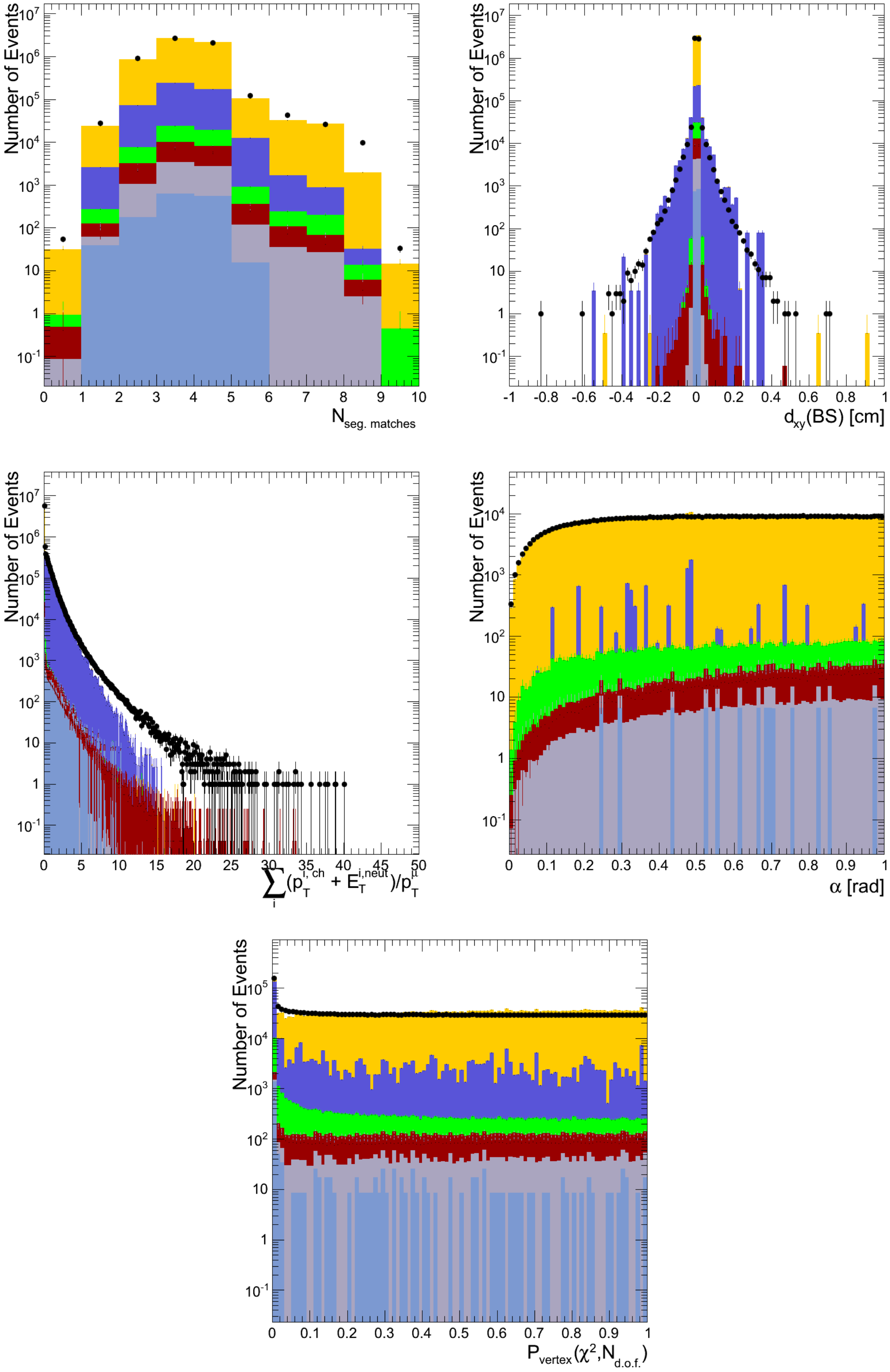

Figure 6.4. Distributions for the variables used to discriminate between signal and various backgrounds in the 7 TeV analysis (as listed in Tab. 6.3), not including the cut on the variable plotted.

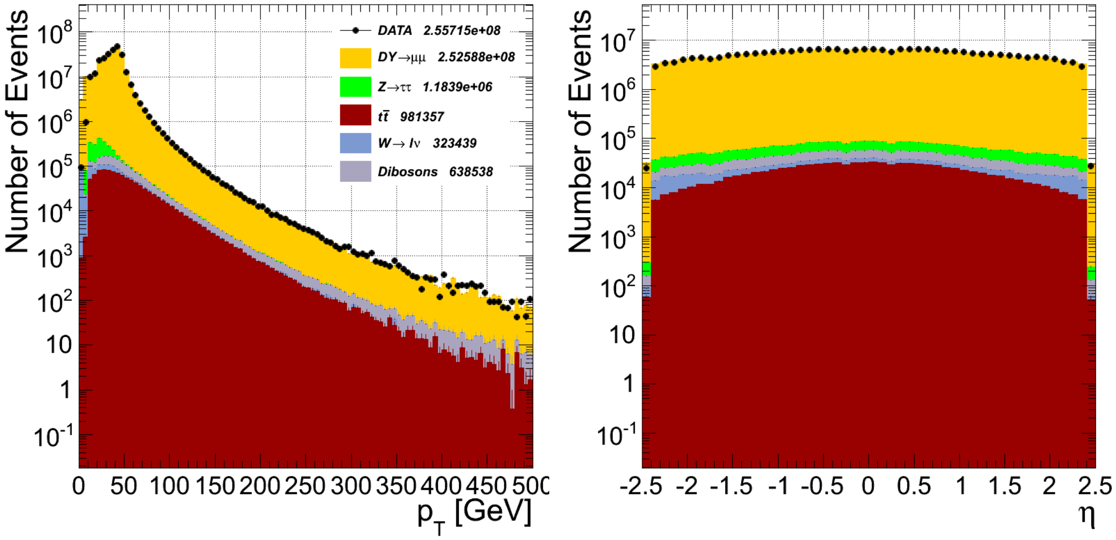

Figure 6.5. Distributions for the variables used to discriminate between signal and various backgrounds in the 8 TeV analysis (as listed in Tab. 6.3), not including the cut on the variable plotted.

As seen, the data and simulation agree well at both the 7 and 8 TeV center-of-mass energies, which is an indication that most of the detector hardware, reconstruction software, and simulation is well understood. The simulated QCD sample has limited statistics after the selection (especially at 8 TeV), which results in fluctuations in some distributions and a discrepancy in the tail of the isolation distribution. These fluctuations do not affect the measurements as the data-driven estimated is used. The difference between p_{T} distributions at the low transverse momentum region between the two center-of-mass energies is expected due to the change in the online p_{T} requirements.

6.2.2 Electron Selection

Dielectron events at 8 TeV are selected by triggering on two electrons with minimum E_{T} requirements of 17 GeV for one of the electrons and 8 GeV for the other. This approach provides the lowest-E_{T} dielectrons so that one can probe the lowest possible dielectron invariant masses.

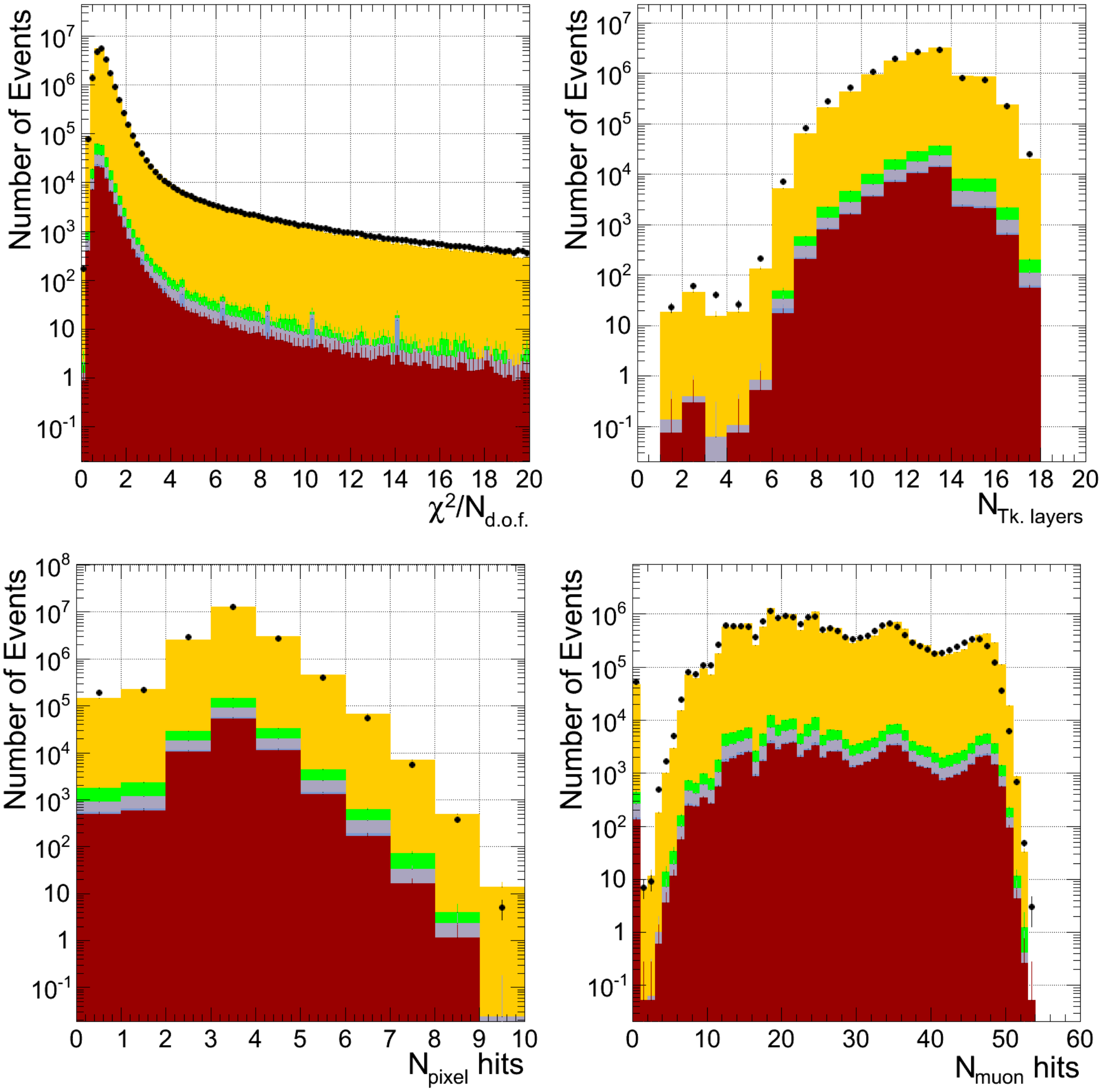

Figure 6.6. Distributions for the variables used to discriminate between signal and various backgrounds in the 8 TeV analysis (as listed in Tab. 6.3), not including the cut on the variable plotted.

The dielectron candidates are selected online by requiring two clusters in the ECAL. The offline reconstruction of the electrons starts by building super-clusters [88] in the ECAL in order to collect the energy radiated by bremsstrahlung in the tracker material. A specialized tracking algorithm is used to accommodate changes of the curvature caused by the bremsstrahlung. The super-clusters are then matched to

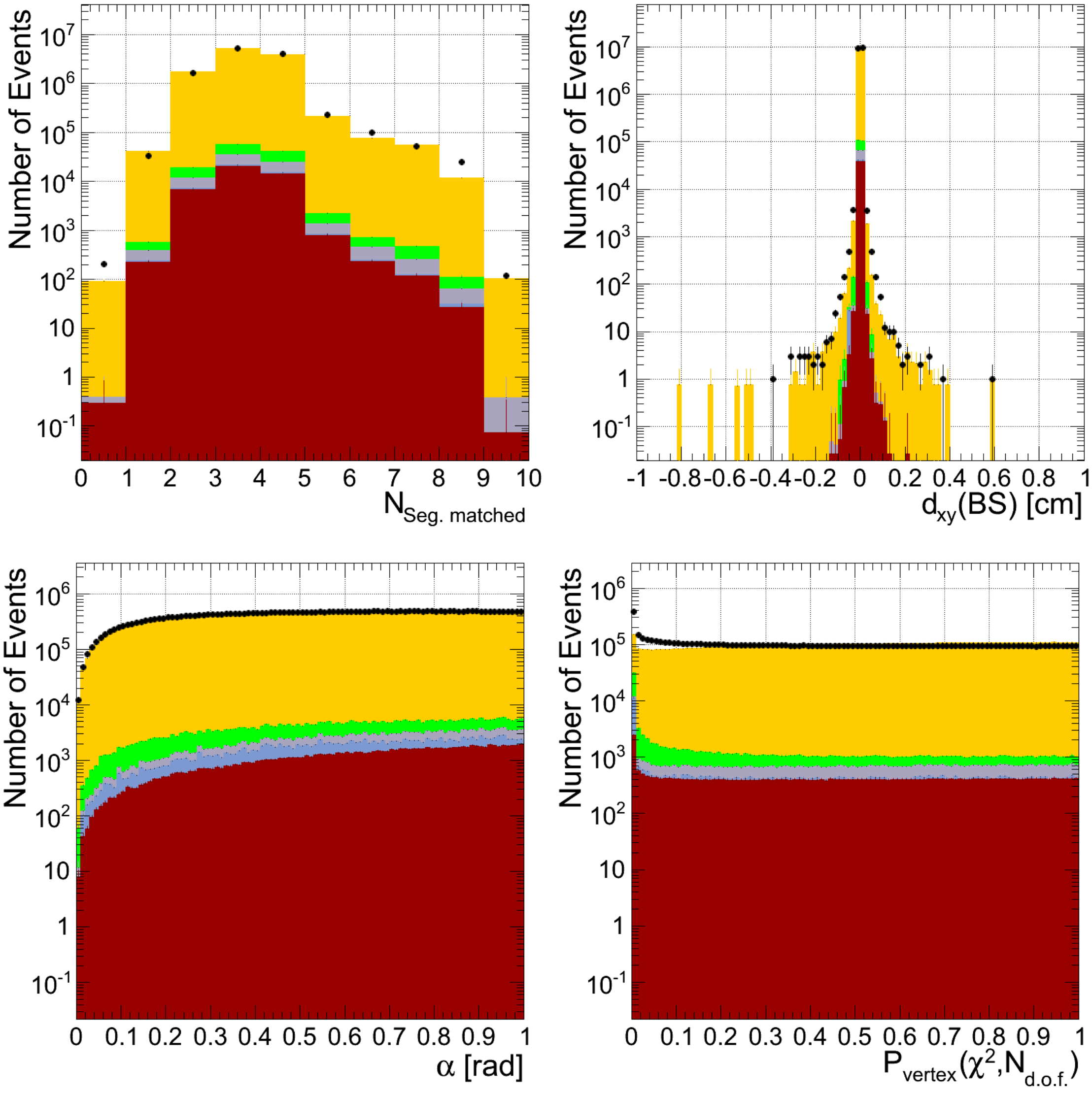

Figure 6.7. Distributions for the variables used to discriminate between signal and various backgrounds in the 8 TeV analysis (as listed in Tab. 6.3), not including the cut on the variable plotted.

the electron tracks. The electron candidates are required to have a minimum E_{T} of 10 GeV after the correction for the ECAL energy scale.

The reconstruction of an electron is based on the CMS particle-flow algorithm [86, 87]. The electrons are identified by means of shower shape variables while the electron isolation criterion is based on a variable that combines tracker and calorimeter information. For isolation, the transverse momenta of the particles within a cone of $\Delta R < 0.3$ are summed, excluding the electron candidate itself. The ratio of the summed transverse momenta (I_{PF}) to the transverse momentum of the electron candidate ($I_{\mathrm{PF}}/p_{\mathrm{T}}$) is required to be less than 0.15 for all the electrons, except for those with $E_{\mathrm{T}} < 20\,\mathrm{GeV}$ in the endcaps, where the requirement is tightened to be less than 0.10. The contribution due to pileup is subtracted from the isolation variable. The isolation criteria are optimized to maximize the rejection of misidentified electrons from QCD multijet production and the non-isolated electrons from the semileptonic decays of heavy quarks. The electron candidates are required to be consistent with particles originating from the primary vertex in the event. The electrons originating from photon conversions are suppressed by requiring that there be not more than 1 expected inner tracker hits on the reconstructed track matched to the electron, and also by rejecting a candidate if it forms a pair with a nearby track that is consistent with a conversion. Additional details on electron reconstruction and identification can be found in [88].

Both electrons are selected with the impact parameter requirements $|d_{xy}| < 0.02$ cm and $|d_z| < 0.1$ cm with respect to the primary vertex. The leading electron candidate in an event is required to have a transverse momentum of $p_{\mathrm{T}} > 20$ GeV, while the trailing electron candidate must have $p_{\mathrm{T}} > 10$ GeV. As with muons, electrons are required to match HLT trigger objects, but no charge requirement is imposed on the electron pairs to avoid efficiency loss due to non-negligible charge misidentification.

In case there are multiple dielectron pairs passing the selection cuts, a lepton pair with the highest invariant mass is kept for further analysis. Nevertheless, the fraction of events with multiple dielectron candidates is rather small: 0.02% of observed events and 0.1% of events in the signal MC sample.

Table 6.4 summarizes the selection cuts used in the differential and double-differential cross section measurement in the dielectron channels.

Fig. 6.8-6.12 show the distributions of the variables listed in Table 6.4. As seen, the distributions for the variables used in the selection are well reproduced in simulation

Table 6.4
Summary of the event selection cuts in dielectron analysis. Values in the brackets denote the cut thresholds in the endcaps.

Selection cut	Cut threshold
Kinematic acceptance	$p_{\mathrm{T}} > 10, 20\,\mathrm{GeV}$
Geometric acceptance	$\lvert\eta\rvert < 2.4$
Electron identification	Medium Working point Track-cluster matching in η-direction, $d\eta_{\mathrm{In}} < 0.004(0.007)$ Track-cluster matching in ϕ-direction, $d\phi_{\mathrm{In}} < 0.06(0.03)$ Lateral shower shape, $\sigma_{i\eta i\eta} < 0.01(0.03)$ Relative hadronic activity, $H/E < 0.12(0.10)$ Conversion rejection requirement Not more than 1 expected inner tracker hits Vertex: $d_0 < 0.02(0.02)$ Vertex: $d_z < 0.1(0.1)$ $\lvert 1/E - 1/p\rvert < 0.05(0.05)$
PF Isolation	$I_{\mathrm{PF}}/p_{\mathrm{T}} < 0.15$ in barrel In endcap, $I_{\mathrm{PF}}/p_{\mathrm{T}} < 0.15$ when $p_{\mathrm{T}} > 20\,\mathrm{GeV}$, and $I_{\mathrm{PF}}/p_{\mathrm{T}} < 0.10$ when $p_{\mathrm{T}} < 20\,\mathrm{GeV}$

in the dielectron analysis as well. The QCD simulated sample has low statistics after the selection and appears in the plots as a set of peaks in the isolated bins. However, this does not affect the analysis as the data-driven QCD background estimate is used in the measurement.

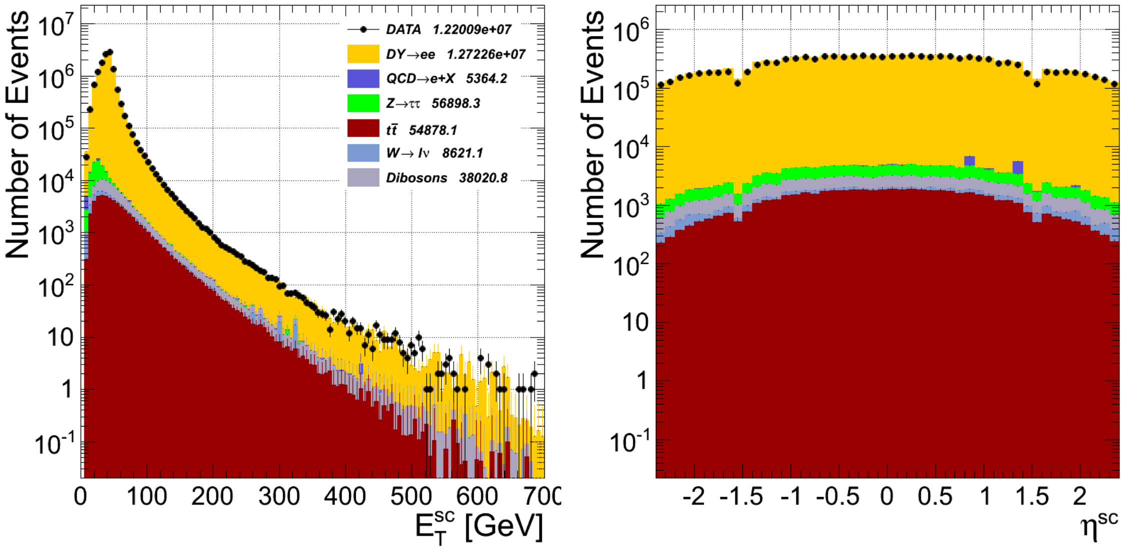

Figure 6.8. Electron supercluster E_{T} (left) and pseudorapidity (right) distributions for data and simulation in the 8 TeV analysis, not including the cut on the variable plotted.

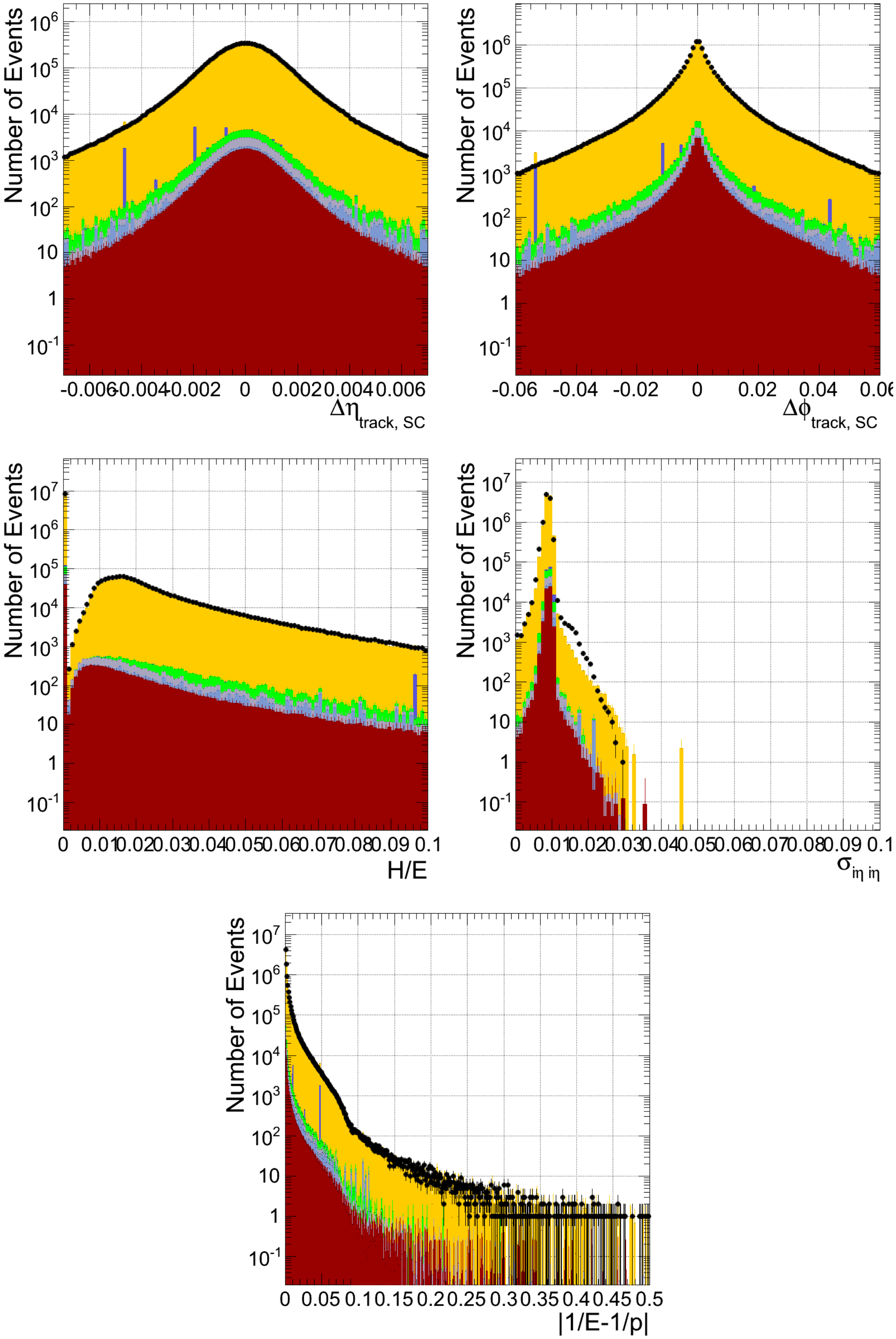

Figure 6.9. Distributions for the variables used to discriminate between signal and various backgrounds in the dielectron channel in the 8 TeV analysis (as listed in Tab. 6.4), not including the cut on the variable plotted. Central pseudorapidity region ($|\eta| < 0.8$) is plotted.

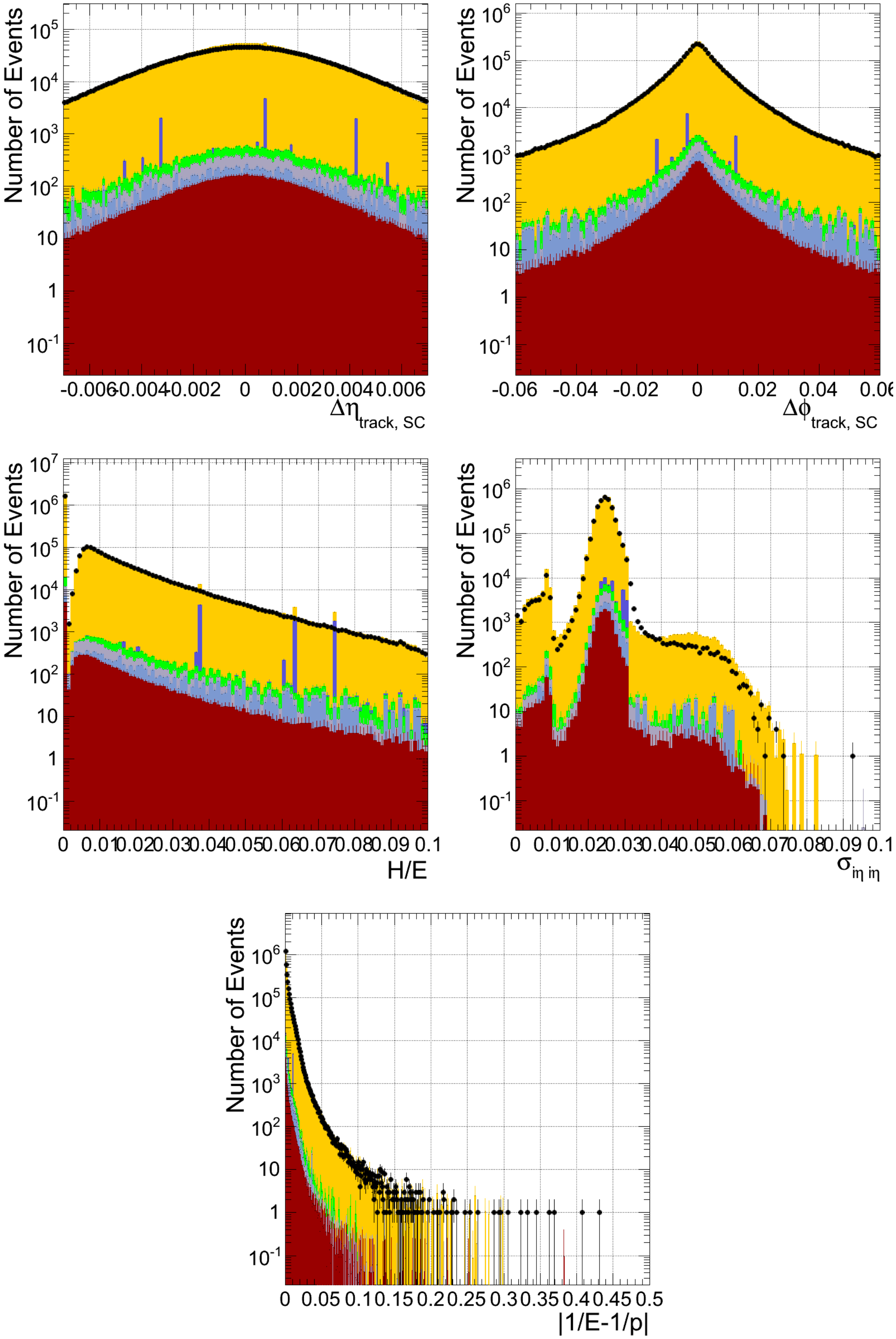

Figure 6.10. Distributions for the variables used to discriminate between signal and various backgrounds in the dielectron channel in the 8 TeV analysis (as listed in Tab. 6.4), not including the cut on the variable plotted. Peripheral pseudorapidity region ($|\eta| > 0.8$) is plotted.

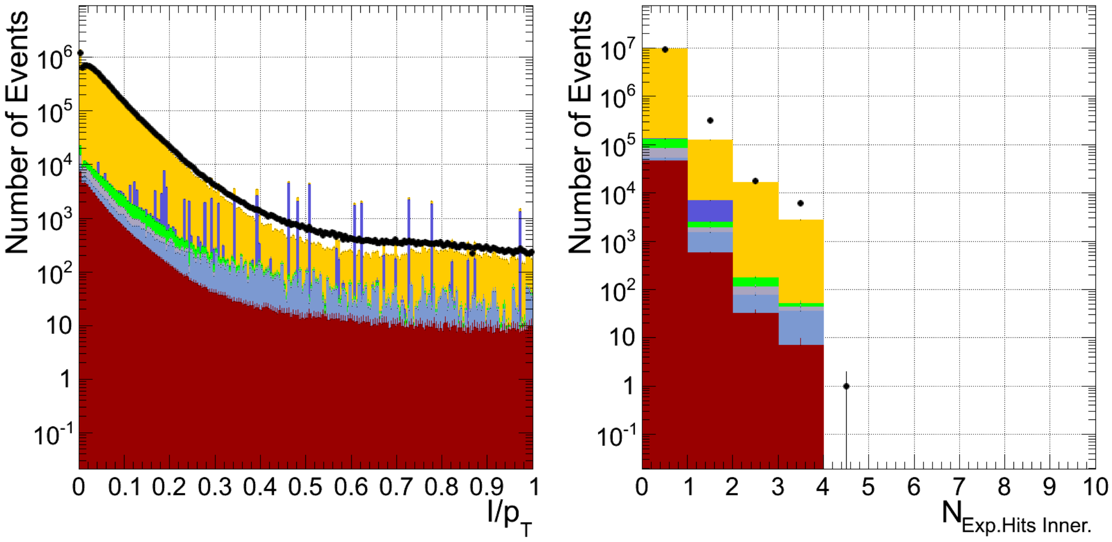

Figure 6.11. Distributions for the variables used to discriminate between signal and various backgrounds in the dielectron channel in the 8 TeV analysis (as listed in Tab. 6.4), not including the cut on the variable plotted. Central pseudorapidity region ($|\eta| < 0.8$) is plotted.

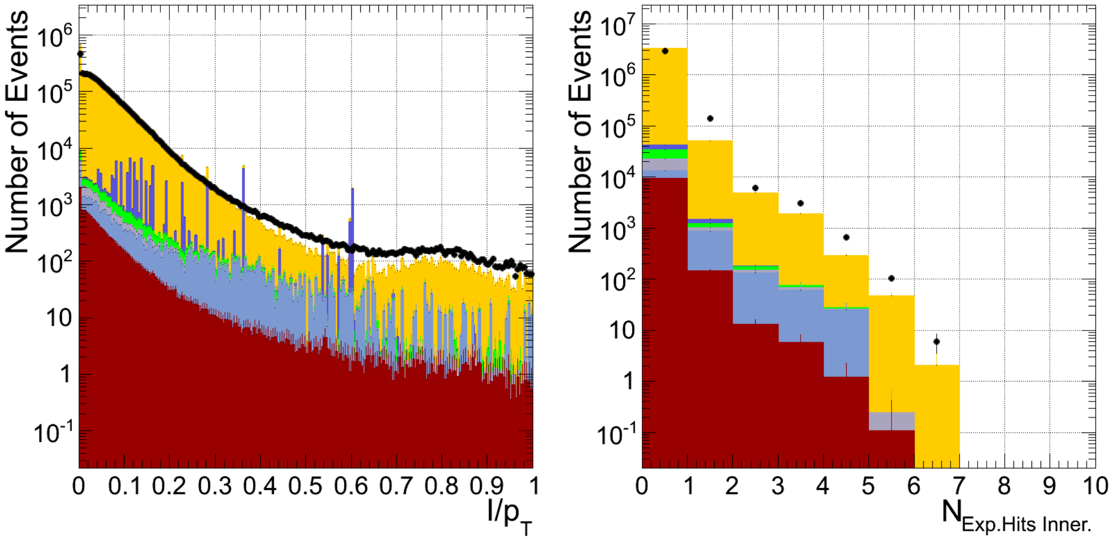

Figure 6.12. Distributions for the variables used to discriminate between signal and various backgrounds in the dielectron channel in the 8 TeV analysis (as listed in Tab. 6.4), not including the cut on the variable plotted. Peripheral pseudorapidity region ($|\eta| > 0.8$) is plotted.

6.3 Background Estimation

The major background contributions in the dielectron channel arise from $\tau^+\tau^-$ and $t\bar{t}$ processes in the low-mass region and from QCD events with multiple jets at high invariant mass. The background composition is somewhat different in the dimuon final state. Multijet events and DY production of $\tau^+\tau^-$ pairs are the dominant sources of background in the dimuon channel at low invariant mass and in the region just below the Z peak. Diboson and $t\bar{t}$ production followed by leptonic decays are the dominant sources of background at high invariant mass. Lepton pair production in $\gamma\gamma$-initiated processes, where both initial-state protons radiate a photon, is significant at high mass. The contribution from this channel is treated as an irreducible background and is estimated with FEWZ [89]. To correct for this background, a bin-by-bin ratio of the DY cross sections with and without the photon induced contribution is calculated (see Appendix E for details). This bin-by-bin correction is applied after the mass resolution unfolding step, whereas other backgrounds for which we have simulated events are corrected for before. This background correction is negligible at low mass and in the Z peak region, rising to approximately 20% in the highest mass bin.

In the dielectron channel, the QCD multijet background is estimated with a data sample collected with the trigger requirement of a single electromagnetic cluster in the event. Non-QCD events such as DY are removed from the data sample using event selection and event subtraction using simulation, leaving a sample of QCD events with characteristics similar to those in the analysis data sample. This sample is used to estimate the probability for a jet to pass the requirements of the electromagnetic trigger and to be falsely reconstructed as an electron. This probability is then applied to a sample of events with one electron and one jet to estimate the background contribution from an electron and a jet passing electron selection requirements. As the contribution from two jets passing the electron selections is considered twice in the previous method, the contribution from a sample with two jets multiplied by the square of the probability for jets passing the electron selection requirements is further subtracted.

The QCD multijet background in the dimuon channel is evaluated by selecting a control data sample before the isolation and charge sign requirements are applied, following the method described in [90].

The largest of the backgrounds consist of final states with particles decaying by EW interaction, producing electron or muon pairs, for example, $t\bar{t}$, $\tau^+\tau^-$, and WW. Notably, these final states contain electron-muon pairs at twice the rate of electron or muon pairs. These electron-muon pairs can be cleanly identified from data and properly scaled (taking into account the detector acceptance and efficiency) in order to calculate the background contribution to the dielectron and dimuon channels.

Background yields estimated from an eμ data sample are used to reduce the systematic uncertainty due to the limited theoretical knowledge of the cross sections of the SM processes. The residual differences between background contributions estimated from data and simulation are taken into account in the systematic uncertainty assignment, as detailed in Section 6.7.

The background estimation methods are discussed in Appendix F in detail.

The dilepton yields for data and simulated events at 7 TeV center of mass energy in bins of invariant mass are reported in Fig. 6.13. As shown in the figure, the QCD multijet process is the dominant background in the low-mass region, contributing up to about 10% in the dimuon rapidity distribution. In the high-mass regions, $t\bar{t}$ and single-top-quark (tW) production processes are dominant and collectively contribute up to about 20%. The photon induced background is absorbed in the signal distribution, no correction is applied at this stage.

The expected shapes and relative dimuon yields from data and MC events in bins of dimuon rapidity, per invariant mass bin, can be seen in Fig. 6.14.

The expected shapes and relative dimuon an dielectron yields from data and MC events at 8 TeV center of mass energy in bins of invariant mass can be seen in Fig. 6.15. As shown in the figure, the background contribution at low mass is no larger than 5% in both decay channels. In the high-mass region, background contamination

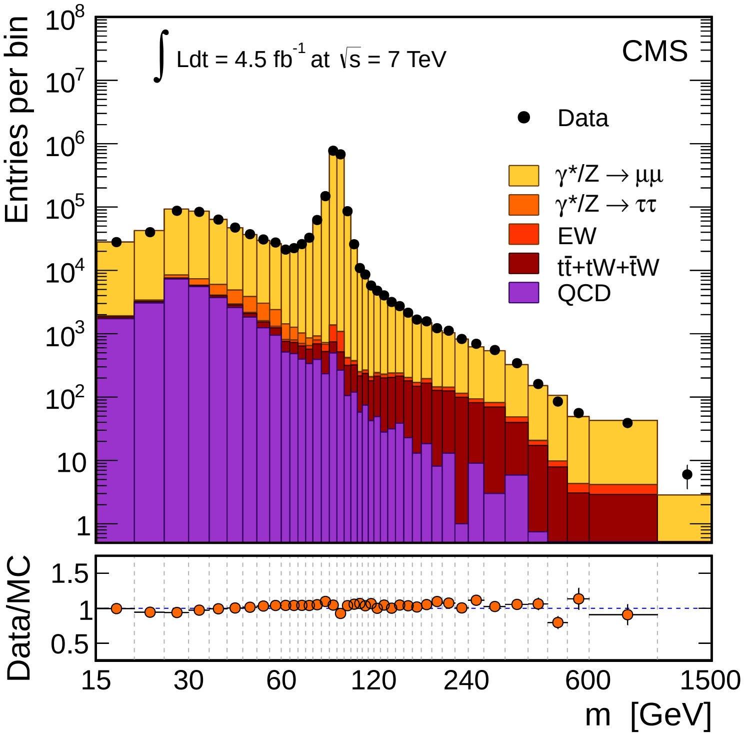

Figure 6.13. The observed dimuon invariant mass spectrum for data and MC events and the corresponding ratios of observed to expected yields. The QCD multijet and $t\bar{t}$ background yields are predicted using control samples in data. The EW histogram indicates the diboson and W+jets production. The NNLO reweighted POWHEG MC signal sample is used. No other corrections are applied. Error bars are statistical only.

is more significant, reaching approximately 50% (30%) in the dielectron (dimuon) distributions.

The expected shapes and relative dilepton yields from data and Monte Carlo events in bins of dilepton rapidity per invariant mass slice can be seen in Fig. 6.16. As shown in the figure, QCD background is dominating in the low mass regions and it contributes up to about 10% in the dimuon rapidity distribution of the regions. In the high mass regions, $t\bar{t}$ and single top backgrounds are dominating and contributing up to about 20% to the total yield.

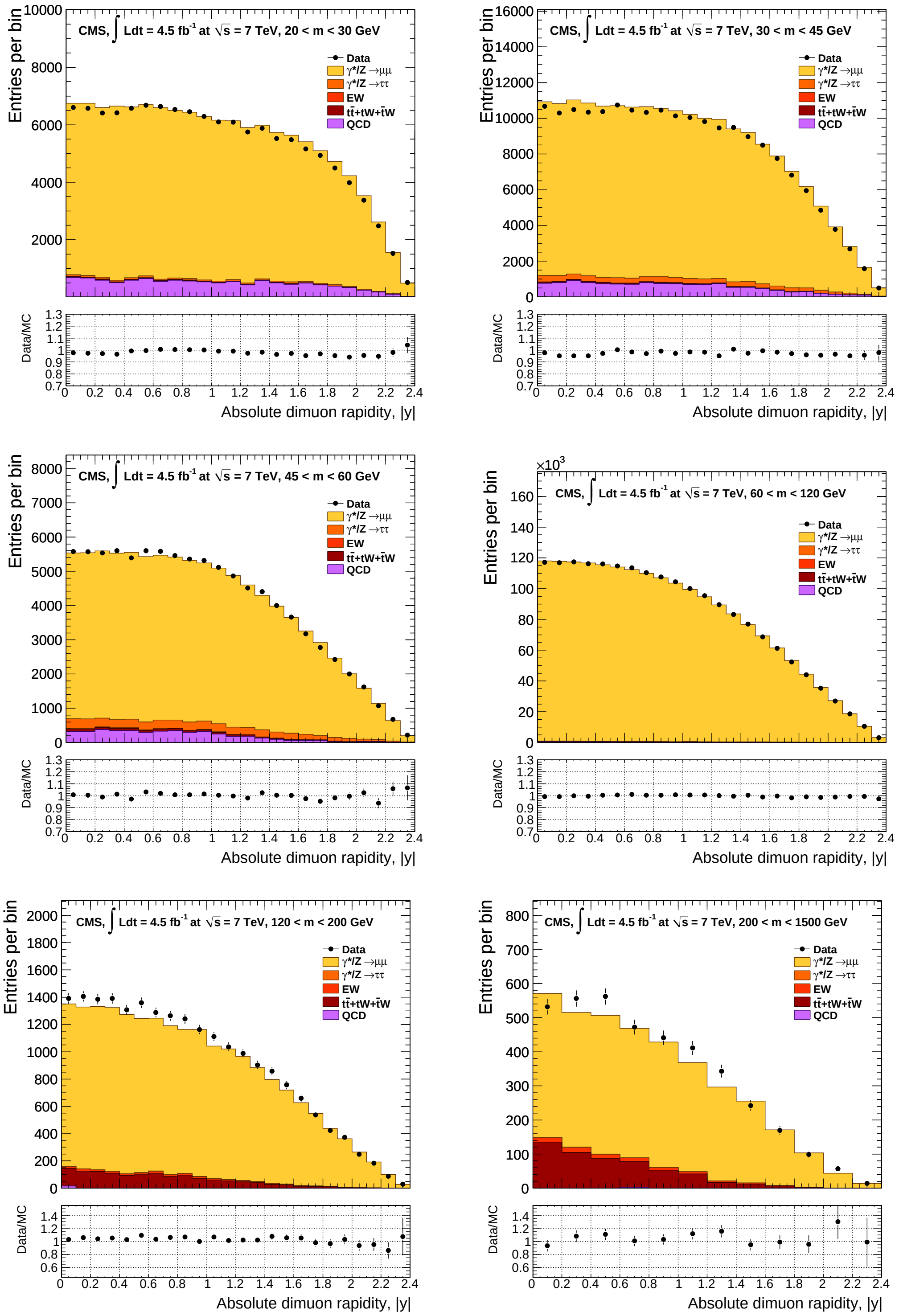

Figure 6.14. The observed dimuon rapidity spectra per invariant mass bin for data and MC events. There are six mass bins between 20 and 1500 GeV, from left to right and from top to bottom. The NNLO reweighted POWHEG MC signal sample is used. The EW histogram indicates the diboson and W+jets production. The normalization factors are determined using the number of events in data in the Z-peak region, and they are applied to all of the mass bins. Error bars are statistical only.

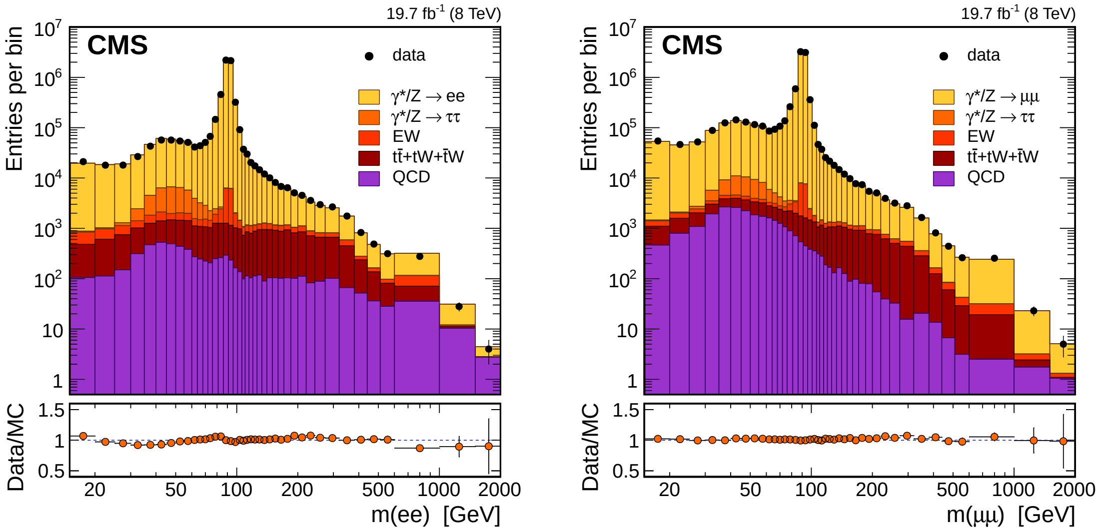

Figure 6.15. The observed dielectron (left) and dimuon (right) invariant mass spectra for data and MC events and the corresponding ratio of observed to expected yields. The EW curve indicates the diboson and W+jets production. The NNLO reweighted Powheg MC signal sample is used. No other corrections are applied. Error bars are statistical only.

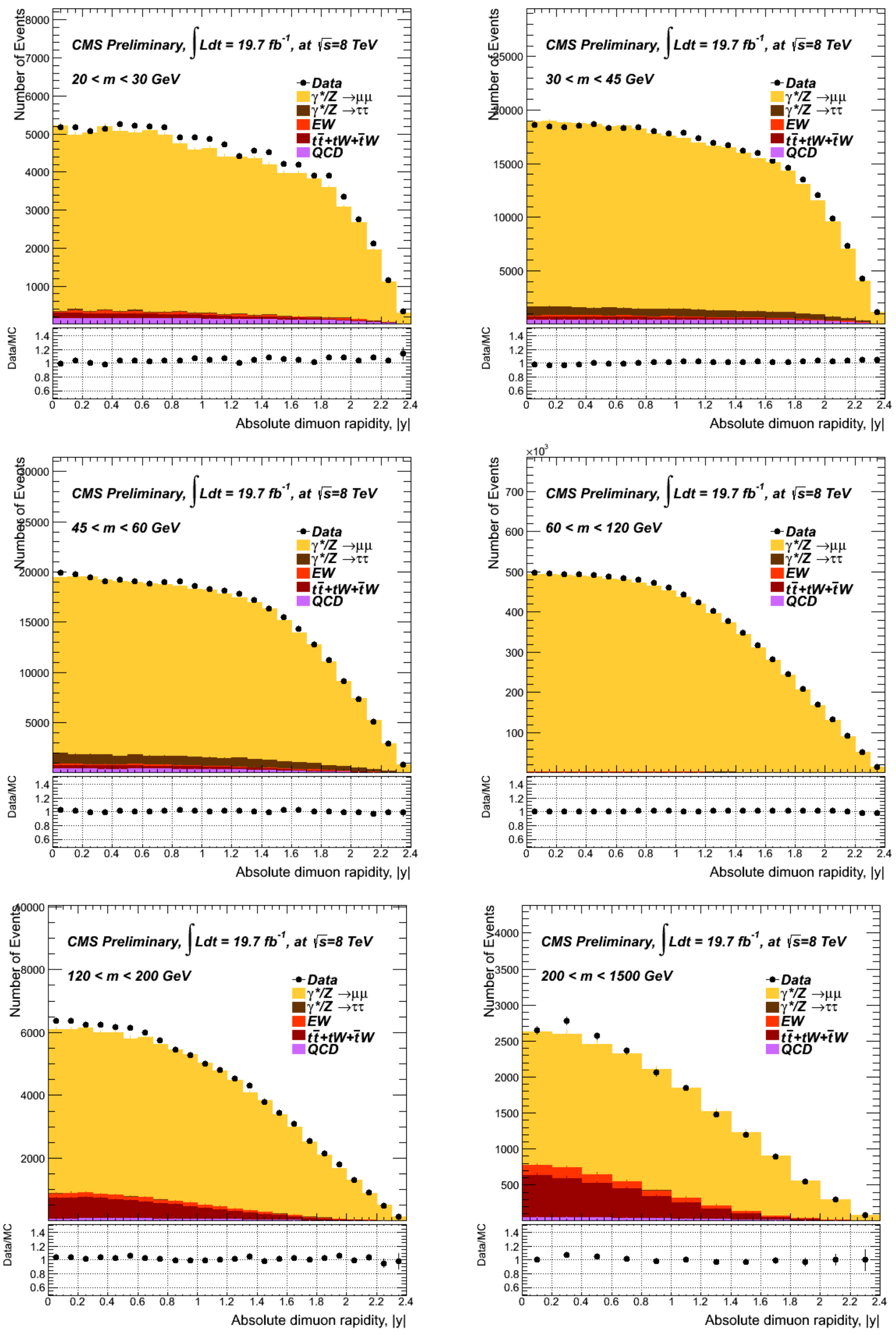

Figure 6.16. The observed dimuon rapidity spectra per invariant mass bin for data and MC events. There are six mass bins between 20 and 1500 GeV, from top left to bottom right. The NNLO reweighted Powheg MC signal sample is used. The normalization factors are determined using the number of events in data in the Z peak region, and they are applied to all of the mass bins. Error bars are statistical only.

6.4 Resolution and Scale Corrections

Lepton energy and momentum mismeasurements can directly affect the reconstructed dilepton invariant mass and are, therefore, important in obtaining a correct differential cross section. Table 6.5 summarizes the dilepton mass resolutions as a function of mass for the CMS detector.

Table 6.5
Dilepton mass resolution as a function of dilepton invariant mass.

m_{ll}	Dimuon mass resol.	Dielectron mass resol.
10 GeV	1.0%	7.2%
100 GeV	2.1%	3.5%
1000 GeV	6.5%	1.7%

The momentum resolution of muons with $p_{\mathrm{T}} < 200\,\mathrm{GeV}$ is dominated by the measurements in the silicon tracker. A residual misalignment remains in the tracker that is not fully reproduced by the simulation. This misalignment leads to a bias in the reconstructed muon momenta which is removed using a momentum scale correction.

The corrections to muon momenta are extracted separately for positively and negatively charged muons using the average of the $1/p_{\mathrm{T}}$ spectra of muons and dimuon mass from Z boson decays in bins of muon charge, the polar angle θ, and the azimuthal angle ϕ. The same procedure is followed for both data and MC samples. The correction to $1/p_{\mathrm{T}}$ has two components; an additive component which removes the bias that originates from tracker misalignment; and a multiplicative component that corrects for residual mismodeling of the magnetic field. For a 40 GeV muon, the additive correction varies from 0.4 % at small $|\eta|$ to 9 % at large $|\eta|$.

The average reconstructed Z boson mass is found to be independent of ϕ. The position of the Z boson mass peak in the corrected distribution is different from the expected Z boson mass [91] by only $(0.10 \pm 0.01)\%$ in data and $(0.00 \pm 0.01)\%$ in simulation. The small remaining shift in data is corrected by an additional overall scale correction. The detailed description of the correction for the muon momentum is given in [92].

The correction to muon momenta is estimated for 2011 runs A and B separately, while a combined estimate is used for 2012 runs A, B, C, and D as no significant run dependency is observed during the latter data-taking period (details about data taking periods are summarized in the Appendix C). Fig. 6.17 shows the comparison between 7 TeV data and DY Powheg MC in the Z peak region after correction to muon momenta are applied.

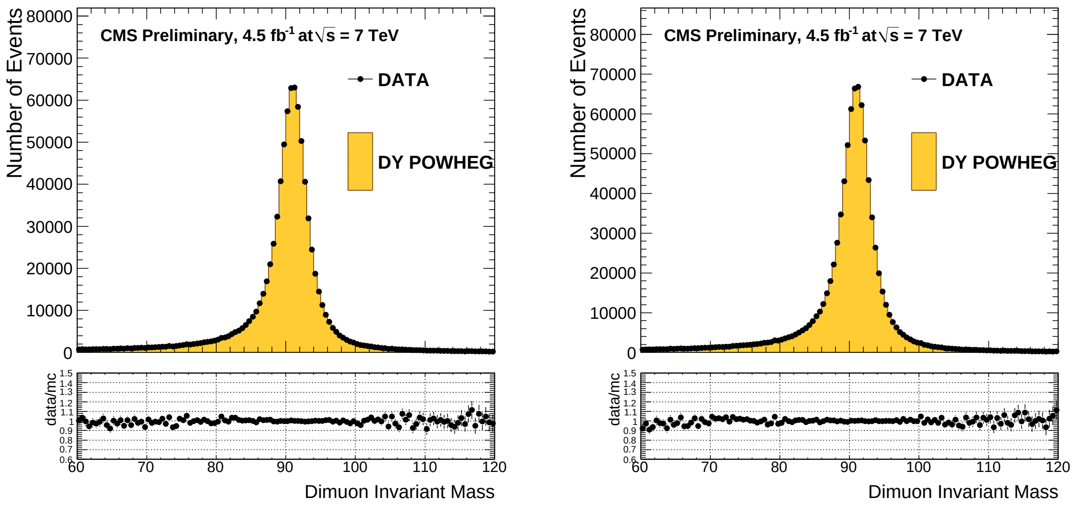

Figure 6.17. Comparison between 2011 data and DY Powheg MC in the Z peak region after the momentum scale correction. Left: 2011 run A, right: 2011 run B.

Fig. 6.18 shows the comparison between data and DY Powheg MC in the Z peak region after corrections applied for 2012 runs A, B, C, and D. As seen, the agreement between the yields from data and simulated after the momentum scale correction is excellent for both the 7 and 8 TeV data taking periods.

The electron energy is derived primarily from the measurements of the energy deposited by the electrons in the ECAL [88]. The electron energy deposits as measured in the ECAL are subject to a set of corrections involving information both from the

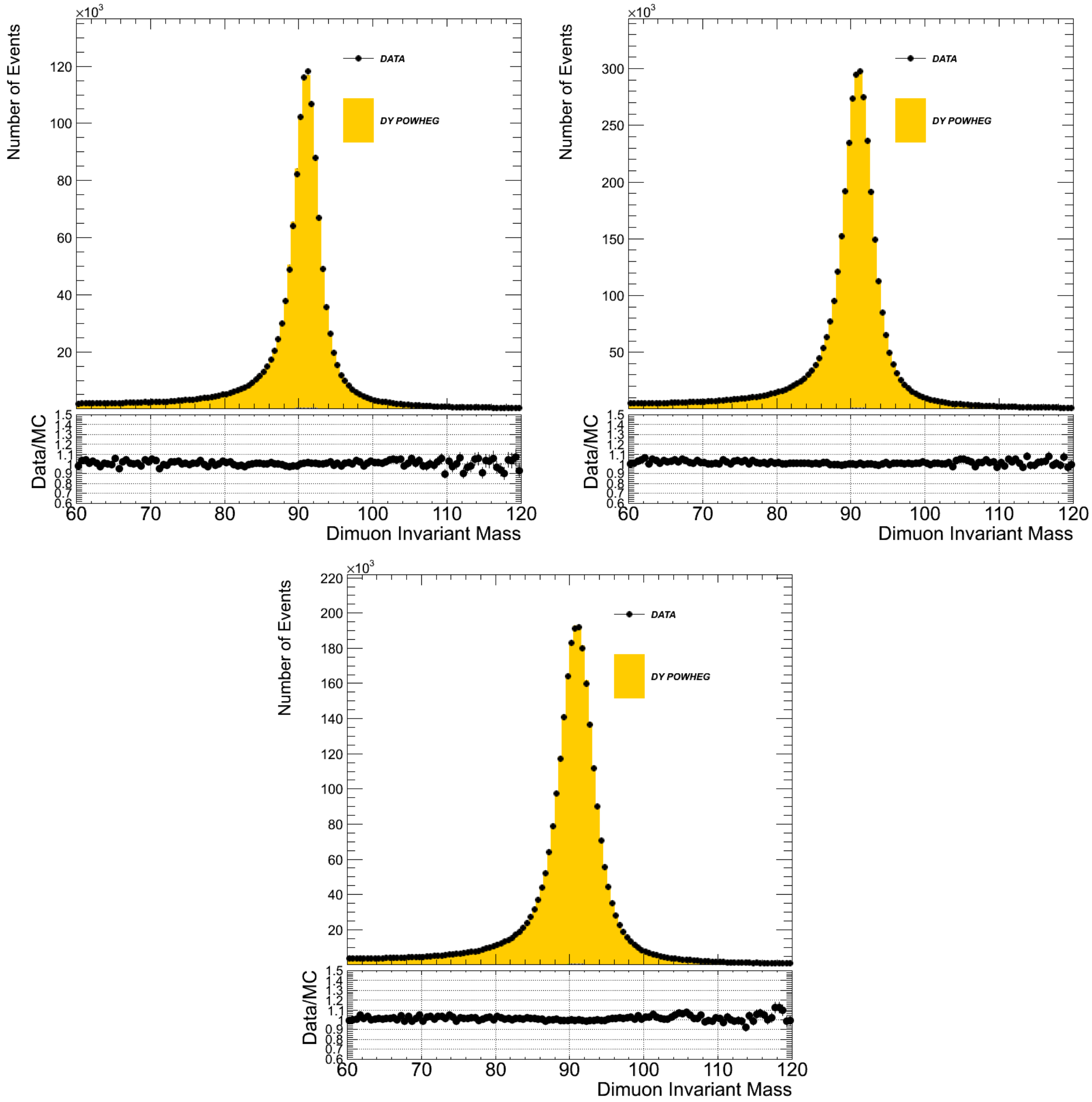

Figure 6.18. Comparison between 2012 data and DY Powheg MC in the Z peak region after the momentum scale correction. From top left to bottom right: barrel-barrel, barrel-endcap, endcap-endcap event classes.

ECAL and the tracker, following the standard CMS procedures for the 8 TeV data set [93]. The final electron energy scale correction that goes beyond the standard set of corrections is derived from the analysis of the Z → e^+e^- peak according to the procedure described in [90], and is a simple multiplicative factor of ∼0.1% applied to the electron energy.

Fig. 6.19 shows the comparison between the data and MC yields before the acceptance and efficiency corrections for before (left) and after (right) energy scale corrections. The agreement between data and simulation after the correction is improved, however, there is some bias on the lower side of the Z peak in the endcap-endcap event category after the electron energy scale correction.

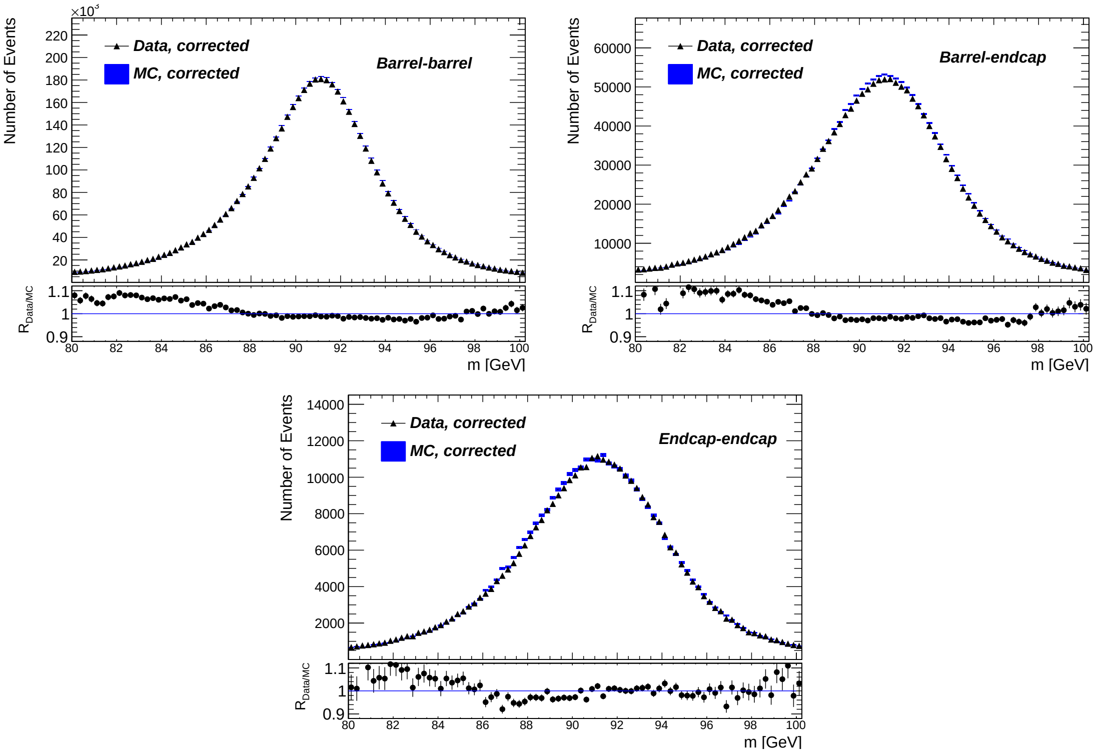

Figure 6.19. Comparison between 2012 data and DY Powheg MC in the Z peak region after the electron energy scale correction. From top left to bottom right: barrel-barrel, barrel-endcap, endcap-endcap event classes.

Fig. 6.21 shows the ratio of pre-unfolded and unfolded yields in the bins of invariant mass and mass-rapidity in the dimuon channel in 7 TeV and 8 TeV analyses.

The detector resolution effects that cause a migration of events among the analysis bins are corrected through an iterative unfolding procedure [94]. This procedure maps

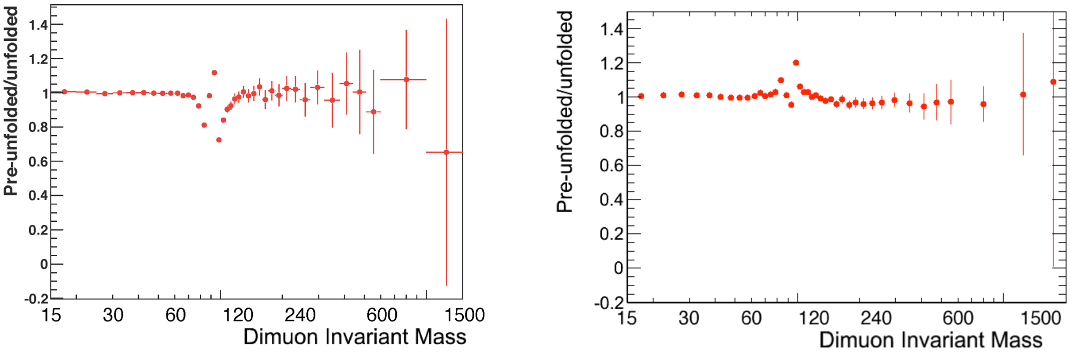

Figure 6.20. Ratio of observed yields before and after detector resolution unfolding as a function of dimuon invariant mass. Left plot: 7 TeV, right plot: 8 TeV.

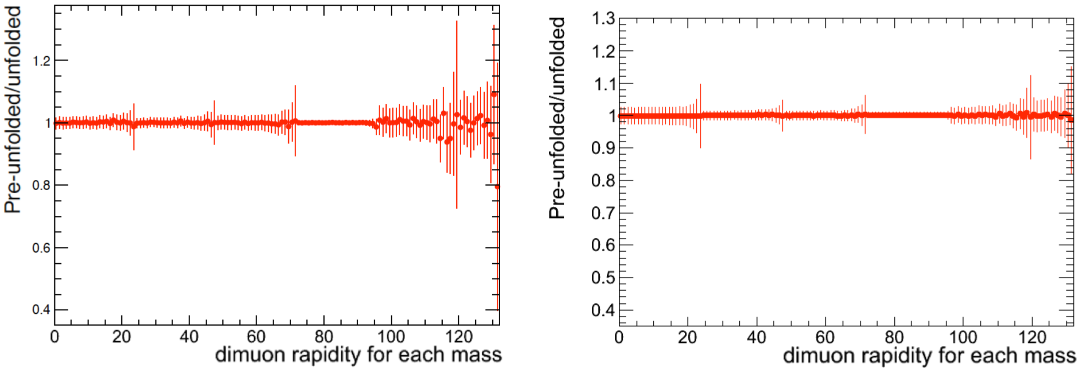

Figure 6.21. Ratio of observed yields before and after detector resolution unfolding as a function of dimuon invariant mass-absolute rapidity. Left plot: 7 TeV, right plot: 8 TeV.

the measured lepton distribution onto the true one, while taking into account the migration of events in and out of the mass and rapidity range of this measurement.

Fig. 6.22 shows the ratio of pre-unfolded and unfolded yields in bins of invariant mass in the dielectron channel, and Fig. 6.23 and 6.24 show the corresponding ratios in bins of invariant mass-rapidity in the dielectron channel.

The size of the effect of migration due to mass resolution effects is similar in the 7 and 8 TeV data. In the dimuon channel, the largest effect is in the peak region and at high masses, reaching up to 20%. In the dielectron channel, the size of the effect

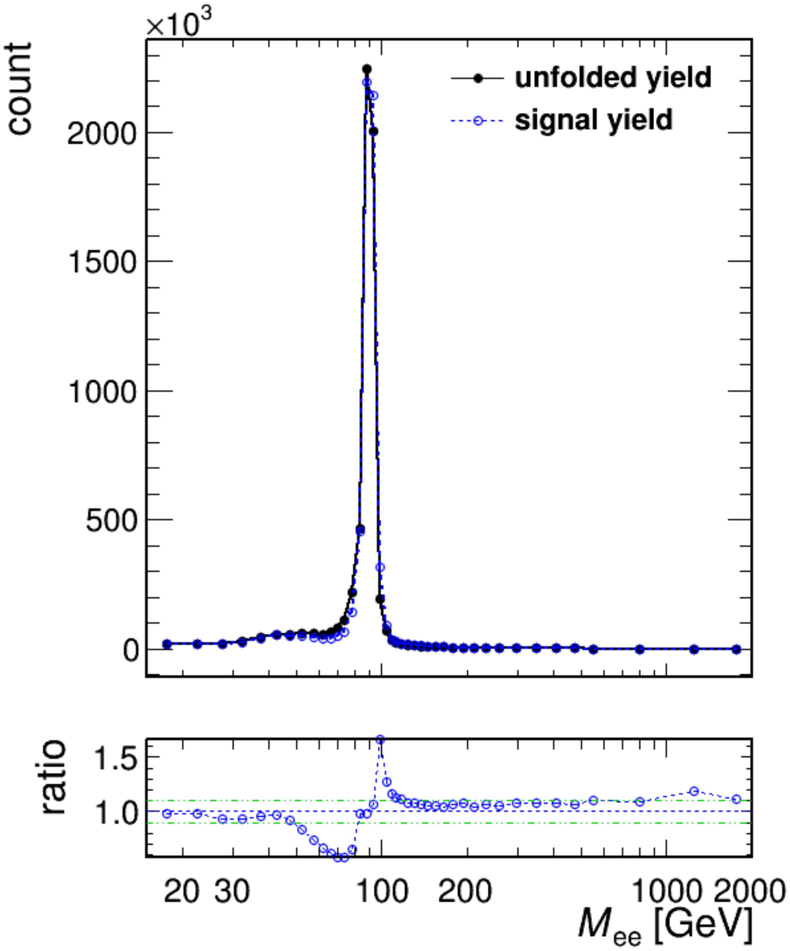

Figure 6.22. Ratio of observed yields before and after detector resolution unfolding as a function of dielectron invariant mass at 8 TeV.

of unfolding is generally more significant, reaching up to 40% in the FSR region and up to 30% in the Z peak region.

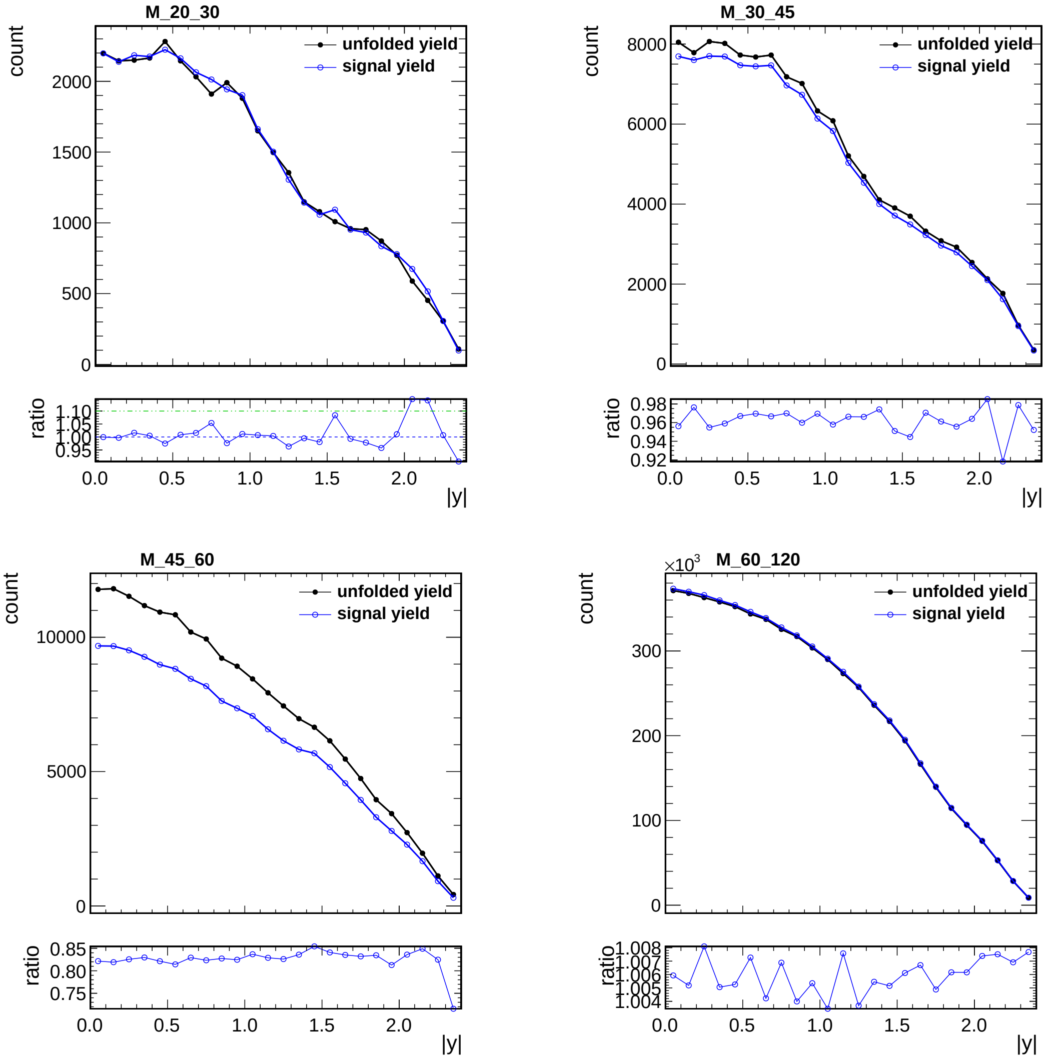

Figure 6.23. Ratio of observed yields before and after detector resolution unfolding as a function of dielectron absolute rapidity in 20–30 GeV, 30–45 GeV 45–60 GeV and 60–120 GeV invariant mass region at 8 TeV (from top left to bottom right).

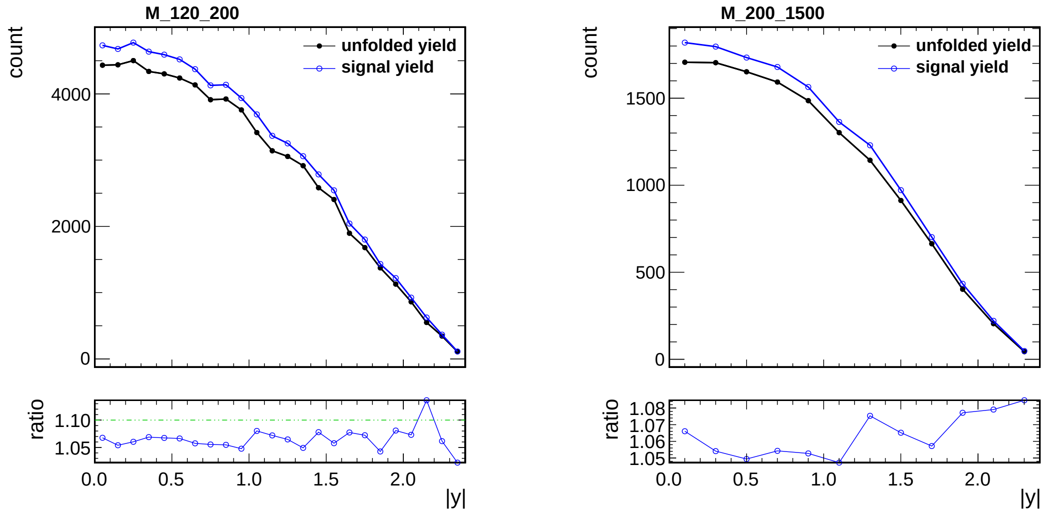

Figure 6.24. Ratio of observed yields before and after detector resolution unfolding as a function of dielectron absolute rapidity in 120–200 GeV and 200–1500 GeV invariant mass region at 8 TeV (from left to right).

6.5 Acceptance and Efficiency

The acceptance (A) is the fraction of events passing the nominal geometric and kinematic cuts for an analysis. The signal event selection efficiency per mass bin ϵ is the fraction of events inside the acceptance that pass the full selection. The following equation holds:

$$A \times \epsilon \equiv \frac{N^A}{N^{\mathrm{gen}}} \cdot \frac{N^\epsilon}{N^A} = \frac{N^\epsilon}{N^{\mathrm{gen}}}, \tag{6.3}$$

where N^{gen} is the number of generated signal events in a given invariant mass bin, N^A is the number of events inside the geometrical and kinematic acceptance, and N^ϵ is the number of events passing the analysis selection. The acceptance and efficiency are estimated using the NNLO reweighted Powheg simulation.

The acceptance calculation depends on higher-order QCD corrections and the choice of PDFs. The use of an NNLO signal MC is essential, especially in the low-mass region where the difference between the NLO and NNLO predictions is sizable.

Fig. 6.25 shows the acceptance, the event efficiency, and $A \times \epsilon$ as functions of the dimuon invariant mass at 7 TeV. The DY acceptance is obtained from simulation.

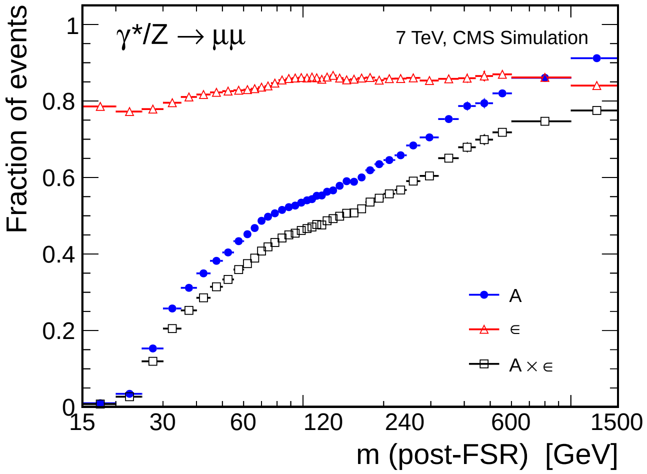

Figure 6.25. The DY acceptance, efficiency, and their product per invariant mass bin in the dimuon channel at 7 TeV, where m(post-FSR) means dimuon invariant mass after the FSR.

In the lowest mass bin it is only about 1%, rapidly increasing to 60% in the Z peak region and reaching over 90% at high mass.

The efficiency is factorized into the reconstruction, identification, and isolation efficiencies, and the event trigger efficiency. The factorization procedure takes into account the asymmetric p_{T} selections for the two legs of the dilepton trigger. The efficiency is obtained from simulation, re-scaled with a correction factor which takes into account differences between data and simulation. The efficiency correction factor is determined in bins of lepton p_{T} and η using $\mathrm{Z} \rightarrow \mu^{+}\mu^{-}$ events in data and simulation with the tag-and-probe method [90] and is then applied as a weight to simulated events on a per-lepton basis (see Appendix F for details). The dimuon event efficiency is 75–80% throughout the entire mass range.

Fig. 6.26 shows the acceptance, the event efficiency, and $A \times \epsilon$ as functions of the dimuon and dielectron invariant mass at 8 TeV. The DY acceptance in the lowest mass bin it is only about 0.5%, rapidly increasing to 50% in the Z peak region and reaching over 90% at high mass.

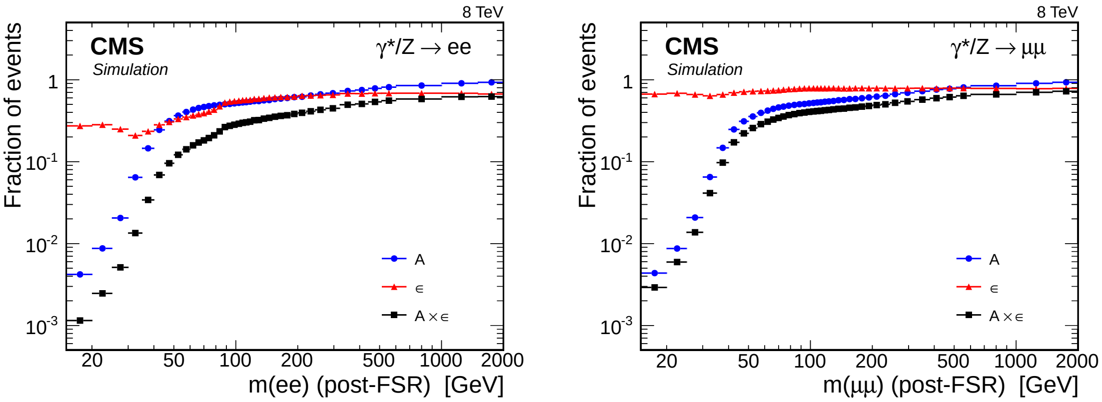

Figure 6.26. The DY acceptance, efficiency, and their product per invariant mass bin in the dielectron (left) and the dimuon channel (right) at 8 TeV, where m(post-FSR) means dielectron invariant mass after the FSR.

The dimuon event efficiency is typically 70–80% throughout the entire mass range. In the dielectron channel, the efficiency at low mass is only 20–40% because of tighter lepton identification requirements, and reaches 65% at high mass. The trigger efficiency for events within the geometrical acceptance is greater than 98% (93%) for the dielectron (dimuon) signal. There is an event efficiency dip in the mass range 30–40 GeV, as seen in Fig. 6.26, that is caused by the combination of two factors. From one side, the lepton reconstruction and identification efficiencies decrease as the lepton p_{T} decreases. From the other side, the kinematic acceptance requirements preferentially select DY events produced beyond the leading order, which results in higher p_{T} leptons with higher reconstruction and identification efficiencies, in the mass range below 30–40 GeV. The effect is more pronounced for dielectrons than for dimuons because the electron reconstruction and identification efficiencies depend more strongly on p_{T}. The efficiency is significantly affected by the pileup in the event. The effect on the isolation efficiency is up to 5% (about 1%) in the dielectron (dimuon) channel.

All electrons with pseudorapidity values from 0.0 to 2.4 are used in this measurement. The lower reconstruction efficiency for electrons found in the barrel-endcap transition region (i.e. $1.442 \leq |\eta| \leq 1.556$) is taken into account in computation of the event efficiency and event efficiency correction. The identical pseudorapidity acceptance definition for electrons and muons facilitates comparing and combining the cross section results for the two channels.

Fig. 6.27 shows the effect of the ECAL gap on MC truth efficiency as a function of dielectron rapidity per invariant mass region.

A significant, mass dependent effect on event efficiency is observed. The probability for an electron to fall within an ECAL gap is just about 4% as estimated from the generator level pseudorapidity distribution, independent on the invariant mass. The loss of events due to the pseudorapidity cut on the reconstructed level is about 3.5–4.5%.

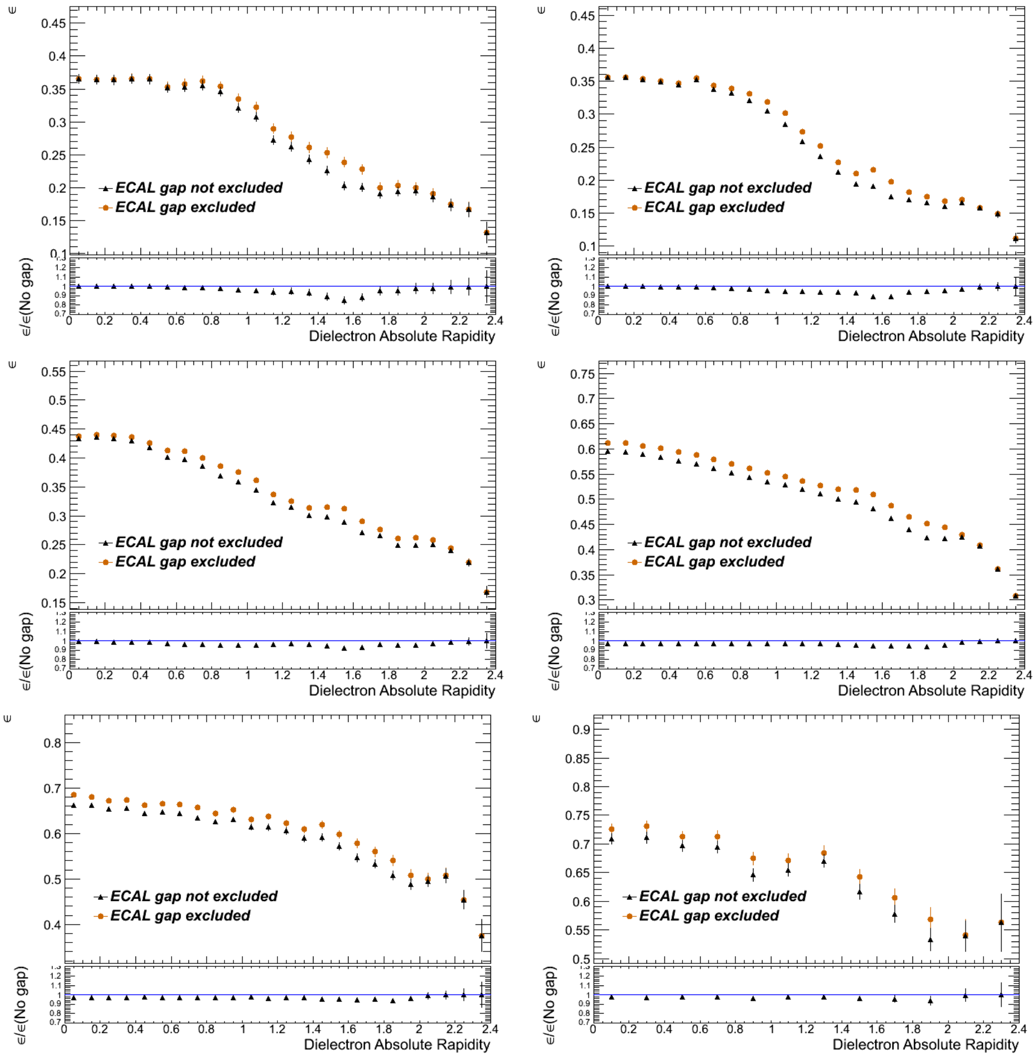

Figure 6.27. MC truth efficiency as a function of the dielectron rapidity per invariant mass region with and without ECAL gap superimposed.

6.6 Final State QED Radiation Effects

Leptons can radiate nearly collinear photons in a process referred to as final state electromagnetic radiation (FSR). This FSR effect changes the observed invariant mass, computed from the 4-momenta of the two muons. If final state photons with sizable energy are emitted, the observed mass can be substantially lower than the propagator in the hard interaction. As a result of the FSR, the events are shifted towards lower masses. The FSR effect is most pronounced just below the Z peak. Indeed, the number of events in the Z peak region is significantly larger than away from the resonance. Thus, the migration of events originating in the Z peak is larger than the migration out of the 40–80 GeV region, creating an excess of events after the FSR.

The correction for FSR effects is performed separately from the correction for the detector resolution effects. The FSR correction procedure is performed in three steps:

- Bin-by-bin correction is used for the events in which pre-FSR leptons fail the acceptance cuts, while post-FSR leptons pass (type A events). FSR will always downshift the p_T, so it will not happen because of the p_T cuts. But FSR could change the direction of the lepton in such a way that it ends up passing η cuts while before FSR it was failing them. This correction is applied before the FSR unfolding, in a similar manner as the MC truth efficiency correction.

- An unfolding procedure is used for the events in which both pre-FSR and post-FSR leptons pass the acceptance cuts (type B events). The resulting invariant mass and rapidity at the pre-FSR or post-FSR level may or may not be in the range of interest, and if not, the event is properly taken care of by the underflow and overflow bins.

- A bin-by-bin correction is used for the events in which pre-FSR leptons pass the acceptance cuts (type C events), but post-FSR leptons fail those cuts. These events normally do not enter the response matrix, but they need to be accounted for. This correction is applied after the FSR unfolding.

The correction for the type A dimuon events is summarized in Fig. 6.28 for 7 and 8 TeV simulation. As seen, the effect of correction is almost negligible, reaching its maximum of 1% right below the Z peak, similarly for both center-of-mass energies considered and both channels. Even though the probability for a lepton to emit a photon is not strongly mass dependent, the presence of an excess of events in the Z peak leads to a larger multiplicity of FSR photons in the 40–80 GeV region, forming a peak. The exact position of the peak is determined by the average mass shift for a dilepton due to FSR.

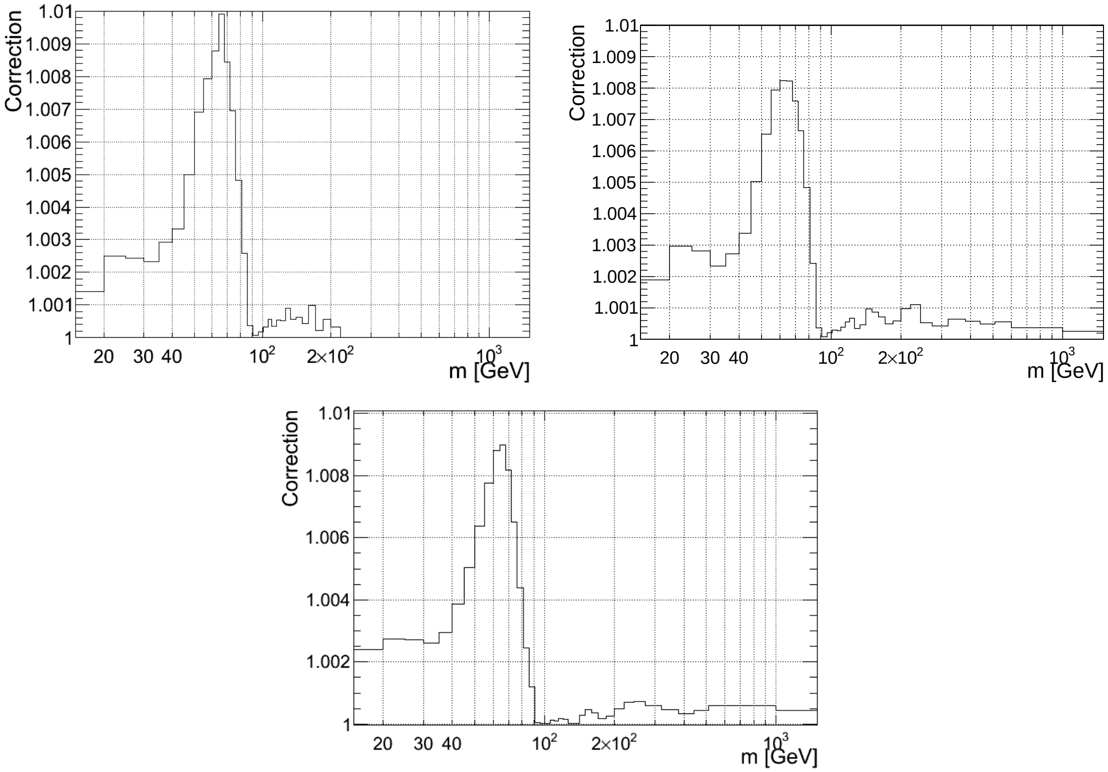

Figure 6.28. FSR correction for the type A events as a function of dilepton invariant mass for dimuon channel at 7 TeV (top left), for dimuon channel at 8 TeV (top right) and for dielectron channel at 8 TeV (bottom) simulation.

The correction for type B events is performed using the unfolding procedure, as for the detector resolution correction, described in Appendix G.

The response matrix is again derived from the Drell–Yan POWHEG MC sample, using the pre-FSR and post-FSR yields. This is shown in Fig. 6.29-6.30. The response matrix is also produced separately for Run2011A and Run2011B. Since there is no visible difference between them the figure shows only the matrix for Run2011A.

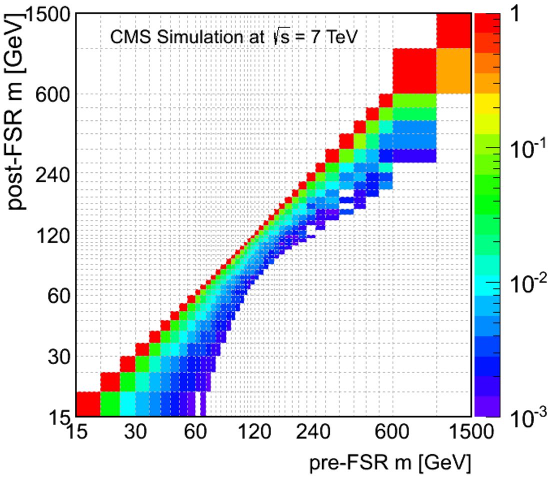

Figure 6.29. The response matrix from 7 TeV simulation for $d\sigma/dm$ measurement in the dimuon channel.

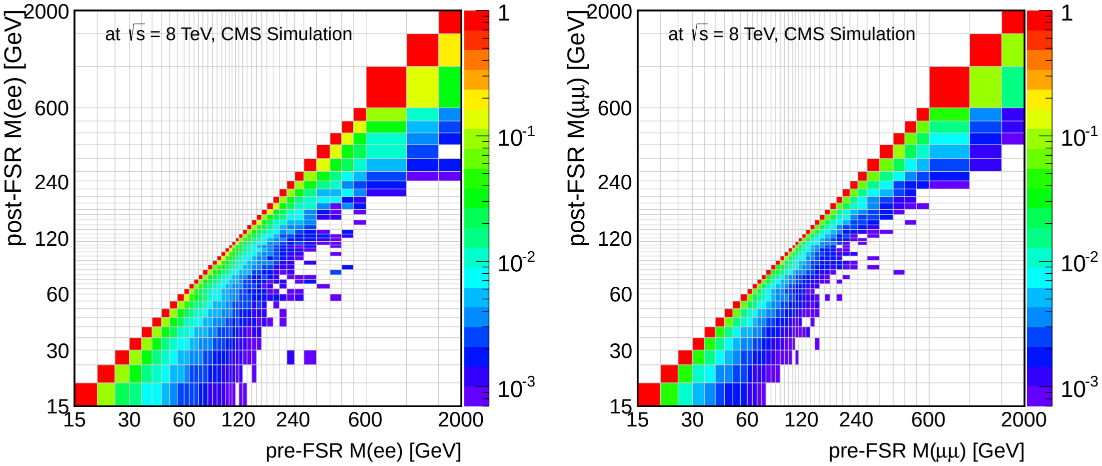

Figure 6.30. The response matrix from 8 TeV simulation for $d\sigma/dm$ measurement. Left plot: dielectron channel, right plot: dimuon channel.

Finally, the bin-by-bin correction for type C dimuon and dielectron events is summarized in Fig. 6.31. As seen, the correction is significant at low mass reaching its maximum nearly 25% in the lowest mass bin, decreasing to negligible levels in the peak region. The size of the correction is similar at both 7 and 8 TeV center-of-mass energies and for both decay channels. The same FSR correction method is applied to the 2D measurement.

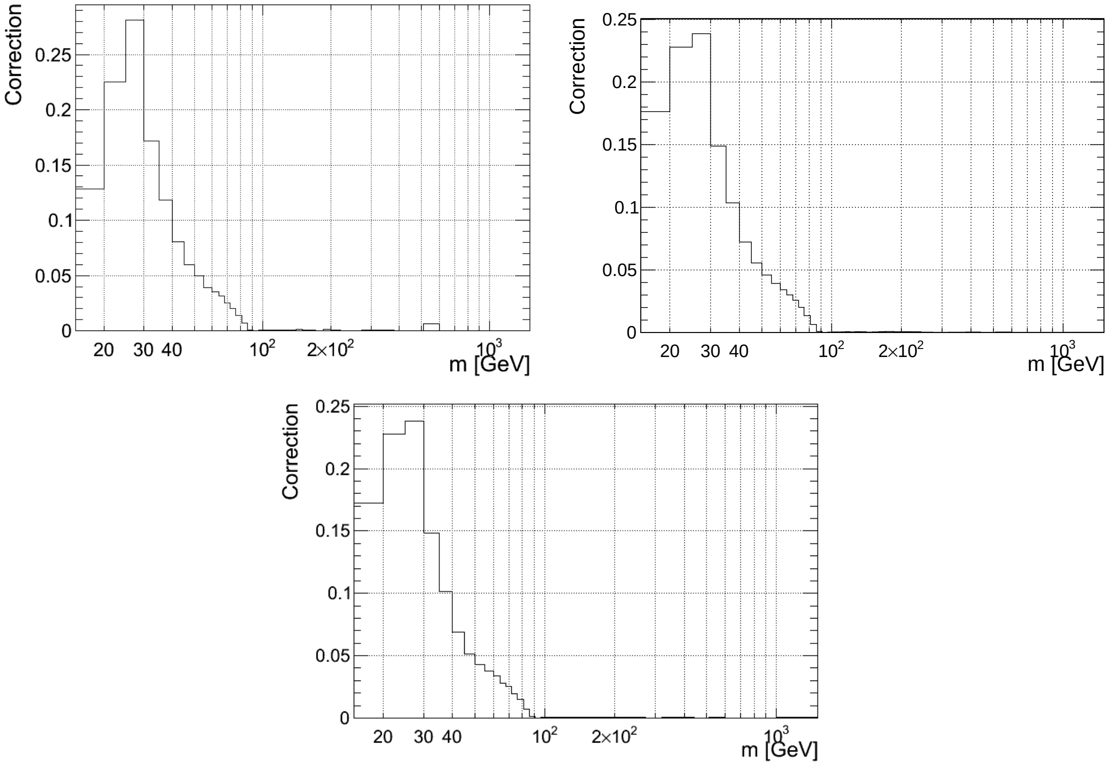

Figure 6.31. FSR correction for the type C events as a function of dilepton invariant mass for dimuon channel at 7 TeV (top left), for dimuon channel at 8 TeV (top right) and for dielectron channel at 8 TeV (bottom) simulation.

6.7 Systematic Uncertainties

In this section, the evaluation of the systematic uncertainties is discussed. The systematic uncertainty tables are summarized in Appendix H for both the differential and the double-differential cross section measurements.

Acceptance uncertainty. The dominant uncertainty sources pertaining to the acceptance are (1) the theoretical uncertainty from imperfect knowledge of the non-perturbative PDFs participating in the hard scattering and (2) the uncertainty in modeling of higher order QCD and EW effects. The latter comes from the procedure to apply weights to the NLO simulated sample in order to reproduce NNLO kinematics and affects mostly the acceptance calculations at very low invariant mass. The PDF uncertainties for the differential and double-differential cross section measurements are calculated using the LHAGLUE interface to the PDF library LHAPDF 5.8.7 [95, 96] by applying a reweighting technique with asymmetric uncertainties as described in [97]. These contributions are largest at low and high masses (4-5%) and decrease to less than 1% for masses at the Z peak.

Efficiency uncertainty. The systematic uncertainty in the efficiency estimation consists of two components: the uncertainty in the efficiency correction factor estimation and the uncertainty related to the number of simulated events. The efficiency correction factor reflects systematic deviations between data and simulation. It varies up to 10 (7)% for the dielectron (dimuon) channel. As discussed in Section 6.5, single-lepton efficiencies of several types are measured with the tag-and-probe procedure and are combined into efficiency correction factors. The tag-and-probe procedure provides the efficiency for each lepton type and the associated statistical uncertainties. A variety of possible systematic biases in the tag-and-probe procedure has been taken into account, such as the dependence on binning in single-lepton p_{T} and η, dependence on the assumed shape of signal and background in the fit model, and the effect of pileup. In the dielectron channel, this uncertainty is as large as 3.2% at low mass, and 6% at high rapidity in the 200–1500 GeV region. The uncertainty in the dimuon channel is about 1% in most of the bins, reaching up to 4% at high rapidity in the 200–1500 GeV mass region. The contribution from the dimuon vertex selection is small because its efficiency correction factor is consistent with being constant.

Muon momentum scale. The uncertainty in the muon momentum scale causes uncertainties in the efficiency estimation and background subtraction and affects the detector resolution correction. The muon momentum scale is calibrated to a precision of 0.02%. The systematic uncertainty in the measured cross sections is determined by varying the muon momentum scale within its uncertainty. The largest effect on the final results is observed in the detector resolution unfolding step, reaching 2%.

Detector resolution. For both e^+e^- and $\mu^+\mu^-$ channels, the simulation of the CMS detector, used for detector resolution unfolding, provides a reliable description of the data. Possible small systematic errors in the unfolding are related to effects such as differences in the electron energy scale and muon momentum scale, uncertainties in FSR simulation and in simulated pileup. The impact of each of these effects on the measurements is studied separately. The detector resolution unfolding procedure itself has been thoroughly validated, including a variety of closure tests and comparisons between different event generators; the systematic uncertainty assigned to the unfolding procedure is based on the finite size of the simulated samples and a contribution due to the systematic difference in data and simulation (the latter must be taken into account because the response matrix is fully determined from simulation).

Background uncertainty. The background estimation uncertainties are evaluated in the same way in both the dielectron and the dimuon channels. The uncertainty in background is comprised of the Poissonian statistical uncertainty of predicted backgrounds and the difference between the predictions from data and simulation. The two components are combined in quadrature. The uncertainty in the estimated background is no larger than 3.0% (1.0%) at low mass, reaching 16.3% (4.6%) in the highest mass bin in the dielectron (dimuon) channel. The uncertainty in the correction for $\gamma\gamma$-initiated processes is estimated using FEWZ 3.1 with the NNPDF2.3QED PDF and consists of the statistical and PDF uncertainty contributions combined in quadrature.

FSR simulation. The systematic uncertainty due to the model-dependent FSR simulation is estimated using two reweighting techniques as described in [19] with the same procedure in both decay channels. The systematic uncertainty from modeling the FSR effects is as large as 2.5% (1.1%) in the dielectron (dimuon) channel in the 45–60 GeV region. The systematic uncertainties related to the FSR simulation in the electron channel primarily affect the detector resolution unfolding procedure. The impact of these uncertainties is greater for the electron channel than for the muon channel because of the partial recovery of FSR photons during the clustering of electron energy in the ECAL. The effect of the FSR simulation on other analysis steps for the electron channel is negligible in comparison to other systematic effects associated with those steps.

Electron energy scale. In the dielectron channel, one of the leading systematic uncertainties is associated with the energy scale corrections for individual electrons. The corrections affect both the placement of a given candidate in a particular invariant-mass bin and the likelihood of surviving the kinematic selection. The energy scale corrections are calibrated to a precision of 0.1–0.2%. The systematic uncertainties in the measured cross sections are estimated by varying the electron energy scale by 0.2%. The uncertainty is relatively small at low masses and reaches up to 6.2% in the Z peak region where the mass bins are the narrowest and the variation of the cross section with mass is the largest.

Luminosity. The luminosity measurement is based on pixel cluster counting from the silicon pixel detector. Its absolute calibration has been determined by means of Van der Meer scans which together with detector operational features give rise to the estimated integrated luminosity uncertainty of 2.2% for the 7 TeV and 2.6% for the 8 TeV data-taking period.

6.7.1 Covariance Matrix

A covariance matrix summarizing uncertainties on the measurements together with their correlations is calculated between the analysis bins and different systematic sources.

First, the observed yield is unfolded, which redistributes the signal and background events according to the unfolding matrix T^{-1}. The total uncertainty before the unfolding is given by a diagonal matrix V_I. The mathematical description of the procedure to obtain the covariance matrix V_{UNF} associated with the unfolding is:

$$V_{\mathrm{UNF}} = T^{-1} V_I {T^{-1}}^T. \tag{6.4}$$

The normalization to the Z boson peak does not change the results of the unfolding procedure.

After the unfolding, the resulting yield is corrected for detector and reconstruction efficiencies. The largest effect in the uncertainty comes from the efficiency corrections for the single leptons, which are estimated with the tag-and-probe method. A large part of this uncertainty comes from systematic effects related to data/MC variations, together with statistical limitations. The efficiency covariance and correlations are trivially related by the efficiency correction uncertainties (i.e., by the square roots of the diagonal elements of the efficiency covariance matrix). The efficiency covariance matrix is denoted by V_{EFF}.

The last step in the procedure is to apply FSR corrections to the measurement. As described earlier, it is based on the FSR unfolding matrix and additional bin-by-bin corrections. There are associated uncertainties in the FSR description. As in the first step, the correlations induced by this procedure are described by the FSR unfolding matrix alone and the covariance matrix V_{FSR} is given by Eq. (6.4), but with the FSR related inputs.

The total covariance matrix V_{tot} is simply the sum of the three uncorrelated sources:

$$V_{\mathrm{tot}} = V_{\mathrm{UNF}} + V_{\mathrm{EFF}} + V_{\mathrm{FSR}}. \tag{6.5}$$

The total uncertainty in the signal yield is propagated through the detector resolution unfolding matrix, as given by Eq. (6.4). Then the uncertainty is increased by contributions due to the statistical inaccuracy of the unfolding matrix elements as well as additional sources of systematic uncertainty associated with the resolution unfolding (e.g., the electron energy scale uncertainty and FSR). The covariance of the efficiency correction factors is evaluated using pseudo-experiments as described for the muon channel analysis. In this case, efficiency correction factors contribute significantly to correlations in the low-mass region. The diagonal covariance of each MC efficiency factor is obtained from the statistical uncertainty. The covariance of the pre-FSR cross section is obtained from the covariance of the post-FSR cross section via error propagation. After the FSR unfolding some covariances with the Z boson peak region become negative. The contribution from the statistical uncertainty of the FSR unfolding matrix is negligible.

6.7.2 Double Ratio Uncertainties

In the double ratio measurements most of the theoretical uncertainties and some experimental uncertainties are reduced.

Special care needs to be taken to estimate the correlated systematic uncertainties. For each correlated systematic source s_i, the relative uncertainty $\delta\rho_{s_i}/\rho_{s_i}$ on the cross section ratio is calculated as:

$$\frac{\delta\rho_{s_i}}{\rho_{s_i}} = \frac{1+\delta_{s_i}(8\,\mathrm{TeV})}{1+\delta_{s_i}(7\,\mathrm{TeV})} - 1, \tag{6.6}$$

where $\delta_{s_i}(7\,\mathrm{TeV})$ and $\delta_{s_i}(8\,\mathrm{TeV})$ are relative uncertainties caused by a source s_i in the cross section measurements at 7 and 8 TeV, respectively. The uncorrelated systematic uncertainties between the two center-of-mass energies are added in quadrature.

Most of the experimental systematic uncertainties are considered to be uncorrelated between the two measurements. Exceptions are the modeling uncertainty which is fully correlated between the 7 and 8 TeV measurements and the systematic uncertainty in the acceptance, which originates mainly from the PDFs.

The uncertainty in the luminosity measurement is also treated as uncorrelated, resulting in an uncertainty of 3.4%.

6.8 Results and Interpretation

6.8.1 Differential Cross Section $d\sigma/dm$ Measurement

Z peak Cross Section Measurement

Measuring the pre-FSR cross section is particularly important, because it facilitates the comparisons with various theoretical tools. The absolute cross section measurement in the Z peak region is a way to verify the correctness of the analysis procedure and an important prerequisite for the differential and double-differential measurements. The pre-FSR Z boson production cross section in the peak region ($60 < m < 120\,\mathrm{GeV}$) is calculated as:

$$\sigma_{\mathrm{Z,\ pre-FSR}} = \frac{N_{\mathrm{u}}^{\mathrm{norm}}}{A^{\mathrm{norm}}\epsilon^{\mathrm{norm}}L}, \tag{6.7}$$

where N_u^{norm} is the number of events after background subtraction and the unfolding procedure for the detector resolution and FSR correction, A^{norm} is the acceptance, ϵ^{norm} is the efficiency in the Z peak region, and L is the total integrated luminosity. The total cross section in the Z peak region is necessary to calculate the normalized differential cross section, and it is also used as a cross check against existing measurements.

The peak cross section measurements at 7 and 8 TeV are summarized in Tab. 6.6-6.7. The measurements are in good agreement with NNLO predictions for the full phase space (e.g. a typical NNLO prediction is 1009 ± 32 pb at 7 TeV and 1137 ± 36 pb at 8 TeV center-of-mass energy) and also with previous CMS measurements [90, 98]. The measurements reported have smaller statistical, and luminosity uncertainties as compared to [90, 98], making it the most precise Z boson production cross section measurement with CMS data at 7 and 8 TeV.

Table 6.6
Absolute cross section measurements in the Z peak region ($60 < m < 120$ GeV) with associated uncertainties at 7 TeV.

Muon channel	**Cross section in the Z peak region**
pre-FSR full acc.	990 ± 10(exp) ± 22(theor) ± 22(lumi) pb
post-FSR full acc.	975 ± 9(exp) ± 22(theor) ± 21(lumi) pb
pre-FSR detector acc.	525 ± 5(exp) ± 1(theor) ± 12(lumi) pb
post-FSR detector acc.	517 ± 5(exp) ± 1(theor) ± 11(lumi) pb

Table 6.7
Absolute cross section measurements in the Z peak region ($60 < m < 120$ GeV) with associated uncertainties at 8 TeV.

Muon channel	**Cross section in the Z peak region**
pre-FSR full acc.	1135 ± 11(exp) ± 25(theor) ± 30(lumi) pb
post-FSR full acc.	1115 ± 11(exp) ± 25(theor) ± 29(lumi) pb
pre-FSR detector acc.	571 ± 6(exp) ± 1(theor) ± 15(lumi) pb
post-FSR detector acc.	558 ± 6(exp) ± 1(theor) ± 15(lumi) pb
Electron channel	
pre-FSR full acc.	1141 ± 11(exp) ± 25(theor) ± 30(lumi) pb
post-FSR full acc.	1101 ± 11(exp) ± 26(theor) ± 29(lumi) pb
pre-FSR detector acc.	572 ± 6(exp) ± 1(theor) ± 15(lumi) pb
post-FSR detector acc.	551 ± 6(exp) ± 1(theor) ± 14(lumi) pb

Normalized Cross Section $d\sigma/dm$ Measurement

In order to reduce systematic uncertainties, the Drell–Yan $d\sigma/dm$ differential cross section is normalized to the cross section in the Z peak region ($60 < m < 120$ GeV). The result of the measurement is calculated as the ratio

$$R^i_{\mathrm{pre-FSR}} = \frac{N^i_{\mathrm{u}}}{A^i \epsilon^i \rho^i} \Bigg/ \frac{N^{\mathrm{norm}}_{\mathrm{u}}}{A^{\mathrm{norm}} \epsilon^{\mathrm{norm}} \rho^{\mathrm{norm}}} \, , \tag{6.8}$$

where N_{u}^{i} is the number of events after background subtraction and the unfolding procedure for the detector resolution and FSR correction, A^{i} is the acceptance, ϵ^{i} is the efficiency, and ρ^{i} is the correction estimated from data in a given invariant mass bin i as defined earlier. N_{u}^{norm}, A^{norm}, ϵ^{norm}, and ρ^{norm} refer to the Z peak region. The DY $d\sigma/dm$ differential cross section is normalized to the cross section in the Z peak region ($60 < m < 120$ GeV). The results are also divided by the invariant mass bin widths, Δm^{i}, defining the shape $\mathrm{r}^{i} = R^{i}/\Delta m^{i}$.

The results of the DY cross section measurement at 7 TeV are presented in Fig. 6.32, and the results of the DY cross section measurement at 8 TeV are presented in Fig. 6.33 for both the dielectron and dimuon channels. Since this is a shape measurement, and the normalization of the spectrum is defined by the number of events in the Z peak region, the uncertainty is calculated for the ratio of yields between each mass bin and the Z peak. The 8 TeV differential cross section measurement is a significant improvement as compared to the 7 TeV result. First of all, the mass range covered by the 8 TeV measurement extends to 2 TeV. Secondly, the statistical uncertainties are reduced by a factor of 2 on average due to the larger sample available for the analysis. Systematic uncertainties in the 8 TeV measurement have been reduced as compared to the 7 TeV measurement because of the scaling of uncertainties on the quantities estimated from data with the sample size, and as a result of switching to data-driven background estimation methods for all the non-QCD backgrounds. The 8 TeV measurement is dominated by systematic uncertainties up to around 320 GeV and statistically dominated at higher masses. In the highest-mass bin, the statistical uncertainty is about 3 times larger than theoretic uncertainty.

The uncertainties in the theoretical predictions due to the imprecise knowledge of the PDFs are calculated with the LHAGLUE interface to the PDF library LHAPDF, using a reweighting technique with asymmetric uncertainties. The scale variation uncertainty of up to 2% is included in the theoretical error band.

The result of the 7 and 8 TeV measurements are in good agreement with the NNLO theoretical predictions as computed with FEWZ using the CT10 PDF set.

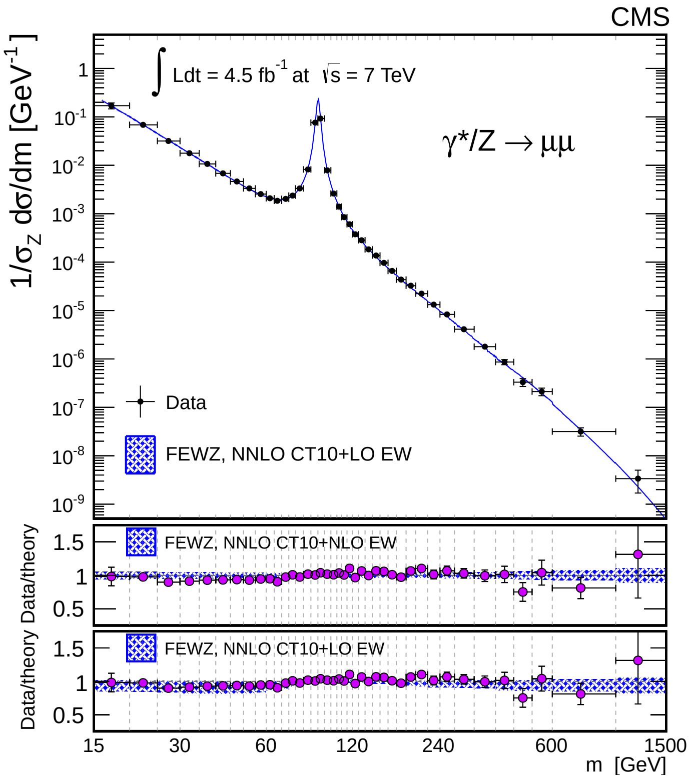

Figure 6.32. The DY dimuon invariant-mass spectrum normalized to the Z boson production cross section ($1/\sigma_Z\, d\sigma/dm$), as measured and predicted by FEWZ+CT10 NNLO calculations, for the full phase space. The vertical error bars for the measurement indicate the experimental (statistical and systematic) uncertainties summed in quadrature with the theoretical uncertainty resulting from the model-dependent kinematic distributions inside each bin. The shaded uncertainty band for the theoretical calculation includes the statistical uncertainty from the FEWZ calculation and the 68% confidence level uncertainty from PDFs combined in quadrature. The effect of NLO EW correction including $\gamma\gamma$-initiated processes (LO EW correction only) is shown in the middle (bottom) plot. The data point abscissas are computed according to Eq. (6) in Ref. [99].

The uncertainty bands of the theoretical calculation include the statistical uncertainty from the FEWZ calculation and the 68% confidence level (CL) uncertainty from PDFs combined in quadrature.

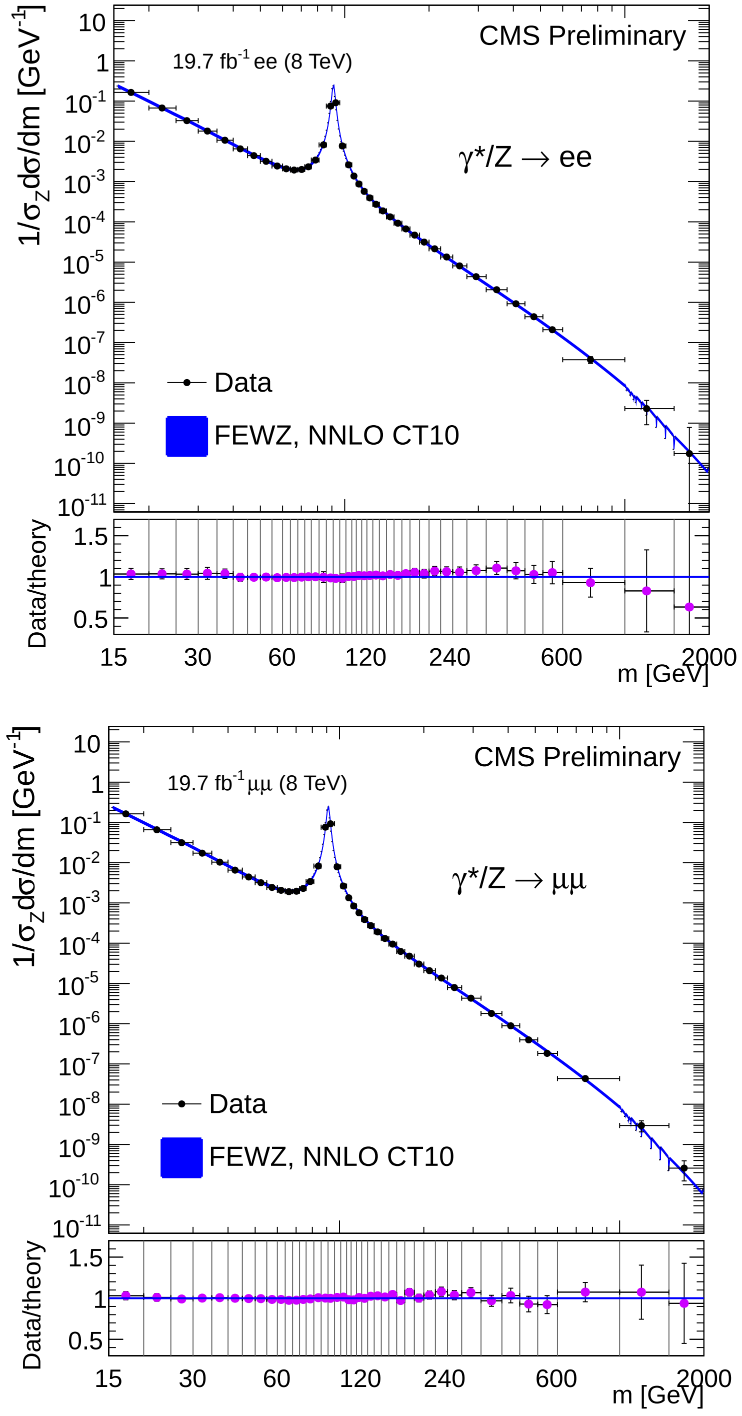

Figure 6.33. The DY dielectron (top) and dimuon (bottom) invariant-mass spectrum normalized to the Z boson production cross section $(1/\sigma_Z\, d\sigma/dm)$, as measured and predicted by Fewz+CT10 NNLO calculations, for the full phase space. The vertical error bars for the measurement indicate the experimental (statistical and systematic) uncertainties summed in quadrature with the theoretical uncertainty resulting from the model-dependent kinematic distributions inside each bin. The shaded uncertainty band for the theoretical calculation includes the statistical uncertainty from the Fewz calculation and the 68% confidence level uncertainty from PDFs combined in quadrature.

The effect of the higher-order EW correction computed with Fewz (described above) is included as an additional correction factor and the ratio between data and the theoretical prediction is shown in the middle of Fig. 6.32. Differences between NLO and NNLO values in the theoretical expectations are significant in the low-mass region, as reported in [100]. Although this measurement is sensitive to NNLO effects, it does not provide sufficient sensitivity to distinguish between different PDF sets. The combination of the dimuon and dielectron channels is discussed in Section 6.8.3.

6.8.2 Double-differential Cross Section $d^2\sigma/dm\,d|y|$ Measurement

Z peak Cross Section Measurement for $|y| < 2.4$

The absolute cross sections in the Z peak region for $|y| < 2.4$, corresponding to the geometrical acceptance of the double-differential cross section measurement calculated following Eq. 6.7, is shown in Tab. 6.8-6.9.

Table 6.8
The cross section measurements at 7 TeV center-of-mass energy in the Z peak region ($60 < m < 120\,\text{GeV}$ and $|y| < 2.4$) and the detector acceptance for the dimuon channel. The uncertainty in the theoretical cross sections indicates the statistical calculation uncertainty and PDF uncertainty in Fewz.

	Cross section in the Z peak region ($60 < m < 120\,\text{GeV}$, $|y| < 2.4$)
data	526 ± 2 (syst) ± 12 (lumi) pb
CT10 NNLO	534.29 ± 0.36 pb
NNPDF2.1 NNLO	524.76 ± 0.68 pb
MSTW2008 NNLO	524.02 ± 0.38 pb
JR09 NNLO	514.16 ± 0.22 pb
ABKM NNLO	534.69 ± 0.43 pb
HERA NNLO	531.92 ± 0.23 pb

The result of the 7 TeV cross section measurement is in agreement with the NNLO theoretical predictions as computed with Fewz taking into account the PDF uncertainty.

Table 6.9
The cross section measurements at 8 TeV center-of-mass energy in the Z peak region ($60 < m < 120\,\mathrm{GeV}$ and $|y| < 2.4$) and the detector acceptance for the dimuon and dielectron channels. The uncertainty in the theoretical cross sections indicates the statistical calculation uncertainty and PDF uncertainty in Fewz.

	Cross section in the Z peak region in the detector acceptance **($60 < m < 120\,\mathbf{GeV}$, $|y| < 2.4$)**
CT10 NNLO	569.7 ± 0.4 (stat) $\pm$ 17.7 (PDF) pb
NNPDF2.1 NNLO	559.3 ± 0.5 (stat) $\pm$ 6.8 (PDF) pb
Muon channel	571 ± 6(exp) $\pm$ 1(theor) $\pm$ 15(lumi) pb
Electron channel	572 ± 6(exp) $\pm$ 1(theor) $\pm$ 15(lumi) pb

At 8 TeV, the cross section measurement is in agreement with the NNLO theoretical predictions computed with Fewz using CT10 NNLO and NNPDF2.1 NNLO PDFs.

Normalized Cross Section $d^2\sigma/dm\,d|y|$ Measurement

The pre-FSR cross sections in bins of the dilepton invariant mass and the absolute value of the dilepton rapidity are measured according to:

$$\sigma^{ij}_{\mathrm{det}} = \frac{N^{ij}_{\mathrm{u}}}{\epsilon^{ij} L}, \tag{6.9}$$

The quantities N^{ij}_{u}, ϵ^{ij} are defined in a given bin (i, j), with i corresponding to the binning in dilepton invariant mass, and j corresponding to the binning in absolute rapidity. L denotes the total integrated luminosity. The cross sections are divided by the dilepton absolute rapidity bin widths, Δy^j, defining the shape $R^{ij} = \sigma^{ij}/(\Delta y^j)$. An acceptance correction to the full phase space would not increase the sensitivity to PDFs. Therefore, the main measurement is performed within the detector acceptance in order to reduce model dependence.

Figure 6.34 shows the results of the double-differential cross section at 7 TeV center-of-mass energy, which are compared to the FEWZ theoretical calculation obtained using the CT10 NLO and NNLO PDFs. The results of the measurement are in better agreement with CT10 NNLO predictions than with CT10 NLO predictions. The CT10 (NLO) and CT10 (NNLO) have been chosen to compare with the measurement in Fig. 6.34 because the CT10 (NLO) have been used for the POWHEG MC signal sample. The uncertainty bands in the theoretical expectations include the statistical and the PDF uncertainties from the FEWZ calculations summed in quadrature (shaded band). The statistical uncertainty (solid band) is smaller than the PDF uncertainty and the latter is the dominant uncertainty in the FEWZ calculations. In general, the PDF uncertainty assignment is different for each PDF set. For instance, CT10 (NLO) and CT10 (NNLO) PDF uncertainties correspond to a 90% CL, so, to get a consistent comparison to other PDF sets the uncertainties are scaled to the 68% CL.

In the low-mass region and the Z peak region, we observe good agreement between data and theory. The NNLO effects are more significant in the low-mass region. The corrections for the $\gamma\gamma$-initiated processes calculated with FEWZ are negligible in the double-differential cross section measurement, because the effects are approximately constant over the investigated rapidity range and statistical fluctuations or other systematic uncertainties are much larger across the invariant-mass range of the measurement.

In order to assess the sensitivity of the double-differential cross section measurement to the PDF uncertainties, we perform a comparison with the theoretical expectations calculated with various PDF sets. Figure 6.35 shows the comparison with currently available NNLO PDF sets, most of which are from the pre-LHC era: CT10, CT10W, NNPDF2.1, HERAPDF15, MSTW2008, JR09, and ABKM09.

As seen in Fig. 6.35, the predictions of various existing PDF sets are rather different, especially in the low- and high-mass regions. Given the uncertainties, the measurements provide sufficient sensitivity to differentiate between different PDFs and can be used to calculate a new generation of PDFs. The uncertainty bands in the theoretical expectations in the figure indicate the statistical uncertainty from the FEWZ calculation.

In the low-mass region (20–45 GeV), the values of the double-differential cross section calculated with the NNPDF2.1 are higher than the values calculated with other PDF sets. The NNPDF2.1 calculation shows good agreement with the measurement result in the 20 – 30 GeV region, but it deviates from the measurement in the 30 – 45 GeV region by about 10%. In the peak region, all predictions are relatively close to each other and agree well with the measurements. At high mass the JR09 PDF calculation predicts significantly larger values than other PDF sets. The statistical uncertainties in the measurements for $m > 200$ GeV are of the order of the spread in the theoretical predictions.

The 8 TeV double-differential cross section measurements are shown in Fig. 6.37-6.36. The figures show the DY rapidity spectrum normalized to the Z peak region ($1/\sigma_Z d^2\sigma/dm\, d|y|$), plotted for different mass regions within the detector acceptance in the dielectron and dimuon channels.

The uncertainty bands in the theoretical expectations include the statistical and the PDF uncertainties from the FEWZ calculations summed in quadrature. The statistical uncertainty is significantly smaller than the PDF uncertainty and the latter is the dominant uncertainty in the FEWZ calculations. In general, the PDF uncertainty assignment is different for each PDF set. The CT10 PDF uncertainties correspond to 90% CL; to permit a consistent comparison with NNPDF2.1 the uncertainties are therefore scaled to 68% CL. The scale variation uncertainty of up to 2% is included in the theoretical error band.

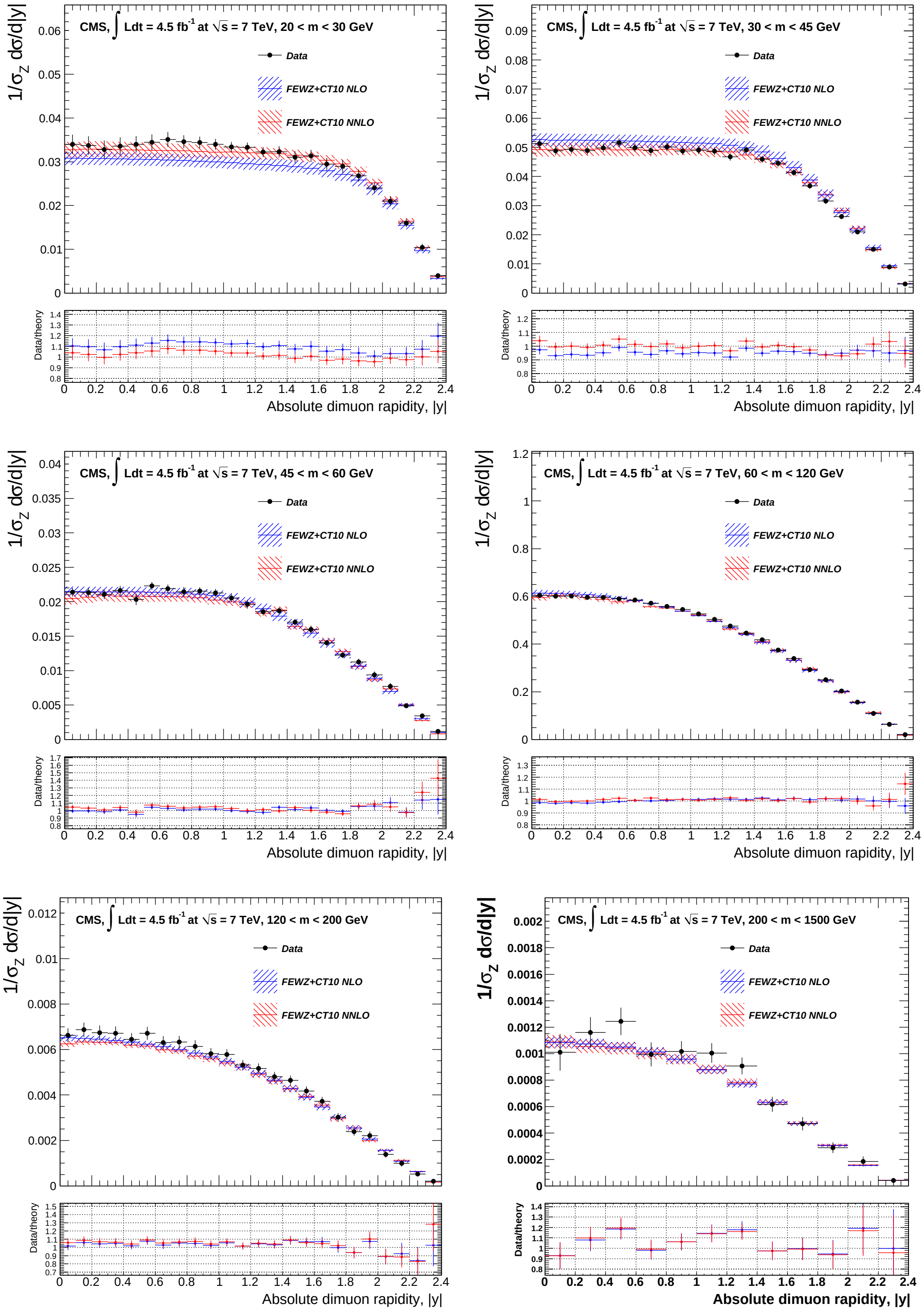

Figure 6.34. The DY rapidity spectrum normalized to the Z peak region ($1/\sigma_Z\, d^2\sigma/d|y|$), plotted for different mass regions within the detector acceptance, as measured and predicted by NLO Fewz+CT10 PDF and NNLO Fewz+CT10 PDF calculations. There are six mass bins between 20 and 1500 GeV, from left to right and from top to bottom. The uncertainty bands in the theoretical predictions combine the statistical and the PDF uncertainties (shaded bands). The statistical component is negligible.

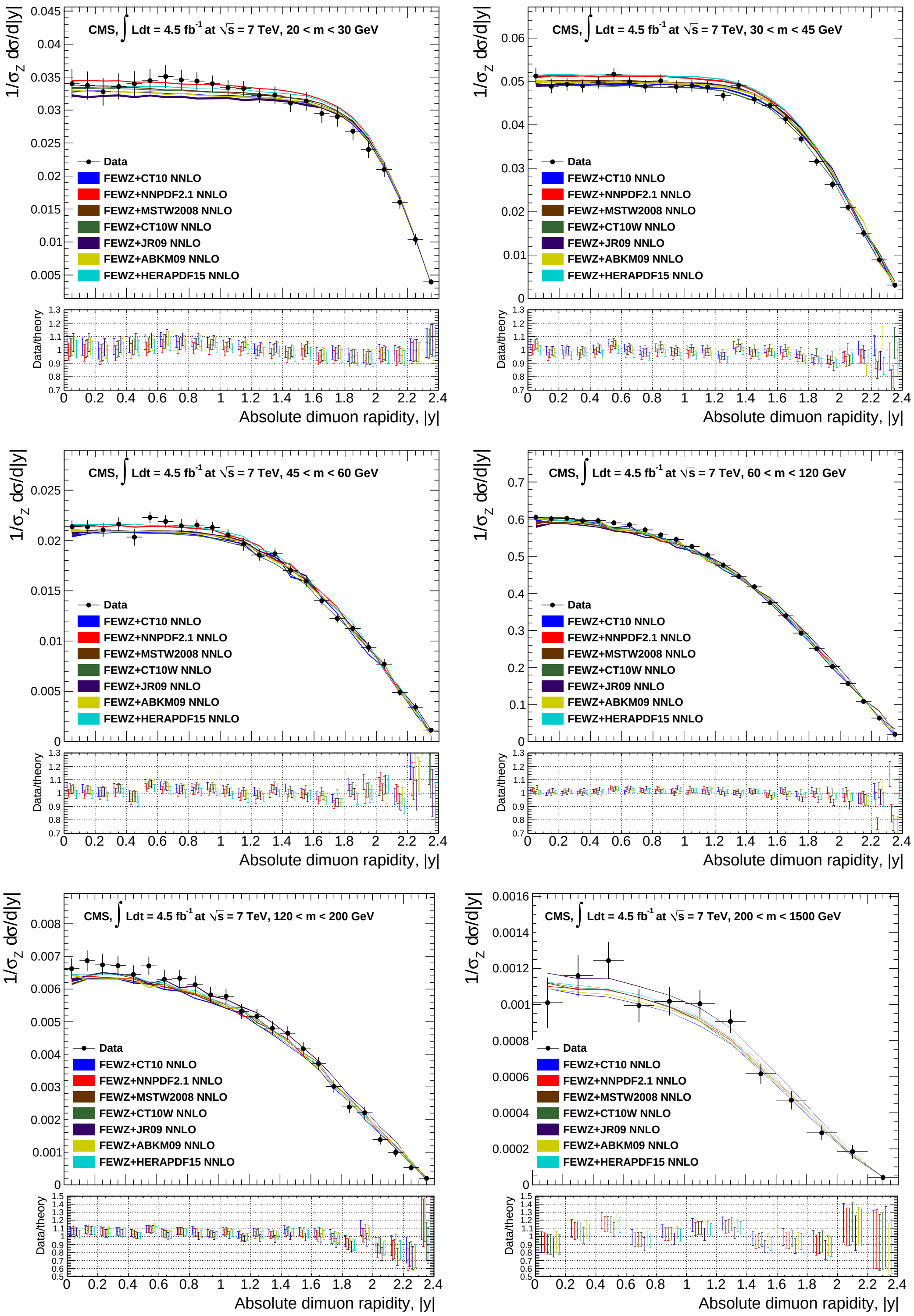

Figure 6.35. The DY rapidity spectrum normalized to the Z peak region ($1/\sigma_Z\, d^2\sigma/d|y|$), compared to theoretical expectations using various PDF sets. The uncertainty bands in the theoretical predictions indicate the statistical uncertainty only. The error bars include the experimental uncertainty in the data and statistical uncertainty in the theoretical expectation, combined quadratically.

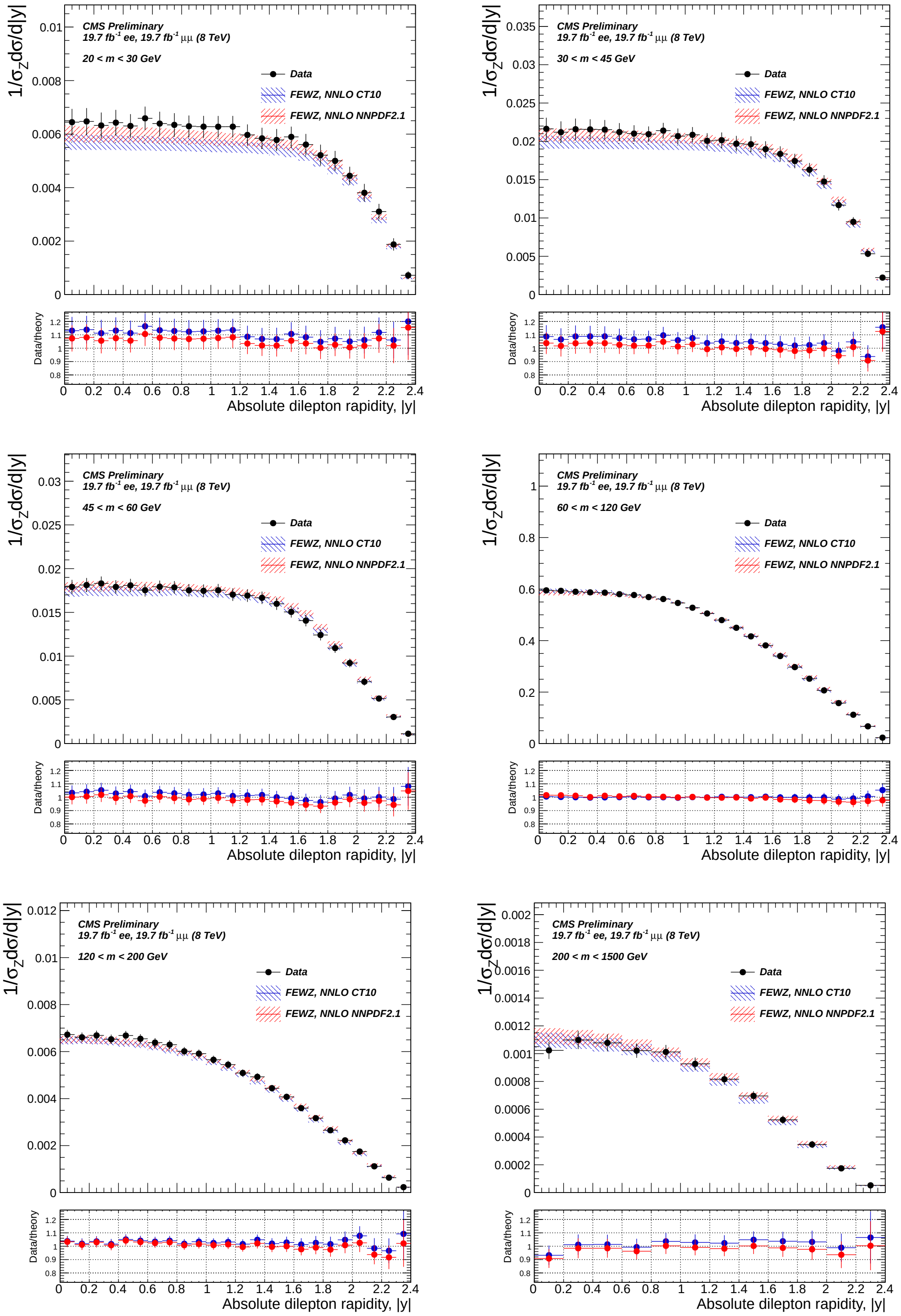

Figure 6.36. The DY dielectron rapidity spectrum with the photon induced contribution subtracted, normalized to the Z peak region, plotted for different mass regions within the detector acceptance, as measured and predicted by NLO Fewz+CT10 PDF and NNLO Fewz+CT10 PDF calculations. There are six mass bins between 20 and 1500 GeV, from left to right and from top to bottom. The uncertainty bands in the theoretical predictions combine the statistical and the PDF uncertainties (shaded bands). The statistical component is negligible.

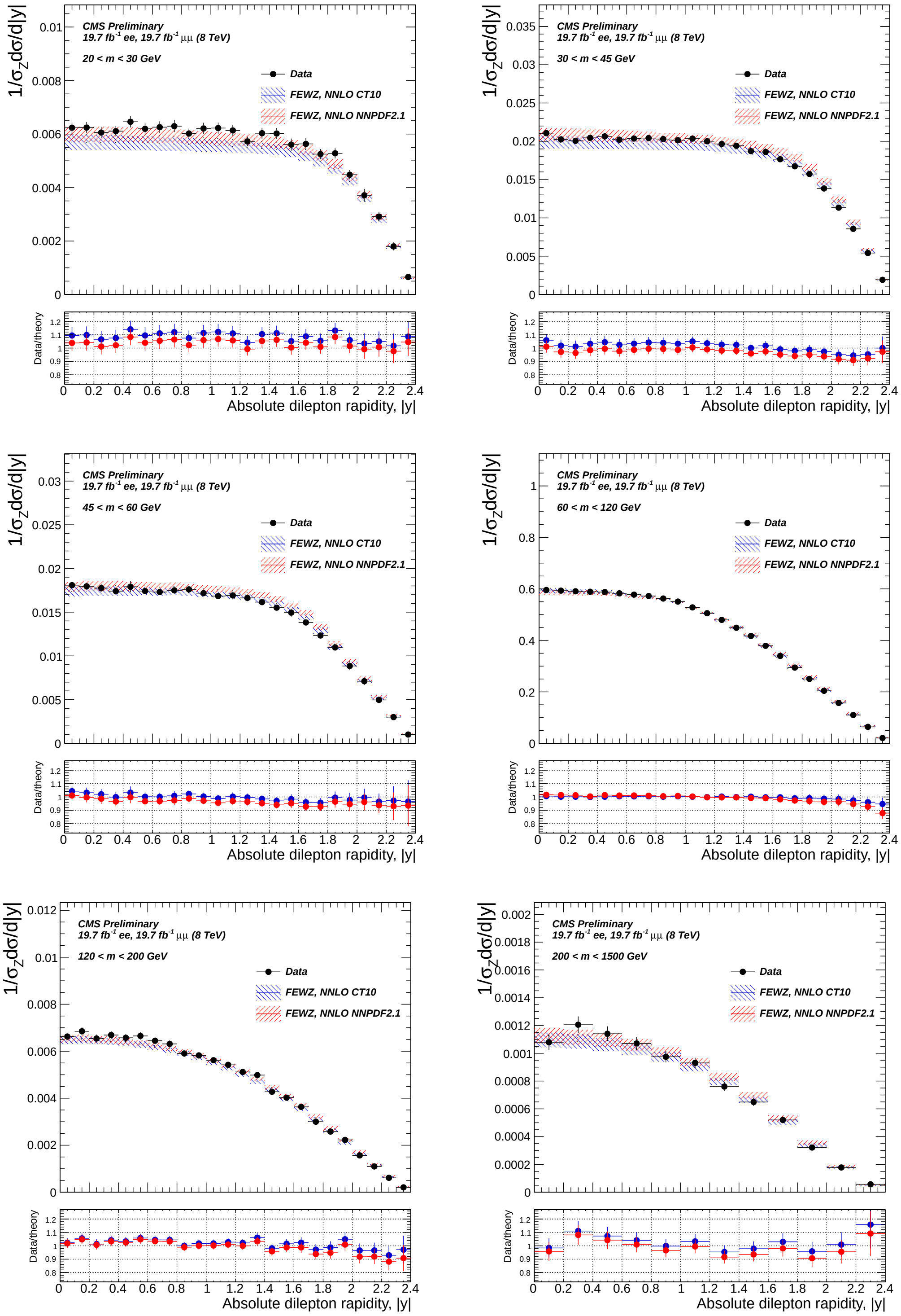

Figure 6.37. The DY dimuon rapidity spectrum with the photon induced contribution subtracted, normalized to the Z peak region $(1/\sigma_Z d^2\sigma/dm\, d|y|)$, plotted for different mass regions within the detector acceptance, as measured and predicted by NLO Fewz+CT10 PDF and NNLO Fewz+CT10 PDF calculations. There are six mass bins between 20 and 1500 GeV, from left to right and from top to bottom. The uncertainty bands in the theoretical predictions combine the statistical and the PDF uncertainties (shaded bands). The statistical component is negligible.

In the low mass region, the results of the measurement are in better agreement with the NNPDF2.1 NNLO calculation. The CT10 NNLO calculation is systematically lower than NNPDF2.1 NNLO in that region. The normalized χ^2 calculated with total uncertainties on the combined results is 1.3 (1.8) between data and the theoretical expectation calculated with NNPDF2.1 (CT10) NNLO PDFs, with 41 degrees of freedom. In the Z peak region, the two predictions are relatively close to each other and agree well with the measurements. The statistical uncertainties in the measurements in the highest mass region are of the order of the PDF uncertainty.

6.8.3 Combination of the e^+e^- and $\mu^+\mu^-$ Cross Section Measurements

To assess the level of compatibility between the dimuon and dielectron measurements χ^2 tests are performed.

As seen in Fig. 6.38, the ratios of differential cross section measurements for the dimuon and dielectron channels are in good agreement.

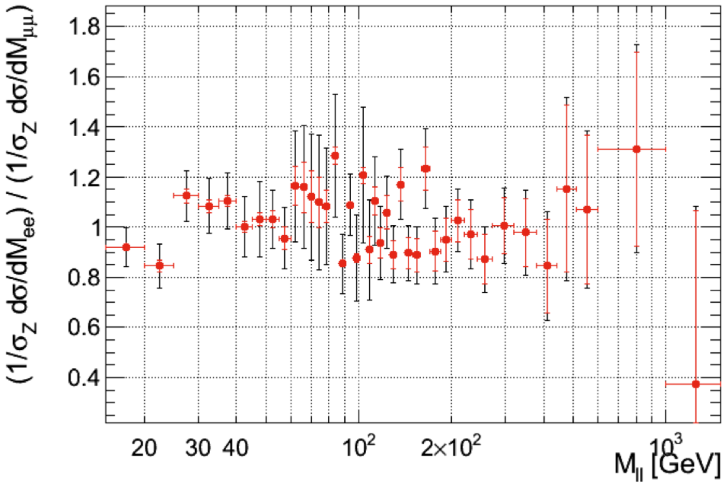

Figure 6.38. The ratio of the DY pre-FSR full acceptance cross section measurements in the dimuon and dielectron channels at 7 TeV.

The χ^2 values calculated between the cross section measurements in the dimuon and dielectron channels at 7 TeV are less than 2 for most of the bins, and all the values are less than 3. The combined $\chi^2/\mathrm{ndf} = 1.06$ considering no correlations. The largest deviations between the cross sections in two channels are observed in the bins 115–120 GeV and 200–220 GeV. Notice here, that the modeling uncertainties on acceptance are considered between the two channels. The combined $\chi^2/\mathrm{ndf} = 0.87$ considering no bin-to-bin correlations and $\chi^2/\mathrm{ndf} = 1.07$ with the full correlation matrix taken into account. Overall, the DY cross section measurements in the dielectron and dimuon channels are in good agreement.

Fig. 6.39 shows the ratio of differential cross section measurements in the dimuon and dielectron channels at 8 TeV center-of-mass energy. As seen, the results are in agreement within associated errors.

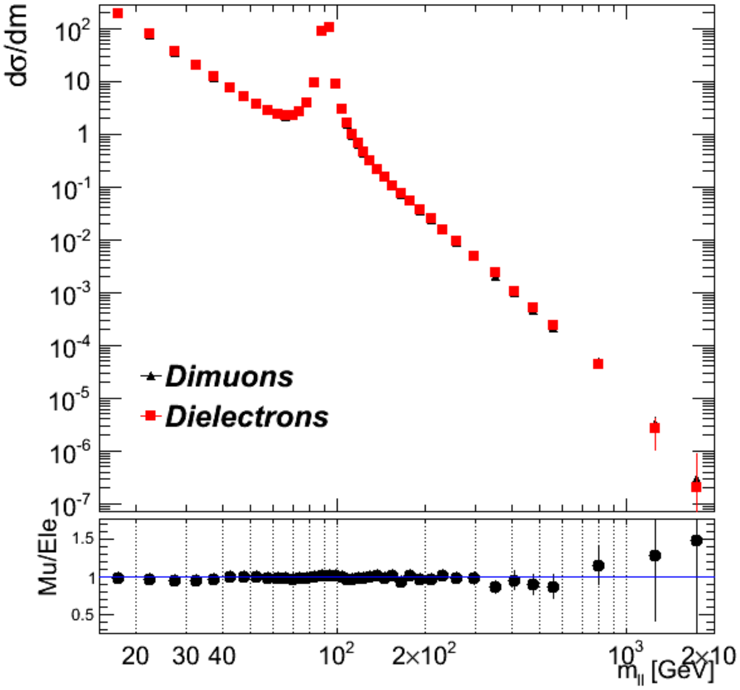

Figure 6.39. Drell–Yan pre-FSR full acceptance cross section measurement with the photon induced contribution subtracted, in the dimuon and dielectron channels at 8 TeV center-of-mass energy.

At 8 TeV, all the χ^2 values calculated between the cross section measurements in the dimuon and dielectron channels are less than 2.5, with the highest value of 2.1 at around 300 GeV. Agreement between the two measurements just below the Z peak is the best. The total $\chi^2/\mathrm{ndf} = 0.62$, considering no bin-to-bin correlations. Overall, the results in the two channels are in good agreement for 8 TeV measurement as well and, therefore, can be combined for greater precision.

Similar tests were repeated for the double-differential cross section measurements. Fig. 6.40 shows the ratio of double-differential cross section measurements in the dimuon and dielectron channels. An agreement between the results in the two channels within associated errors have been observed in all the mass bins. Deviations in the high-rapidity region are generally larger.

The χ^2/ndf values between dielectron and dimuon cross section measurements are less than 1.5 in all the mass regions. Generally, the agreement between the two measurements is very good. However, the pull values in the high-rapidity region are larger as the deviations are more significant. It can be concluded that the double-differential cross section measurements in the two channels are in good agreement and can be combined for greater precision.

The cross section measurements in the two channels are combined using the procedure defined in [101]. Given the results in the dimuon and dielectron channels, and their symmetric and positive definite covariance matrices, the estimates of the true cross section values are found as unbiased linear combinations of the input measurements having a minimum variance, a full covariance matrix for the uncertainties is also extracted with this method.

The uncertainties are considered to be uncorrelated between the two channels. Exceptions are the modeling uncertainty which is 100% correlated and the uncertainty in the acceptance, which originates mainly from the PDFs. The acceptance is almost identical between the two channels and the differences in uncertainties between them are negligible. Thus, when combining the measurements the uncertainty in the acceptance is added (in quadrature) to the total uncertainty after the combination is done. The acceptance uncertainty does not include correlations between analysis bins.

Fig. 6.41-6.42 show the Drell–Yan cross section measurements in the dimuon and dielectron channels combined normalized to the Z resonance region with the FSR

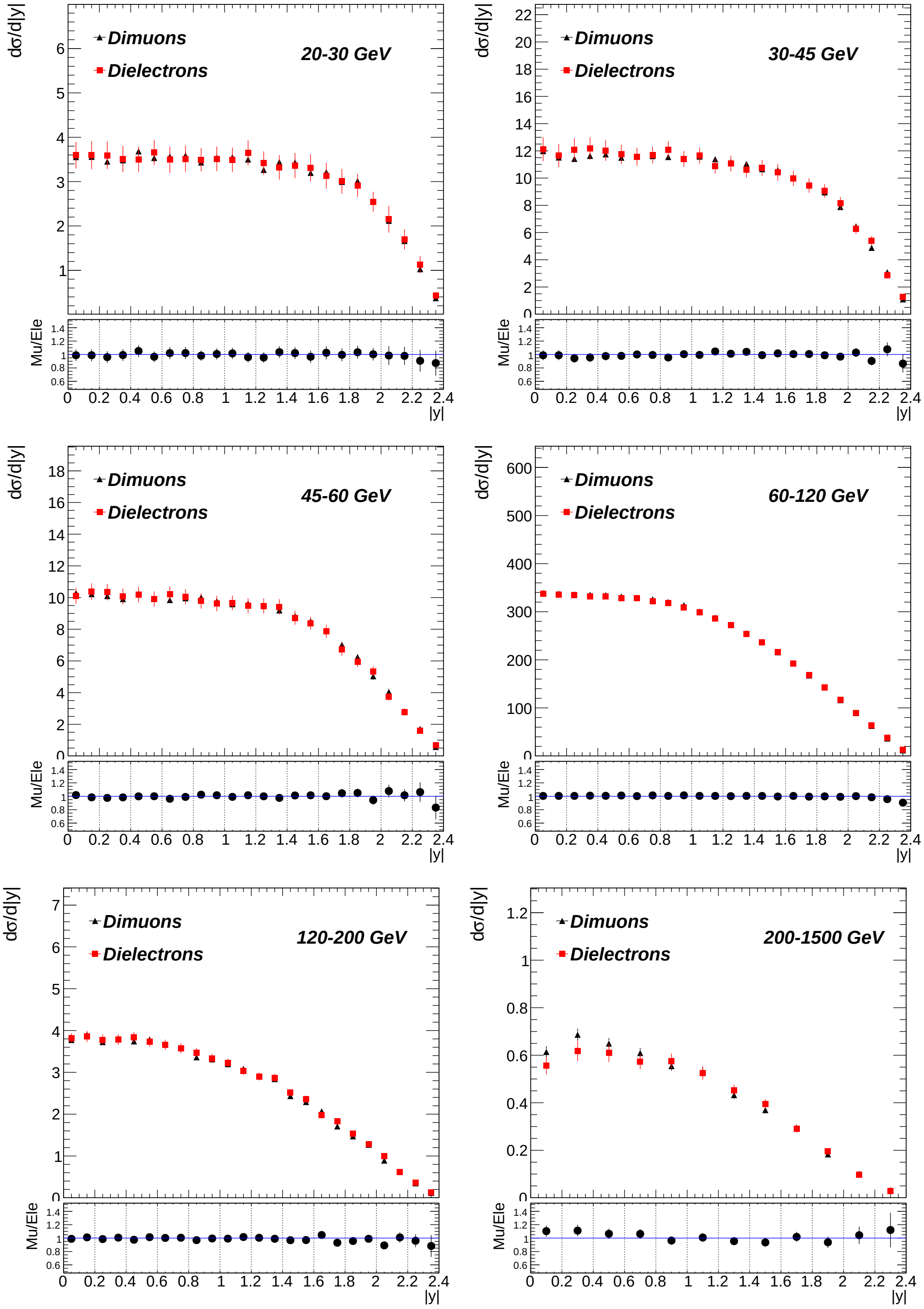

Figure 6.40. The absolute DY dilepton rapidity spectra $d^2\sigma/dm\,d|y|$ with the photon induced contribution subtracted, plotted for different mass regions within the detector acceptance, as measured in dielectron and dimuon channels superimposed. There are six mass bins between 20 and 1500 GeV, from left to right and from top to bottom. The uncertainty bands in the theoretical predictions combine the statistical and systematic uncertainties.

effect taken into account at 7 and 8 TeV center-of-mass energy. The χ^2_{ndf} is 1.1 between 7 TeV data and theory expectation, which takes into account the correlations.

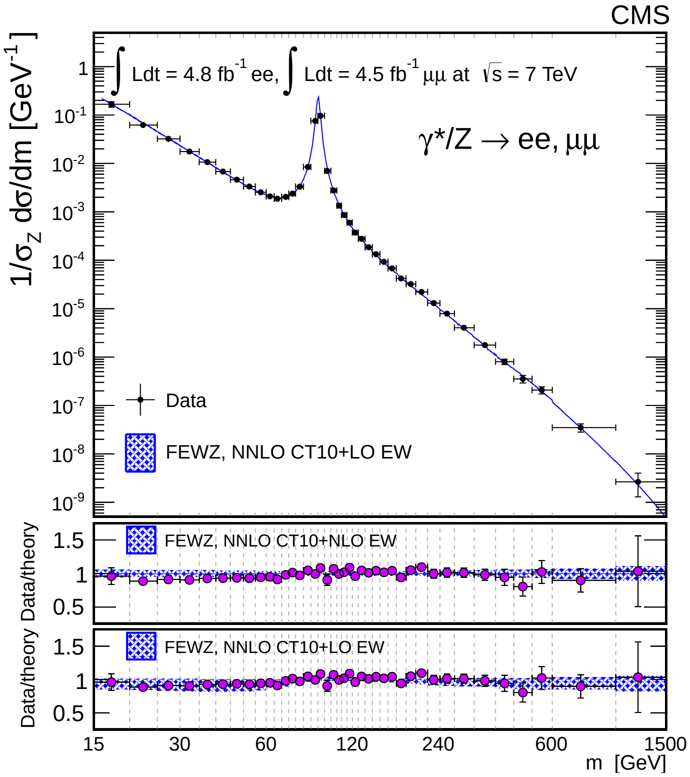

Figure 6.41. Drell–Yan cross section measurement in dimuon and dielectron channels combined normalized to the Z resonance region at 7 TeV with the FSR effect taken into account.

The result of the combined measurement is in agreement with the NNLO theoretical predictions as computed with Fewz using CT10 NNLO. The χ^2_{ndf} is 1.0 between 8 TeV data and theory expectation, which takes into account the correlations.

6.8.4 Double Ratio Measurements

The ratios of the normalized differential and double-differential cross sections for the DY process at the center-of-mass energies of 7 and 8 TeV in bins of dilepton invariant mass and dilepton absolute rapidity are presented. The pre-FSR double ratio in bins of invariant mass is calculated according to

$$R(\to \gamma^*/\mathrm{Z} \to l^+l^-) = \frac{(1/\sigma_\mathrm{Z}\frac{d\sigma}{dm})(8\,\mathrm{TeV})}{(1/\sigma_\mathrm{Z}\frac{d\sigma}{dm})(7\,\mathrm{TeV})},$$

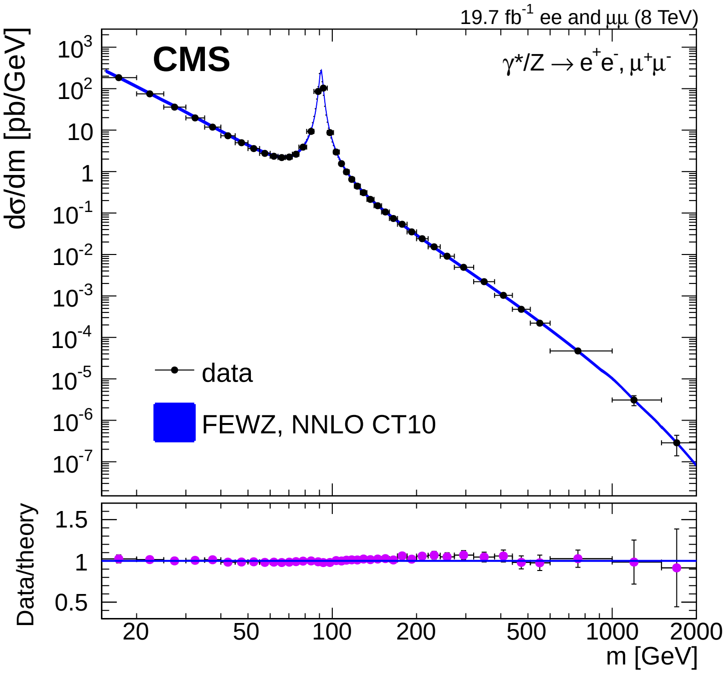

Figure 6.42. Drell–Yan cross section measurement in dimuon and dielectron channels combined normalized to the Z resonance region at 8 TeV with the FSR effect taken into account.

while the pre-FSR double ratio in bins of mass and rapidity is calculated as

$$R_{\text{det}}(\to \gamma^*/\text{Z} \to l^+l^-) = \frac{(1/\sigma_{\text{Z}}\frac{d^2\sigma}{dm\,d|y|})(8\,\text{TeV}, p_{\text{T}} > 10,\ 20\,\text{GeV})}{(1/\sigma_{\text{Z}}\frac{d^2\sigma}{dm\,d|y|})(7\,\text{TeV}, p_{\text{T}} > 9,\ 14\,\text{GeV})},$$

where σ_{Z} is the cross section in the Z peak region; l denotes e or μ. The same binning is used for differential measurements at 7 and 8 TeV in order to compute the ratios consistently.

The double ratio measurements provide a high sensitivity to NNLO QCD effects and could potentially yield precise constraints on the PDFs, as the theoretical systematic uncertainties in the cross section calculations at different center-of-mass energies have substantial correlations. Tab. 6.10 summarizes the uncertainty sources that cancel out in the double ratio measurements.

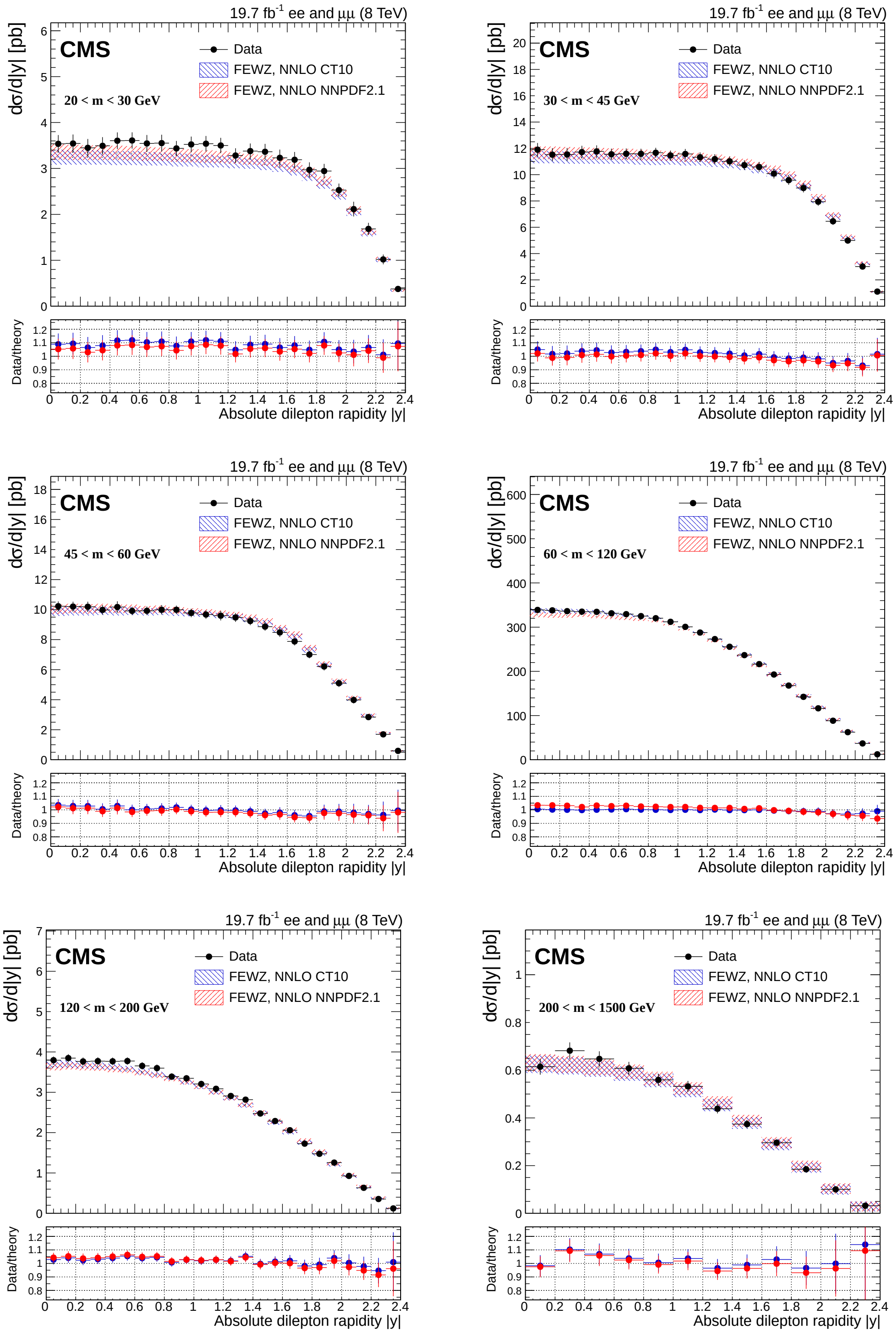

Figure 6.43. The absolute DY dilepton rapidity spectrum $d^2\sigma/dm\,d|y|$ with the photon induced contribution subtracted, in the combined channel, plotted for different mass regions within the detector acceptance, as measured and predicted by NLO Fewz+CT10 PDF and NNLO Fewz+CT10 PDF calculations. There are six mass bins between 20 and 1500 GeV, from left to right and from top to bottom. The uncertainty bands in the theoretical predictions combine the statistical and the PDF uncertainties (shaded bands). The statistical component is negligible.

Table 6.10
Summary of the uncertainty sources that cancel out in the double ratio measurements.

Uncertainty source	$d\sigma/dm$	$d^2\sigma/dm\,d\lvert y\rvert$
PDF	Cancels	Cancels
Acc. Mod.	Cancels	–
FSR	Cancels	Cancels

Fig. 6.44 shows the results of the DY cross section double ratio measurement in the dimuon channel. The theoretical prediction for the double ratio is calculated using Fewz with the CT10 NNLO PDF set. The shape of the distribution is defined entirely by the $\sqrt{s}$ and the Bjorken x dependencies of the PDFs, as the dependency on the hard scattering process cross section is canceled out. In the Z peak region, the expected double ratio is close to 1 by definition. It increases linearly as a function of the logarithm of the invariant mass in the region below 200 GeV, where partons with small Bjorken x ($0.001 < x < 0.1$) contribute the most. At high mass, a high x region is probed ($x > 0.3$). The PDFs at smaller $\sqrt{s}$ fall more steeply at large x, leading to an exponential growth of the double ratio as a function of mass above 200 GeV.

The uncertainty bands in the theoretical prediction of the double ratio include the statistical and the PDF uncertainties from the Fewz calculations summed in quadrature. The experimental systematic uncertainty calculation is described in Section 6.7. The scale variation uncertainty of up to 2% is included in the theoretical error band.

Agreement is observed between the double ratio measurement and the CT10 NNLO PDF theoretical prediction within uncertainties. The χ^2 probability from a comparison of the predicted and measured double ratios is 87% with 40 degrees of freedom, calculated with the total uncertainties. At high mass, the statistical component of the uncertainty becomes significant, primarily from the 7 TeV measurements.

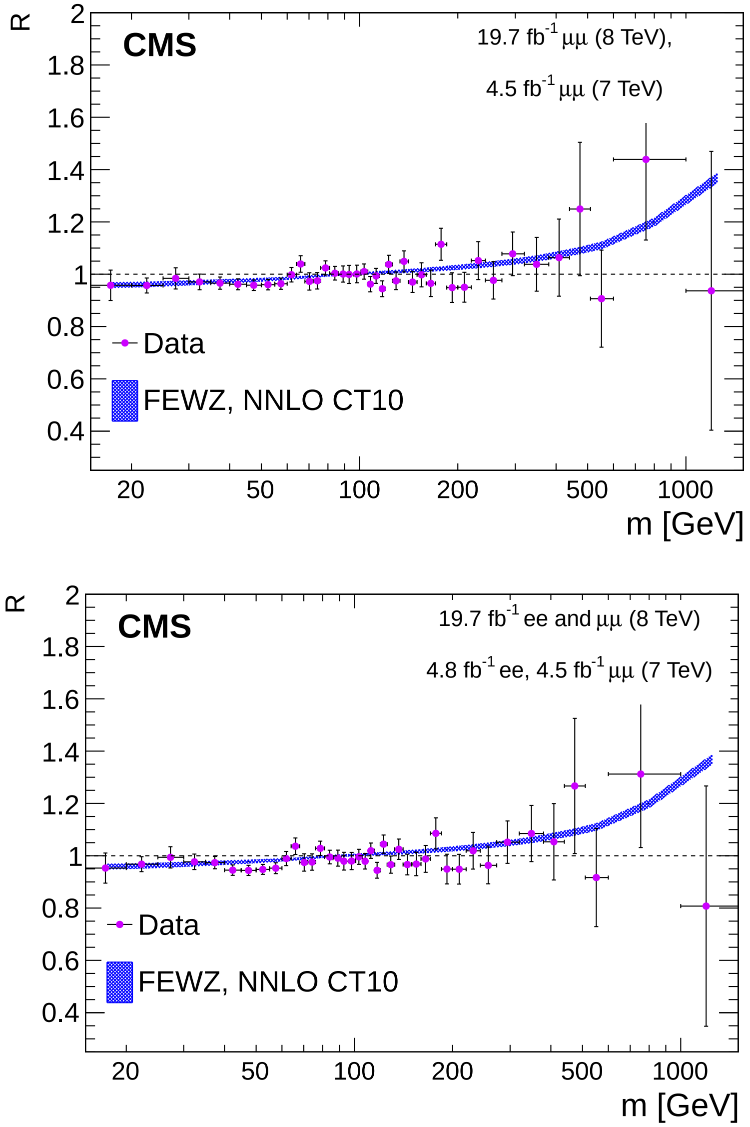

Figure 6.44. Measured ratio of DY normalized differential cross sections at center-of-mass energies of 7 and 8 TeV in the dimuon (top) and combined dilepton channels (bottom) as compared to NNLO Fewz calculations obtained with CT10 NNLO PDF. The uncertainty bands in the theoretical predictions combine the statistical and PDF uncertainties (shaded bands); the latter contributions are dominant.

The double ratio predictions calculated with the CT10 NNLO and NNPDF2.1 NNLO PDFs agree with the measurements. Below the Z peak, NNPDF2.1 NNLO

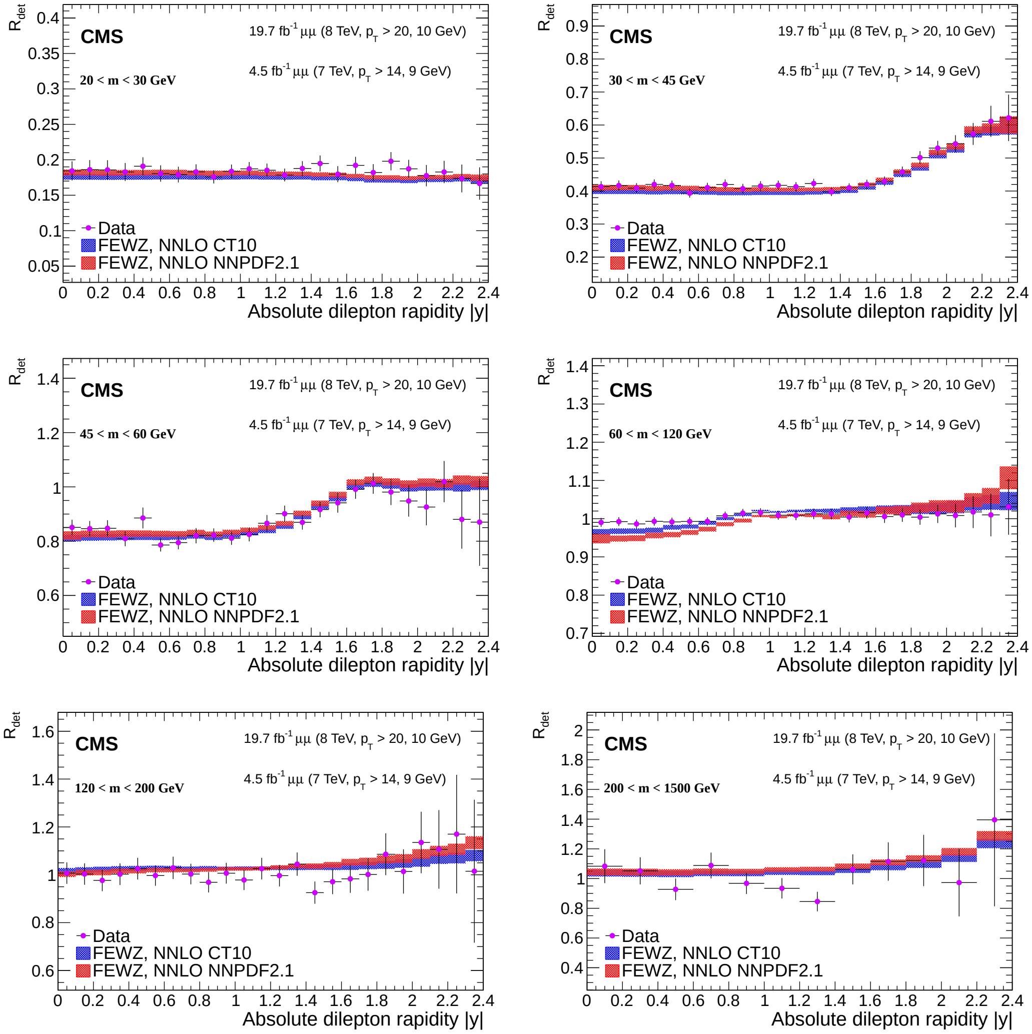

Figure 6.45. Measured ratio of DY normalized differential cross sections, within the detector acceptance, at center-of-mass energies of 7 and 8 TeV in the dimuon channel, plotted for different mass regions and compared to NNLO Fewz calculations obtained with the CT10 PDFs. There are six mass bins between 20 and 1500 GeV, from left to right and from top to bottom. The uncertainty bands in the theoretical predictions combine the statistical and PDF uncertainties (shaded bands); the latter contributions are dominant.

PDF theoretical predictions are in a closer agreement with the measurement. In the Z peak region, a difference in the slope of both theoretical predictions as compared to the measurement is observed in the central absolute rapidity region. In the high-rapidity and high-mass regions, the effect of the limited number of events in the 7 TeV measurement is significant. In the 120–200 GeV region, the measurement is at the lower edge of the uncertainty band of the theory predictions.

Fig. 6.46 shows the combined double ratio measurement as a function of rapidity in various invariant mass regions. The shape of the theoretical prediction of the double ratio is nearly independent of the dilepton rapidity at low mass, showing an increase as a function of rapidity by up to 20% in the Z peak region and at high mass, and a significant dependence on rapidity in the 30–60 GeV region. The uncertainty bands in the theoretical predictions of the double ratio include the statistical and the PDF uncertainties from the FEWZ calculations summed in quadrature. The estimated uncertainties related to QCD renormalization and factorization scale dependence (up to 2%) are included in the theoretical error band.

The double ratio predictions calculated with the CT10 NNLO and NNPDF2.1 NNLO PDFs agree with the measurements. Below the Z peak, NNPDF2.1 NNLO PDF theoretical predictions are in a closer agreement with the measurement. In the Z peak region, a difference in the slope of both theoretical predictions as compared to the measurement is observed in the central absolute rapidity region. In the high-rapidity and high-mass regions, the effect of the limited number of events in the 7 TeV measurement is significant. In the 120–200 GeV region, the measurement is at the lower edge of the uncertainty band of the theory predictions.

The DY differential cross section has been measured by the CDF, D0, ATLAS, and CMS experiments [19, 68, 69, 102–104]. The current measurement of the Drell–Yan differential $d\sigma/dm$ cross section extends the mass coverage range from 1.5 TeV reported in the latest CMS and ATLAS measurements up to 2 TeV and improve the precision of the cross section measurement at low mass and the Z peak region due to larger statistics samples and the reduction of experimental systematic uncertainties as a result of the application of data-driven techniques. The double-differential $d^2\sigma/dmd|y|$ distributions are determined not only in the Z peak region as in the

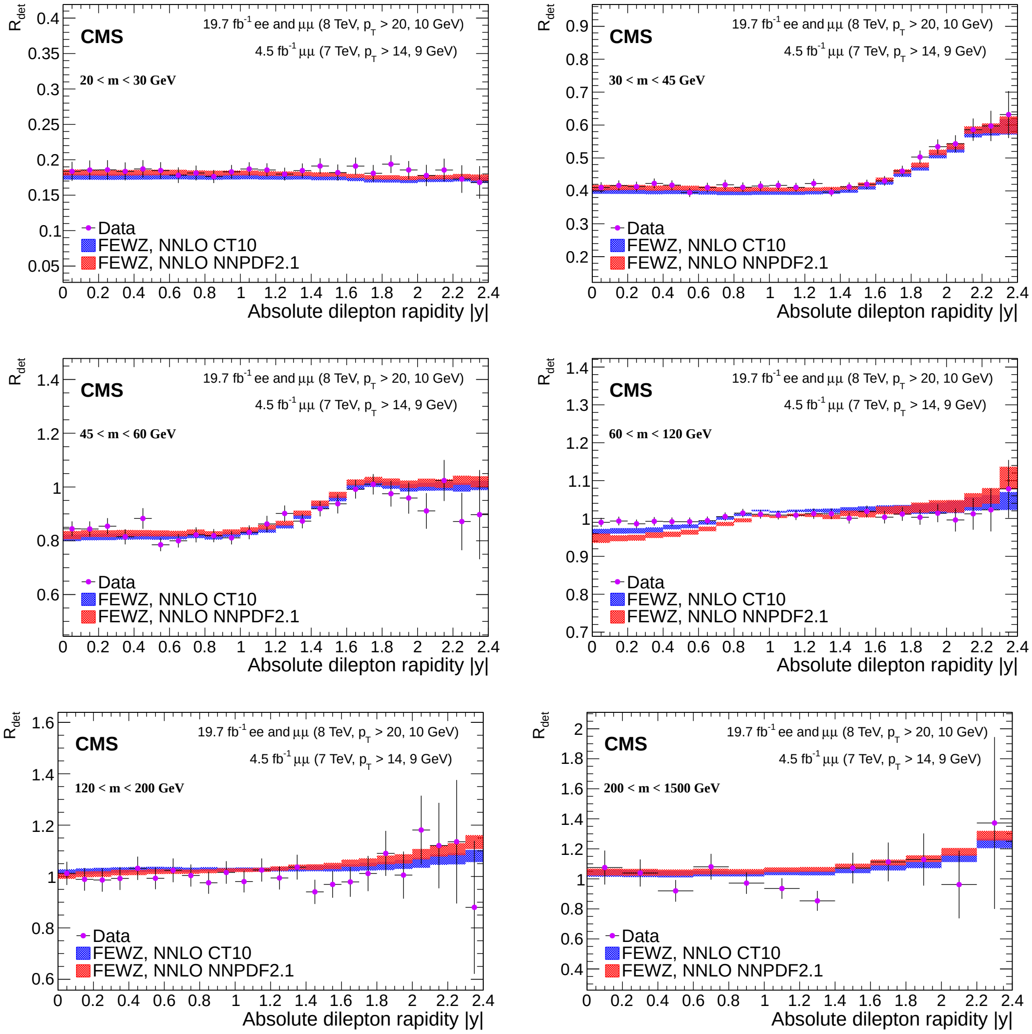

Figure 6.46. Measured ratio of DY normalized differential cross sections, within the detector acceptance, at center-of-mass energies of 7 and 8 TeV in the combined dilepton channel, plotted for different mass regions and compared to NNLO Fewz calculations obtained with the CT10 PDFs. There are six mass bins between 20 and 1500 GeV, from left to right and from top to bottom. The uncertainty bands in the theoretical predictions combine the statistical and PDF uncertainties (shaded bands); the latter contributions are dominant.

measurements with Tevatron data, but also at low and high masses, therefore, significantly improving the potential for PDF constraints with DY data. The DY analysis presented covers the ranges $0.0003 < x < 0.5$ and $500 < Q^2 < 90000\,\mathrm{GeV}^2$ in Bjorken x scaling variable and evolution scale Q^2. The current measurements appear to be in agreement with the previous measurements. One of the novel additions of the present DY analysis is the first double ratio measurement with Drell–Yan data, which is a tool for the reduction of PDF uncertainties due to the cancellation of theoretical systematic uncertainties between measurements at various data-taking periods.

6.9 PDF Constraints with Drell–Yan Data

Drell–Yan data provides an important input for modern PDF fits. Most of the currently available PDFs are significantly influenced by the fixed-target DY experimental data. The data used for the constraints is in the mass range of $50 < m < 600$ GeV and the absolute rapidity range of $|y| < 2.2$. At the LHC, a small x and high Q^2 kinematic region is probed, where the contribution of parton sub-processes involving light sea and especially strange sea quarks is significantly increased which motivates the use of the CMS DY data as an input for PDF fits.

The rapidity distributions of the gauge bosons γ^*/Z are sensitive to the parton content of the proton, and the very high energy of the LHC allows the PDFs to be probed in a wide region of Bjorken x and Q^2: $0.0003 < x < 0.5$ and $500 < Q^2 < 90000\ \mathrm{GeV}^2$. Since the y distribution is symmetric around zero in proton-proton collisions, only the differential cross section in $|y|$ is normally considered in order to reduce the statistical errors.

The measurements of the double-differential cross section $d^2\sigma/dm\,d|y|$ in DY production are used in the following to provide direct quantitative tests of perturbative QCD and help to constrain the quark, antiquark and gluon content of the proton.

The NNPDF approach described in Section 3.2.3 is used as a framework for the calculations. The prior PDF distributions are calculated using the NNPDF2.1 NNLO PDF set composed of 100 simulated replications. The χ^2 values estimated between the theoretical cross sections and the DY cross section measurement per degree of freedom are used as an input for the NNPDF reweighting procedure. The correlations among analysis bins are taken into account. Various combinations of input data are considered.

Fig. 6.47 shows the impact of the 7 TeV DY double-differential cross section measurement on the total valence and gluon parton distributions. As seen, some reduction of the PDF uncertainty band is observed on the total valence quark PDF in the low and high-x region. The effect of DY data on the gluon distributions is insignificant.

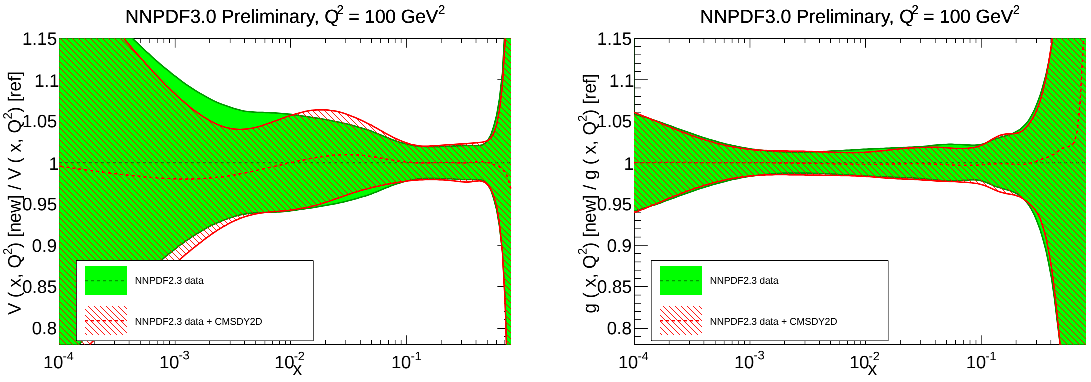

Figure 6.47. Impact of the 7 TeV DY double-differential cross section measurement on the total valence (left) and gluon (right) parton distributions in NNPDF 3.0 fit.

Fig. 6.48 illustrates the impact of the 7 TeV DY double-differential cross section measurement on the NNPDF fit, using the HERA input data only. As seen, a significant impact on the u and d quark distributions is observed in the low, intermediate and high-x regions. The reduction of systematic uncertainties by up to 30% is observed.

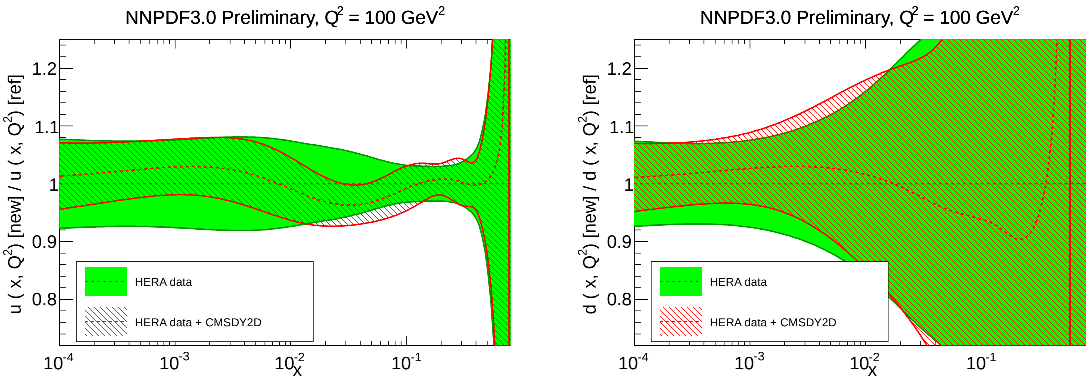

Figure 6.48. Impact of the 7 TeV DY double-differential cross section measurement on the up (left) and down (right) valence quark distributions in NNPDF 3.0 fit using the HERA input data.

Fig. 6.49-6.50 show the impact of the DY double-differential cross section measurement at 8 TeV on the individual quark, antiquark and gluon distributions.

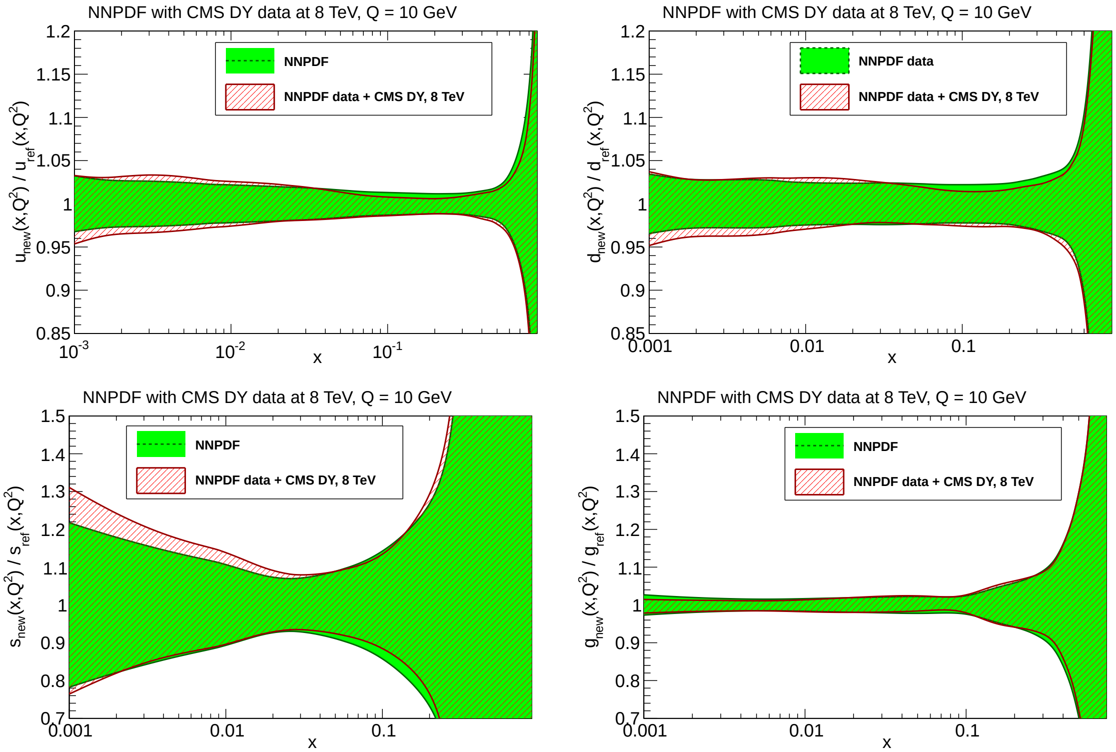

Figure 6.49. Impact of the 8 TeV DY double-differential cross section measurement on the individual quark and gluon distributions in NNPDF fit. From top left to bottom right: u quark, d quark, s quark and gluon PDFs.

As seen, the effect of the 8 TeV data on the parton distributions in the NNPDF fit is significant. Inclusion of the DY double-differential cross section data causes a reduction of error and also shifts the central values of the PDF. The effect is particularly pronounced on the poorly known s quark and antiquark PDFs This is expected, since at the LHC the relative contributions of different parton sub-processes to the DY production are significantly different from the past experiments, with the dominant contribution shifted from first generation quarks (u and d) to strange quarks and antiquarks, carrying 15–20% of the proton momentum.

Finally, the impact of the DY normalized differential cross section ratios at center-of-mass energies of 7 and 8 TeV on PDF fits is quantified. Fig. 6.51-6.52 show the

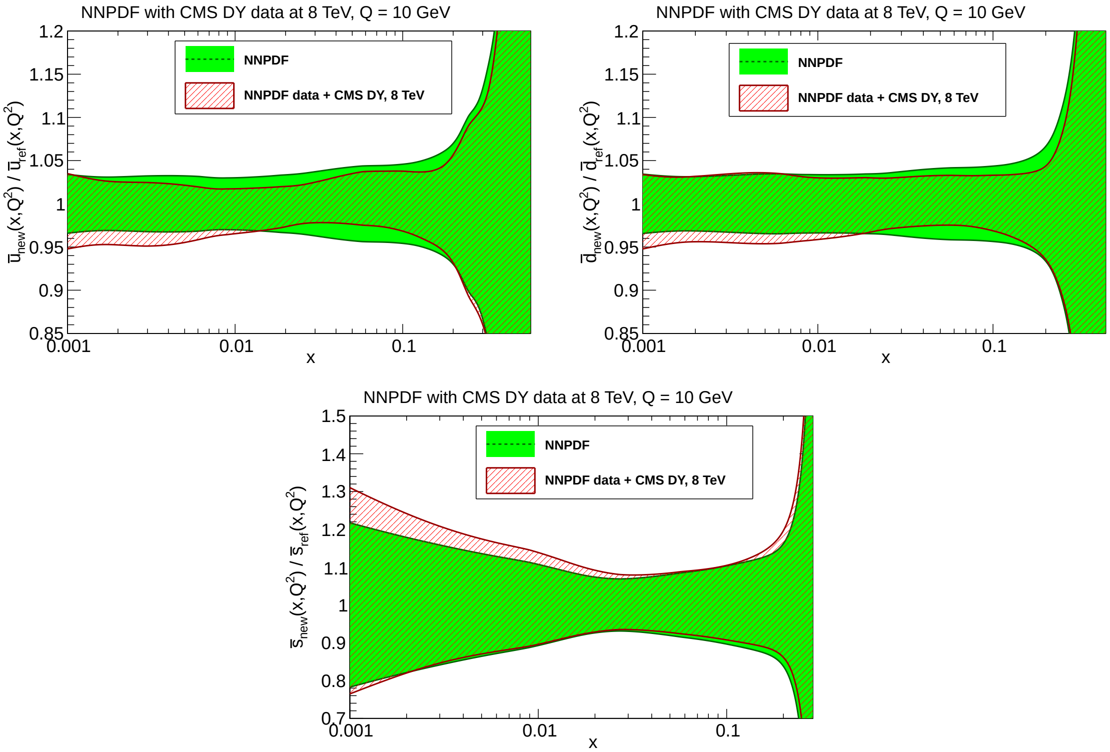

Figure 6.50. Impact of the DY double-differential cross section measurement on the individual antiquark parton distributions in NNPDF fit. From top left to bottom right: $\bar{\mathrm{u}}$ antiquark, $\bar{\mathrm{d}}$ antiquark and $\bar{\mathrm{s}}$ antiquark PDFs.

impact of the DY double ratios on the individual parton distributions in NNPDF fit.

The results observed with double ratio measurements are quite impressive: the reduction of PDF errors is even larger than for the absolute cross sections, because of the cancellation of theoretical systematic uncertainties between 7 and 8 TeV. As seen, the reduction of the uncertainties is between 5–40% and the shift of the central values is up to 10% with the DY double ratio data included.

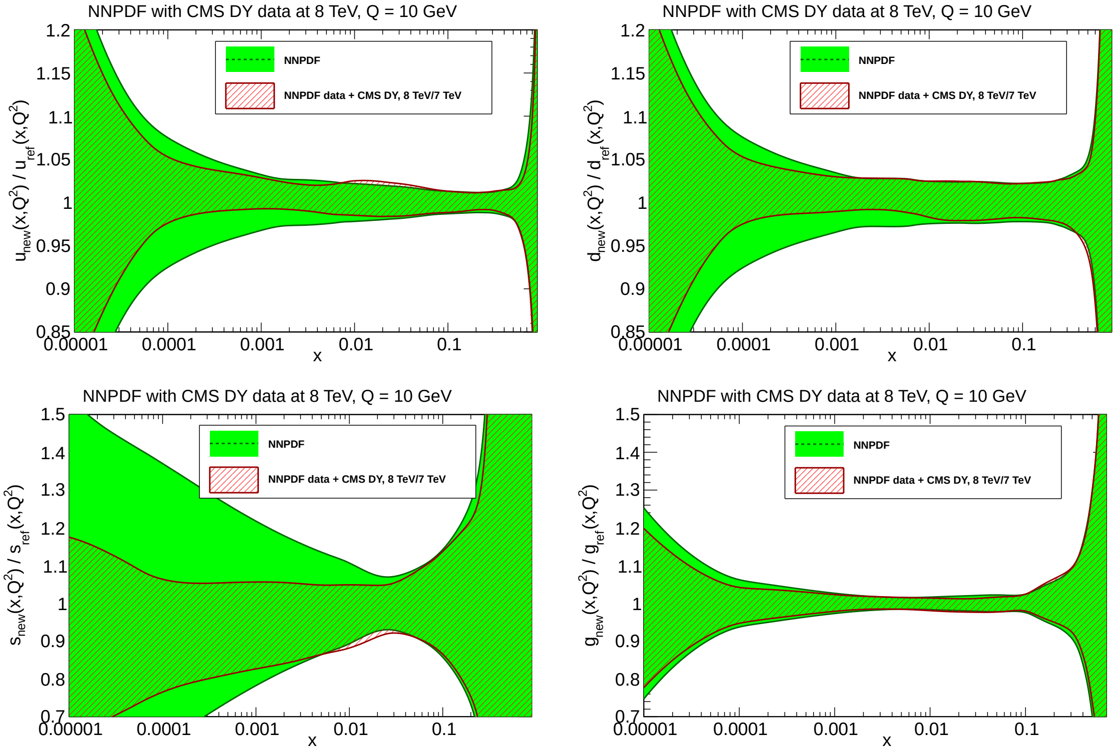

Figure 6.51. Impact of the DY normalized differential cross section ratios, at center-of-mass energies of 7 and 8 TeV on the individual quark parton distributions in NNPDF fit. From top left to bottom right: u quark, d quark, s quark and gluon PDFs.

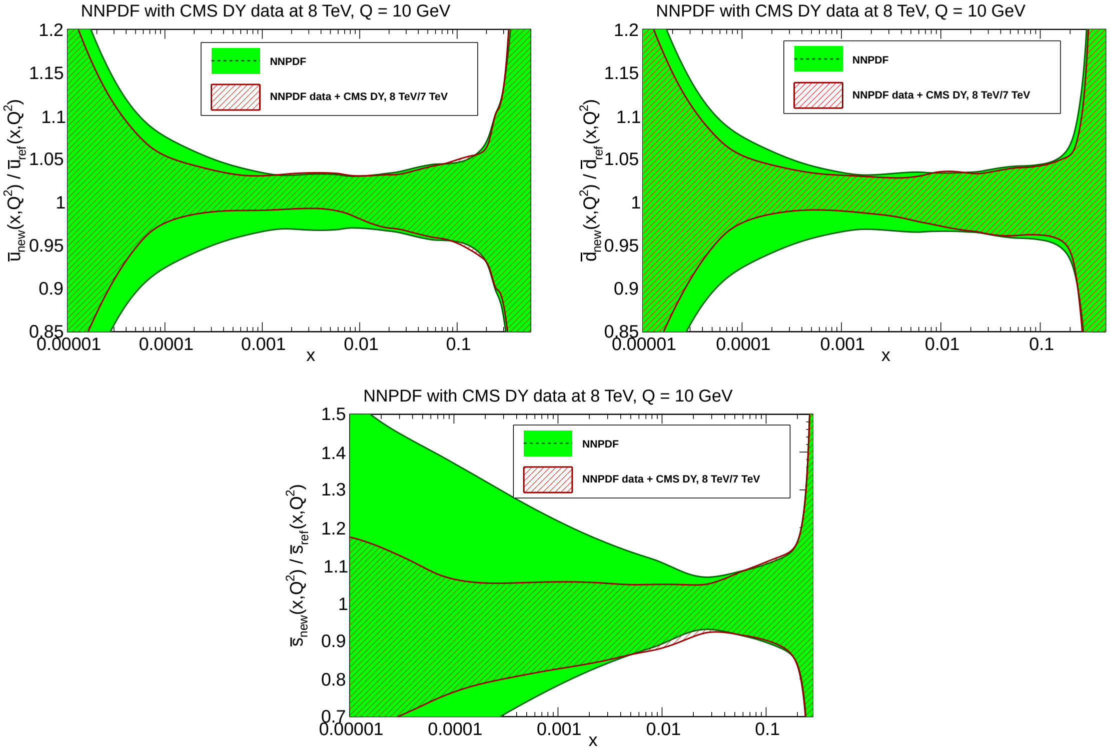

Figure 6.52. Impact of the DY normalized differential cross section ratios, at center-of-mass energies of 7 and 8 TeV on the individual antiquark parton distributions in NNPDF fit. From top left to bottom right: $\bar{\mathrm{u}}$ antiquark, $\bar{\mathrm{d}}$ antiquark and $\bar{\mathrm{s}}$ antiquark PDFs.

7. SUMMARY AND CONCLUSIONS

The main result of this thesis is the precision measurement of the Drell–Yan cross section in order to constrain the parton distribution functions (PDFs). The three following measurements are presented: the Drell–Yan differential cross section $d\sigma/dm$ measurement in the dielectron and dimuon channels, the double-differential cross section $d^2\sigma/dmd|y|$ in the dielectron and dimuon channels, and the first measurement of the ratio of the normalized differential cross sections at 7 and 8 TeV. The measurements are carried out with proton-proton collision data collected using the CMS detector at the LHC with integrated luminosities of $4.8\,\mathrm{fb}^{-1}$ (dielectron) and $4.5\,\mathrm{fb}^{-1}$ (dimuon) at $\sqrt{s} = 7\,\mathrm{TeV}$, and $19.7\,\mathrm{fb}^{-1}$ at $\sqrt{s} = 8\,\mathrm{TeV}$ center-of-mass energy.

The $d\sigma/dm$ and $d^2\sigma/dmd|y|$ measurements are in agreement with the NNLO theoretical predictions, as computed with FEWZ [81] using the CT10, NNPDF2.1, MSTW2008, HERAPDF15, JR09, ABKM09, and CT10W PDFs. The double ratio measurement agrees with the theory prediction within the systematic and PDF uncertainties.

Given the uncertainties of the double-differential cross section and the double ratio measurements presented, they provide sufficient sensitivity to constrain PDFs. The Z boson production cross section presented is the most precise measurement of that type perfromed with CMS data.

The effects of inclusion of DY data in the PDF fits have been explored using the neural network PDF framework [52]. An effect of reduction of PDF uncertainty of 5–40% and a shift of the central values of the PDF by a similar amount has been observed. Using the double ratio measurement resulted in a reduction of uncertainties even larger as compared to the absolute cross sections, because of the cancellation of theoretical systematic uncertainties between 7 and 8 TeV. The effect is particularly pronounced on the poorly known strange quark PDF, as well as the light sea quarks at small values of longitudinal momentum fractions carried by a parton.

APPENDICES

A. REFERENCE FRAMES

Various reference frames are used to describe the kinematics of proton-proton collisions. The most commonly used reference frames are discussed.

In the following, the 4-momentum of the gauge boson is denoted by $q^\mu = (Q, \mathbf{q})$, where Q is the energy and $\mathbf{q}$ is the 3-momentum of the boson.

A.1 Laboratory Frame

The laboratory frame is a frame of reference attached to the laboratory in which the experiment is performed (for example, the particle detector). This is the reference frame in which the laboratory is at rest. In this reference frame the 4-vector q^μ has the components $q^\mu = (Q, \mathbf{q}) = (\nu, 0, 0, |\mathbf{q}|)$. The vector $\mathbf{q}$ in the laboratory-system is directed along the z axis.

A.2 Center-of-mass Frame

The center-of-mass frame (CM frame) is a coordinate system in which the center-of-mass is at rest. Also, the total linear momentum is zero and the total energy of the system is equal to the minimal energy as seen from all possible inertial reference frames.

A.3 Breit Frame

In the Breit reference frame [105] colliding protons are assumed to be moving fast, the quark and antiquark involved in the hard process are assumed to carry fractions x_1 and x_2 of the proton momenta, respectively.

Let us denote the 4-momentum of the gauge boson in the Breit frame by $q^{'\mu} = (Q^{'}, \mathbf{q}')$. This coordinate system is defined by the condition that the energy transfer is zero: $Q^{'} = 0$. Thus, it is only the momentum that is transferred to partons in the Breit frame. We can establish that such a coordinate system exists, if we recall that the 4-momentum $q^{'\mu}$ is space-like: $q^{'\mu}q^{'}_{\mu} = -\mathbf{q}^{'\mathbf{2}} < \mathbf{0}$. Therefore, the laboratory system is related to the Breit frame by relativistic transformation. The energy of the 4-vector $q^{'\mu}$ in the Breit frame is connected with that in the laboratory-system by:

$$Q^{'} = \frac{\nu - (\mathbf{q} \cdot \boldsymbol{\nu})}{(1 - \nu^2)^{1/2}} = 0, \tag{A.1}$$

where $\boldsymbol{\nu}$ is the velocity of the laboratory-system relative to the Breit frame, and ν is the energy in the laboratory frame. It follows from the previous equation that the magnitude of $\boldsymbol{\nu}$ is:

$$\nu = \nu/q_{||} = \nu(\nu^2 - q^2 - q_{\perp}^2)^{1/2}, \tag{A.2}$$

where $q_{||}$ denotes the component of the vector $\mathbf{q}$ parallel to $\boldsymbol{\nu}$, and $\mathbf{q}_{\perp}$ is the transverse component of the vector $\mathbf{q}$. From Eq. (A.1) it follows that $q_{||} > 0$. The relativistic transformation for the longitudinal component of the vector $\mathbf{q}^{'}$ has the form:

$$\mathbf{q}_{||}^{'} = \frac{\mathbf{q}_{||} - \nu\boldsymbol{\nu}}{(\mathbf{1} - \nu^{\mathbf{2}})^{\mathbf{1/2}}}. \tag{A.3}$$

Under the assumption that $q_{\perp} \neq 0$ and $q_{\perp} = 0$ one gets also:

$$\boldsymbol{\nu} = \nu\mathbf{q}/|\mathbf{q}|^{\mathbf{2}} \tag{A.4}$$

A.4 Collins-Soper Frame

In the Collins-Soper (CS) frame [106] the gauge boson is at rest, meaning $q^{\mu} = (Q, 0, 0, 0)$. The frame is characterized by two properties. First, the y axis is perpendicular to the plane spanned by the two hadron momenta P_1 and P_2 and second, the z axis cuts the angle between P_1 and P_2 into two equal halves, see Fig. A.1 for details.

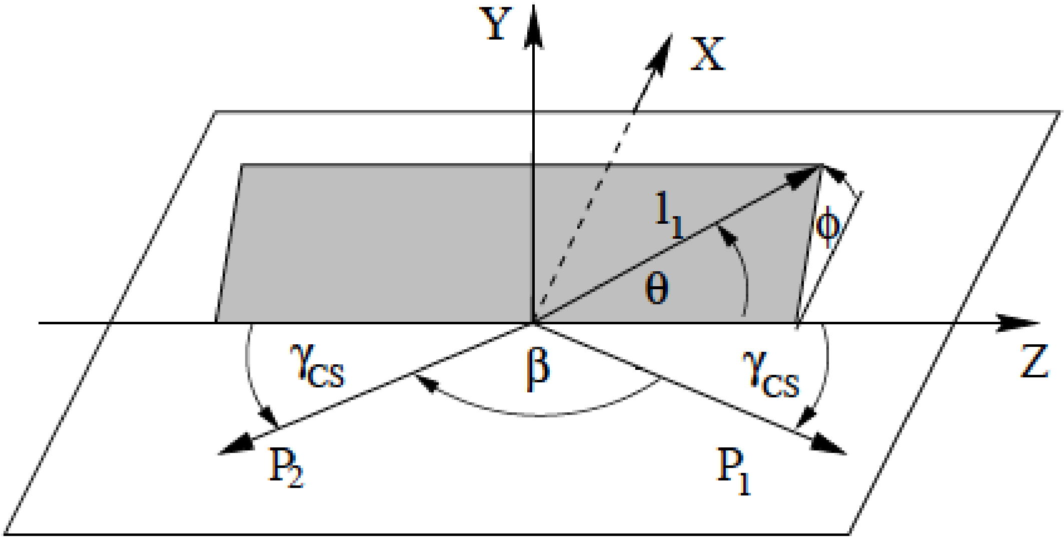

Figure A.1. The Collins-Soper frame: the z axis cuts the angle between P_1 and P_2 into halves (the half angle is called the Collins-Soper angle CS) while the x axis is perpendicular to P_1 and P_2. The direction of one lepton momentum l_1 can then be given by the angles ϕ and θ.

B. PILEUP REWEIGHTING

The effect of multiple proton-proton interactions per bunch crossing is referred to as pileup. Pileup effects are taken into account in MC samples which are generated with the inclusion of multiple proton-proton interactions that have timing and multiplicity distributions similar to those expected in data. To match the observed instantaneous luminosity profile of the LHC, the simulated events are reweighted to yield the same distribution of the mean number of proton-proton interactions per bunch crossing as observed in data.

The number of pileup events in data and MC simulated with Poissonian out-of-time scenario (referred to as S10 scenario in the note, see [107] for details) is shown in Fig. B.1.

Following the official CMS recipe described in [107], MC samples are reweighted using the simulation truth instead of the number of pileup interactions. The target pileup distribution for data is derived by using the per-bunch-crossing-per-luminosity section instantaneous luminosity from the LumiDB together with the total inelastic cross section to generate an expected pileup distribution, correctly weighted by the per-bunch-crossing-per-luminosity section integrated luminosity over the entire data-taking period.

The average weight distribution corresponding to this reweighting procedure is shown in Fig. B.2. The average pileup weight in MC is 1.01.

Pileup affects the Drell–Yan analysis mainly through the lepton isolation efficiency. The effect of pileup interactions on efficiencies was inspected. For that, the reconstruction and identification, and isolation efficiencies were studied as a function of the number of reconstructed primary vertexes in an event. Fig. B.3 summarizes the effect of pileup on the muon and electron efficiencies respectively. At 7 TeV, the effect of pileup was less significant (yielding 9 interactions per bunch crossing on average

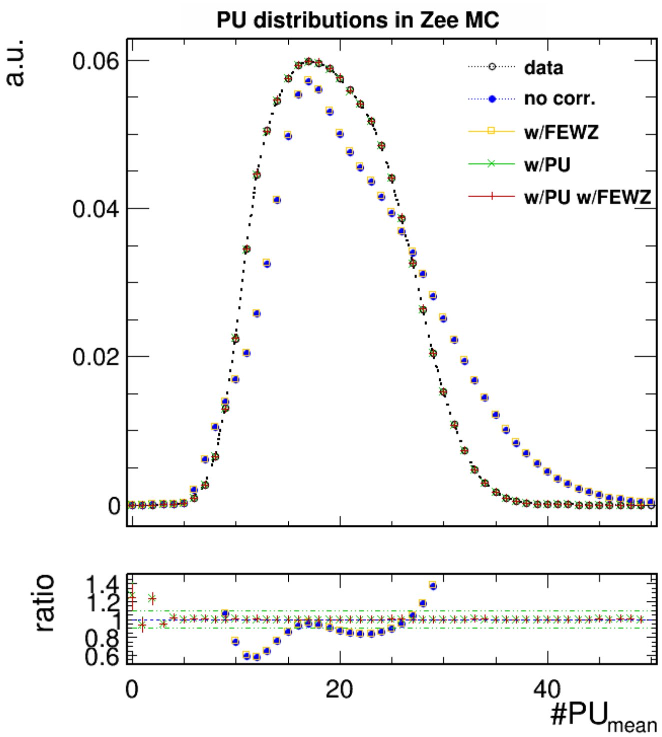

Figure B.1. The pileup distribution in 8 TeV data and MC simulated with S10 scenario.

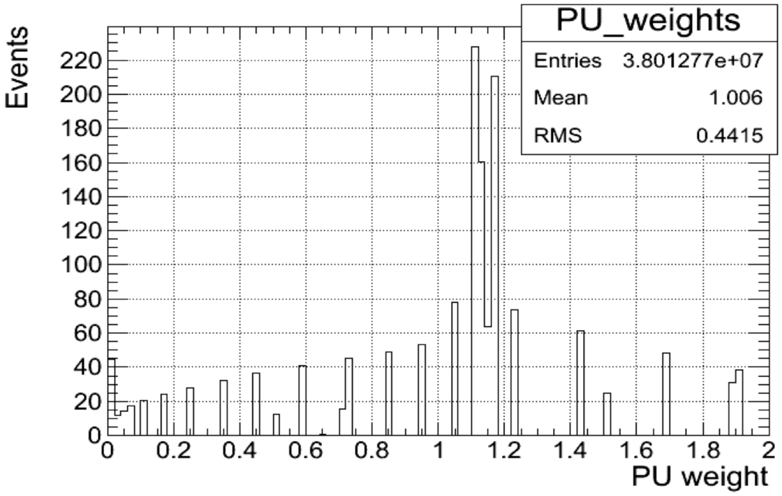

Figure B.2. The average pileup weight distribution in signal MC at 8 TeV.

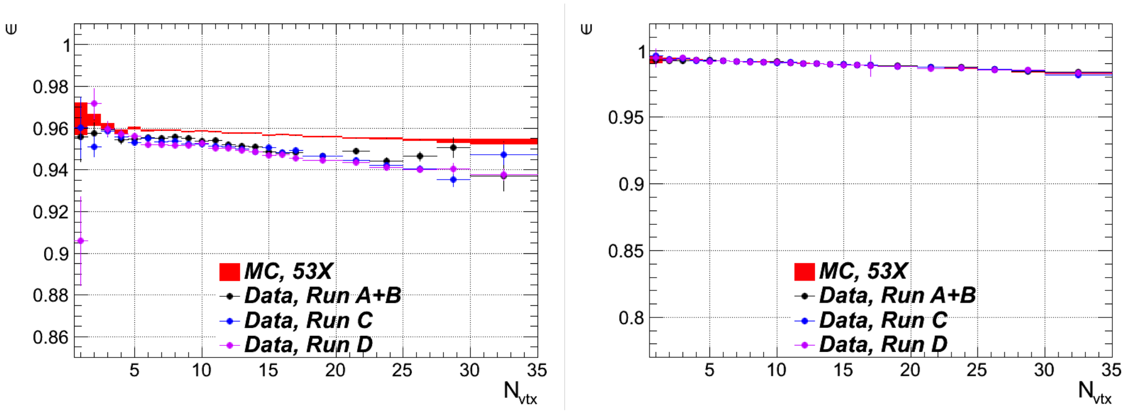

Figure B.3. The muon reconstruction and identification, and muon isolation efficiencies (from left to right) as a function of the number of reconstructed primary vertexes in an event.

as compared to 18 interactions at 8 TeV) affecting primarily the electron isolation efficiency (up to 5% effect) and leading to the effect on the muon isolation efficiency of less than 1%.

C. DATA AND MONTE CARLO SAMPLES

C.1 Data and Monte Carlo Samples

The measurements of the differential and double-differential cross sections reported are based on data recorded in 2012 with the CMS detector at the LHC at $\sqrt{s} = 8\,\mathrm{TeV}$, corresponding to an integrated luminosity of $19.7\,\mathrm{fb}^{-1}$ in both the dielectron and dimuon channels. For the double ratio calculations, the $\sqrt{s} = 7\,\mathrm{TeV}$ data set recorded in 2011 corresponding to an integrated luminosity of $4.5\,\mathrm{fb}^{-1}$ (dimuon) and $4.8\,\mathrm{fb}^{-1}$ (dielectron) is used. Tables C.1 and C.2 summarize the details of the data samples.

Table C.1
Details of the 7 TeV datasets.

Run	Dataset	Run range
A	/DoubleMu/Run2011A-May10ReReco-v1/AOD	160404-163869
A	/DoubleMu/Run2011A-PromptReco-v4/AOD	165071-166922
A	/DoubleMu/Run2011A-05Aug2011-v1/AOD	170053-172619
A	/DoubleMu/Run2011A-PromptReco-v6/AOD	172620-175770
B	/DoubleMu/Run2011B-PromptReco-v1/AOD	175832-180296
A	/SingleMu/Run2011A-08Nov2011-v1/AOD	160404-173692
B	/SingleMu/Run2011B-19Nov2011-v1/AOD	178420-180296

The dilepton datasets used for most of the analysis steps. Single muon datasets are used for the efficiency estimation purposes only. MuEG and SinglePhoton primary datasets are used for the fake-lepton background estimates.

Table C.2
Details of the 8 TeV datasets.

Run	Dataset	Run range
A	/DoubleMu/Run2012A-22Jan2013-v1/AOD	190645-193621
A	/DoubleElectron/Run2012A-22Jan2013-v1/AOD	
B	/DoubleMuParked/Run2012B-22Jan2013-v1/AOD	193834-196531
B	/DoubleElectron/Run2012B-22Jan2013-v1/AOD	
C	/DoubleMuParked/Run2012C-22Jan2013-v1/AOD	198049-203742
C	/DoubleElectron/Run2012C-22Jan2013-v1/AOD	
D	/DoubleMuParked/Run2012D-22Jan2013-v1/AOD	203777-208686
D	/DoubleElectron/Run2012D-22Jan2013-v1/AOD	
A	/SingleMu/Run2012A-22Jan2013-v1/AOD	190645-193621
B	/SingleMu/Run2012B-22Jan2013-v1/AOD	193834-196531
C	/SingleMu/Run2012C-22Jan2013-v1/AOD	198049-203742
D	/SingleMu/Run2012D-22Jan2013-v1/AOD	203777-208686
A	/MuEG/Run2012A-22Jan2013-v1/AOD	
B	/MuEG/Run2012B-22Jan2013-v1/AOD	
C	/MuEG/Run2012C-22Jan2013-v1/AOD	
D	/MuEG/Run2012D-22Jan2013-v1/AOD	
A	/Photon/Run2012A-22Jan2013-v1/AOD	
B	/SinglePhoton/Run2012B-22Jan2013-v1/AOD	
C	/SinglePhoton/Run2012C-22Jan2013-v1/AOD	
D	/SinglePhotonParked/Run2012D-22Jan2013-v1/AOD	

The measurement relies on the official JSON files. Only the luminosity sections certified as having all the CMS sub-detectors functioning are used for the measurement.

Monte Carlo (MC) samples are used in the analysis for determining efficiencies, acceptances, and for the determination of systematic errors. Data-driven methods are applied to determine efficiency correction factors and backgrounds. Although we partially rely on MC in data-driven methods, the purpose of applying such techniques is not to depend on the precise agreement between data and MC. MC event samples have been generated using a variety of generators. All MC samples are processed with the full CMS detector simulation based on GEANT4 [108] and include trigger simulation and the full chain of CMS event reconstruction.

The Drell–Yan signal samples are generated with the NLO generator POWHEG interfaced with the PYTHIA V6.4.24 [109] parton-shower generator (referred to as the POWHEG MC). Both $t\bar{t}$ decays to jet final states and single top samples are produced with the MADGRAPH generator [110] at leading order (LO). The tau decays and inclusive $t\bar{t}$ samples were performed with TAUOLA generator [111]. The $t\bar{t}$ sample is re-scaled to the NLO cross section of 263.1 pb. Diboson samples (WW/WZ/ZZ) were produced with a combination of MADGRAPH and TAUOLA generators, and QCD background events are produced with PYTHIA. The proton structure is defined using the CT10 [82] parton distribution functions. All samples are generated using the PYTHIA Z2 tune [112] to model the underlying event.

Pileup effects are taken into account in MC samples which are generated with the inclusion of multiple proton-proton interactions (average of 18 interactions per bunch crossing) that have timing and multiplicity distributions similar to those expected in data.

The POWHEG MC is based on NLO calculations and a correction is added to take NNLO effects into account (see Appendix C). The NNLO effects alter the cross section as a function of the dilepton kinematic variables and are important in the low-mass region and in renormalizing the cross section.

D. KINEMATICS REWEIGHTING

D.1 Kinematics Reweighting

The Powheg is a dedicated parton-level generator [113]. By design, it allows to include higher-order QCD corrections in the calculation. Including the NNLO QCD effects is, however, computationally expensive provided that a large statistics sample is required for an accurate measurement. Therefore, the Powheg MC sample is generated based on NLO and an additional correction is further applied to take the NNLO effects into account. It is essential to promote the simulated signal samples to NNLO in order to properly describe the low-mass region ($m < 40\,\mathrm{GeV}$).

The correction is determined from the ratio between the double-differential cross sections (binned in rapidity and P_{T}) calculated at NNLO with Fewz [81] and at NLO with the Powheg MC. For a given mass range it is defined in bins of dilepton rapidity y and dilepton transverse momentum P_{T}:

$$\omega(P_{\mathrm{T}}, y) = \frac{(d^2\sigma/dP_{\mathrm{T}}dy)_{\mathrm{FEWZ}}}{(d^2\sigma/dP_{\mathrm{T}}dy)_{\mathrm{POWHEG}}} \tag{D.1}$$

Below, the NNLO kinematics correction procedure of the signal MC is described.

The NNLO kinematics correction factors are first derived in the bins of dilepton P_{T} and rapidity. The distribution in rapidity is rather monotonous and does not require a lot of bins, therefore, the P_{T} binning optimization is the most important.

The P_{T} binning is optimized taking into account the shape of the k-factor distribution as a function of dilepton transverse momentum in a given mass region. Fig. D.1-D.4 show the P_{T} dependencies of the k-factors in various mass ranges.

As seen, at low mass the k-factor grows significantly with transverse momentum suggesting that a large number of bins should be used.

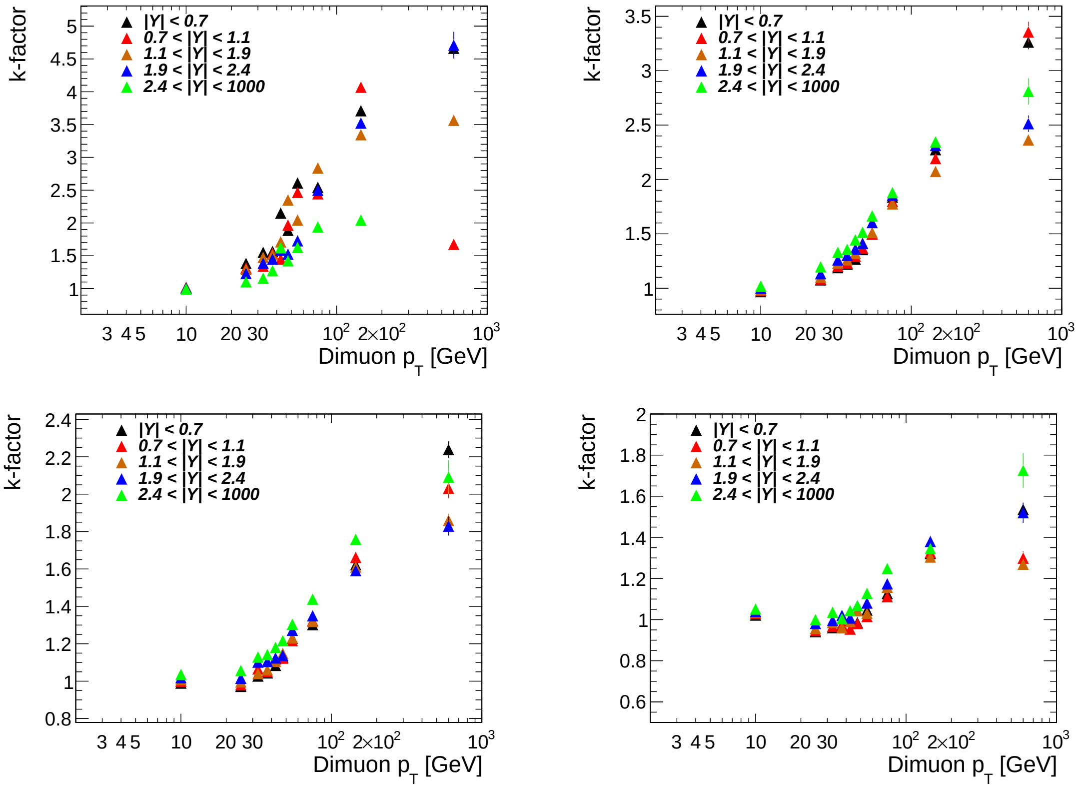

Figure D.1. The NNLO/NLO k-factor as a function of dilepton P_{T}. From top left to bottom right: 15–20 GeV, 20–30 GeV, 30–45 GeV, and 45–60 GeV mass regions.

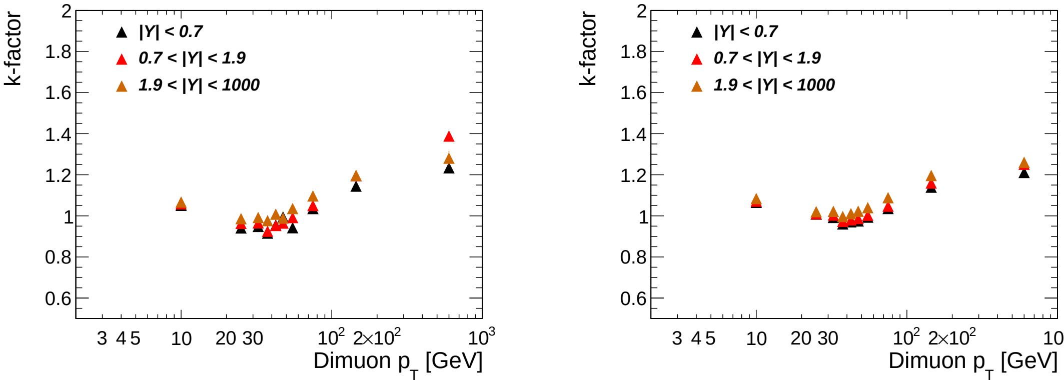

Figure D.2. The NNLO/NLO k-factor as a function of dilepton P_{T}. From top left to bottom right: 60–72 GeV, 72–106 GeV mass region.

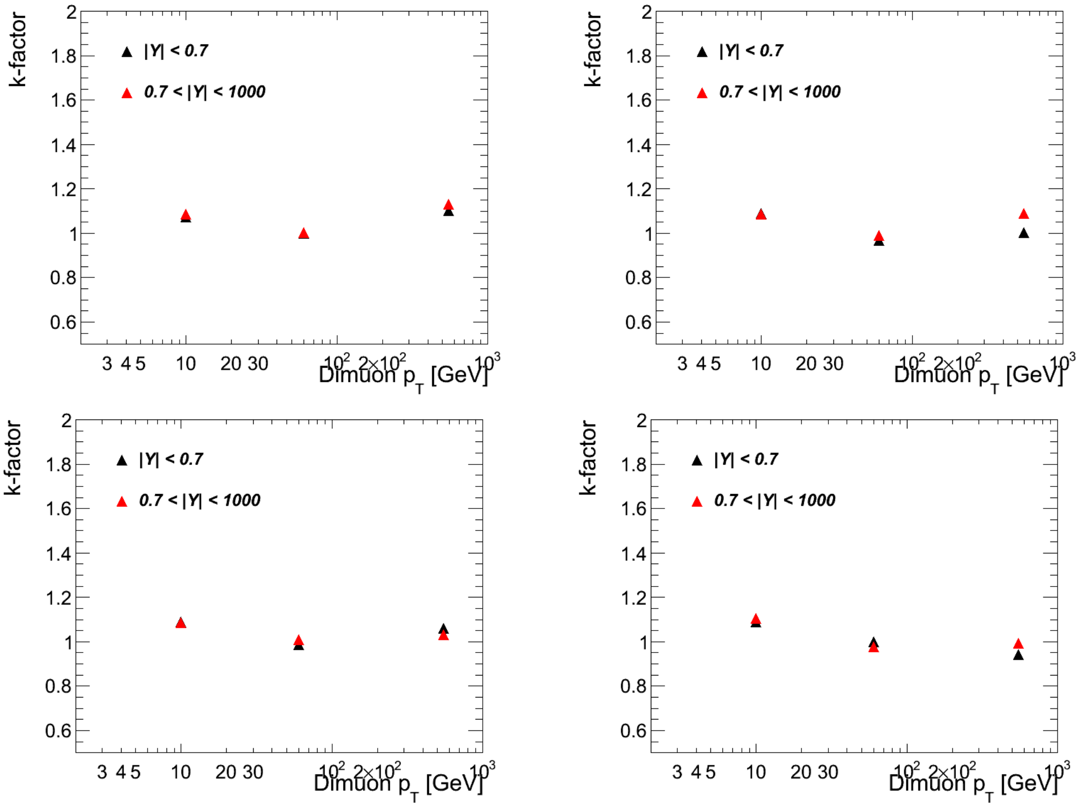

Figure D.3. The NNLO/NLO k-factor as a function of dilepton P_{T}. From top left to bottom right: 106–120 GeV, 120–133 GeV, 133–150 GeV, and 150–171 GeV mass regions.

In the Z peak region, the distribution flattens and becomes nearly independent on P_{T} at high mass. Based on that, following binning was suggested:

- 15 – 64 GeV mass region

  $|y|$: 0, 0.7, 1.1, 1.9, 2.4, 1000.0

  P_{T}: 0, 20, 30, 35, 40, 45, 50, 60, 90, 200, 1000 GeV

- 64 – 106 GeV mass region

  $|y|$: 0, 0.7, 1.9, 1000.0

  P_{T}: 0, 20, 30, 35, 40, 45, 50, 60, 90, 200, 1000 GeV

- Mass greater than 120 GeV

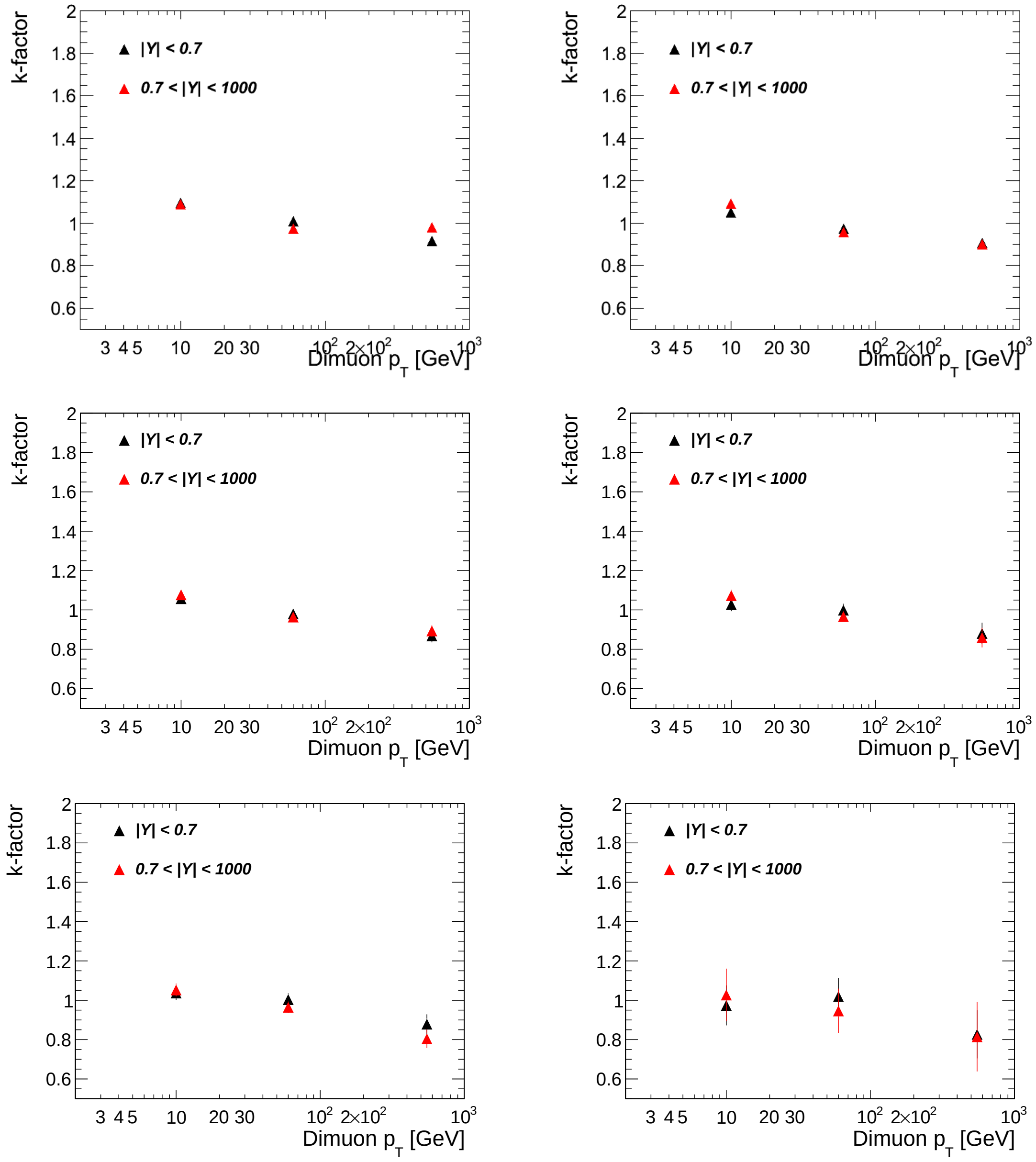

Figure D.4. The NNLO/NLO k-factor as a function of dilepton P_{T}. From top left to bottom right: 171–200 GeV, 200–400 GeV, 400–510 GeV, 510–600 GeV, 600–1000 GeV, and 1000–1500 GeV mass regions.

$|y|$: 0, 0.7, 1000.0

P_{T}: 0, 20, 100, 1000 GeV

D.2 Validation

A set of tests was performed to validate and assert the correctness of the reweighting procedure, focusing primarily on the binning, normalization and the residual differences between the mass spectra before and after the reweighting.

The absolute cross section calculated with FEWZ is compared to the signal MC truth pre-FSR cross section after reweighting. It is clear, that after reweighting we should obtain the absolute cross section equal to that from FEWZ by construction, and the only deviations would be possible due to binning effects, MC statistics and FEWZ integration precision. One can expect binning effect to become negligible if an infinitesimally fine binning in P_T and rapidity is used, provided the statistics in MC is infinitely large. Fig. D.5 shows the absolute cross section calculated with FEWZ compared to the signal MC truth pre-FSR cross section after reweighting. As seen, the agreement is very good.

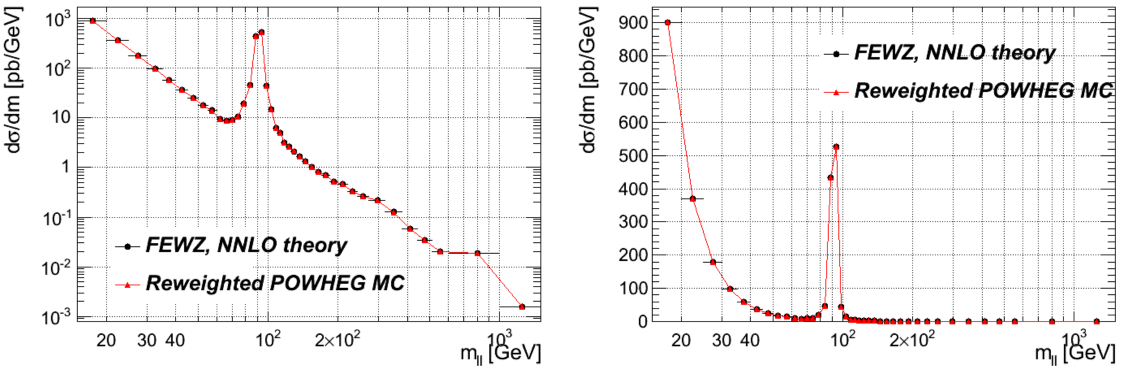

Figure D.5. The absolute cross section calculated with FEWZ compared to the signal MC truth pre-FSR cross section after reweighting, left plot: logarithmic scale on y axis, right plot: linear scale on y axis.

The ratio of absolute cross sections calculated with POWHEG and FEWZ before and after the NNLO kinematics reweighting is shown in Fig. D.6. As seen, the ratio of POWHEG after the NNLO kinematics reweighting and FEWZ absolute cross sections is in agreement within errors.

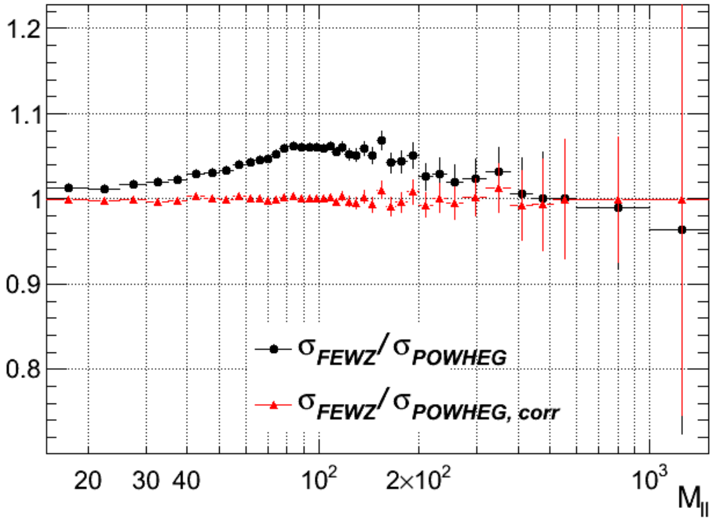

Figure D.6. The ratio of absolute cross sections calculated with Powheg and Fewz before and after the NNLO kinematics reweighting applied to the Powheg MC sample.

The modeling error, reflecting a residual disagreement between the MC truth pre-FSR quantities after reweighting and Fewz quantities, is evaluated as relative difference between the pre-FSR Fewz corrected acceptances calculated with Fewz and Powheg:

$$\frac{\delta A}{A} = \left|\frac{A^{\text{Powheg}}_{\text{NNLO}} - A^{\text{FEWZ}}}{A^{\text{Powheg}}_{\text{NNLO}}}\right| \tag{D.2}$$

Fig. D.7 shows the modeling error as a function of dilepton invariant mass. As seen, due to a smart choice of the binning it was possible to reduce the modeling error down to 2% at low mass, around 0.1% in the peak region and within 1% at high mass.

With the nominal binning considered, we expect an average weight distribution to have a mean value consistent with the k-factor obtained with single bin calculation within errors. The RMS is an estimator of the magnitude of a varying quantity. In our case, the weight is not a random variable, however it is subject to random noise (due to limited statistics in Fewz and MC). Thus, RMS would not go to zero even if statistics was infinite (both in Fewz and MC). RMS in this case is an estimator for two effects: (1) P_{T} dependency of the k-factor (systematic effect) (2) statistics

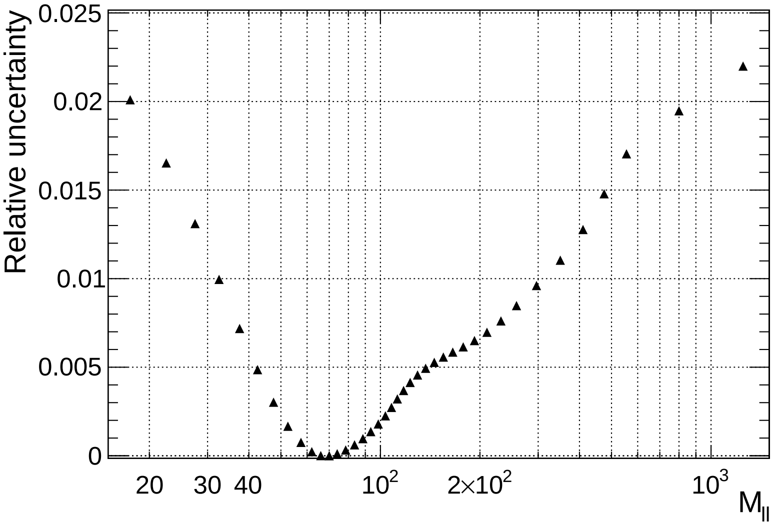

Figure D.7. The modeling error as a function of dilepton invariant mass at 8 TeV.

in MC sample (random Gaussian effect). Note, the *k*-factor is defined as the ratio of NNLO QCD, NLO EW to NLO QCD, NLO EW cross sections, where the EW correction include the weak contribution, but do not include any QED (FSR, ISR and interference-type terms) or photon induced contributions.

E. BACKGROUND ESTIMATION

E.1 Background Estimation Methods

A combination of techniques is used to determine contributions from various background processes. Wherever feasible, the background rates are estimated from data, reducing the uncertainties related to simulation of these sources.

E.1.1 True Dilepton Backgrounds

Non-QCD backgrounds in both the dimuon and dielectron channels are estimated using the data-driven e μ method. The relationship between the number of estimated l^+l^- ($\mu^+\mu^-$ or $\mathrm{e}^+\mathrm{e}^-$) and observed e μ events can be expressed as:

$$N^{ll}_{\mathrm{est}} = N^{\mathrm{e}\mu}_{\mathrm{obs}}/N^{\mathrm{e}\mu}_{\mathrm{MC}} \cdot N^{ll}_{\mathrm{MC}} \tag{E.1}$$

where $N^{\mathrm{e}\mu}_{\mathrm{MC}}$ includes decay channels that can lead to both the eμ and l^+l^- final states: $t\bar{t}$, tW, WW, WZ, ZZ, and the Z $\rightarrow \tau^+\tau^-$. The expected fraction of events decaying to eμ and l^+l^- is 2, but in realistic conditions (e.g. proton collision at the LHC) some deviations are observed because of leptons from QCD (15-40 GeV) and final state radiation effect (40–60 GeV).

Below 40 GeV, leptons in jets arise primarily from semileptonic decays of heavy quarks. It is difficult to model this background process using Monte Carlo because the trigger and Drell–Yan selection efficiency is very low. Nevertheless, events of that type remain in both the eμ and dilepton samples after the selection.

Any possible excess of the observed same-sign eμ and l^+l^- yields over those calculated for electroweak background sources must be due to decays of b-quarks. The expected heavy flavor background in the opposite-sign dilepton sample can be estimated from the following ratio:

$$N^{l^\pm l^\pm} = \frac{N^{l^+l^+} + N^{l^-l^-}}{R}. \tag{E.2}$$

The constant, R, can be calculated from the time-integrated b mixing probability, which represents the fraction of events in which one b-quark forms a neutral B-meson, oscillates to its anti-particle state and decays, while the $\overline{\mathrm{b}}$-antiquark in the event decays in its original flavor state.

To validate the correctness of the method the closure test was performed on MC events.

Fig. E.1 shows the results of the closure tests in the bins of mass and mass-rapidity.

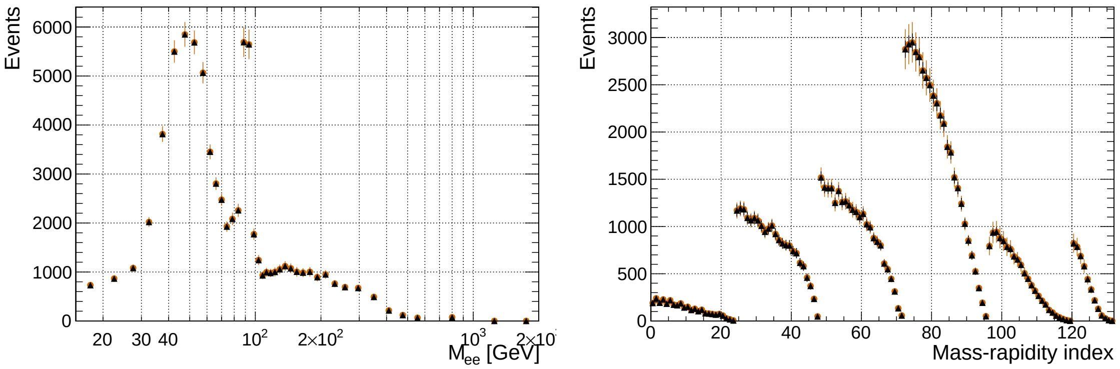

Figure E.1. Total non-QCD background as estimated from MC and as predicted by the data-driven eμ method applied to MC (closure test). Left: estimated in the bins of invariant mass, right: estimated in the invariant mass-rapidity bins.

As seen, there is a perfect agreement in the closure test validating the correctness of the method.

Fig. E.2 shows the non-QCD background in the bins of invariant mass as predicted with the data-driven eμ method and as estimated with MC. Fig. E.3 shows the non-QCD background in the bins of invariant mass-rapidity (2D) as predicted with the data-driven eμ method and as estimated with MC.

As seen, the results agree well within the uncertainties. With the data-driven technique, we assign the systematic uncertainty based on two sources:

- Poissonian statistical uncertainty of predicted backgrounds (which is treated as systematic),

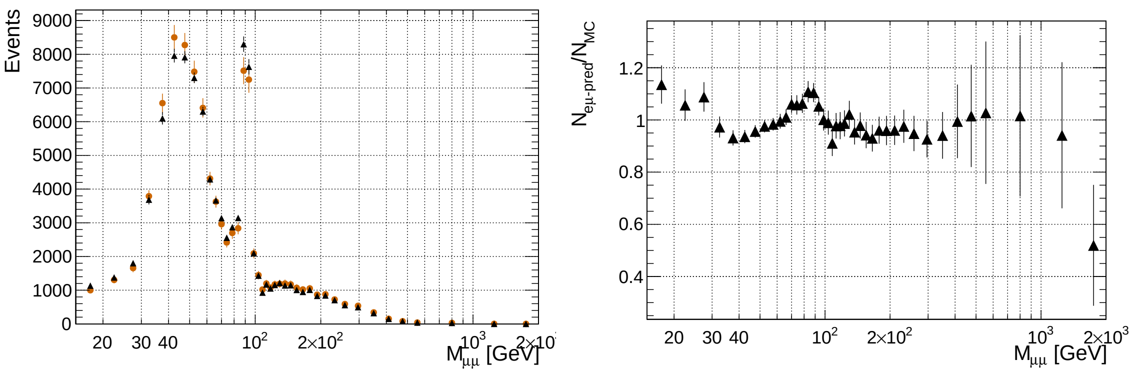

Figure E.2. Total non-QCD background in the bins of invariant mass as estimated from MC and as predicted by the data-driven eμ method. The bottom pad shows the corresponding ratio with associated errors. The vertical error bars include the total statistical and systematic uncertainties. The ratio plot includes the total uncertainty on the data-driven and MC based estimates combined in quadrature assuming no correlations.

- Deviation of the data-driven prediction from the arithmetic mean (N_{average}) of the data-driven prediction and corresponding MC expectation.

The resulting uncertainty is a combination of these two sources in quadrature:

$$\frac{\delta N_{\text{bg}}}{N_{\text{u}}} = \sqrt{(\frac{(N_{\text{data driven}} - N_{\text{average}})}{N_{\text{u}}})^2 + (\frac{\sqrt{N_{\text{data driven}}}}{N_{\text{u}}})^2}. \tag{E.3}$$

here, $N_{\text{data driven}}$ denotes the data-driven background prediction. In case of a MC based estimation, the systematic uncertainty on the background estimation consists of two components:

- Poissonian statistical uncertainty from the MC sample (which is treated as systematic),
- Systematic uncertainty due to the knowledge of the theoretical cross section,

the two components are combined in quadrature:

$$\delta N^{\text{bg}}/N_{\text{u}} = \sqrt{(\delta\sigma_{\text{theor}})^2 + (\frac{\sqrt{N_{\text{MC}}}}{N_{\text{u}}})^2}. \tag{E.4}$$

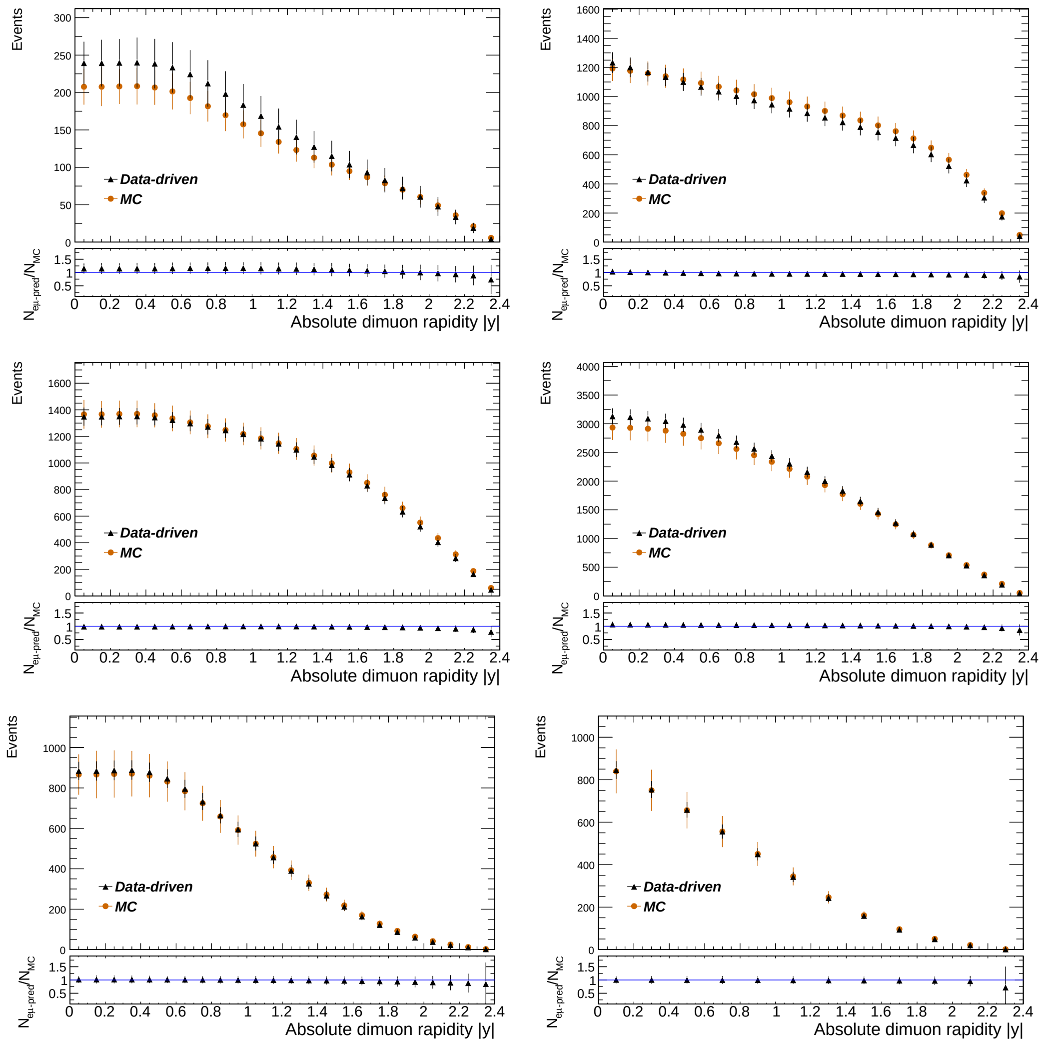

Figure E.3. Total non-QCD background in the bins of invariant mass-rapidity as estimated from MC and as predicted by the data-driven eμ method. The vertical error bars include the total statistical and systematic uncertainties. The ratio plots include the total uncertainty on the data-driven and MC based estimates combined in quadrature assuming no correlations.

where N_{MC} is the MC based background estimate. MC samples are very limited in statistics at high mass so the corresponding statistical uncertainty is very large. Therefore, this method provides a very conservative systematic uncertainty estimation. The uncertainty from data-driven estimated is smaller than the MC based estimated in majority of the mass-rapidity bins.

E.1.2 Fake Lepton Backgrounds

In addition to the true dilepton events from electroweak processes, there are events in which reconstructed objects are falsely identified as electrons or muons. These can be QCD multijet events where two jets pass the lepton selection criteria or W+jets events where the W boson decays to a lepton and a neutrino, and a jet is misidentified as a lepton.

Fake muon background estimation with ABCD method

The QCD background in the dimuon channel is evaluated using a data-driven technique. The method uses both the muon isolation and the sign of the charge as two independent discriminant variables to identify a signal region and three background regions in the two dimensional muon charge sign-isolation feature space. The background estimate is then based on the ratio between the number of events in the different regions [90].

Fig. E.4 shows two dimensional plots for the variables of the ABCD method, muon isolation on the x axis and the sign of the dimuon candidate on the y axis. The left plot is for QCD background and the right plot is for DY POWHEG signal. As shown, region A is a signal region and the most of the signal events are in the region (minimal contribution in region B, C and D). QCD has a significant contribution in regions C and D, therefore using the ratio of A and B and the ratio of C and D in QCD, we can reduce the QCD contamination in region A. We use the data sample to determine events in region B, C and D. A small correction is applied to correct the correlation between variables and take into account signal contamination.

Fake electron background estimation with fake rates method

The QCD background in the dielectron channel is evaluated using a data-driven technique. The probability for a reconstructed object to pass the requirements of an electromagnetic trigger and to be falsely reconstructed as an electron is determined from a specially selected sample of these objects. This sample of events is taken

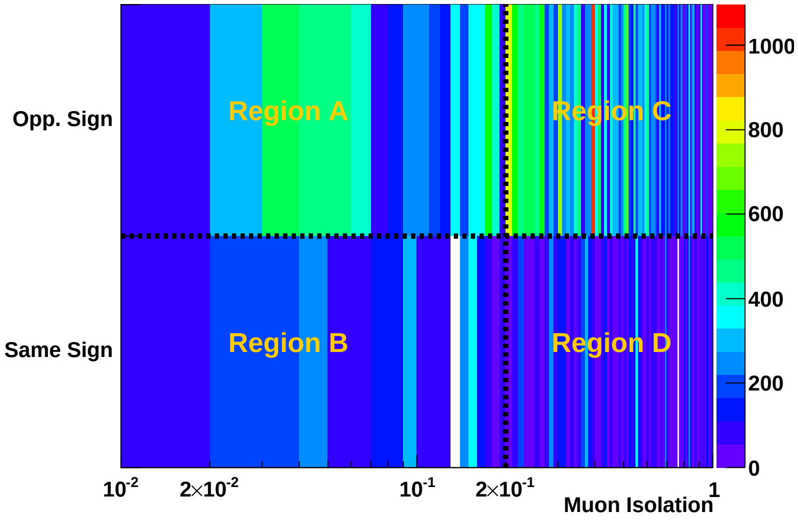

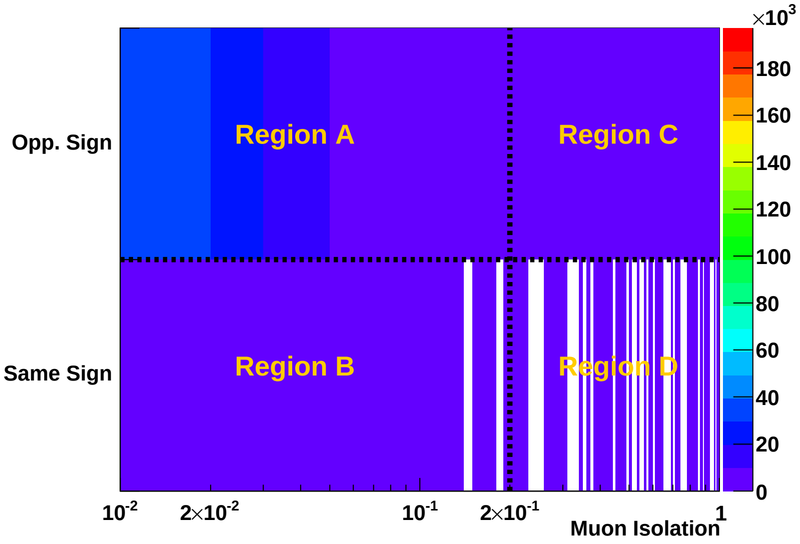

Figure E.4. Two dimensional plot for the variables of ABCD method in QCD (top) and DY Powheg (bottom).

from the same double-electron trigger used to select Drell–Yan events, but with the number of real electrons significantly reduced. To identify the background from real electrons events, only events with two electron candidates are selected. If one electron candidate passes the full electron selection or the invariant mass of the pair of electron candidates is greater than 150 GeV, the event is rejected. This significantly reduces the background from real Drell–Yan events. The remaining background from Drell–Yan, $t\bar{t}$ and real dielectron events is then subtracted using Monte Carlo. Using this sample of events the probability of an object being misidentified as an electron is measured as a function of object E_T and absolute pseudorapidity $|\eta|$.

The number of $\mathrm{e}^+\mathrm{e}^-$ background events is then determined from a sample of events collected with the double-electron trigger in which at least one electron candidate fails the full electron selection of the analysis. The events from this sample are assigned weights based on the expected misidentification probability for the failing electron candidates, and the sum of the weights yields the prediction for the background from this source. Since events in this double-electron trigger sample with at least one electron failing the full selection contain a fraction of genuine dielectron events, the contribution of the latter is subtracted using simulation.

The expected shapes and the relative yields of dielectron events from data and simulation in bins of invariant mass are shown in Fig. E.5 in the same format as the dimuon channel. The genuine electron background is largest in high-mass regions, where it reaches up to 15–20% of the observed yields due to $t\bar{t}$ events. At the lowest masses, the genuine electron background level, which is dominated by the DY → $\tau^+\tau^-$ contribution, becomes significant at ~50 GeV, where it ranges up to 10%. In other mass ranges the genuine electron background is typically a few percent and, in particular, it is very small (less than 0.5%) in the Z peak region. The background associated with falsely identified electrons is relatively small in the full mass range.

E.1.3 Photon Induced Background

The lepton pair production in $\gamma\gamma$-initiated processes, where both initial-state protons radiate a photon, is significant at high and low masses, outside the Z peak region. The contribution from this channel is treated as an irreducible background, and is estimated with Fewz and the NNPDF2.3QED PDF set.

The multiplicative correction to the in-acceptance cross section is estimated as:

$$\sigma_{\text{DY, meas}} = \sigma_{\text{DY, th}}/\sigma_{\text{DY+PI, th}} \cdot \sigma_{\text{DY+PI, meas}}, \tag{E.5}$$

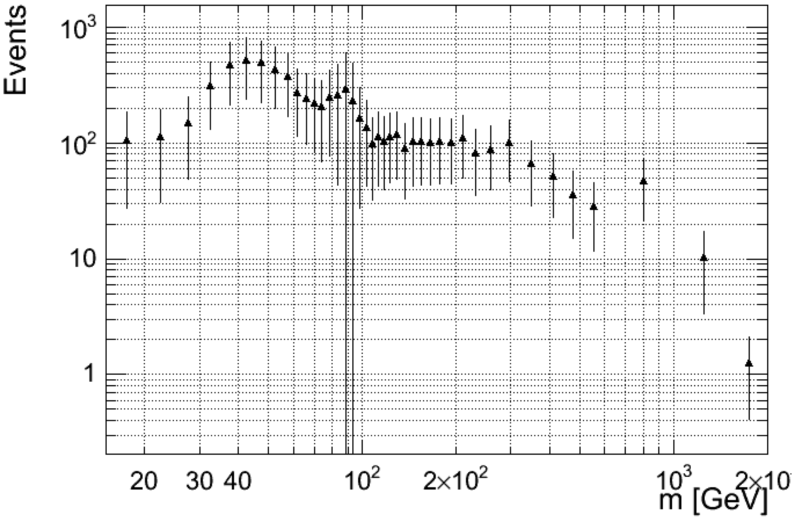

Figure E.5. The estimated dielectron fake electron background invariant mass spectra. Estimated using the measured rate of fake electron production.

and is applied bin-by-bin to the measured cross section.

It is essential to apply a multiplicative correction rather than additive as the cross section is corrected for PI background before the acceptance correction. Thus, applying the acceptance correction derived from DY only, would properly correct the DY component of the observed yields while strongly under-correcting the photon induced (PI) component.

Fig. E.6-E.7 show the contribution of the photon induced background in bins of mass and rapidity.

The contribution in the 20–30 GeV bin is not shown as it is negligible. As seen, the effect of the photon-induced background on the 1D result is up to 40% increasing with mass. The effect on the 2D result is up to 8%, decreasing with rapidity, consistent with the 1D calculation.

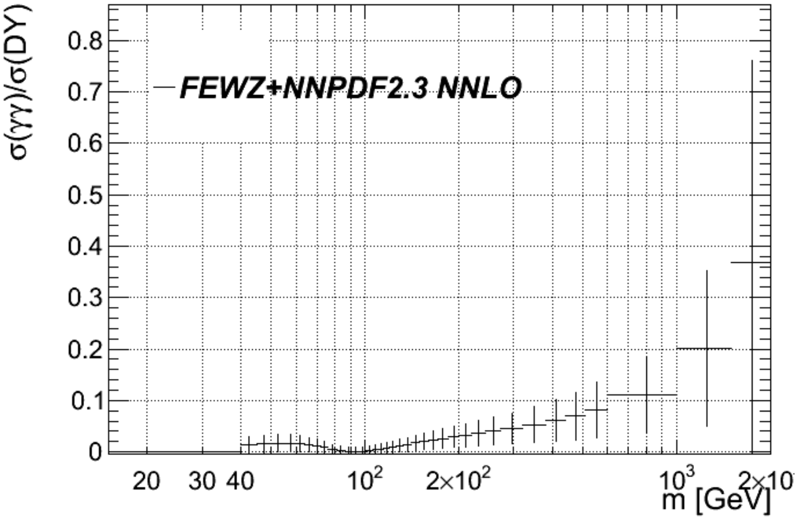

Figure E.6. The ratio of the cross section of $\gamma\gamma$-initiated processes to the measured Drell–Yan cross section in bins of mass estimated with Fewz and NNPDF2.3QED PDF set.

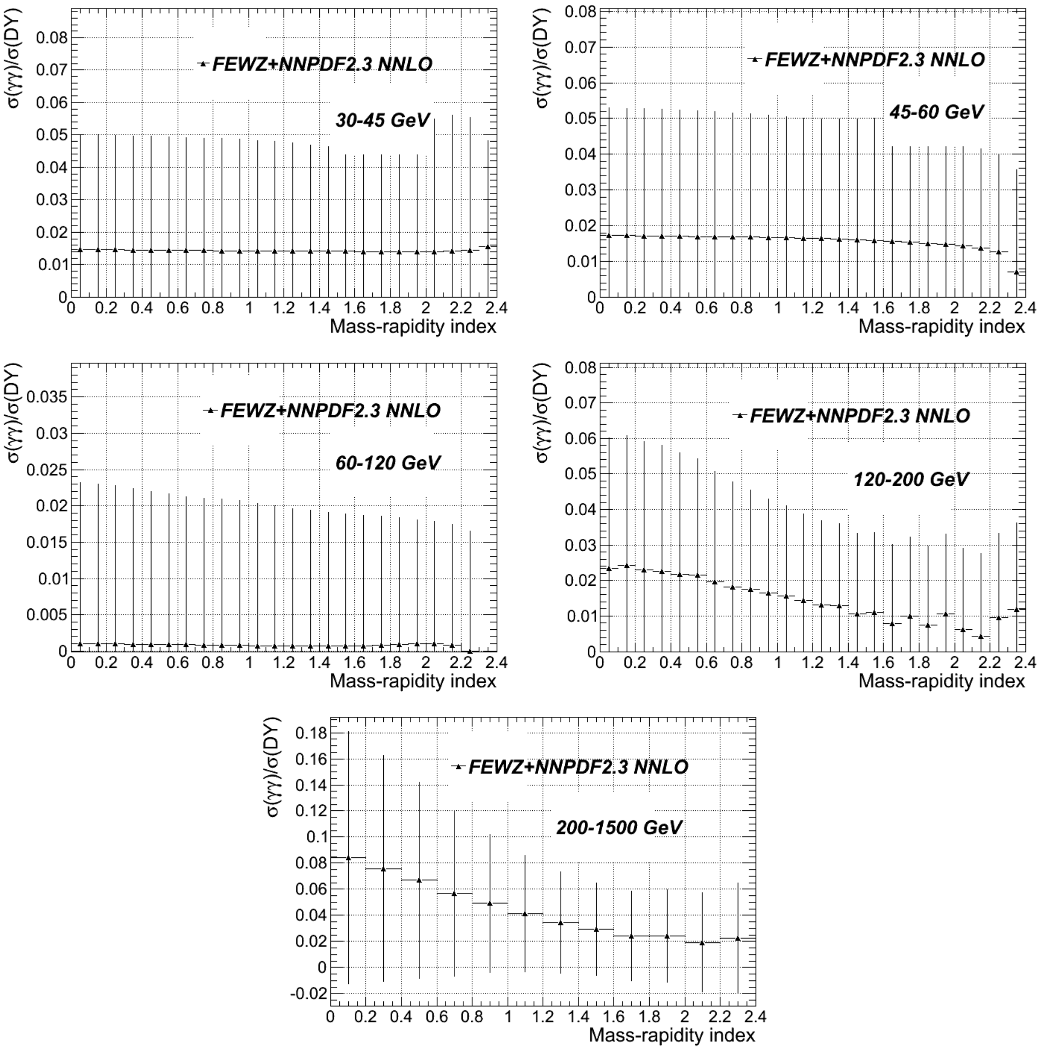

Figure E.7. The ratio of the cross section of $\gamma\gamma$-initiated processes to the measured Drell–Yan cross section in bins of mass-rapidity as estimated with FEWZ and NNPDF2.3QED PDF set. The vertical error bar includes the statistical and the PDF systematic uncertainty. The statistical uncertainty is negligible.

F. DATA-DRIVEN EFFICIENCY CORRECTIONS

F.1 Data-driven Efficiency Corrections

The event efficiency from simulation is corrected by an efficiency scale factor ρ, which takes into account differences between data and simulation. The procedures outlined below are used to extract the efficiency corrections for both the $d\sigma/dm$ and the $d^2\sigma/dmd|y|$ cross section measurements in the dielectron and dimuon channels.

The scale factor ρ reflects both the single-lepton and the dilepton selections. The single-lepton properties (including the trigger) are determined using $\mathrm{Z} \to l^+l^-$ events in data and simulation, where one lepton, the tag, satisfies the tight selection requirements, and the selection criteria are applied to the other lepton as a probe (tag-and-probe method [90]). An event sample with a single-lepton trigger (the tag) is used to evaluate this scale factor. A simultaneous fit to the invariant mass spectra for passing and failing probes in both dielectron and dimuon channels is performed using identical signal shape and appropriate background shapes; the efficiency is then computed from the normalizations of the signal shapes in the two spectra.

The total event selection efficiency in the dimuon channel is factorized in the following way:

$$\varepsilon = \varepsilon_{\text{reco+id}} \cdot \varepsilon_{\text{iso}} \cdot \varepsilon_{\text{trig}}, \tag{F.1}$$

and in the following way in the dielectron channel:

$$\varepsilon = \varepsilon_{\text{reco}} \cdot \varepsilon_{\text{id+iso}} \cdot \varepsilon_{\text{trig}}, \tag{F.2}$$

see [19] for more details on the factorization.

Both dielectron and dimuon analyses use double-lepton triggers with asymmetric p_{T} selections for each leg and, therefore, the efficiency for a lepton to trigger the high-p_{T} leg (leg 1) is different from the efficiency for a lepton to trigger the low-p_{T} leg (leg 2). We define single-leg efficiencies where $\varepsilon(l, \text{trig1})$ is the efficiency of a lepton selected offline to be matched to one leg of the double-lepton trigger, and $\varepsilon(l, \mathrm{trig2})$ is the efficiency of a lepton selected offline to be matched to the other leg of the double-lepton trigger. The efficiency factor $\varepsilon(l, \mathrm{trig1})$ corresponds to a lepton matched to the leg of the double-lepton trigger that has the higher p_{T} threshold. The double-lepton trigger efficiency can then be factorized with single-lepton trigger efficiencies in the following way, which takes into account the different efficiencies for the two legs:

$$\begin{aligned}\varepsilon(\mathrm{event}, \mathrm{trig}) &= 1 - P(\mathrm{one\ leg}, \mathrm{failed}) - P(\mathrm{two\ legs}, \mathrm{failed}) \\ &= \varepsilon(l_1, \mathrm{trig1}) \cdot \varepsilon(l_2, \mathrm{trig2}) + \varepsilon(l_1, \mathrm{trig2}) \cdot \varepsilon(l_2, \mathrm{trig1}) \\ &- \varepsilon(l_1, \mathrm{trig1}) \cdot \varepsilon(l_2, \mathrm{trig1}),\end{aligned} \tag{F.3}$$

where

- $P(\mathrm{one\ leg}, \mathrm{failed})$ is the probability that exactly one lepton fails to trigger a leg, i.e. $\varepsilon(l_1, \mathrm{trig1}) \cdot (1 - \varepsilon(l_2, \mathrm{trig2})) + \varepsilon(l_2, \mathrm{trig1}) \cdot (1 - \varepsilon(l_1, \mathrm{trig2}))$;
- $P(\mathrm{two\ legs}, \mathrm{failed})$ is the probability that both leptons fail to trigger a leg, i.e. $(1 - \varepsilon(l_1, \mathrm{trig1})) \cdot (1 - \varepsilon(l_2, \mathrm{trig1}))$.

For MC, counting is appropriate efficiency estimation technique for all the efficiency types as there is no background. For data, fitting technique is essential to estimate the number of probes in the kinematic regions where background is significant. It is particularly important for the reconstruction, identification and isolation efficiencies. The counting is sufficient for trigger efficiency calculation in data because after the full selection, even before trigger matching of the probe, the sample of Z bosons is very clean. The background in this case is less than 10% in both dielectron and dimuon channels, and even that background comes primarily from events with true dileptons (such as WW/WZ/ZZ), $t\bar{t}$ or $\mathrm{Z} \to \tau^+\tau^-$).

Fitting approach is used to estimate all the individual efficiencies in data and simulated samples in the dimuon channel. In the dielectron channel, a combined approach is invoked as summarized in Tab. F.1. The mass range for both the count and fit techniques is taken from 60 to 120 GeV.

Table F.1

Techniques used to find the pass and fail counts in the tag and probe method in the dielectron channel.

Efficiency type	data	MC
ϵ_{reco}	fit	count
ϵ_{id}	fit	count
ϵ_{HLT}	count	count

F.1.1 Details on the Fit Hypothesis

The fit hypothesis is optimized to model the signal and background shapes. A combination of a Voigtian and a Crystal Ball fit functions is used to model the signal shape in the dimuon case. The motivation to use the Crystal Ball function is to properly take the FSR effect into account. As a result of FSR, the peak shape becomes asymmetric at the low-mass side. For the background, comparisons between exponential and Chebychev quadratic polynomial probability density functions were performed. It was observed, that the background shapes were significantly different depending on the value of the probe transverse momentum (which is defined by the signal and background content). For the background, a combination of the exponential and Chebychev quadratic polynomial fit functions is used. The former is used at low p_{T} up to 20 GeV and the latter is used for $p_{\mathrm{T}} > 20$ GeV region.

In the dielectron channel, the signal for both pass and fail categories is modeled by a template extracted from signal MC for the corresponding kinematics and selection. The template is smeared by convoluting with a Gaussian resolution function because MC does not model resolution perfectly. The parameters of the Gaussian smearing (mean and width) are free parameters of the model. The background probability density function is an exponential.

The goodness of the fit was evaluated using the pulls, comparing the data and the model probability density functions. The pull is calculated as:

$$\text{Pull} = \frac{N_{\text{data}} - N_{\text{model}}}{\sigma_{\text{model}}} \tag{F.4}$$

The comparison of the one-leg trigger (Mu8) efficiencies as a function of probe p_{T} obtained using the various model probability density functions is illustrated in Fig. F.1.

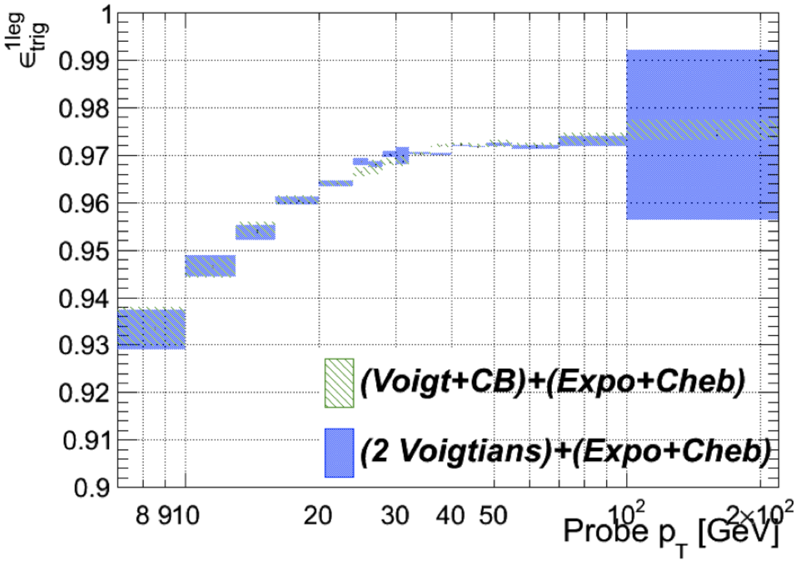

Figure F.1. The one-leg trigger efficiency as a function of probe p_{T} extracted with optimum fit hypotheses: double Voigtian signal and exponential or Chebychev background, a combination of a Voigtian and a Crystal Ball signal and exponential or Chebychev background. Only central values with band showing the spread are shown.

As seen, negligible differences in the efficiency values are observed in most of the bins, except for a few bins in the region of 30–60 GeV. This region is expected to be affected by the FSR effect the most. Some difference in the error assignment is observed at high p_{T}.

F.1.2 Electron Efficiencies and Scale Factors

The electron efficiencies estimated using the tag-and-probe method are presented in Fig. F.2-F.5. The approach is described in [20] in a greater detail. The electron E_{T}

regions are subdivided into 6 regions by values 10, 15, 20, 30, 40, 50, and 500 GeV. Here we used a modified binning in $|\eta|$. The 6 division points are 0., 0.8. 1.444, 1.566, 2.0, and 2.4. Lowering of the $|\eta|$ value for the last bin from 2.5 to 2.4 improved the efficiency in the last bin. This is due to the lower efficiency on the edge of the detector acceptance, as exemplified in

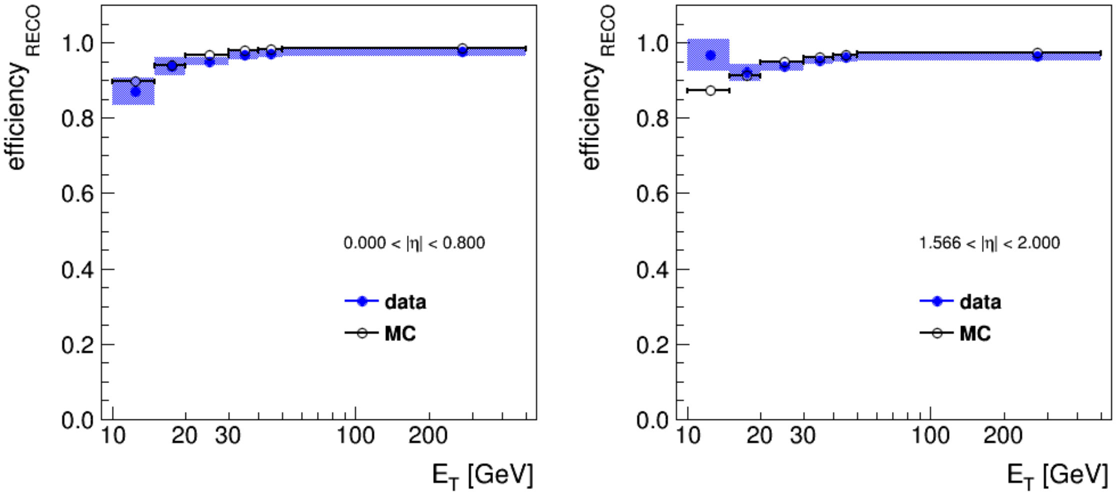

Figure F.2. Tag-and-probe electron reconstruction efficiencies.

Fig. F.6-F.7 show the electron event efficiency scale factors as a function of invariant mass and rapidity for reconstruction, identification and isolation, and trigger efficiencies.

F.1.3 Muon Efficiencies and Scale Factors

The muon efficiencies estimated using the tag-and-probe method in bins of probe muon p_T and η. The following p_T bin edges are used:

- Identification efficiency: 10, 17, 30, 40, 50, 70, 250, 1000 GeV
- Isolation efficiency: 10, 17, 22, 30, 40, 50, 65, 250, 1000 GeV
- Trigger efficiency: 10, 20, 25, 30, 40, 50, 65, 250, 1000 GeV

Following η bin edges are used:

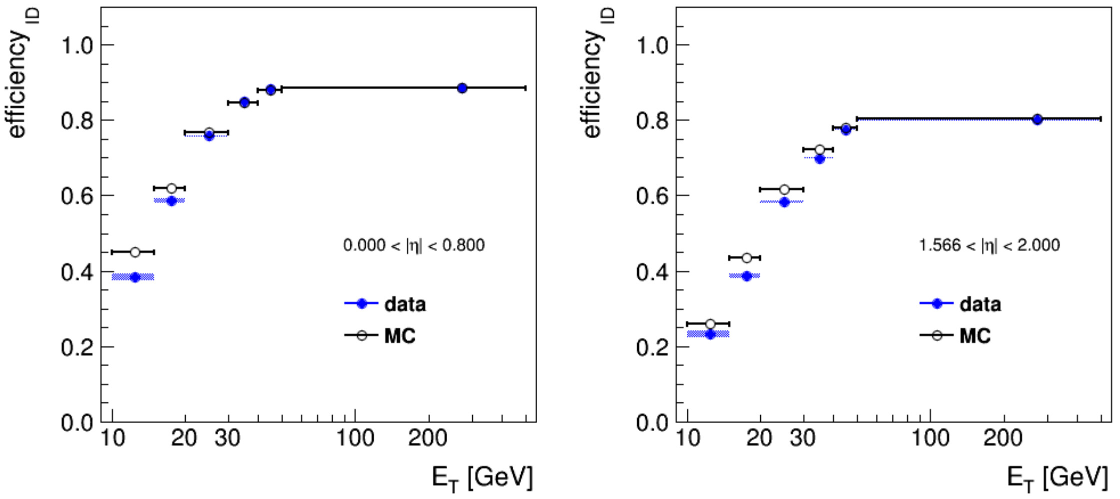

Figure F.3. Tag-and-probe electron identification efficiencies.

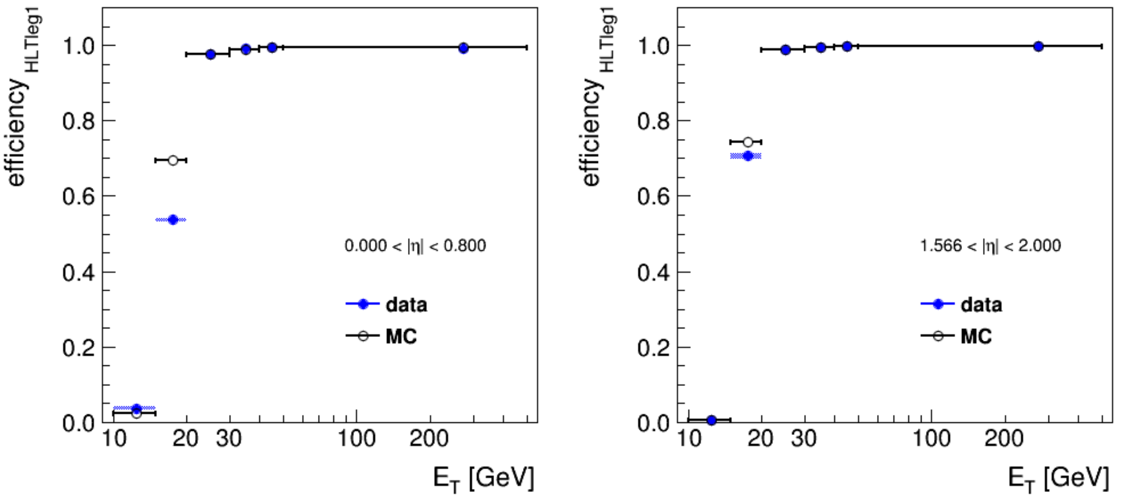

Figure F.4. Tag-and-probe electron HLT efficiencies of a higher-p_T leg.

- Identification efficiency: $-2.4, \; -2.1, \; -1.9, \; -1.5, \; -1.1, \; -0.9, \; -0.7, \; -0.5, \; -0.3, \; -0.1, \; 0.1, \; 0.3, \; 0.5, \; 0.7, \; 0.9, \; 1.1, \; 1.5, \; 1.9, \; 2.1, \; 2.4$

- Isolation, trigger efficiency: $-2.4, \; -2.1, \; -1.9, \; -1.7, \; -1.5, \; -1.1, \; -0.9, \; -0.7, \; -0.5, \; 0.5, \; 0.7, \; 0.9, \; 1.1, \; 1.5, \; 1.7, \; 1.9, \; 2.1, \; 2.4$

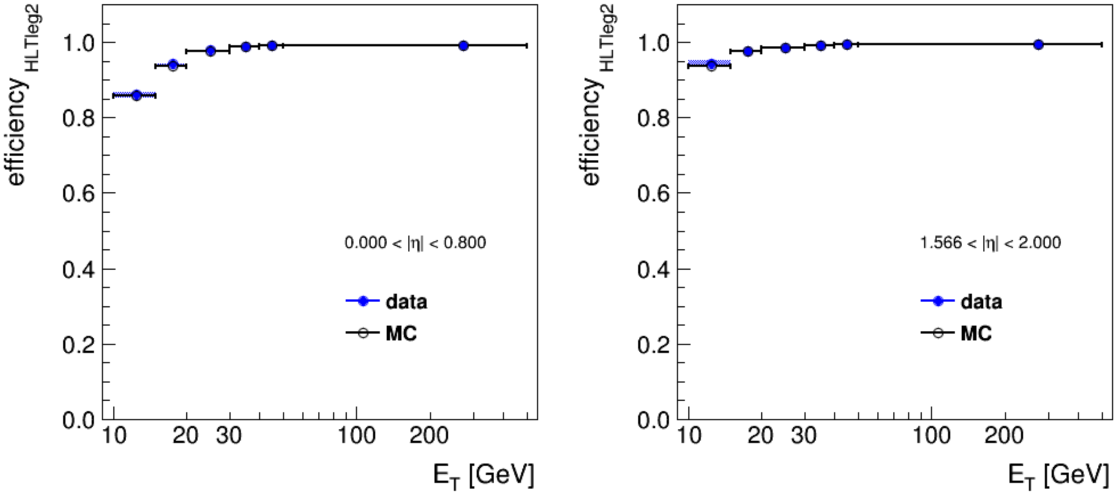

Figure F.5. Tag-and-probe electron HLT efficiencies of a lower-p_{T} leg.

Fig. F.8 shows the reconstruction and identification as a function of probe muon p_{T} and η for various data taking periods from data and simulation at 7 and 8 TeV. As seen, the efficiencies obtained on MC sample are generally larger than data. No significant run dependency is observed in the muon reconstruction and identification efficiencies. However, the efficiencies from 2012 run D are the smallest and the efficiencies from runs A+B are the largest with the spread of less than 0.5% between the two.

Fig. F.9 shows the reconstruction and identification as a function of probe muon p_{T} and η for various data taking periods from data and simulation at 7 and 8 TeV. The muon isolation efficiencies obtained on MC and data samples are generally very close, so a very small values of efficiency correction factors are expected. The turn on region in p_{T} is up to around 40 GeV, which is similar to the values observed in 2011 studies. No significant run dependency is observed in the muon isolation efficiencies in both data-taking periods.

Fig. F.10-F.11 shows the trigger efficiency as a function of probe muon p_{T} and η for various data taking periods from data and simulation at 7 and 8 TeV. In general, we observe a good agreement between the trigger efficiencies extracted from data and

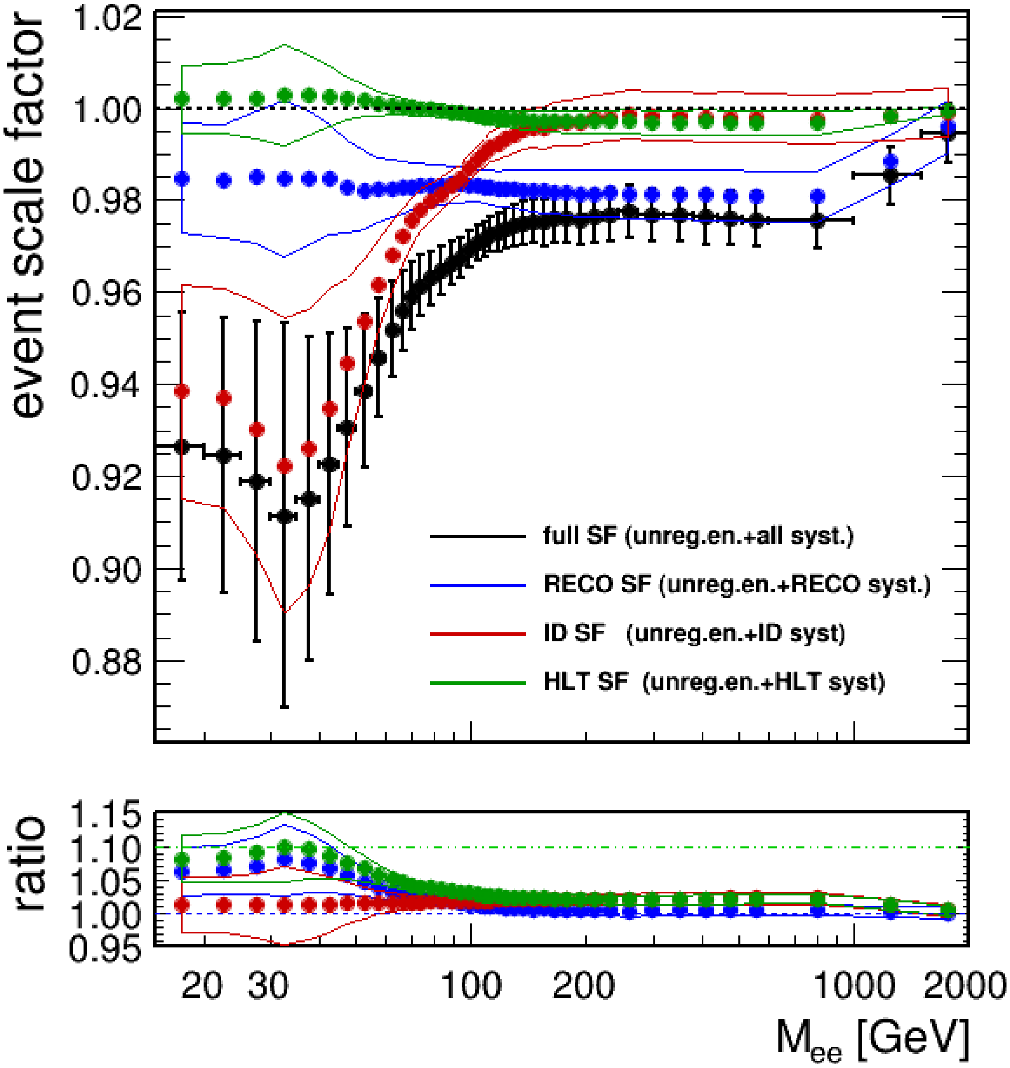

Figure F.6. The electron event efficiency scale factors in 1D for reconstruction, identification and isolation, and trigger efficiencies.

the signal MC sample. However, for the $Mu8$ trigger efficiency, the turn on curve has a different shape, having about 1% higher efficiencies at low p_{T} and lower efficiencies in the high p_{T} region for the data sample.

The muon trigger efficiencies obtained on MC are generally lower as compared to data. These deviations are more pronounced in the endcap region, increasing with

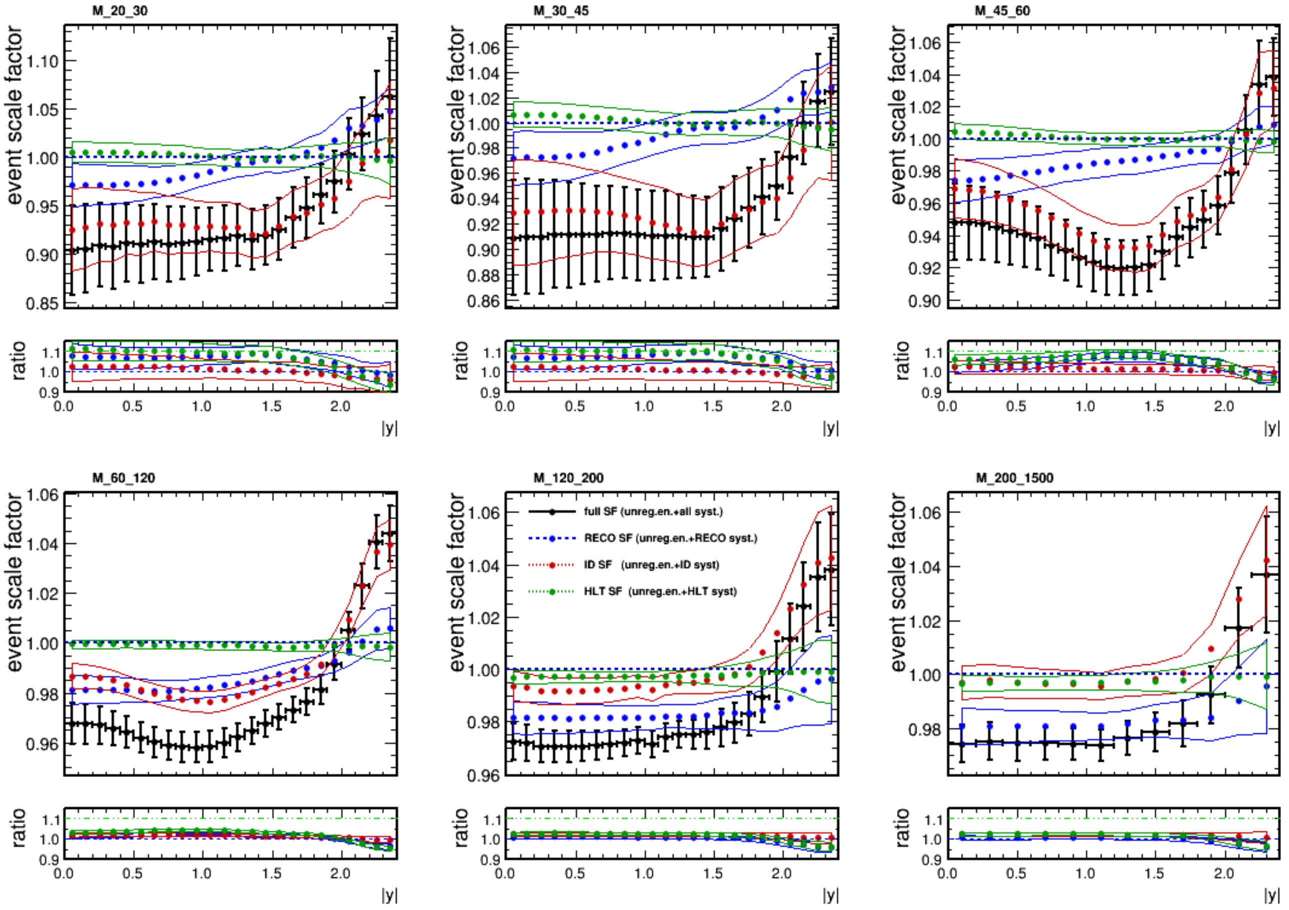

Figure F.7. The electron event efficiency scale factors in 2D for reconstruction, identification and isolation, and trigger efficiencies.

pseudorapidity. Therefore, large scaling factor is expected in the high dimuon rapidity region. No significant run dependency is observed in the muon trigger efficiencies.

In the dimuon channel, the size of the correction at low mass is the largest, reaching up to 6%. In the Z peak region and high-mass the efficiency correction is just about 2%.

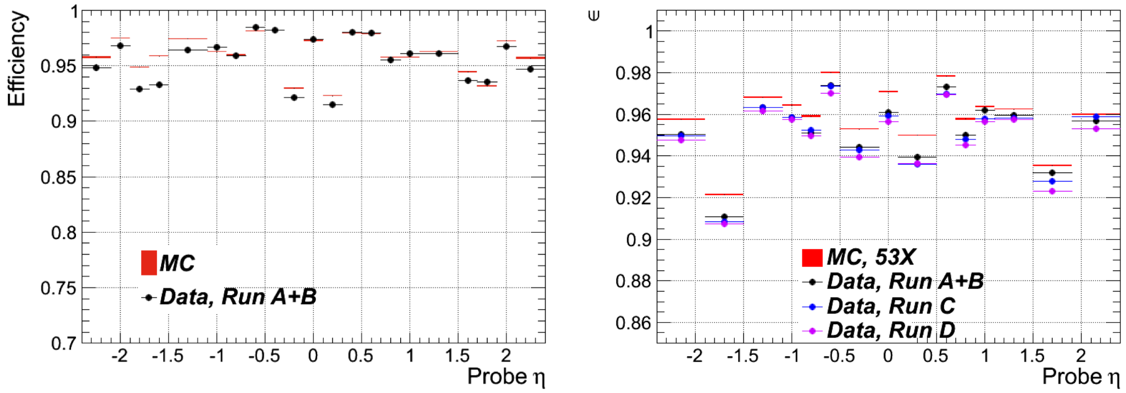

Figure F.8. Muon reconstruction and identification efficiencies as a function of probe muon η for various data taking periods, estimated with data-driven T&P method from 7 (left) and 8 TeV (right) data and simulation.

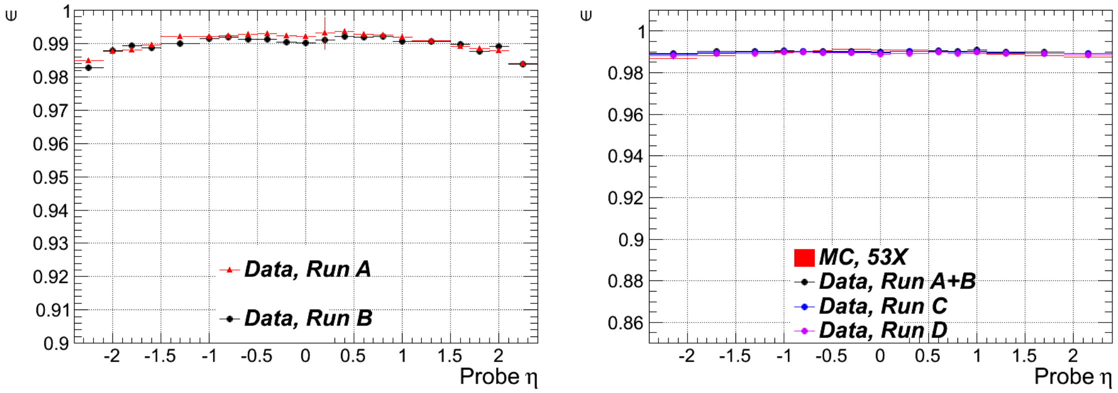

Figure F.9. Muon isolation efficiencies as a function of probe muon η for various data taking periods, estimated with data-driven T&P method from 7 (left) and 8 TeV (right) data and simulation.

F.1.4 Uncertainty in Efficiency Correction

Various sources of uncertainty affecting the efficiency correction estimation in the dimuon channel are evaluated. This includes the uncertainty in line shape modeling, uncertainty in binning of correction maps and other sources described below.

- *Uncertainty in line shape modeling.* This uncertainty is estimated by comparing two (or more) alternative fit hypotheses in the simultaneous maximum likeli-

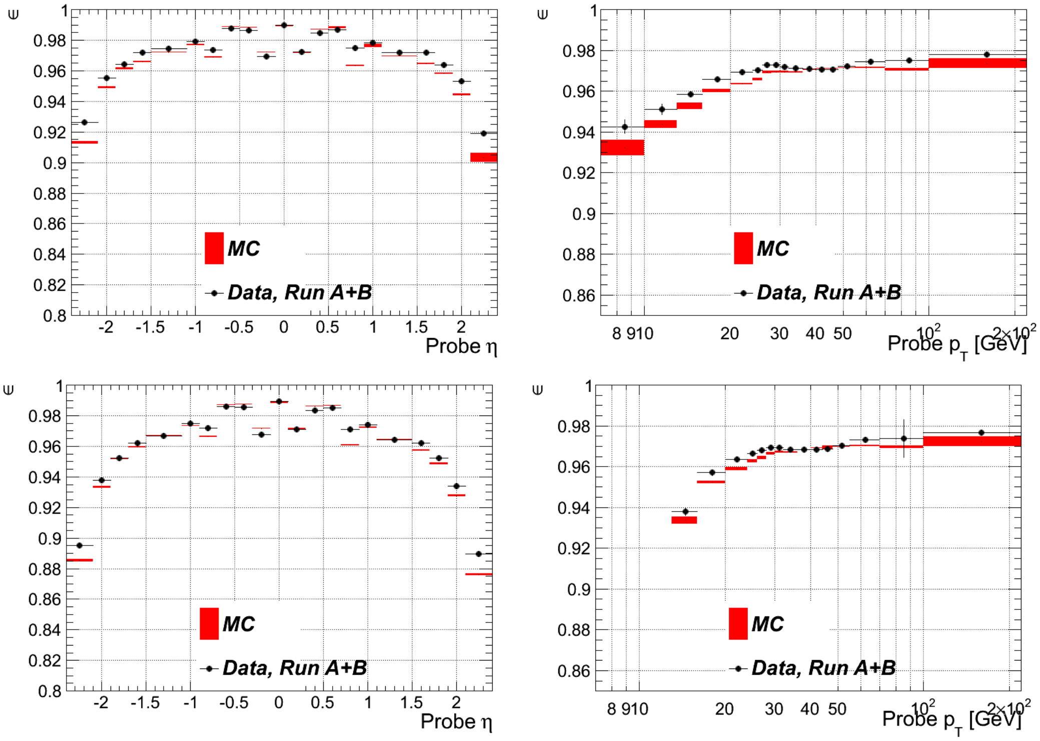

Figure F.10. Muon trigger efficiencies as a function of probe muon p_{T} and η for various data taking periods, estimated with data-driven T&P method from 7 TeV data and simulation. Top row: soft-leg efficiencies, bottom row: tight-leg efficiencies.

hood fit. The efficiencies extracted with 2 signal hypotheses: (1) double Voigtian and (2) combination of a Voigtian and a Crystal Ball fit function are compared. For the background, an exponential and a quadratic polynomial hypotheses are compared. This uncertainty is evaluated to be up to 1% for identification, up to 0.5% for isolation, and rather small for trigger: 0.2%, reaching its maximum in the low p_{T} bins. The Voigtian and Crystal Ball fit functions are chosen because they are better in describing the signal shape (especially in the tails of the peak distribution) than a Voigtian or a double Voigtian. The motivation to use the Crystal Ball function is to properly take the FSR effect into account. As a result of FSR, the peak shape becomes asymmetric at the low mass side. For the background, it is observed that the shapes are significantly different

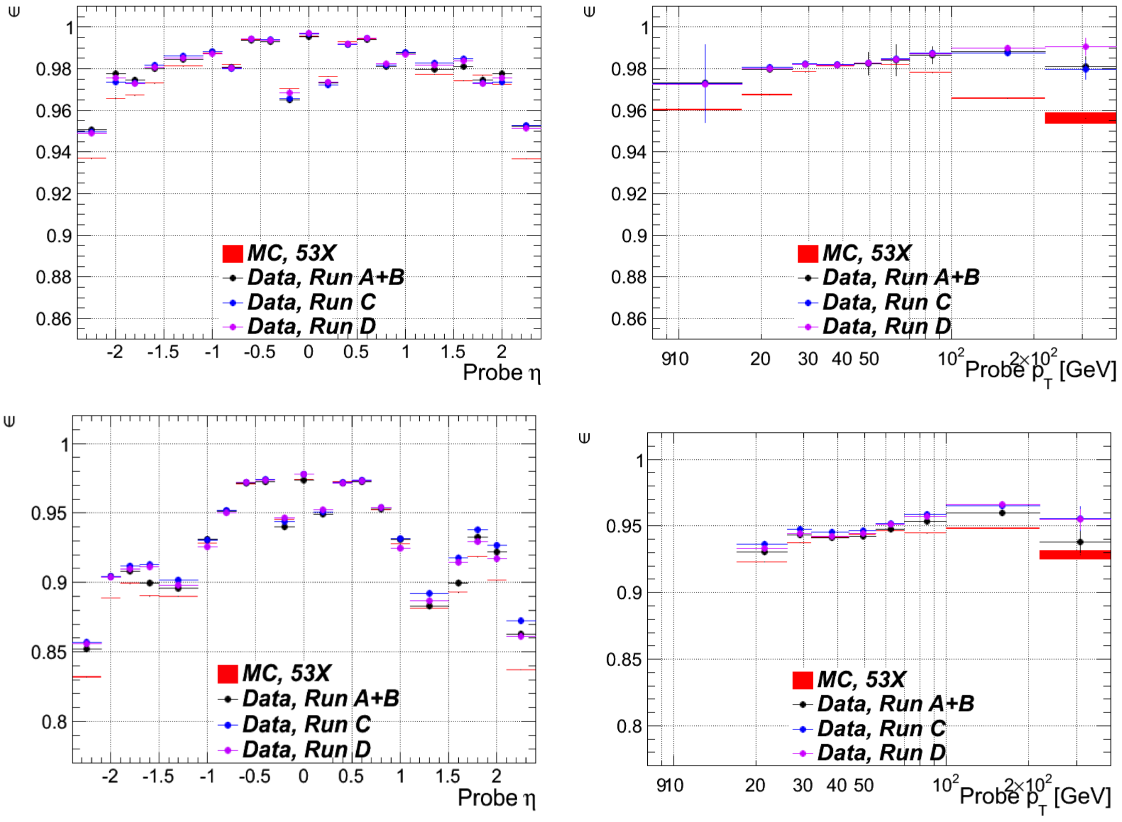

Figure F.11. Muon trigger efficiencies as a function of probe muon p_{T} and η for various data taking periods, estimated with data-driven T&P method from 8 TeV data and simulation. Top row: soft-leg efficiencies, bottom row: tight-leg efficiencies.

depending on the value of the probe transverse momentum. As a result, an exponential appears to perform better in the low-p_{T} region ($p_{\mathrm{T}} < 30\,\mathrm{GeV}$) and the Chebychev quadratic polynomial is better for higher p_{T}. See Appendix F for more details.

- *Uncertainty due to the binning of the correction maps in probe p_{T} and η.* Efficiency correction factors are applied to weight the MC events. Thus, averaging the correction factor can introduce a bias, especially in the bins of η since the muon identification efficiency is rapidly changing with η in the regions close to wheel gaps in the muon system. This source of uncertainty was also considered in [78], and is estimated there to be up to 1% for Z $\rightarrow \mu^+\mu^-$ (the corresponding effect is smaller if the binning is finer).

This uncertainty is evaluated by repeating the tag-and-probe efficiency scale factor estimation procedure with various bin choices (coarse and fine) and then repeating the reweighting procedure to propagate the weights to the MC yield. This uncertainty is evaluated to be within 0.5% for identification efficiency scale factors, and almost negligible for isolation (0.1%) and trigger efficiency scale factors (0.2%). The uncertainty is larger in the cases when one of the muons is in the η neighborhood of wheel gaps (the corresponding difference in efficiency values per eta bin may reach up to 3%). This source of uncertainty is weakly dependent on statistics.

- *Other sources of uncertainties.* Other sources of uncertainty in the efficiency correction factor, including pileup, dimuon candidate selection are considered. We assign a flat uncertainty of 0.3% for identification and 0.2% for the isolation and trigger efficiency scale factors to take these effects into account.

These uncertainties are evaluated by recomputing the final result multiple times using an ensemble of the single-muon efficiency maps where the entries are modified randomly within ±1 standard deviation of the combined statistical and systematic uncertainties in the $p_{\mathrm{T}} - \eta$ map bins. A hundred efficiency correction map replications are obtained with the map variation technique, and the MC yield with efficiency corrections applied as weights is calculated for each map replication. The root-mean-square (RMS) characterizing the spread of these yields is calculated per mass bin, and the value of RMS normalized to the number of replicas is used as an estimate for the corresponding uncertainty.

The contribution from the dimuon vertex selection is small because its efficiency scale factor is consistent with being constant; the statistical fluctuations are treated as systematic.

G. RESOLUTION UNFOLDING

The effect of detector resolution leads to a migration of events from bin i of the true invariant mass distribution to bin k of the reconstructed mass distribution. For a better comparison of observed dilepton spectra with theory, this effect of migration is corrected through unfolding. The procedure uses the yield distribution determined from simulation by mapping it onto the measured one to obtain the true distribution. The unfolding procedures for differential and double-differential cross section calculations are described below.

G.1 $d\sigma/dm$ Differential Cross Section Measurement

The true event count distribution $N_{T,i}$ is related to the observed reconstructed distribution $N_{obs,i}$ through:

$$N^{\text{data}}_{\text{obs},k} = \sum_i T_{ik} N^{\text{data}}_{T,i}, \tag{G.1}$$

where T_{ik} is the probability for event originating in the bin i to be found in the observed array in the bin k, and T is a square, nearly diagonal matrix with almost all the off-diagonal elements normally less than 0.1 as shown in Fig. G.1.

The elements of the T matrix are computed as

$$T_{ik} = \frac{N_{\text{obs},ik}}{N_{T,i}} \tag{G.2}$$

where the counts N come from a calibration Monte Carlo sample, $N_{\text{obs},ik}$ is the count of events originating in the true bin i and observed in the bin k, while the $N_{T,i}$ is the total number of events in the true bin i.

In the case when the histogram represents a spectrum of a physical observable, such as an invariant mass spectrum, with each bin corresponding to a range of invariant mass, it is possible that some observed events, or some true events, will be outside of the range of interest. In this case, overflow and underflow bins are added to both of the histograms, and the summation goes over $N + 2$ bins, where N is the number of bins defined for the Drell–Yan cross section measurement in the range from 15 GeV to 1500 GeV and two more bins for histogram underflow and overflow. The scheme itself remains unchanged. A few significant off-diagonal elements are located adjacent to the main diagonal. Both response matrices are invertible.

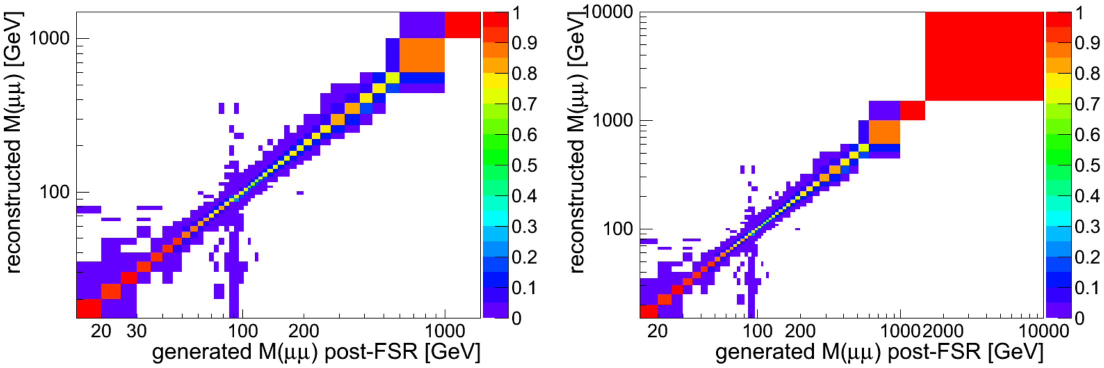

Figure G.1. The response matrices from simulation for $d\sigma/dm$ measurement. Left: NxN response matrix, right: $(N+2)$x$(N+2)$ response matrix with overflow and underflow bins included.

The validity of the unfolding method is tested on the pure signal MC (the closure test). The resulting unfolding yields are in perfect agreement with the true distribution for both the case with underflow and overflow bins included and without as shown in Fig. G.4. The underflow and overflow bins are included in both the response matrix and the true and measured invariant mass distributions.

The comparison of the unfolded observed yields to the true distribution are shown in Fig. G.3.

G.1.1 Alternative Unfolding Methods

The standard ROOT implementation of the Gauss-Jordan matrix inversion technique with full pivoting and including the underflow and overflow bins is used in the 7 TeV analysis. In the 8 TeV analysis, the calculations are performed using the iterative Bayesian approach [94] implemented in the RooUnfold package [114].

The validity of the unfolding method using the iterative Bayesian approach is also tested on the pure signal MC (closure test). The resulting unfolding yields are found

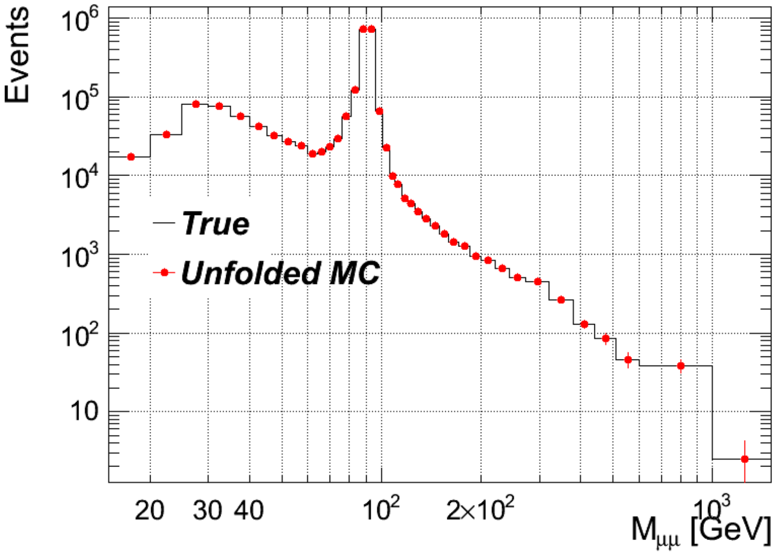

Figure G.2. The comparison of the unfolded yields from MC to the true distribution in bins of dimuon invariant mass (the closure test).

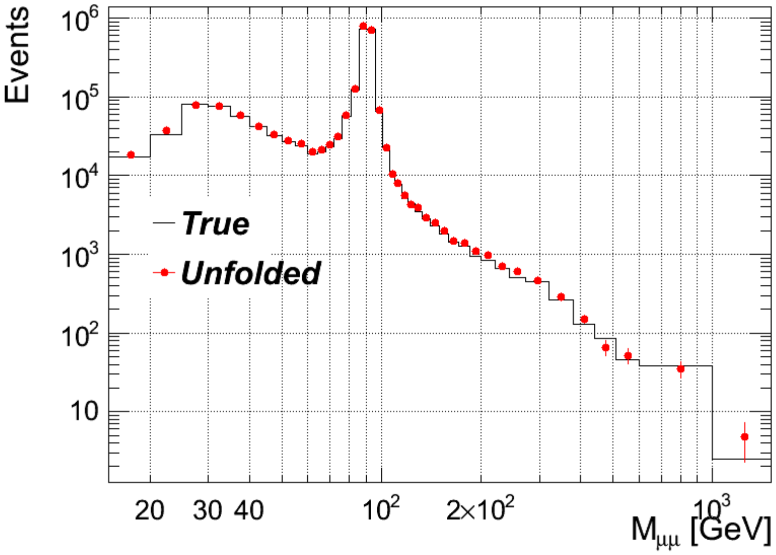

Figure G.3. The comparison of the observed yield after unfolding to the true distribution in bins of dimuon invariant mass.

in perfect agreement with the true distribution for both the case with underflow and overflow bins included and without as shown in Fig. G.4.

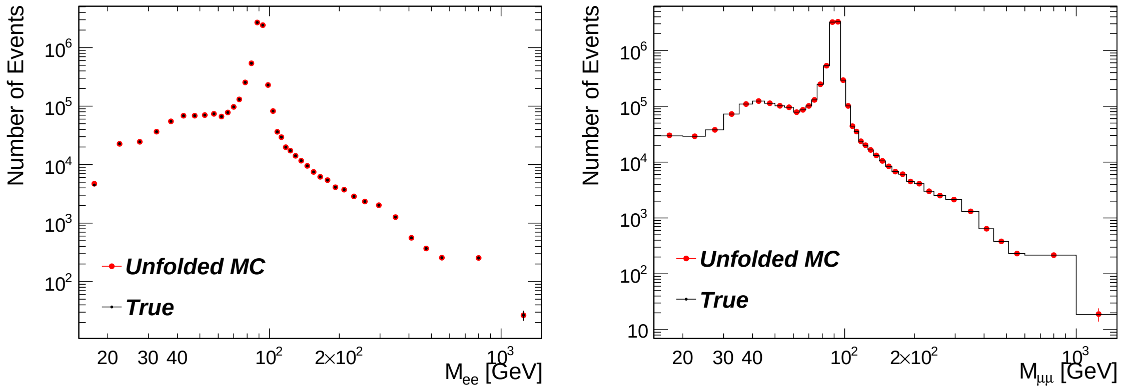

Figure G.4. The comparison of the unfolded yields from MC to the true distribution in bins of dilepton invariant mass (closure test). Dielectron channel (left) and the dimuon channel (right).

Fig. G.5 shows the comparison of the cross section calculated using the matrix inversion and the Bayesian iterative approach in the dielectron channel. As seen, the

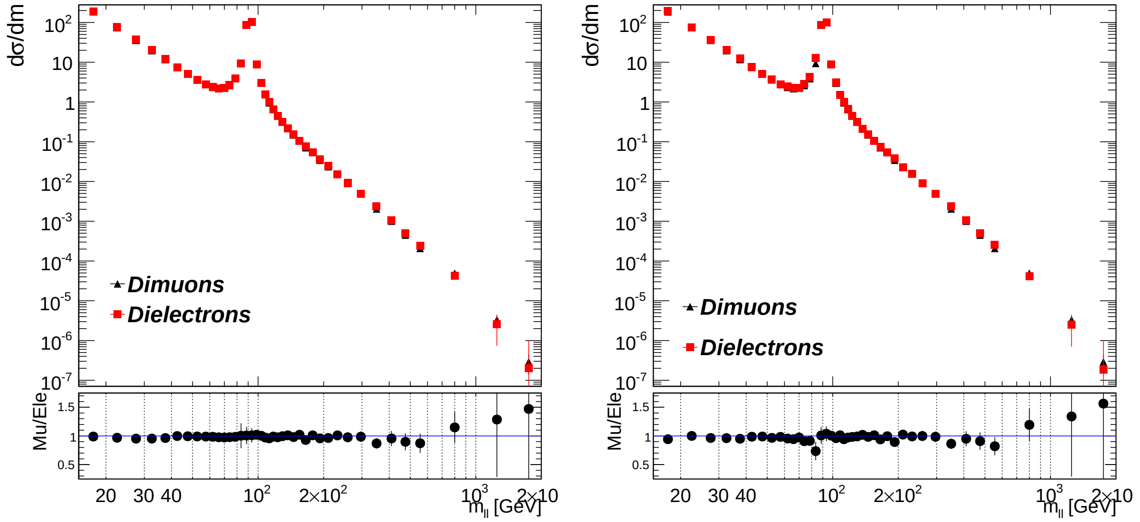

Figure G.5. The comparison of the cross sections in bins of dielectron invariant mass calculated at 8 TeV using two alternative unfolding techniques: matrix inversion with no regularization (right) and the Bayesian iterative technique (left).

effect the difference is rather large in the Z peak region. The corresponding effect in the dimuon channel is negligibly small.

G.2 $d^2\sigma/dmd|y|$ Double-differential Cross Section Measurement

For the double-differential cross section measurement a dedicated procedure has been developed in order to take into account the effect of migration in bins of dilepton rapidity. The typical scale of the effect of migration between rapidity bins is defined by the rapidity resolution in a given invariant mass region, which varies from $\Delta y/y = 0.002$ at low mass and low rapidity to $\Delta y/y = 0.05$ at high masses.

To minimize the effect of migration in rapidity bins, the rapidity bin size was restricted to 0.1 in the region $m < 200$ GeV and 0.2 in the highest mass bin (200–1500 GeV). The corresponding rapidity bin size is considerably greater then the rapidity resolution scale in a given mass range.

Within the framework of the unfolding method for the double-differential cross section measurement, a two dimensional yield distribution in bins of dimuon invariant mass and rapidity is mapped onto a one dimensional vector. Once the flattened distribution is obtained, the unfolding procedure follows closely the standard technique for the differential $d\sigma/dm$ measurement described above.

The unfolding response matrix T_{ik}, giving the fraction of events from bin i of the true (post-FSR) distribution that end up reconstructed in bin k is calculated from the Monte Carlo simulation according to:

$$N_{\text{obs},i} = \sum_k T_{ik} N_{\text{true},k}, \tag{G.3}$$

here, the indices correspond to the flattened yield vector. The response matrix derived from the yields in bins of dilepton invariant mass and rapidity is shown in Fig. G.6.

Notice, that the structure of the response matrix is quite different from the corresponding matrix derived using the yields binned in invariant mass only. The matrix consists of three diagonal-dominated blocks with each block corresponding to a given generated and reconstructed invariant mass bin. There are two types of off-diagonal elements in this response matrix. The elements adjacent to the main diagonal, orig-

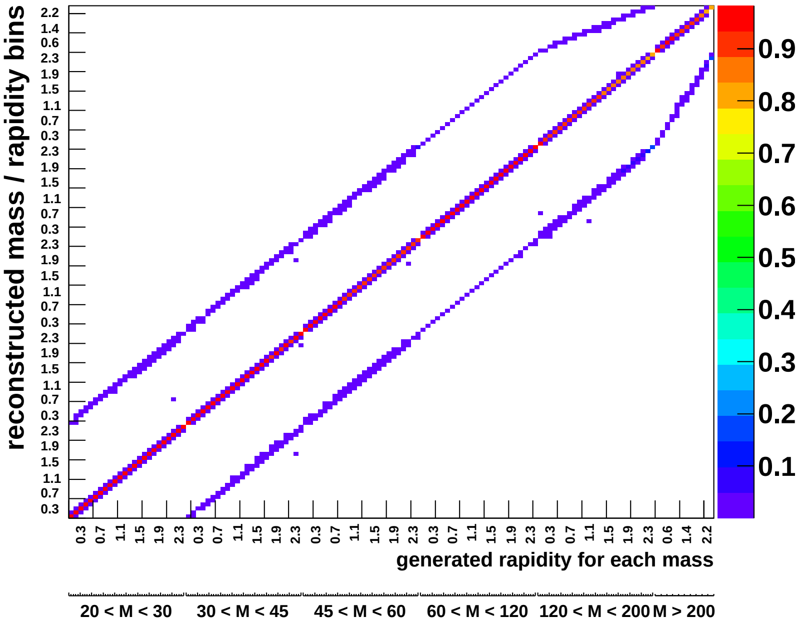

Figure G.6. The response matrix from simulation for the $d^2\sigma/dmd|y|$ measurement.

inate due to migration between rapidity bins within the same mass slice. Two additional sets of diagonal dominated blocks originate as a result of migration between mass slices.

The response matrix is inverted and used to unfold the flattened spectrum:

$$N_{u,k} = N_{\text{true},k} = \sum_i (T^{-1})_{ki} N_{\text{obs},i}. \tag{G.4}$$

Finally, the unfolded distribution is inflated back to the two dimensional invariant mass-rapidity distribution by performing index transformation.

The comparison of the observed yields before and after unfolding is shown in Fig. G.7.

A set of tests is performed to validate and justify this unfolding procedure as shown in Fig. G.8. A closure test confirmed the arithmetic validity of the procedure, and the stability and robustness of the method with respect to statistical fluctuations in the matrix elements was established with an ensemble of pseudo-experiments. The

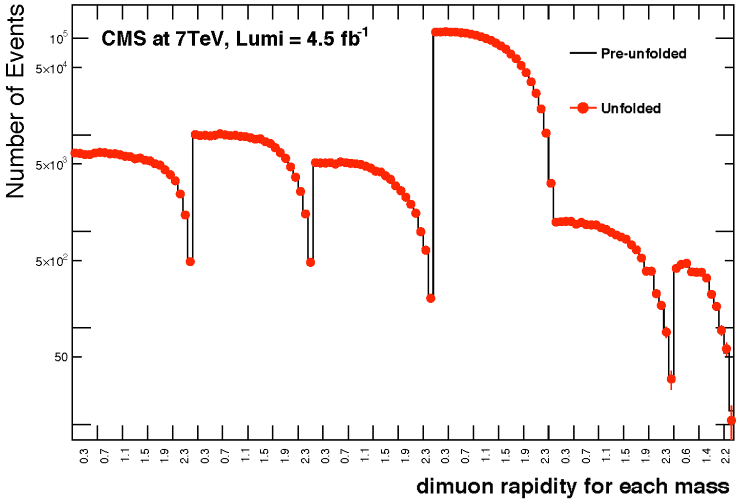

Figure G.7. The comparison of the observed yields in bins of dimuon rapidity-invariant mass before and after unfolding.

tests show that the conventional unfolding procedure described above is applicable for the unfolding of the dilepton rapidity-invariant mass yields.

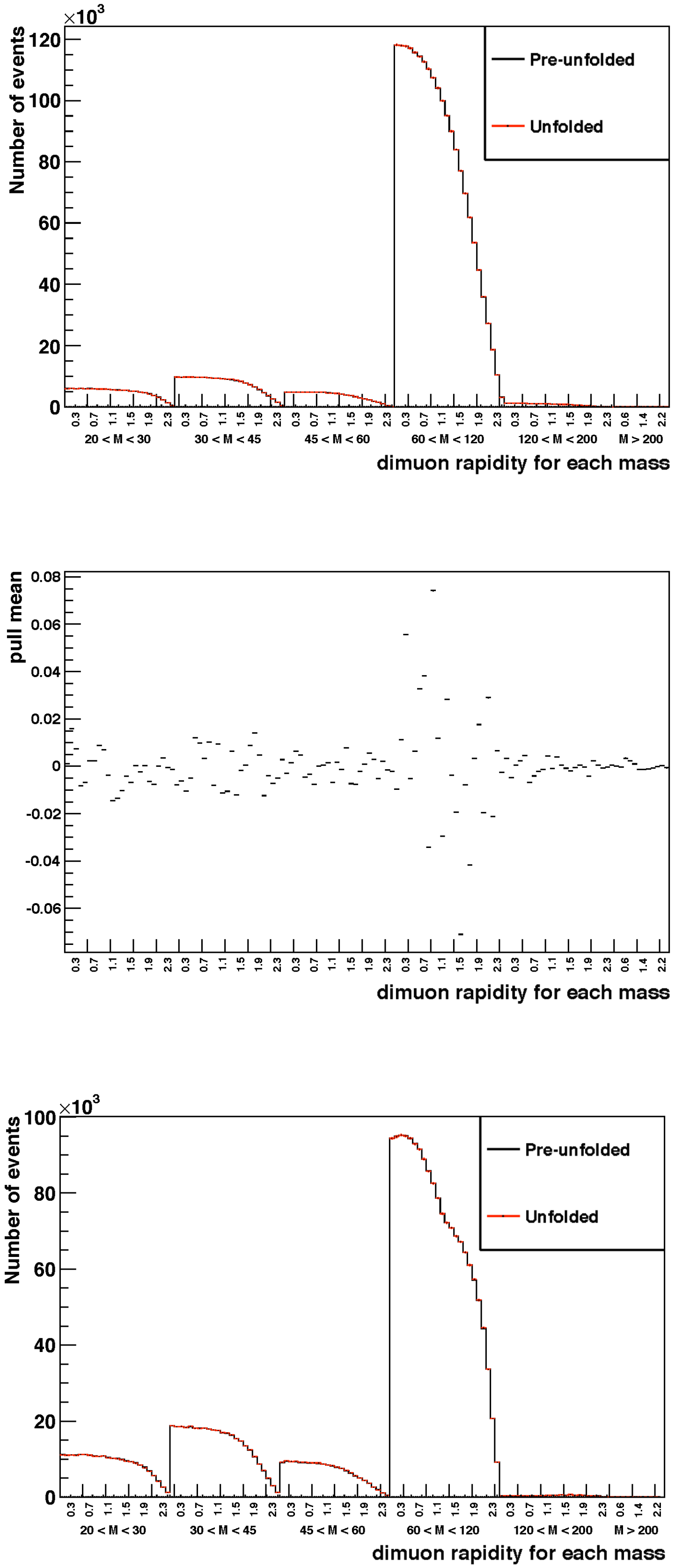

Figure G.8. Results for a set of tests: closure test (top), pull mean distribution from ensemble test (middle), and toy MC test (bottom).

H. SYSTEMATIC UNCERTYAINTY TABLES

H.1 Summary of the Systematic Uncertainties

The systematic uncertainties at 7 TeV in the dimuon channel are summarized in Tables H.1 and H2. for the $d\sigma/dm$ differential cross section measurement and Tables H.3-H.8 for $d^2\sigma/dmd|y|$ double-differential cross section measurement.

The systematic uncertainties at 8 TeV in the dielectron and dimuon channels are summarized in Tables H.9-H.12.

Table H.1
Summary of the systematic uncertainties for the dimuon channel $d\sigma/dm$ measurement (15–150 GeV). The "Total" is a quadratic sum of all sources except for the Acc.+PDF and Modeling.

m (GeV)	Eff. ρ (%)	Det. res. (%)	Bkg. est. (%)	FSR (%)	Total (%)	Acc.+PDF (%)	Model. (%)
15–20	1.90	0.03	0.28	0.54	2.09	2.29	9.70
20–25	2.31	0.24	0.63	0.47	2.47	3.15	3.10
25–30	2.26	0.27	2.95	0.40	3.76	2.73	1.90
30–35	1.48	0.17	1.94	0.46	2.50	2.59	0.70
35–40	1.19	0.09	1.26	0.66	1.88	2.61	0.50
40–45	1.12	0.07	0.97	0.30	1.54	2.49	0.30
45–50	1.10	0.07	0.86	0.44	1.50	2.51	0.10
50–55	1.07	0.10	0.67	0.58	1.42	2.44	0.10
55–60	1.07	0.15	0.69	0.77	1.52	2.36	0.20
60–64	1.06	0.19	0.35	0.94	1.50	2.27	0.20
64–68	1.06	0.22	0.24	1.06	1.55	2.22	0.30
68–72	1.06	0.30	0.20	1.13	1.60	2.20	0.20
72–76	1.05	0.51	0.15	1.13	1.65	2.18	0.20
76–81	1.06	0.94	0.25	1.01	1.77	2.15	0.20
81–86	1.11	1.56	0.10	0.69	2.06	2.18	0.10
86–91	1.07	2.21	0.01	0.23	2.48	2.12	0.20
91–96	1.08	2.55	0.01	0.12	2.78	2.14	0.20
96–101	1.29	2.32	0.08	0.15	2.68	2.12	0.30
101–106	1.31	1.69	0.14	0.19	2.17	2.07	0.30
106–110	1.32	1.05	0.28	0.22	1.76	2.01	0.50
110–115	1.34	0.65	0.34	0.25	1.59	1.97	0.60
115–120	1.33	0.47	0.43	0.27	1.55	1.95	0.60
120–126	1.36	0.37	0.56	0.29	1.60	1.91	0.50
126–133	1.35	0.33	0.70	0.30	1.65	1.88	0.60
133–141	1.31	0.42	0.90	0.32	1.75	1.85	0.70
141–150	1.29	0.64	1.08	0.35	1.91	1.81	1.00

Table H.2
Summary of the systematic uncertainties for the dimuon channel $d\sigma/dm$ measurement (150–1500 GeV). The "Total" is a quadratic sum of all sources except for the Acc.+PDF and Modeling.

m (GeV)	Eff. ρ (%)	Det. res. (%)	Bkg. est. (%)	FSR (%)	Total (%)	Acc.+PDF (%)	Model. (%)
150–160	1.36	0.87	1.20	0.39	2.13	1.82	1.10
160–171	1.42	0.99	1.48	0.39	2.39	1.82	1.10
171–185	1.53	0.96	1.72	0.41	2.61	1.75	1.10
185–200	1.60	0.77	1.80	0.51	2.67	1.75	1.10
200–220	1.71	0.52	1.82	0.42	2.64	1.53	1.00
220–243	1.75	0.39	2.28	0.44	3.01	1.48	1.50
243–273	1.86	0.49	2.46	0.46	3.23	1.40	1.40
273–320	1.90	0.72	2.37	0.50	3.24	1.31	1.30
320–380	1.90	0.96	2.88	0.57	3.73	1.28	1.50
380–440	1.93	1.31	3.54	0.57	4.44	1.45	1.20
440–510	1.97	1.74	4.64	0.57	5.50	1.60	1.30
510–600	2.02	1.79	4.48	0.57	5.28	0.50	2.10
600–1000	2.01	1.13	5.07	0.57	5.61	0.41	2.40
1000–1500	2.14	0.48	15.34	0.57	15.51	0.24	3.10

Table H.3

Summary of systematic uncertainties in the dimuon channel for $20 < m < 30$ GeV bin as a function of $|y|$. The “Total” is a quadratic sum of all sources.

$\|y\|$	Eff. ρ (%)	Det. res. (%)	Bkg. est. (%)	FSR (%)	Total (%)
	$20 < m < 30$ GeV				
0.0–0.1	6.21	0.29	0.57	0.76	6.29
0.1–0.2	6.01	0.37	0.56	0.58	6.07
0.2–0.3	6.01	0.33	0.55	1.15	6.15
0.3–0.4	5.57	0.41	0.48	0.57	5.63
0.4–0.5	5.21	0.45	0.56	0.70	5.31
0.5–0.6	4.87	0.32	0.57	0.54	4.94
0.6–0.7	4.51	0.33	0.52	0.64	4.60
0.7–0.8	3.89	0.38	0.55	0.42	3.97
0.8–0.9	3.42	0.31	0.54	0.57	3.52
0.9–1.0	3.14	0.26	0.53	0.77	3.29
1.0–1.1	2.92	0.49	0.53	0.61	3.07
1.1–1.2	2.87	0.50	0.58	0.47	3.01
1.2–1.3	3.09	0.44	0.51	0.46	3.20
1.3–1.4	3.62	0.37	0.62	0.47	3.72
1.4–1.5	3.87	0.50	0.60	0.92	4.05
1.5–1.6	4.12	0.55	0.59	0.44	4.22
1.6–1.7	4.40	0.62	0.66	0.48	4.52
1.7–1.8	4.76	0.51	0.65	0.45	4.85
1.8–1.9	4.82	0.76	0.71	0.69	4.98
1.9–2.0	4.88	0.60	0.69	0.56	4.99
2.0–2.1	4.84	0.46	0.72	1.26	5.07
2.1–2.2	5.22	0.67	0.89	1.68	5.59
2.2–2.3	6.84	1.16	1.02	3.37	7.78
2.3–2.4	8.40	1.14	1.56	4.96	9.94

Table H.4
Summary of systematic uncertainties in the dimuon channel for $30 < m < 45$ GeV bin as a function of $|y|$. The "Total" is a quadratic sum of all sources.

$\|y\|$	Eff. ρ (%)	Det. res. (%)	Bkg. est. (%)	FSR (%)	Total (%)
	$30 < m < 45$ GeV				
0.0–0.1	3.03	0.08	0.36	0.88	3.18
0.1–0.2	2.72	0.03	0.38	0.82	2.87
0.2–0.3	2.50	0.07	0.42	0.98	2.71
0.3–0.4	2.30	0.03	0.38	1.13	2.59
0.4–0.5	2.21	0.11	0.38	1.03	2.47
0.5–0.6	2.25	0.10	0.34	0.74	2.39
0.6–0.7	2.39	0.05	0.37	0.69	2.51
0.7–0.8	2.46	0.05	0.40	0.89	2.65
0.8–0.9	2.48	0.05	0.37	0.63	2.58
0.9–1.0	2.39	0.05	0.38	0.74	2.53
1.0–1.1	2.32	0.11	0.39	0.80	2.48
1.1–1.2	2.18	0.03	0.40	0.58	2.29
1.2–1.3	2.12	0.06	0.44	0.71	2.28
1.3–1.4	2.04	0.04	0.34	0.53	2.13
1.4–1.5	2.03	0.04	0.37	0.63	2.16
1.5–1.6	2.02	0.07	0.39	0.66	2.16
1.6–1.7	2.02	0.12	0.36	0.87	2.24
1.7–1.8	2.14	0.06	0.33	0.80	2.31
1.8–1.9	2.47	0.10	0.45	1.13	2.75
1.9–2.0	2.74	0.20	0.45	1.08	2.99
2.0–2.1	3.21	0.20	0.53	1.67	3.66
2.1–2.2	3.86	0.19	0.71	2.52	4.67
2.2–2.3	5.36	0.21	2.30	2.88	6.51
2.3–2.4	6.71	0.09	2.38	6.30	9.51

Table H.5

Summary of systematic uncertainties in the dimuon channel for $45 < m < 60$ GeV bin as a function of $|y|$. The "Total" is a quadratic sum of all sources.

$\|y\|$	Eff. ρ (%)	Det. res. (%)	Bkg. est. (%)	FSR (%)	Total (%)
	$45 < m < 60$ GeV				
0.0–0.1	1.75	0.02	0.48	0.93	2.04
0.1–0.2	1.70	0.15	0.49	1.19	2.14
0.2–0.3	1.64	0.05	0.54	1.74	2.45
0.3–0.4	1.52	0.07	0.50	1.60	2.26
0.4–0.5	1.45	0.04	0.54	3.12	3.48
0.5–0.6	1.37	0.08	0.47	0.71	1.61
0.6–0.7	1.38	0.04	0.50	1.09	1.83
0.7–0.8	1.38	0.05	0.56	1.71	2.27
0.8–0.9	1.39	0.02	0.49	0.62	1.60
0.9–1.0	1.44	0.07	0.54	0.70	1.69
1.0–1.1	1.44	0.02	0.48	1.07	1.86
1.1–1.2	1.53	0.08	0.42	1.92	2.50
1.2–1.3	1.63	0.10	0.47	1.25	2.11
1.3–1.4	1.55	0.03	0.38	0.72	1.75
1.4–1.5	1.40	0.23	0.38	0.77	1.65
1.5–1.6	1.31	0.03	0.33	2.29	2.66
1.6–1.7	1.34	0.11	0.39	1.37	1.96
1.7–1.8	1.41	0.04	0.70	1.17	1.96
1.8–1.9	1.52	0.07	0.30	3.04	3.42
1.9–2.0	1.69	0.02	0.31	4.16	4.50
2.0–2.1	1.78	0.06	0.55	5.31	5.63
2.1–2.2	2.21	0.31	1.27	4.42	5.11
2.2–2.3	2.96	0.11	0.62	9.98	10.4
2.3–2.4	4.76	0.11	0.26	15.1	15.8

Table H.6
Summary of systematic uncertainties in the dimuon channel for $60 < m < 120$ GeV bin as a function of $|y|$. The "Total" is a quadratic sum of all sources.

$\lvert y \rvert$	Eff. ρ (%)	Det. res. (%)	Bkg. est. (%)	FSR (%)	Total (%)
	$60 < m < 120$ GeV				
0.0–0.1	0.83	0.004	0.04	0.29	0.88
0.1–0.2	0.83	0.01	0.04	0.29	0.88
0.2–0.3	0.84	0.01	0.04	0.29	0.89
0.3–0.4	0.87	0.01	0.04	0.29	0.92
0.4–0.5	0.89	0.01	0.04	0.29	0.94
0.5–0.6	0.90	0.01	0.04	0.29	0.94
0.6–0.7	0.89	0.01	0.04	0.29	0.94
0.7–0.8	0.89	0.02	0.04	0.29	0.94
0.8–0.9	0.92	0.01	0.03	0.29	0.97
0.9–1.0	0.97	0.02	0.03	0.34	1.03
1.0–1.1	1.03	0.03	0.04	0.30	1.08
1.1–1.2	1.10	0.02	0.03	0.29	1.13
1.2–1.3	1.16	0.02	0.03	0.31	1.20
1.3–1.4	1.20	0.04	0.03	0.32	1.24
1.4–1.5	1.23	0.03	0.05	0.32	1.27
1.5–1.6	1.29	0.01	0.05	0.33	1.33
1.6–1.7	1.40	0.02	0.08	0.43	1.47
1.7–1.8	1.53	0.02	0.08	0.43	1.59
1.8–1.9	1.67	0.03	0.05	0.46	1.73
1.9–2.0	2.06	0.04	0.05	0.36	2.09
2.0–2.1	2.78	0.01	0.14	0.62	2.86
2.1–2.2	3.87	0.04	0.07	0.70	3.94
2.2–2.3	5.34	0.02	0.02	0.91	5.41
2.3–2.4	6.41	0.06	0.04	2.08	6.74

Table H.7

Summary of systematic uncertainties in the dimuon channel for $120 < m < 200$ GeV bin as a function of $|y|$. The "Total" is a quadratic sum of all sources.

$\|y\|$	Eff. ρ (%)	Det. res. (%)	Bkg. est. (%)	FSR (%)	Total (%)
	$120 < m < 200$ GeV				
0.0–0.1	1.68	0.28	2.17	0.56	2.81
0.1–0.2	1.60	0.16	2.03	0.72	2.68
0.2–0.3	1.56	0.26	2.09	1.05	2.82
0.3–0.4	1.57	0.53	1.89	0.78	2.63
0.4–0.5	1.49	0.27	1.67	0.67	2.35
0.5–0.6	1.47	0.25	1.69	0.38	2.29
0.6–0.7	1.57	0.33	1.97	0.54	2.60
0.7–0.8	1.43	0.39	1.62	0.37	2.22
0.8–0.9	1.42	0.07	1.92	0.52	2.44
0.9–1.0	1.35	0.48	1.53	0.37	2.13
1.0–1.1	1.31	0.16	1.37	0.41	1.94
1.1–1.2	1.34	0.36	1.39	0.45	2.02
1.2–1.3	1.51	0.45	1.35	0.57	2.15
1.3–1.4	1.82	0.06	1.26	0.40	2.25
1.4–1.5	2.17	0.85	1.04	0.44	2.59
1.5–1.6	2.76	0.14	1.08	0.43	3.00
1.6–1.7	3.44	0.30	0.83	0.39	3.57
1.7–1.8	4.09	0.41	0.94	1.02	4.34
1.8–1.9	5.37	0.17	1.03	1.09	5.57
1.9–2.0	6.62	0.10	0.84	1.20	6.78
2.0–2.1	8.52	0.16	0.89	0.60	8.58
2.1–2.2	12.3	0.85	0.70	0.51	12.3
2.2–2.3	16.8	0.41	0.95	1.91	16.9
2.3–2.4	20.2	0.51	1.91	1.26	20.4

Table H.8

Summary of systematic uncertainties in the dimuon channel for $200 < m < 1500$ GeV bin as a function of $|y|$. The "Total" is a quadratic sum of all sources.

$\|y\|$	Eff. ρ (%)	Det. res. (%)	Bkg. est. (%)	FSR (%)	Total (%)
	$200 < m < 1500$ GeV				
0.0–0.2	2.18	0.30	7.51	0.56	7.85
0.2–0.4	1.84	0.04	5.31	0.47	5.64
0.4–0.6	1.68	0.32	4.33	0.53	4.69
0.6–0.8	1.70	0.07	4.57	0.58	4.91
0.8–1.0	1.83	0.12	3.47	0.66	3.99
1.0–1.2	2.28	0.44	3.10	0.66	3.93
1.2–1.4	3.50	0.08	1.92	0.59	4.03
1.4–1.6	5.28	0.65	2.15	0.56	5.77
1.6–1.8	7.14	0.19	2.11	0.98	7.51
1.8–2.0	10.4	0.86	2.17	0.61	10.6
2.0–2.2	17.8	0.15	0.99	0.98	17.8
2.2–2.4	28.8	0.42	1.99	1.36	28.9

Table H.9

Summary of the systematic uncertainties for the dimuon channel $d\sigma/dm$ measurement (15–150 GeV). The "Total" is a quadratic sum of all sources except for the Acc.+PDF and Modeling.

m (GeV)	Mom. scale (%)	Eff.ρ (%)	Det. res. (%)	Bkg. est. (%)	FSR (%)	Total (%)	Acc.+PDF (%)	Model. (%)
15-20	0.02	1.35	0.43	0.51	0.43	1.57	4.00	2.01
20-25	0.15	0.99	0.62	1.01	0.37	1.60	3.78	1.65
25-30	0.19	0.81	0.44	1.21	0.34	1.57	3.57	1.31
30-35	0.15	0.69	0.35	1.30	0.33	1.56	3.35	1.00
35-40	0.09	0.56	0.31	1.27	0.26	1.45	3.12	0.72
40-45	0.05	0.56	0.32	1.14	0.25	1.33	2.90	0.49
45-50	0.06	0.51	0.46	1.10	0.34	1.34	2.68	0.30
50-55	0.08	0.42	0.64	1.02	0.47	1.36	2.46	0.17
55-60	0.12	0.38	0.96	1.00	0.60	1.57	2.26	0.08
60-64	0.14	0.35	1.68	1.13	0.78	2.20	2.08	0.02
64-68	0.17	0.32	2.17	0.90	0.99	2.58	1.92	0.00
68-72	0.24	0.31	2.74	0.65	1.11	3.05	1.80	0.00
72-76	0.43	0.30	2.55	0.43	1.05	2.84	1.70	0.01
76-81	0.79	0.30	1.90	0.18	0.83	2.25	1.64	0.03
81-86	1.28	0.32	1.49	0.07	0.53	2.06	1.61	0.06
86-91	1.74	0.38	1.75	0.01	0.24	2.51	1.60	0.10
91-96	1.96	0.40	1.96	0.01	0.10	2.80	1.62	0.14
96-101	1.81	0.40	1.85	0.06	0.11	2.62	1.66	0.18
101-106	1.38	0.39	1.57	0.18	0.15	2.14	1.72	0.23
106-110	0.90	0.38	1.72	0.38	0.18	2.02	1.80	0.27
110-115	0.55	0.39	1.46	0.45	0.20	1.68	1.89	0.32
115-120	0.36	0.39	1.66	0.50	0.22	1.83	1.99	0.37
120-126	0.28	0.42	1.51	0.55	0.23	1.70	2.10	0.41
126-133	0.28	0.45	1.52	0.58	0.24	1.73	2.23	0.46
133-141	0.36	0.43	1.56	0.86	0.26	1.89	2.37	0.49
141-150	0.52	0.42	1.64	0.92	0.28	2.01	2.53	0.53

Table H.10
Summary of the systematic uncertainties for the dimuon channel $d\sigma/dm$ measurement (150–2000 GeV). The "Total" is a quadratic sum of all sources except for the Acc.+PDF and Modeling.

m (GeV)	Mom. scale (%)	Eff.ρ (%)	Det. res. (%)	Bkg. est. (%)	FSR (%)	Total (%)	Acc.+PDF (%)	Model. (%)
150-160	0.68	0.46	1.78	0.95	0.31	2.20	2.69	0.56
160-171	0.78	0.49	1.84	1.26	0.32	2.44	2.86	0.59
171-185	0.74	0.52	1.71	1.32	0.33	2.37	3.03	0.61
185-200	0.60	0.55	1.69	1.75	0.33	2.59	3.19	0.65
200-220	0.44	1.10	1.19	1.71	0.34	2.42	3.44	0.70
220-243	0.36	1.25	1.06	2.09	0.35	2.70	3.62	0.76
243-273	0.42	1.34	1.11	2.14	0.37	2.82	3.80	0.85
273-320	0.59	1.53	1.07	2.18	0.40	2.96	3.97	0.96
320-380	0.80	1.87	1.31	3.31	0.45	4.12	4.23	1.10
380-440	1.02	1.23	1.58	4.66	0.46	5.20	4.19	1.28
440-510	1.22	1.36	1.37	5.15	0.46	5.65	4.40	1.48
510-600	1.38	1.56	1.62	5.34	0.45	5.97	4.65	1.70
600-1000	1.55	1.77	1.60	4.62	0.46	5.44	4.92	1.95
1000-1500	1.76	2.39	1.94	13.89	0.46	14.34	5.33	2.20
1500-2000	2.17	3.39	2.30	59.31	0.46	59.50	5.62	2.42

Table H.11
Summary of the systematic uncertainties for the dielectron channel $d\sigma/dm$ measurement (15–150 GeV). The “Total” is a quadratic sum of all sources except for the Acc.+PDF and Modeling.

m (GeV)	E−scale (%)	Eff.ρ (%)	Det. res. (%)	Bkg. est. (%)	FSR (%)	Coll. CS (%)	Total (%)	Acc.+PDF (%)	Model. (%)
15-20	0.16	3.44	0.51	1.69	0.38	1.06	4.03	4.24	2.01
20-25	0.23	2.85	0.63	2.16	0.38	1.67	4.02	3.82	1.65
25-30	0.08	3.39	0.49	2.89	0.52	2.08	4.97	3.60	1.31
30-35	0.18	4.34	0.40	2.88	0.54	2.41	5.78	3.36	1.00
35-40	0.20	3.54	0.35	0.85	0.47	2.30	4.35	3.13	0.72
40-45	0.11	2.95	0.34	0.89	0.39	1.94	3.68	2.91	0.49
45-50	0.05	2.38	0.40	1.04	0.30	1.72	3.15	2.69	0.30
50-55	0.06	2.02	0.50	1.07	0.21	1.48	2.78	2.48	0.17
55-60	0.03	1.78	0.63	1.13	0.25	1.30	2.57	2.29	0.08
60-64	0.09	1.65	0.84	0.95	0.48	1.14	2.42	2.13	0.02
64-68	0.35	1.51	0.94	0.76	0.75	1.14	2.40	1.99	0.00
68-72	0.73	1.40	1.02	0.67	1.01	0.84	2.39	1.87	0.00
72-76	1.70	1.23	0.95	0.43	1.22	0.94	2.80	1.77	0.01
76-81	3.43	0.93	0.65	0.22	1.15	0.88	3.90	1.67	0.03
81-86	6.19	0.68	0.34	0.09	0.65	0.89	6.34	1.62	0.06
86-91	2.37	0.49	0.06	0.02	0.25	0.67	2.52	1.60	0.10
91-96	1.99	0.45	0.05	0.02	0.50	0.45	2.15	1.62	0.14
96-101	4.88	0.44	0.21	0.05	0.59	0.05	4.94	1.67	0.18
101-106	3.38	0.48	0.35	0.13	0.53	0.14	3.48	1.74	0.23
106-110	2.20	0.60	0.60	0.20	0.51	0.38	2.45	1.83	0.27
110-115	1.59	0.63	0.61	0.30	0.50	0.19	1.92	1.93	0.32
115-120	1.35	0.72	0.73	0.43	0.52	0.13	1.83	2.04	0.37
120-126	1.10	0.76	0.78	0.57	0.53	0.16	1.74	2.16	0.41
126-133	0.89	0.85	0.84	0.74	0.55	0.02	1.75	2.31	0.46
133-141	0.87	0.90	0.91	0.89	0.57	0.45	1.92	2.45	0.49
141-150	0.85	0.98	0.99	1.12	0.58	0.32	2.09	2.62	0.53

Table H.12

Summary of the systematic uncertainties for the dielectron channel $d\sigma/dm$ measurement (150–2000 GeV). The "Total" is a quadratic sum of all sources except for the Acc.+PDF and Modeling.

m (GeV)	E−scale (%)	Eff.ρ (%)	Det. res. (%)	Bkg. est. (%)	FSR (%)	Coll. CS (%)	Total (%)	Acc.+PDF (%)	Model. (%)
150-160	0.52	1.08	1.07	1.33	0.67	0.18	2.20	2.80	0.56
160-171	0.76	1.17	1.21	1.53	0.70	0.34	2.52	2.98	0.59
171-185	0.55	1.18	1.12	1.82	0.72	0.19	2.61	3.14	0.61
185-200	0.78	1.30	1.19	2.15	0.71	0.41	3.00	3.34	0.65
200-220	0.84	0.94	0.86	2.62	0.54	0.02	3.09	3.41	0.70
220-243	0.42	1.01	0.86	2.74	0.60	0.01	3.14	3.57	0.76
243-273	0.72	1.08	0.87	3.19	0.65	0.01	3.61	3.74	0.85
273-320	0.71	1.10	0.86	3.67	0.64	0.37	4.06	3.89	0.96
320-380	0.99	1.19	0.93	3.75	0.73	0.01	4.22	4.07	1.10
380-440	0.51	1.13	1.02	5.42	0.76	0.10	5.70	4.24	1.28
440-510	0.60	0.82	0.48	6.33	0.44	0.13	6.45	4.41	1.48
510-600	1.14	0.78	0.74	7.90	0.43	0.37	8.07	4.65	1.70
600-1000	2.01	0.74	0.35	13.79	0.34	0.12	13.97	4.91	1.95
1000-1500	3.23	0.75	0.38	39.86	0.20	0.33	40.00	5.20	2.20
1500-2000	4.78	0.77	0.41	237.35	0.33	0.23	237.40	5.50	2.42

LIST OF REFERENCES

LIST OF REFERENCES

[1] S. Weinberg. Implications of dynamical symmetry breaking. *Phys. Rev. D*, 13:974, 1976.

[2] L. Randall and R. Sundrum. A Large Mass Hierarchy from a small Extra Dimension. *Phys. Rev. Lett.*, 83:3370, 1999.

[3] L. Susskind. Dynamics of spontaneous symmetry breaking in the Weinberg-Salam theory. *Phys. Rev. D*, 20:2619, 1979.

[4] V. Trimble. Existence and nature of dark matter in the universe. *Annu. Rev. Astron. Astrophys.*, 25:425, 1987.

[5] S. Weinberg. A Model of Leptons. *Phys. Rev. Lett.*, 19:1264, 1967.

[6] R. Hamberg, W. van Neerven, and T. Matsuura. A complete calculation of the order α_s^2 correction to the Drell–Yan K-factor. *Nucl. Phys. B*, 359:343, 1991.

[7] S. Catani, L. Cieri, G. Ferrera, D. de Florian, and M. Grazzini. Vector boson production at hadron colliders: a fully exclusive QCD calculation at NNLO. *Phys. Rev. Lett.*, 103:082001, 2009.

[8] S. Catani and M. Grazzini. An NNLO subtraction formalism in hadron collisions and its application to Higgs boson production at the LHC. *Phys. Rev. Lett.*, 98:222002, 2007.

[9] K. Melnikov and F. Petriello. Electroweak gauge boson production at hadron colliders through $\mathrm{O}(\alpha_s^2)$. *Phys. Rev. D*, 74:114017, 2006.

[10] M. Klein and R. Yoshida. Collider physics at HERA. *Progress in Particle and Nuclear Physics*, 61:343, 2008.

[11] SLAC Collaboration. Precise measurements of the proton and deuteron structure functions from a global analysis of the SLAC deep inelastic electron scattering cross sections. *Phys. Lett. B*, 282:475, 1992.

[12] G. Moreno et al. Dimuon production in proton-copper collisions at $\sqrt{s} = 38.8\,\mathrm{GeV}$. *Phys. Rev. D*, 43:2815, 1991.

[13] R. Towell et al. Improved measurement of the $\bar{d}/\bar{u}$ asymmetry in the nucleon sea. *Phys. Rev. D*, 64:052002, 2001.

[14] CDF Collaboration. Direct measurement of the W Production Charge Asymmetry in $\mathrm{p\bar{p}}$ Collisions at $\sqrt{s} = 1.96\,\mathrm{TeV}$. *Phys. Rev. Lett.*, 102:181801, 2009.

[15] D0 Collaboration. Measurement of the shape of the boson rapidity distribution for $\mathrm{p\bar{p}} \rightarrow \mathrm{Z}/\gamma^* \rightarrow \mathrm{e^+e^-} + X$ events produced at $\sqrt{s}$ of 1.96 TeV. *Phys. Rev. D*, 76:012003, 2007.

[16] S. Forte and G. Watt. Progress in the Determination of the Partonic Structure of the Proton. *Annu. Rev. Nucl. Part. Sci.*, 63, 2013.

[17] R. Ball et al. Parton Distribution Benchmarking with LHC Data. *JHEP*, 04:125, 2013.

[18] M. Mangano and J. Rojo. Cross Section Ratios between different CM energies at the LHC: opportunities for precision measurements and BSM sensitivity. *JHEP*, 08:010, 2012.

[19] CMS Collaboration. Measurement of the differential and double-differential Drell–Yan cross sections in proton-proton collisions at $\sqrt{s} = 7$ TeV. *JHEP*, 12:030, 2013.

[20] CMS Collaboration. Measurements of differential and double-differential Drell-Yan cross sections in proton-proton collisions at 8 TeV. *arXiv:1412.1115*, 2014. Submitted to Eur. Phys. J. C.

[21] P. Higgs. Massless Particles and Gauge Fields. *Phys. Lett.*, 12:132, 1964.

[22] S. Glashow. Partial Symmetries of Weak Interactions. *Nucl. Phys.*, 22:579, 1961.

[23] S. Glashow, J. Iliopoulos, and L. Maiani. Weak Interactions with Lepton-Hadron Symmetry. *Phys. Rev. D*, 2:1285, 1970.

[24] J. Goldstone, A. Salam, and S. Weinberg. Broken Symmetries. *Phys. Rev.*, 127:965, 1962.

[25] N. Cabibbo. Unitary Symmetry and Leptonic Decays. *Phys. Rev. Lett.*, 10:531, 1963.

[26] M. Kobayashi and T. Maskawa. CP-violation in Renormalizible Theory of Weak interaction. *Progr. Theoret. Phys.*, 49:652, 1973.

[27] P. Higgs. Spontaneous Symmetry Breakdown without Massless Bosons. *Phys. Rev.*, 145:1156, 1966.

[28] F. Hasert et al. Observation of neutrino-like interactions without muon or electron in the Gargamelle neutrino experiment. *Phys. Lett. B*, 46:138, 1973.

[29] F. Hasert et al. Search for elastic muon-neutrino electron scattering. *Phys. Lett. B*, 46:121, 1973.

[30] UA1 Collaboration. Experimental observation of isolated large transverse energy electrons with associated missing energy at $\sqrt{s} = 540$ GeV source. *Phys. Lett. B*, 112:103, 1983.

[31] UA2 Collaboration. Observation of single isolated electrons of high transverse momentum in events with missing transverse energy at the CERN. *Phys. Lett. B*, 122:476, 1983.

[32] UA2 Collaboration. Evidence for Z → e^+e^- at the CERN $p\bar{p}$ Collider. *Phys. Lett. B*, 129:130, 1983.

[33] R. Barate et al. Search for the standard model Higgs boson at LEP. *Phys. Lett. B*, 565:61–75, 2003.

[34] ATLAS Collaboration. Observation of a new particle in the search for the Standard Model Higgs boson with the ATLAS detector at the LHC. *Phys. Lett. B*, 716:1, 2012.

[35] CMS Collaboration. Observation of a new boson at a mass of 125 GeV with the CMS experiment at the LHC. *Phys. Lett. B*, 716:30, 2012.

[36] M. Peskin and D. Schroeder. *An Introduction To Quantum Field Theory.* Westview Press, 1995.

[37] G. Branco, L. Lavoura, and J. Silva. *CP violation.* Clarendon Press, 1999.

[38] J. Beringer et al. (Particle Data Group). 2012 Review of Particle Physics. *Phys. Rev. D*, 86, 2012.

[39] J. Pumplin et al. New Generation of Parton Distributions with Uncertainties from Global QCD Analysis. *JHEP*, 07:035, 2002.

[40] F. Halzen and D. Martin. *Quarks and Leptons: An Introductory Course in Modern Particle Physics.* Wiley, New York, USA, 1984.

[41] A. De Rujula, H. Georgi and H. Politzer. The Breakdown of Scaling in Neutrino and electron Scattering. *Phys. Rev. D*, 10:2141, 1974.

[42] Y. Dokshitzer. Calculation of the Structure Functions for Deep Inelastic Scattering and e^+e^- Annihilation by Perturbation Theory in Quantum Chromodynamics. *Sov. Phys. JETP*, 46:641, 1977.

[43] V. Gribov and L. Lipatov. Deep inelastic e p scattering in perturbation theory. *Sov. J. Nucl. Phys.*, 15:438, 1972.

[44] G. Altarelli and G. Parisi. Asymptotic Freedom in Parton Language. *Nucl. Phys. B*, 126:298, 1977.

[45] `http://mstwpdf.hepforge.org/`.

[46] `http://www.phys.psu.edu/~cteq/`.

[47] H1 and ZEUS Collaborations. Combined measurement and QCD analysis of the inclusive $e^{\pm}p$ scattering cross sections at HERA. *JHEP*, 01:109, 2010.

[48] `http://sophia.ecm.ub.es/nnpdf/`.

[49] P. McGaughey et al. Cross sections for the production of high-mass muon pairs from 800 GeV proton bombardment of 2H. *Phys. Rev. D*, 50:3038, 1994.

[50] H1 Collaboration. Measurement of DIS cross section at HERA. *Braz. J. Phys.*, 37:793, 2007.

[51] R. Ball et al. A first unbiased global NLO determination of parton distributions and their uncertainties. *Nucl. Phys. B*, 838:136, 2010.

[52] D. Ball, V. Bertone, F. Cerutti, L. Del Debbio, S. Forte et al. Impact of Heavy Quark Masses on Parton Distributions and LHC Phenomenology. *Nucl. Phys. B*, 849:296, 2011.

[53] G. Altarelli, R. Ellis, and G. Martinelli. Large Perturbative Corrections to the Drell–Yan Process in QCD. *Nucl. Phys. B*, 157:461, 1979.

[54] K. Harada, T. Kaneko, and N. Sakai. Hadronic Lepton-Pair Production Beyond the Leading Order in Perturbative QCD. *Nucl. Phys. B*, 155:169, 1979.

[55] S. Drell and T. Yan. Massive lepton-pair production in hadron-hadron collisions at high energies. *Phys. Rev. Lett. 25, 316*, 1970.

[56] J. Christenson et al. Observation of Massive Muon Pairs in Hadron Collisions. *Phys. Rev. Lett.*, 25:1523, 1970.

[57] CMS Collaboration. Forward-backward asymmetry of Drell–Yan lepton pairs in pp collisions at $\sqrt{s} = 7$ TeV. *Phys. Lett. B*, 718:752–772, 2013.

[58] U. Baur. Weak Boson Emission in Hadron Collider Processes. *Phys. Rev. D*, 75:013005, 2007.

[59] T. Kinoshita. Mass Singularities of Feynman Amplitudes. *J. Math. Phys.*, 3:650, 1962.

[60] U. Baur, O. Brein, W. Hollik, C. Schappacher, and D. Wackeroth. Electroweak radiative corrections to neutral-current Drell–Yan processes at hadron colliders. *Phys. Rev. D*, 65:033007, 2002.

[61] G. Grunberg. Renormalization-scheme-invariant QCD and QED: The method of effective charges. *Phys. Rev. D*, 29:2315–2338, May 1984.

[62] E. Mirkes and J. Ohnemus. W and Z polarization effects in hadronic collisions. *Phys. Rev. D*, 50:5692–5703, Nov 1994.

[63] J. Collins and D. Soper. Angular distribution of dileptons in high-energy hadron collisions. *Phys. Rev. D*, 16:2219–2225, Oct 1977.

[64] E. Mirkes and J. Ohnemus. Angular distributions of Drell-Yan lepton pairs at the Fermilab Tevatron: Order α_s^2 corrections and Monte Carlo studies. *Phys. Rev. D*, 51:4891–4904, May 1995.

[65] A. Ito. Measurement of the continuum of dimuons produced in high-energy proton-nucleus collisions. *Phys.Rev. D*, 23:604, 1981.

[66] K. Anderson. Production of Muon Pairs by 225-GeV/c $\pi^{\pm}$, K^{+}, $\mathrm{p}^{\pm}$ Beams on Nuclear Targets. *Phys. Rev. Lett.*, 42:944, 1979.

[67] J. Badler et al. Experimental cross section for dimuon production and the Drell–Yan model. *Phys. Lett. B*, 89:145, 1979.

[68] CDF Collaboration. Measurement of $d\sigma/dm$ and forward-backward charge asymmetry for high mass Drell–Yan e^+e^- pairs from collisions at $\sqrt{s} = 1.8$ TeV. *Phys. Rev. Lett.*, 87:131802, 2001.

[69] D0 Collaboration. Measurement of the high-mass Drell–Yan cross section and limits on quark-electron compositeness scales. *Phys. Rev. Lett.*, 82:4796, 1999.

[70] A. Bodek et al. Implication of W-Boson Charge Asymmetry Measurements in pp Collisions for Models of Charge Symmetry Violations in Parton Distributions. *Phys. Rev. Lett.*, 83:15, 1999.

[71] P. Nadolsky et al. Implications of CTEQ global analysis for collider observables. *Phys. Rev. D*, 78:013004, 2008.

[72] `http://www.hep.phy.cam.ac.uk/~wjs/plots/plots.html`.

[73] R. Corke and T. Sjostrand. Multiparton Interactions and Rescattering. *JHEP*, 01:035, 2010.

[74] CMS Collaboration. The CMS experiment at the CERN LHC. *JINST*, 3:S08004, 2008.

[75] `http://lpc.web.cern.ch/lpc/`.

[76] CMS Collaboration. Energy Calibration and Resolution of the CMS Electromagnetic Calorimeter in *pp* Collisions at $\sqrt{s} = 7$ TeV. *JINST*, 8:P09009, 2013.

[77] CMS Collaboration. The magnet project: Technical design report. *CERN/LHCC*, 97:10, 1997.

[78] CMS Collaboration. Performance of CMS muon reconstruction in pp collision events at $\sqrt{s} = 7$ TeV. *JINST*, 7:P10002, 2012.

[79] J. Han. The Differential cross section distribution of Drell-Yan dielectron pairs in the Z boson mass region. 2008.

[80] Y. Li and F. Petriello. Combining QCD and electroweak corrections to dilepton production in the framework of the FEWZ simulation code. *Phys. Rev. D*, 86:094034, 2012.

[81] R. Gavin, Y. Li, F. Petriello, and S. Quackenbush. FEWZ 2.0: A code for hadronic Z production at next-to-next-to-leading order. *Comput. Phys. Commun.*, 182:2388, 2011.

[82] H. Lai, M. Guzzi, J. Huston, Z. Li, P. Nadolsky et al. New parton distributions for collider physics. *Phys. Rev. D*, 82:074024, 2010.

[83] A. Martin, W. Stirling, R. Thorne and G. Watt. Parton distributions for the LHC. *Eur. Phys. J. C*, 63:189, 2009.

[84] P. Jimenez-Delgado and E. Reya. Dynamical next-to-next-to-leading order parton distributions. *Phys. Rev. D*, 79:074023, 2009.

[85] S. Alekhin, J. Blumlein, S. Klein, and S. Moch. The 3, 4, and 5-flavor NNLO Parton from Deep-Inelastic-Scattering Data and at Hadron Colliders. *Phys. Rev. D*, 81:014032, 2010.

[86] CMS Collaboration. Commissioning of the particle-flow event reconstruction with the first LHC collisions recorded in the CMS detector. *CMS Physics Analysis Summary CMS-PAS-PFT-10-001*, 2010.

[87] CMS Collaboration. Commissioning of the particle-flow reconstruction in minimum-bias and jet events from pp collisions at 7 TeV. *CMS Physics Analysis Summary CMS-PAS-PFT-10-002*, 2010.

[88] CMS Collaboration. Energy calibration and resolution of the CMS electromagnetic calorimeter in pp collisions at $\sqrt{s} = 7$ TeV. *JINST*, 8:P09009, 2013.

[89] R. Boughezal, Y. Li and F. Petriello. Disentangling radiative corrections using high-mass drell–yan at the lhc. *Phys. Rev. D*, 89:034030, 2014.

[90] CMS Collaboration. Measurement of the W and Z inclusive production cross sections at $\sqrt{s} = 7$ TeV with the CMS experiment at the LHC. *JHEP*, 01:080, 2011.

[91] Particle Data Group. Review of Particle Physics. *Phys. Rev. D*, 86:010001, 2012.

[92] A. Bodek et al. Extracting muon momentum scale corrections for hadron collider experiments. *Eur. Phys. J. C*, 72:2194, 2012.

[93] CMS Collaboration. Measurement of the properties of a Higgs boson in the four-lepton final state. *Phys. Rev. D*, 89:092007, 2014.

[94] G. D'Agostini. A multidimensional unfolding method based on Bayes' theorem. *Nucl. Instrum. Meth. A*, 362:487, 1995.

[95] D. Bourilkov. Study of parton density function uncertainties with LHAPDF and PYTHIA at LHC. *arxiv:hep-ph/0305126*, 2003.

[96] M. Whalley, D. Bourilkov and R. Group. The Les Houches accord PDFs (LHAPDF) and LHAGLUE. *arxiv:hep-ph/0508110*, 2005.

[97] D. Bourilkov, R. Group and M. Whalley. LHAPDF: PDF use from the Tevatron to the LHC. *arxiv:hep-ph/0605240*, 2006.

[98] CMS Collaboration. Measurement of the inclusive W and Z cross sections at 8 TeV. *Phys. Rev. Lett.*, 112:191802, 2014.

[99] G. Lafferty and T. Wyatt. Where to stick your data points: The treatment of measurements within wide bins. *Nucl. Instr. Meth. A*, 355:541, 1995.

[100] CMS Collaboration. Measurement of the Drell–Yan Cross Section in pp Collisions at $\sqrt{s} = 7$ TeV. *JHEP*, 10:007, 2011.

[101] A. Valassi. Combining correlated measurements of several different physical quantities. *Nucl. Instrum. Meth. A*, 500:391, 2003.

[102] CDF Collaboration. Measurement of $d\sigma/dy$ of Drell–Yan e^+e^- pairs in the Z mass region from $p\bar{p}$ collisions at $\sqrt{s} = 1.96$ TeV. *Phys. Lett. B*, 692:232, 2010.

[103] ATLAS Collaboration. Measurement of the high-mass Drell–Yan differential cross-section in pp collisions at $\sqrt{s} = 7$ TeV with the ATLAS detector. *Phys. Lett. B*, 725:223, 2013.

[104] ATLAS Collaboration. Measurement of the low-mass Drell–Yan differential cross section at $\sqrt{s} = 7\,\text{TeV}$ using the ATLAS detector. *JHEP*, 1406:112, 2014.

[105] M. Baldin and V. Goldanski. *Kinematics of Nuclear Reactions.* Oxford, Pergamon, 1961.

[106] J. Collins and D. Soper. Angular distribution of dileptons in high-energy hadron collisions. *Phys. Rev. D*, 16:7, 1977.

[107] CMS Pileup MC Reweighting Utilities twiki page: `https://twiki.cern.ch/twiki/bin/viewauth/CMS/PileupMCReweightingUtilities`.

[108] GEANT4 Collaboration. GEANT4: A simulation toolkit. *Nucl. Instrum. Meth. A*, 506:250, 2003.

[109] T. Sjöstrand, S. Mrenna, and P. Skands. PYTHIA 6.4 Physics and Manual. *JHEP*, 05:026, 2006.

[110] J. Alwall et al. Madgraph v5: going beyond. *JHEP*, 06:128, 2011.

[111] Z. Was. TAUOLA the library for tau lepton decay. *Nucl. Phys. Proc. Suppl.*, 98:96, 2001.

[112] R. Field. Min-Bias and the Underlying Event at the LHC. *Acta. Phys. Polon. B*, 42:2631, 2011.

[113] S. Alioli, P. Nason, C. Oleari, and E. Re. NLO vector-boson production matched with shower in POWHEG. *JHEP*, 07:060, 2008.

[114] T. Adye. Unfolding algorithms and tests using RooUnfold. *Proceedings of the PHYSTAT 2011 Workshop*, page 313318, 2011.